Monte Carlo Modelling for Photon and Proton Therapy in Heterogenous Tissue and Prosthesis Material

Swansea University
Prifysgol Abertawe

Ahmad A Abbas

Submitted to Swansea University in fulfilment of the requirements for the degree of Doctor of Philosophy

School of Medicine

Swansea University

2023

Abstract

Treatment outcomes in radiotherapy can be improved by reducing uncertainties in patient set-up, beam delivery and dose distribution. Clarification of arrangements can minimize the dose distributed to normal tissues, and facilitate dose escalation. However, heterogeneity can increase any ambiguities associated with dose distribution. The treatment planning system (TPS) cannot effectively calculate dose distribution in complex heterogeneous areas, which increases uncertainty. This research aims to study microscopic dose distribution in temporal bone, cochlea and pancreatic stents as applicable to modern radiotherapy treatments. To achieve this aim a multiscale approach will be used, as it provides essential information about differences in dose distribution between TPS/clinical CT and Monte Carlo (MC)/Micro CT for photons and protons.

In the first part of this study, two DICOM series of pancreatic cancer patients were used with an inserted stent. A new model includes the atomic composition of the stent material, and new stent contouring was introduced to overcome a CT artefact. A PRIMO Monte Carlo model was tuned and compared with the TPS dose distribution and a one-beam volume-modulated arc therapy (VMAT) plan was created. A significant dose difference was observed when comparing the new model and TPS, suggesting increased uncertainty of the dose distribution in clinical practice.

An open-access DICOM format of the data for the resected temporal bone and cochlea tissue was used with the FLUKA MC code to imitate potential high-dose scenarios associated with VMAT using the FLOOD option. Twenty-three photon and proton energy levels ranging from 0.055 to 5.5 MeV for photons and 37.59 to 124.83 MeV for protons were simulated separately to calculate dose distribution. Micro CT data shows three density levels in the temporal bone and cochlea. The photon distribution in the low energy range 0.055-0.09 MeV, the largest proportion of the dose (48.8%) was deposited within high-density bone, whereas above 0.125 MeV, the change on dose distribution started to occur where there was greater deposition in low-density tissue, reaching 53%. The dose distribution in the soft bone's intermediate density was 26.4% at 0.07 MeV and dropped to 19.7% at 2.5 MeV. There is a 29% percentage difference in dose distribution on the soft bone between the low and high energy. The dose distribution did not change significantly in proton between the low, intermediate and high-density areas. The dose distribution in 37.59 MeV shows 54.86% in low density, 19.75% in intermediate density and 25.39% in high density. A similar outcome was observed in high energy 124.83 MeV, a dose distribution was 54.21% in low density, 19.79% intermediate density and 26% in high density.

An advanced model was created to connect the results to a clinical routine when treating brain tumours using the VMAT technique. Cases were selected from 280 data sets of patients diagnosis with gliomas. Eleven different scenarios were identified. The advanced model shows five cases with an enhanced mean dose. The TPS overestimated the mean dose in all cases. In some instances, A significant mean dose variance of 8.8% was noticed in two cases. Extra cases were selected with a distance between the target and cochlea less than 1 cm. The cases show a significant difference in the mean dose and normal tissue complication probability (NTCP) models.

A model was created to connect the results with Gamma Knife treatment. Thirty-four cases of schwannoma were used, and four revealed a significant difference in the scattering dose to the cochlea. The maximum difference in mean dose achieved reached 8.3%.

Uncertainty due to dose distribution can affect treatment outcomes. For example, hearing loss and tinnitus can be side effects of brain cancer radiotherapy treatment. It was found that increasing the dose led to a corresponding increased dose reaching the cochlea. Increasing the model accuracy using micro-CT data and MC computation helps to control the dose to the cochlea by controlling dose distribution. In addition, pancreatic cancer can help achieve higher dose escalation to provide better outcomes to patients. Using dose-to-medium calculation, manufactures data associated with stent materials, and models based on Micro CT of resected organs can reveal uncertainty in dose distribution in heterogeneous areas.

Declaration

This work has not previously been accepted in substance for any degree and is not being concurrently submitted in candidature for any degree.

Signed .....AHMAD ABBAS..... (candidate)

Date .....20/3/2023.....

STATEMENT 1

This thesis is the result of my own investigations, except where otherwise stated. Where correction services have been used, the extent and nature of this correction is clearly marked in a footnote(s).

Other sources are acknowledged by footnotes giving explicit references. A bibliography is appended.

Signed .....AHMAD ABBAS..... (candidate)

Date .....20/3/2023.....

STATEMENT 2

I hereby give consent for my thesis, if accepted, to be available for photocopying and for inter-library loan, and for the title and summary to be made available to outside organisations.

Signed .....AHMAD ABBAS ..... (candidate)

Date .....20/3/2023.....

Contents

Acknowledgements

This work would not have been possible without the guidance, support, and commitment of my supervisor Dr Richard Hugtenburg. It has been a privilege to have a supervisor who always supports me and is willing to provide me with invaluable advice, teaching opportunity, and the opportunity to supervise master students. Thank you for the great experience during my PhD and support during the global pandemic. I can not thank you enough for believing in my abilities and being family during this difficult time.

I want to thank the staff of the department of Medical Physics in Singleton Hospital, especially Mr Adam Selby, for their assistance in this study. I also need to thank Dr Owen Nicholas for allowing me to collaborate with him. I look forward to our future collaboration.

Finally, I want to thank my wonderful family. To my mum and dad, thank you for instilling in me a strong work ethic and emphasis on education. To my beautiful wife and gorgeous children who support me during my study. Thank you for your love and for being a golden ray of sunshine in an otherwise challenging time. It is to you that I dedicate this work.

List of figures

List of tables

List of Abbreviations

Abbreviation	Definition
3DCRT	Three-dimensional conformal radiotherapy
AAA	Analytical anisotropic algorithm
ASCII	American standard code for information interchange
CERR	Computational environment for radiological research
CPU	Central processing unit
CT	Computer tomography
CTV	Clinical target volume
DD	Dose difference
DICOM	Digital imaging and communication in medicine
DNA	Deoxyribonucleic acid
DTA	Distance to agreement
DVH	Dose volume histogram
EUD	Equivalent uniform dose
FHWM	Full width of half the maximum
GI	Gastrointestinal
GPR	Gamma passing rate
GTV	Gross tumour volume
HU	Hounsfield unit
IGRT	Image guided radiotherapy
IMPT	Intensity modulated proton therapy
IMRT	Intensity modulated radiotherapy
KeV	Kilo electron volts
LINAC	Linear accelerator
LKB	Lyman-Kutcher Burman
MC	Monte Carlo
MLC	Multi leaf collimator
MRI	Magnetic resonance imaging
MU	Monitor unit
NHS	National health service
NTCP	Normal tissue complication probability
OAR	Organ at risk
OF	Output factor
PA	Percentage of agreement
PDD	Per cent depth dose

PSF	Phase space file
PTV	Planning tumour volume
QUANTEC	Quantitative analyses of normal tissue effect in the clinic
RT	Radiotherapy treatment
SNHL	Sensorineural hearing loss
SSD	Source to surface distance
T1	Longitudinal relaxation time
T2	Transverse relaxation time
TD	Tolerance dose
TLD	Thermoluminescent dosimeter
TPR	Tissue phantom ratio
TPS	Treatment planning system
UK	United Kingdom
VMAT	Volumetric modulated arc therapy
VS	Vestibular schwannoma

Chapter 1: Introduction and background

1.1 Short history of radiotherapy

In 1895, the medical field entered a new era when Wilhelm Conrad Roentgen discovered X-rays, and their potential for both imaging and treatment was recognized. Since then, medical imaging has been used to visualize different body parts and abnormal tissues, for example, tumour regions. Visualizing different body parts can be achieved as a result of the unique properties of X-rays. X-rays respond differently when interacting with soft tissue and bones, and this allows for identification of the differences in the various densities present in the human body. X-ray imaging subsequently evolved into computer tomography (CT), which creates a 2D slice image that can be transformed into a more complicated 3D image using computer tools (1). In addition to imaging, X-rays are used in the treatment of cancer.

Cancer can be treated to increase the chances of survival through a variety of methods, such as surgery, chemotherapy and radiotherapy, or a combination of these. This thesis will focus on radiotherapy, in which high-energy X-rays, protons or ions are used to destroy the deoxyribonucleic acid (DNA) to slow down or prevent cancer cell reproduction. Radiotherapy aims to eliminate cancer cells, while avoiding damaging as many normal cells as possible. A linear accelerator delivers high energy particles to kill cancer cells. Further details of the different types of radiotherapy treatment and their interactions are covered in the coming chapters. Some cancers can be cured, whereas others cannot. Radiotherapy also helps reduce cancer symptoms to provide patients with a better quality of life this is known as palliation. Normal cells can repair themselves more efficiently than cancer cells.

The minimum time required for a normal cell to repair itself is six hours. For this reason, radiotherapy doses are delivered in fractions. Fractionation describes the daily delivery of a small proportion of a dose until the end of the treatment course is reached. Any radiotherapy treatment plan aims to deliver the highest dose possible to target cells, sparing normal cells as much as possible. Radiotherapy can result in many side effects; some occur immediately after the treatment and others after many years. Side effects can be reduced by increasing the treatment plan's accuracy by using an advanced algorithm, increasing the contouring accuracy using advanced techniques, implementing a higher imaging resolution and acquiring a better understanding of the different interactions of those particles with different densities (2–5).

1.1.1 Toxicity of radiotherapy treatment

Toxicity from radiotherapy can be divided into two main categories: acute toxicity and late effect toxicity. Acute toxicity arises during treatment or within a short period post-treatment. It affects areas containing tissues with a high cell turnover rate, such as the bone marrow, mucosa, and skin, and starts to disappear once the tissue repopulates. Late effect toxicity occurs after 90 days, and in some cases, many years after treatment. These late effects are more aggressive and can affect all types of tissue. Furthermore, they are progressive and irreversible (6). Figure 1.1 demonstrates the different types of toxicity and their effects on patients.

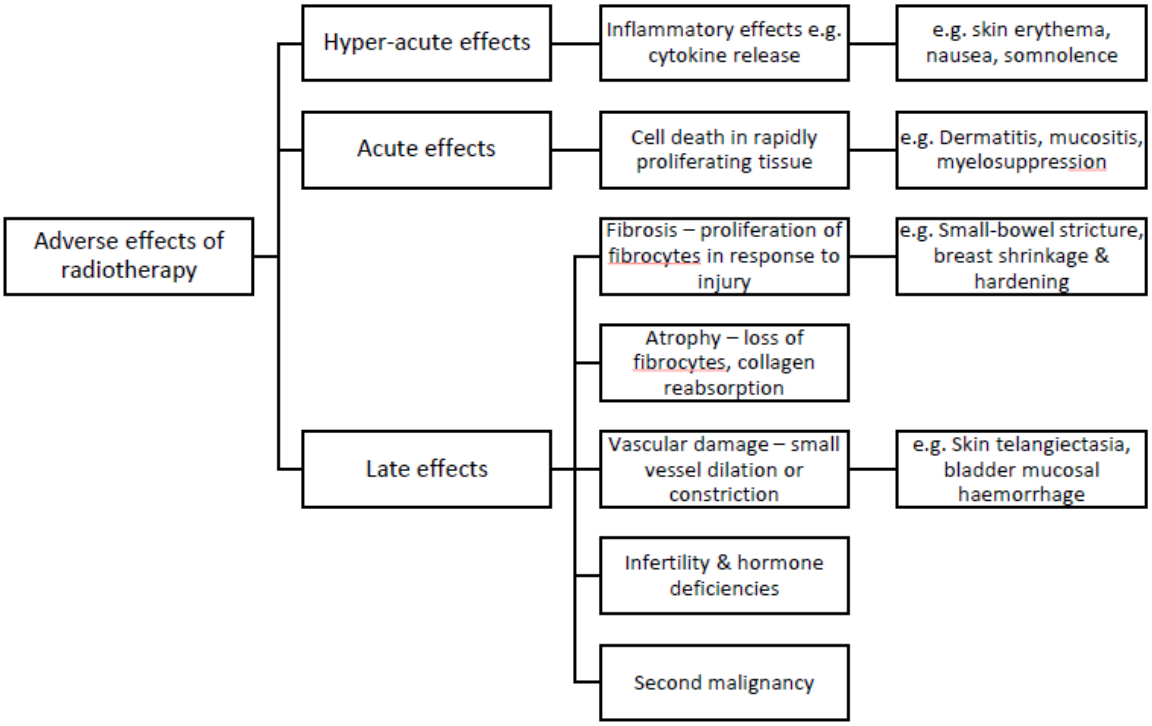

Figure 1.1: Illustrate the types of toxicity that occur in radiotherapy (7).

Local tumour control is a strategy implemented principally to reduce the long-term side effects of radiotherapy treatment as much as possible. Any escalation in the dose can improve tumour control, but also increases the side effects. Understanding the normal tissue response can help to increase the dose without passing the threshold at which damage occurs. Figure 1.2 illustrates a response curve for normal tissue following a sigmoid curve dose-response. A dose below the threshold indicates no toxicity in normal tissue (7). Treatment for cancers that affect the head, neck, anus or cervix can achieve a high rate of local control, but for many other cancers, the

required rate cannot be achieved without a concurrent high level of toxicity. Increasing delivery dose accuracy can help lower radiotherapy toxicity, and leave open the option for dose escalation. Understanding the micro level of dose distribution to add a correction rate to the different treatment sites can significantly increase treatment accuracy, especially in areas of heterogeneity.

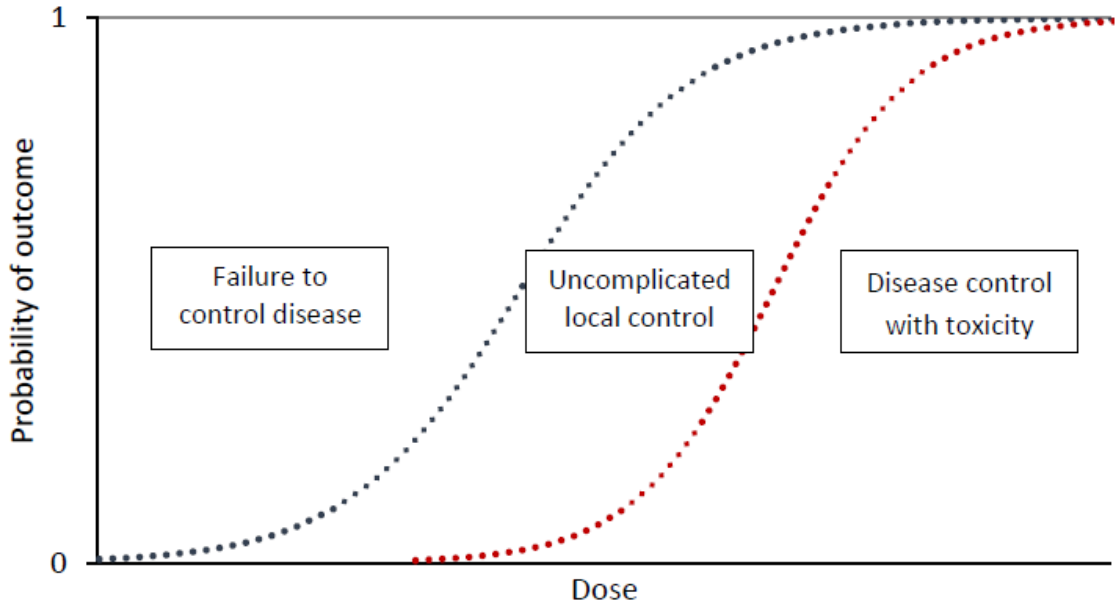

Figure 1.2: Illustration of the threshold response curve of normal tissue.

Toxicity rate is not only dependent on the dose rate but also the volume received during radiation, which is why the tolerance dose is correlated with the volume of the organ receiving the dose. An example illustrating toxicity rate is the liver, which has a large functional reserve and the loss of a small portion will not significantly alter physiological function. Thus, a high dose can be delivered to a small portion of the liver despite the probability of damage, as the overall physiological function will remain within the normal range. However, a low dose administered to a large volume of the liver can lead to a significant reduction in liver function, as it represents a high risk of toxicity. However, the aforementioned example simplifies the relationship between dose and volume, and in reality the organs are not homogenous architecturally. The theory of volume measurement for unevenly spread radiosensitive organs creates some uncertainty (8). Furthermore, the cancer cells within a tumour are not homogenous in terms of their insensitivity, and the heterogeneity of these cells cause a reduction in the dose-response curve (9).

1.1.2 Radiotherapy planning and treatment planning system

As explained, the aim of radiotherapy treatment is to deliver a high dose to the target to eliminate the cancer cells, and many steps can achieve that. The first step involves loading the images into dedicated software called a treatment planning system (TPS). CT images are required for all patients, but some tumour locations, such as the brain, require magnetic resonance imaging (MRI) images to highlight the details missed in a CT. Furthermore, the target is contoured and any organ at risk (OAR) must be avoided. After contouring, a plan is created choosing the best beam angles, shape, and size to deliver the dose to the target, ensuring it does not pass the OAR threshold. Next, the TPS begins calculating the dose distribution absorbed by different organs using different input information. Dose distribution can be visualized using a dose-volume histogram (DVH) or isodoses. All these dose distributions assume the dose calculated by TPS is accurate. However, assumptions and approximations are involved in TPS, calculating the dose distribution to allow for a fast calculation time. This assumption may cause differences in true dose distribution, especially in areas comprised of different densities. The Monte Carlo (MC) algorithm is considered the gold standard when calculating dose distribution for radiotherapy. MC simulates radiation transport on a particle-by-particle basis delivering high accuracy. However, this high accuracy has a downside: an MC is computer intensive requiring a long time to complete one plan.

1.2 Radiotherapy current status

Radiotherapy has become an essential cancer care treatment, and it has been estimated that radiation therapy covers 50% of treatment (10). Rapid advancements in radiotherapy are due to advancements in computing speed, treatment planning systems, a better understanding of radiobiology and the development of image-guided radiation therapy. Advancements in linear accelerators and delivery techniques decrease the margin around the target and any uncertainty. Traditional 2D radiation therapy has been replaced by three-dimensional conformal radiation therapy (3D CRT), intensity-modulated radiation therapy, image-guided radiotherapy, and stereotactic body radiation therapy. In the United Kingdom, there are 62 radiotherapy centres (11).

Proton therapy is a form of radiation therapy that takes advantage of proton properties to enhance the sparing of normal tissue (12). Protons and photons interact differently with matter, which is key to utilizing these differences in proton therapy. Although proton therapy is considered an expensive modality to establish, its numerous benefits such as lower side effect when treating

head and neck, thoracic, craniospinal, and paediatric central nervous system cancers, mean proton centres have been established worldwide (13). In 2020 there were around 100 centres around the world, and 20 new centres were planned across Europe during the last five years (14). The National Health Service (NHS) has commissioned a highly specialized program of proton therapy overseas to access proton therapy, focusing on complicated cases relating to the brain and head and neck in paediatric and young adult patients. In 2021, the NHS opened two proton therapy centres at a cost of 250 million pounds (15–17).

1.3 Human skeletal system

Gaining an overview of the skeletal system, and specifically, focusing on bone composition, is essential to understanding this research study. The human skeletal system provides shape and support to the human body, and the bones also served to protect the internal organs, such as the brain and heart. Furthermore, the bone marrow inside the bones produces red blood cells, platelets, and white blood cells. The white blood cells are essential to the human immune system. Bones also play an essential role in body motion and the storage of minerals and fats in the human body (18).

1.3.1 Categories of bones

Human bones can be divided into four general categories: long bones, short bones, flat bones, and irregular bones. Long bones are essential for moving and always hard ends. Examples of long bones are the thigh bones and forearms. On the other hand, short bones do not heavily contribute to motion but provide stability and support. Examples of short bones are the ankle in the feet and the carpals in the hands. The flat bones, including some of the bones in the skull, protect the internal organs. Finally, irregular bones, like the vertebrae or facial bones, provide protection for the spinal cord, shape the human body, and contribute to the human face shape (18,19).

1.3.2 Bone composition and skull bone

Bone tissue can be clustered into two main groups: cortical bone and trabecular bone. The cortical bone, also known as the compact or hard bone, forms 80% of the skeleton system. The trabecular bone, also called the spongy or cancellous bone, comprises 20% of the skeleton. The cortical bone is dense, hard, and covers the bone marrow. An example of a cortical bone is the

long bone, which consists of a honeycomb-like structure, and has a trabecular bone at its end (19). The skull is one of the many bones that shapes the human skeletal system. The human skull is made up of 22 bones that protect the brain. The skull itself has eight bones, and 14 are facial bones. The cranium, the upper part of the skull, consists of the frontal bone, sphenoid bone, temporal bone, parietal bone, and occipital bone. The majority of the cranial bones are categorized as flat bones and are composed of three layers. The outer and inner layers are made from cortical bone and the middle layer consists of less dense spongy bone (19). The focus of this thesis will be on the temporal bone. The temporal bone is located in the lower lateral area of the skull. It can be divided into four regions: the squamous, mastoid, petrous and tympanic.

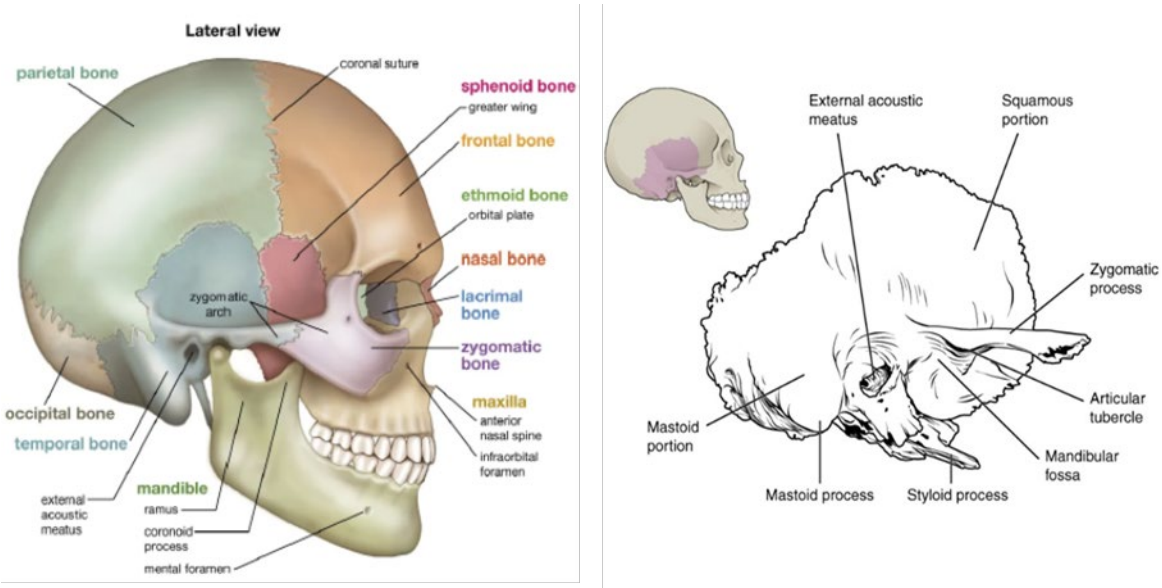

Figure 1.3: Skull anatomy (20,21)

The primary focal region for this thesis is the petrous, because it contains the middle and inner portions of the ear. The middle ear includes the mastoid air cells, which are a group of spaces filled with air located in the temporal bone. The inner ear is composed of a bony labyrinth, comprising the cochlea, vestibule, and semi-canals. The inner ear also contains an endolymph fluid, mostly composed of potassium and sodium.

1.3.3 Prosthesis and metal

Advancements in medicine have allowed for the implanting of high Z metal inside the human body to replace areas of damaged tissue, such as in the case of stents, cranial implants, maxillofacial implants, hip replacements, bone fractures, and bone scaffolds. It has also been

estimated that 4% of patients treated with radiotherapy have metal implants (22). The presence of high Z material can affect radiotherapy treatment due to extensive differences in density between normal tissue and metal. Furthermore, metal implants create atomic number disparities, such as a variation in attenuation index (23). The heterogeneity from a metal implant can affect every step-in radiotherapy, as in the case of the conversion curve (within the treatment planning system) created from Hounsfield unit data provided by computer tomography. The conversion curve can provide inaccurate results if the HU window is not extended to cover metal implants. Metal implants create artifacts in medical images, which can affect the estimate of electron density of the normal tissue surrounding the implant. Implants can also affect dose distribution at the target and organs at risk near the implant. Accurate dose distribution can alter the effectiveness of such a treatment. Almatani (2017) closely addressed this issue in prostate cancer patients with hip prosthesis. They approach was to use the MC algorithm with a cone beam computed tomography to enhance the accuracy of dose distribution. The outcomes of such a study were the provision of a more accurate dose distribution than would be available in a treatment planning system (24).

1.4 Thesis aim

The overall aim of the thesis is to reduce uncertainty with regard to dose distribution, in radiotherapy due to heterogeneity in the target and OAR. The methodology undertaken to achieve an overall aim is the use of a multiscale approach, which can provide essential information regarding the difference in dose distribution between TPS/clinical CT and MC/Micro CT for photons and protons. In addition, the results from a multiscale simulation may be applied to different modalities to study clinical effects. To achieve an overall aim, the use of micron dimension structures need to be accomplished, even though many difficulties need to be overcome. Clinical CT resolution misses some of the details that can increase the uncertainties associated with the treatment and use of micro-CT data that would not be possible clinically, but can provide a higher resolution, particularly in the small heterogeneous area of the cochlea. However, using Micro CT data is not a straightforward task and requires many steps to be performed to allow data to be used on different platforms. A higher resolution image is not sufficient without the use of a high-accuracy simulation algorithms. The MC algorithm is a golden standard for simulating different interactions, and it is used in this thesis to provide high accuracy results with a combination of Micro CT. Following this, a different model may be created to connect the results

of the multiscale with radiotherapy treatment in gliomas cases and Gamma Knife treatment of schwannomas. The other aim is to create a more accurate model for liver stent patients, to evaluate dose distributions in the presence of a high-density stent. A combination of different approaches of delineation, mimicking the material inputs of the stent, and using MC simulation are used to achieve the aim of reducing uncertainty in dose distribution in areas of high density.

1.5 Research output and support for research at Swansea university

While engaging in thesis studies, I have guided and supported four MSc students toward completing their research projects. The first thesis is "Hippocampal contouring and sparing in primary brain cancer patients using advanced radiotherapy treatment planning techniques such as IMT and proton therapy" by Fleman Patrice Aka (2020). He demonstrated that IMPT could be an effective technique in sparring hippocampal in adult patients with primary brain tumours compared to IMRT and 3DCRT. The second thesis is entitled "The effects of material heterogeneity on the characteristics of Bragg peak as described by a mathematical model" by Angharad Gair (2021). She demonstrated the effect of density in proton therapy using material that mimics the lung parenchyma. In addition, she overcame the obstacles of using DICOM on FLUKA and created a successful Monte Carlo model of a heterogenous area to obtain the result. The third thesis is "Oesophageal proton beam therapy- dose escalation, robust optimization strategies, uncertainties, and impact on dosimetry for distal oesophageal cancer" by Mme Esien (2022). She successfully achieved proton dose escalation in the thesis using SCOPE 2 constraints and a robust plan strategy. The last thesis is entitled "Investigation of the differences between photon and proton radiotherapy when treating internal mammary nodes in breast cancer patients, including hypofractionation" by Shannon Dowen (2022). She demonstrated that proton therapy could deliver a higher dose to the target and a lower dose to the OAR than VMAT. Her second finding was that proton hypofractionation could deliver a low dose to the heart, which helps reduce the probability of cardiovascular disease arising as a side effect of treatment. I collaborated with Dr Owen Nicholas when he was preparing his thesis for a Doctor of Medicine degree titled "Developing the role of proton beam therapy in oesophageal cancer". My role involved finding different beam arrangements to reduce the dose delivered to the substructure of the heart. In a collaborative work, I am a co-author of an accepted ESTRO abstract titled "Isotoxic dose escalation with proton beam therapy for distal oesophageal cancer" (25). I have also presented my work at South Wales applied

mathematics for biomedical advances (SWAMBA), focusing on mathematical oncology (June 2022). In addition, I have supervised and helped in Master program labs in DICOM RT, DVHs, and gamma analysis with CERR. Another lab I supervised in involved modelling with FLUKA, Using DICOM and structure in FLUKA, and using MATLAB to manipulate DICOM CT.

1.6 Thesis structure

Chapter 2: briefly reviews different treatment modalities for photons and protons. Understanding the different modality advantages requires the creation of suitable treatment planning for the clinical chapter. Furthermore, this chapter helps create a model that uses dosages to medium and imitates the chosen treatment in the MC algorithm using micro-CT data.

Chapter 3: Presents the main theory behind use of the MC simulation for photons and protons. In addition, it explains the primary reduction technique, advantages, and disadvantages of MC, the FLUKA algorithm and the principal radiation interactions. MC knowledge is required to create a model with low statistical uncertainties in a short simulation time. In the last section, there is an in depth review of the difference between dose to medium and dose to water.

Chapter 4: Validation of the eclipse treatment planning system with the Penelope MC algorithm using PRIMO. A MC plan cannot be compared with a treatment planning system if validation is not carried out. This chapter is an essential step before proceeding to the next chapters.

Chapter 5: An investigation of the stent effect in pancreatic cancer applying an advanced contouring and material identification model. The aim is to decrease uncertainty by using the correct materials of the stent, the advanced model, and MC by changing the material of the stent.

Chapter 6: investigates use of Micro CT and MC in the cochlea, a highly heterogeneous area. The simulation included multiple photon energy levels within the treatment beam to understand dose distribution in the Micro CT level for photon treatment. A digital imaging and communication in medicine (DICOM) manipulation, MATLAB processing and a MC algorithm are required to build a basic model to evaluate the results.

Chapter 7: The basic model from the previous chapter evolves to an advanced model, and is applied to different glioma patients. This chapter connects the model to the clinical environment choosing different energy fluences. The results of the basic model from the previous chapter must

be connected with a clinical routine to evaluate the effects. This chapter builds a bridge to connect the basic model to the clinical routine.

Chapter 8: The basic model from the previous chapter evolves into an advanced model and is applied to different schwannoma cases with treatment from a Gamma Knife. This chapter applied a multiscale result to a Gamma Knife to study the scatter on the cochlea, which is the primary concern in schwannoma cases.

Chapter 9: details the investigation using Micro CT and MC in the cochlea. A proton beam with different energy levels is used to investigate behaviour in the micro-CT data. This chapter focuses on dose distribution and not the range change, due to heterogeneity in the area.

Chapter 10: This chapter summarizes the results of the thesis and discusses recommendations for future works.

Chapter 2: Radiotherapy treatment modalities

2.1 Treatment modalities

2.1.1 Radiotherapy

Radiotherapy is a cancer treatment modality, and is considered the second most effective treatment after surgery. The latest data from the national radiotherapy dataset shows approximately 50% of 375,400 cancer patients received radiotherapy between 2016-2018 in UK (26,27). Radiotherapy uses high-energy X-rays to destroy cancerous cells, and can be used as a curative or palliative treatment to reduce cancer symptoms. The aim of radiation treatments is to deliver a high dose to the target area, and the lowest possible dose to normal tissue. The therapeutic ratio aims to balance the tumour dose and controls for side effects in normal tissue (28). The field of radiotherapy is constantly improving to increase accuracy of delivery of high doses to cancerous tissue, while avoiding normal tissue (29). Examples of new techniques are intensity-modulated radiotherapy (IMRT), proton therapy, image-guided radiotherapy (IGRT), and volumetric modulated arc therapy (VMAT). One constraint when delivering a higher dose to target tissue is the threshold of the normal tissue.

In some cases, damage to healthy tissue is unavoidable, and this then late toxicity effects like secondary cancer and cardiac defects (30,31). Recent research has forecast that, by 2030, there will be 4.17 million cancer survivors (32). Due to the high number of predicted survivors, more research needs to be conducted to develop radiotherapy techniques with sufficient accuracy to reduce late toxicity, which affects patients' quality of life and increases the cost when treating side effects (31).

2.1.1.1 Development of IMRT

Intensity-modulated radiotherapy has been established as a recommended technique for many cancer treatments, including prostate cancer (33). Conformal radiotherapy has evolved to a level where multiple static beams are delivered in a way that takes on the shape of the target area to reduce the dose to the OAR. Figure 2.1.a shows the conformal plan for four static beams. The conformal beam delivers a uniform radiation fluence profile that can be modified using tools such as wedges or compensators for intensity modulation. As shown in figure 2.1.b, in IMRT, fluence

can be modulated arbitrarily using a multi leaf collimator (MLCs). IMRT allows for an increase in dose to target and maintain a clinically acceptable level of toxicity to the OAR (34). Many researchers have compared IMRT, 2D and conventional three dimensional conformal radiotherapy (3DCRT), in dosimetry and have concluded that IMRT has advantages over traditional techniques (29). The IMRT technique allows for homogenous dose distribution in the region of interest, while focusing on sparing specific at-risk organs with low threshold levels, such as the hypothalamus. One of the advantages of the IMRT, which is frequently used in head and neck cases, is its ability to deliver simultaneous integrated boosts (35). Furthermore, IMRT can deliver different doses to multiple targets simultaneously reducing treatment times (36).

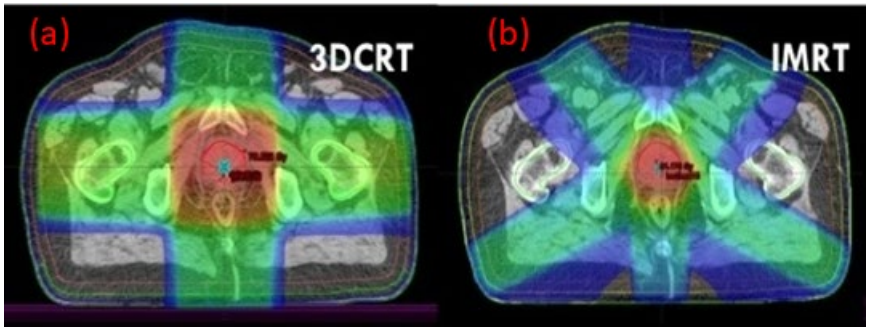

Figure 2.1: a) a 3DCRT plan. b) an IMRT plan.

Figure 2.1.b demonstrates the radiation fluence profile in IMRT that produced the final dose distribution requested, which can be achieved using MLCs with multiple beams. Originally, MLCs were only used to confirm the tumour outline, as seen in the beam eye view. Eventually, MLCs evolved to carry out additional functions, such as shaping of the fluence in the target area in order to perform IMRT. Two IMRT techniques can achieve ideal fluence: the step and shoot method and dynamic MLCs. Step and shoot involves the summations of multiple static sequences, as shown in figure 2.2.a. The ideal fluence from the step and shoot technique depends on many physical factors, including leaf width, leaf gap, and maximum number of segments. In the dynamic MLCs, as shown in figure 2.2.b, the radiation beam is continually on, and the MLCs move at different speeds and shapes, as planned in the treatment planning system. The dynamic technique does not have individual segments, thereby granting the planning team increased flexibility (37).

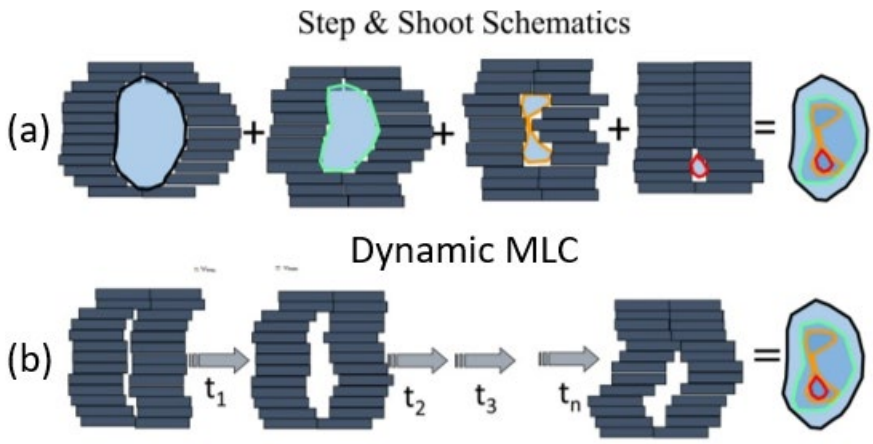

Figure 2.2: a) Step and shot technique used in IMRT to deliver the ideal fluence during treatment. b) Dynamic MLCs, where the continuous delivery of treatment is achieved by changing the velocity of the MLCs during treatment (38).

Much research has been done to investigate the risk of radiation-induced secondary primary cancer when using the IMRT technique. Research has concluded that IMRT ranges from a similar to an insignificantly higher risk rate than conventional radiotherapy. However, this rate still falls below the recommended threshold (39,40). IMRT delivers a low level of radiation to normal tissue, with no significant increase in the dose-volume histogram. In clinical practice, patients undergoing brain treatment receive a dose of 50 Gy when using IMRT, although a higher dose is required for conformal treatment. A study compared both techniques, and the findings revealed both techniques have a similar risk percentage for secondary cancer. However, in the case of the conformal technique, increasing energy leads to an increase in neutron leakage from the treatment head, heightening the risk to patients. Some studies have argued that a weighted factor should be implemented for neutrons (40–42). A solitary monitor unit (MU) refers to the electric charge measurement detected within the ionization chamber positioned at the head of the linear accelerator. This measurement corresponds to a dosage of 1 cGy administered to a water phantom under established conditions (43). This measurement holds significance because the linear accelerator's output is exclusively quantified by the charge passing through the ionization chamber. The benchmark conditions may differ across departments, and the charge quantity within the ionization chamber of the linear accelerator that signifies 1 cGy under these reference conditions can vary from one machine to another. Hence, the utilization of 1 MU serves to standardize treatment devices within a particular radiotherapy facility (43). The IMRT technique allows

treatment over a small field size, but many researchers argue that a higher low dose would be delivered to a small area of normal tissue. Furthermore, a higher MU is used, resulting in higher head leakage (44). This argument is valid, but the leakage at a low dose to normal tissue is not significantly high. Furthermore, the extra dose delivered to normal tissue falls within the recommended threshold. A study by Ruben *et al.* explained that the amount of MU used in IMRT is directly related to the software and hardware. The study tries to reduce the dose out of the field by improving conformity when using the IMRT technique. They reported a decrease of 11% within the patient, with an additional increase in MU, collimator scatter and head leakage. However, the total difference between the out of field dose and the total delivered dose was 0.14%, which is not considered significant. The study concluded that increasing the dose outside the field of treatment was not clinically significant, and could be reduced further using more advanced software and hardware (45).

2.1.1.2 Implementation of IMRT

IMRT can provide many advantages, but to benefit from the technique's full potential, many challenges need to be navigated (46). At each stage of radiotherapy, a specific challenge is encountered. For example, during the planning stage, inverse optimization requires high computing power and robust determination at many treatment sites (47). Furthermore, the dose-escalation technique requires a high degree of conformity to avoid any additional dose being added to the OARs without precise delineation (48). With CT scans only, achieving high delineation accuracy in the brain or head and neck is not achievable. In these complicated areas, CT images do not necessarily show sufficient detail in the soft tissue, as MRI images are used in the delineation stage (49,50). The tumour volume contoured into several volumes to safeguard the prescribed dose is not missing any parts of the volume. The first volume is gross tumour volume (GTV), which demonstrates tumour position as seen in the images. The second volume is clinical target volume (CTV), which includes the gross tumour volume and added volume of suspected tumours that cannot be detected in the images. The last is planning target volume (PTV), which includes clinical target volume and added margin to account for patient positing, size, shape and position relative to the treatment beams as shown in figure 2.3. The PTV is a geometrical concept to guarantee that CTV gets the prescribed dose (51).

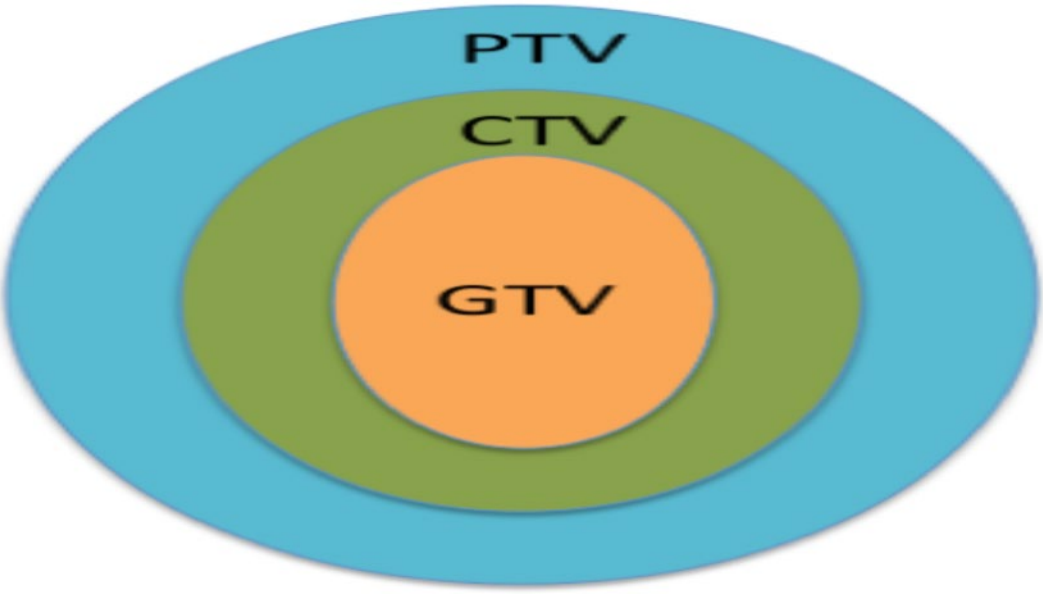

Figure 2.3 A tumour with different volumes

A significant increase in accuracy in the gross tumour volume, clinical target volume, planning tumour volume and OAR is realized when using fused images, and some studies demonstrate that adding positron emission tomography in brain delineation results in improvements (52,53). High-accuracy delineation requires the use of additional imaging modalities, which is costly as well as time-consuming for the radiation oncologist to delineate. For example, in the case of brain planning, approximately ten OARs need to be delineated by looking at more than 70 slices of CT-MRI images, and an experienced radiation oncologist requires approximately two hours to contour all the required regions (54). A radiotherapy researcher aims for targeted radiotherapy, which requires a sharp dose decline from the target area to the OARs, and patient setup is one of the challenges in this case. Many linear accelerator (LINAC) machines use on-treatment imaging like cone-beam computer tomography to reduce uncertainty due to patient setup (55). Figure 2.3 shows a LINAC with an x-ray tube and flat panel detector (FPD), which can be used on each treatment day to ensure no change in patient position during the session.

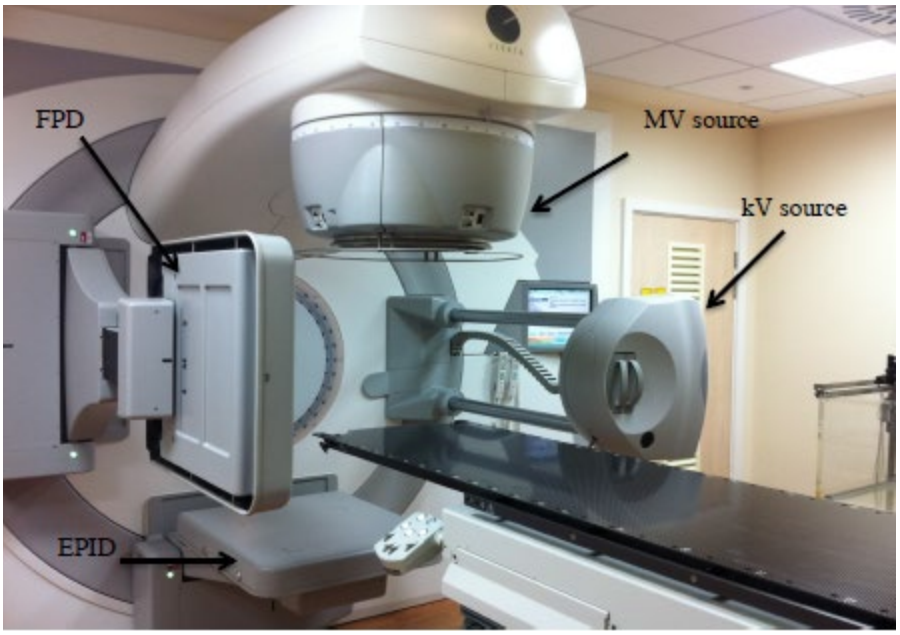

Figure 2.4: Elekta linear accelerator at Singleton Hospital.

In radiotherapy, each plan must be verified before the delivery of treatment to the patient. The conformal technique requires less verification than IMRT. In IMRT, there is a step to verify that MLCs are operating as planned. Additionally, accurate communication between the treatment plan system and treatment machine needs to be verified to allow the correct sequence of MLCs to be transferred (29). In the past, the plan was verified using a phantom, and the phantom would be irradiated according to the patient's original treatment plan. After irradiation of the phantom, the dose distribution and dose measurement were compared with the treatment plan threshold. This verification technique is time-consuming: verification of the treatment plan for nasopharyngeal carcinoma, for instance, takes about three hours of machine time and lasts approximately eight hours in total (29). With the development of MLCs and more complex techniques being set up, the old verification method is not practical for use as part of the daily routine. A new virtual technique was developed, which requires less time to conduct. The virtual technique calculates each beam's monitor units and fluence map individually using an MU calculator (56). An IMRT can have many control points, some of which involve small field sizes, which require a low radiation output. Delivering a low dose in a small field is challenging, and requires careful monitoring of the dose calculation. Many researchers discuss the accuracy of the analytical algorithm in dose dosimetry in small fields. LINAC's ability to deliver short exposure each time must be carefully monitored (57,58). To overcome this challenge, IMRT uses a specific program for pre-treatment and also for

patients' quality assurance. Furthermore, a specific phantom can ensure the delivered dose is similar to the calculated dose in the patient's treatment plan, falling within the acceptable limit (59,60). In complicated cases with regions of high heterogeneity and complex beam arrangements, a secondary dose calculation algorithm is needed to ensure treatment with a high-accuracy is achieved (61,62).

2.1.1.3 IMRT in the clinical routine

Despite the multiple challenges posed by using IMRT, many centres worldwide use IMRT as the primary treatment technique (60). A survey carried out in the United Kingdom (UK) reveals the most common treatment technique used in head and neck cancer is IMRT (63). The brain region has many radiosensitive OARs, and delivering a high dose to the target without increasing the risk of toxicity is difficult. The hypothalamus, spinal cord, brainstem, and optic nerve are examples of serial organs at risk, as surpassing tolerance level can result in significant damage and affect the patients' quality of life. Irradiating a brain region without causing a significant toxicity level requires a sharp drop in the dose in the region of OARs, without reducing the dose received by the target. A PARSPORT study concluded a significant reduction in side effects, particularly saliva production if sparing the parotid glands when using IMRT to treat pharyngeal squamous cell carcinoma (64). Comparisons between conformal radiotherapy and IMRT implicate the sparing of the parotid gland to improve salivary function, showing that IMRT achieved a higher sparing percentage than conformal radiotherapy (65). Adaptation of IMRT in clinical centres was slow in the 1990s in the United Kingdom (66). In 2007, a survey was carried out in the UK showing that half of centres had insufficient resources to implement IMRT techniques, missing the required funding and appropriate equipment (67). However, IMRT remains an essential technique, especially in prostate, head and neck cases.

2.1.1.4 Principles of VMAT

A technique designed to deliver doses continuously in an arc shape around the patient is volumetric modulated arc radiotherapy (68). In other words, VMAT is an upgraded technique of IMRT, as shown in figure 2.4. VMAT can deliver an intensity-modulated dose distribution similar to IMRT; however, it does so more quickly than other techniques (69).

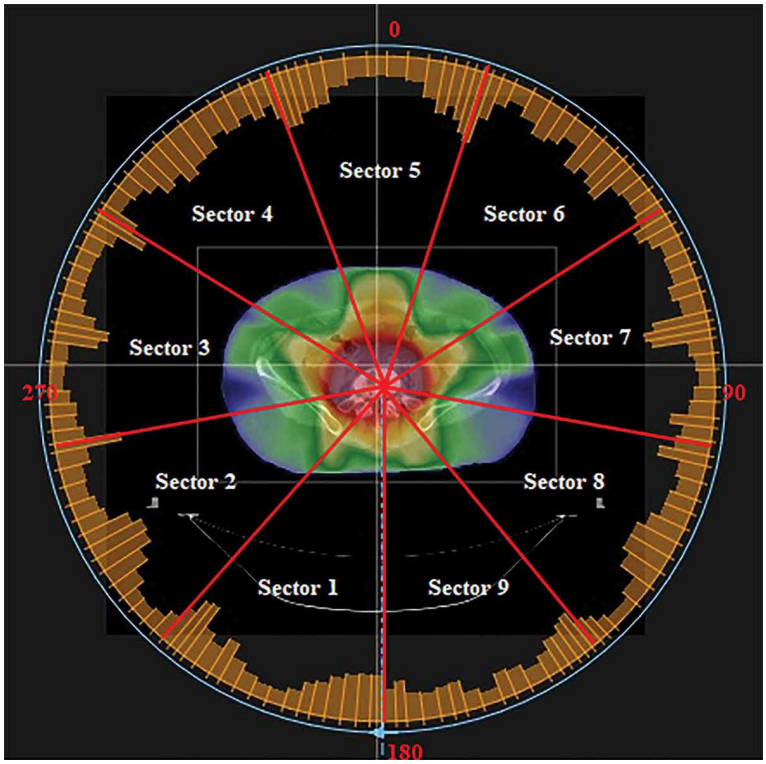

Figure 2.5: The VMAT, which delivers continuous radiation in an arc shaped rotation changing the LINAC head's speed and MLCs (70).

The VMAT was introduced in the 1990s, but was not commercially available until 2009 (71). The first machine to use arc therapy was tomotherapy, in which a fan beam can rotate around a patient in a process similar to that used in a CT machine. Tomotherapy delivers an intensity-modulated dose in the form of a slice through the targeted region while a patient is lying in the machine (72). Adequate dose distribution can be achieved in tomotherapy using a simple binary collimator. However, the requirement for a dedicated machine to deliver arc therapy led the researchers to develop a more affordable technique to be implemented in the LINAC machine. The VMAT research concentration delivered the dose in a single arc to achieve the same level of dose distribution to the IMRT (73). The coplanar VMAT method involves designing multiple arcs within a single axial plane to enable the administration of elevated doses at points where the beams intersect (74). Non-coplanar radiotherapy employs multiple radiation beams, either stationary or moving, which are not situated within the same geometric plane in relation to the patient. This approach diminishes the convergence of beams away from the tumour site. Non-coplanar radiotherapy finds greater prevalence in intracranial stereotactic radiotherapy, single-fraction radiosurgery, and stereotactic body radiotherapy. These methods frequently administer larger

individual treatment doses and necessitate exceptionally precise, well-defined dosage transitions beyond the planned treatment area, all aimed at minimizing radiation exposure to nearby healthy tissue (75). The figure 2.6 demonstrates the difference between the coplanar arc and the non-coplanar arc.

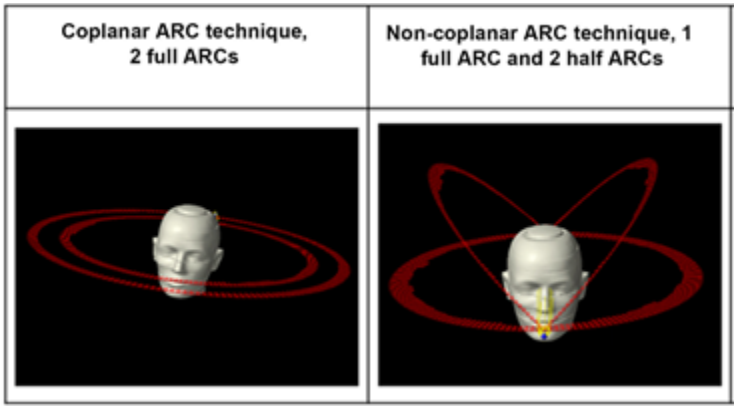

Figure 2.6 coplanar arc and non-coplanar arc (74)

Bortfeld's research concluded that delivering a dose in a short and abutting arc can result in dose distribution similar to IMRT (76). Bortfeld's work was one of the first theoretical explanations describing how VMAT can achieve similar dose distribution to IMRT (76). Single arc delivery requires a sequence of arbitrary MLC shapes, each with a specific monitor unit. In clinical practice, this means the gantry's speed and dose rate must be adjusted at each control point (77). Additionally, the sequence and speed of the MLC must be synchronized with the gantry speed. The high specification control of the system when governing these multi changes explains why VMAT was not immediately commercially available (78). Modern LINAC control systems can control for multiple changes in different parts, with specific synchronization being undertaken to deliver a highly complex treatment plan (78).

2.1.1.5 VMAT in clinical routine

The availability of the VMAT technique in radiotherapy centres allows the radiation oncologist flexibility to choose the optimal technique to deliver the lowest possible dose to the OAR. Today, VMAT can deliver a very efficient treatment plan, with a significantly shorter treatment time than IMRT. A further advantage is that VMAT requires fewer MUs compared to IMRT. An example of this can be seen in the case of a prostate cancer patient treated with IMRT

at Mary Bird Perkins Cancer Centre, where the treatment took 9.5 minutes to complete, but only 1.4 minutes using VMAT. The short treatment time led to less patient motion and increased the free machine time, making it possible to accept more patients (79,80). Many researchers are studying the benefits of using VMAT compared to other techniques. A comparison study between treatment plan deliveries using VMAT and IMRT in ten left breast cancer patients concluded VMAT achieved a lower dose to the heart by 29.5% compared to IMRT. Cancer in the left breast is considered difficult to treat, because the heart can succumb to late toxicity if it receives too high a dose. Overall, VMAT spared the right breast and lungs more than IMRT. Another study supports the conclusion that VMAT can reduce the dose to the OAR for patients with left breast cancer. Furthermore, treatment time when using VMAT was 3.7 minutes compared to IMRT at 9.8 minutes (81). Due to the breathing motion, a shorter treatment time is useful as it means less patient motion, decreasing the MU needed for the treatment (82).

2.1.2 Proton therapy

The notion of using high energy positive charge particles to treat cancer patients was introduced in 1946 (83). The first treatment using protons took place in Berkeley National Laboratory in 1954 (84). The research on proton therapy led to the establishment of the first proton centre, which was built in 1990 (85). The adaptation of proton therapy in clinical centres has been prolonged, due to the high costs, which are almost 2.4 times higher than for radiotherapy. However, during the last few years, proton therapy has garnered the trust of many radiotherapy specialists and the media, because of the advantages of proton therapy in terms of achieving accelerated technology adaptation (86).

2.1.2.1 Principle of proton therapy

The unique physical characteristics of the proton allow it to travel through a medium without losing a large amount of energy. Ideally, at a certain predetermined depth the proton energy would be deposited at maximum strength. However, as the photon travels through a medium it loses some of its energy. Furthermore, the photon does not deposit all its energy at a certain target point, but continues to release energy even after passing through it (87–89). Thus, in proton therapy the proton behaves differently. It has a low entrance dose that builds up until it reaches a maximum peak, after which it deposits energy. The peak showing the proton behaviour

is termed the Bragg peak, as shown in figure 2.5. The minimal or zero deposit around the target area in proton therapy makes it a very attractive technique when wishing to increase the dose to the target without affecting the OARs, which is vital to improving the patient's quality of life (90).

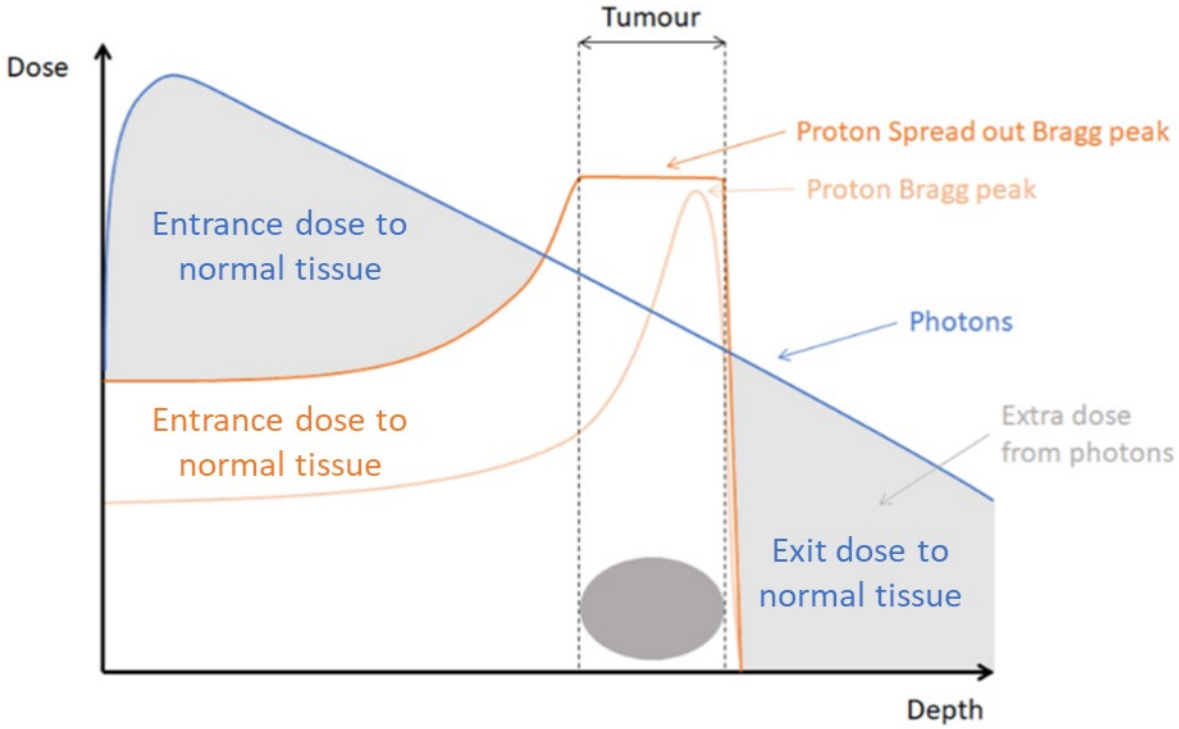

Figure 2.7: The depth dose of photons and protons (91).

In clinical practice, some cases require deep treatment. For example, to reach the depth of a target located 20 cm to 30 cm deep, proton energy needs to be around 200-250 MeV. Unfortunately, the magnitude of the Bragg peak is typically smaller than the volume at the target area. To overcome this obstacle, beam modulation is essential to imitate the size of the target area. The spread-out Bragg Peak is achieved using multiple modulations, as illustrated in figure 2.5. Proton therapy operates via two methods: passive scattering and pencil beam scanning. Before explaining the difference between the two operating systems, a brief explanation of the proton treatment system component is provided.

2.1.2.2 Accelerators

The particle accelerator is the main component used in radiotherapy and proton therapy to accelerate and align particles to reach the desired energy level. In today's centres, three main linear

accelerators are available, each with different technologies and usability. The three types are linear accelerators, cyclotrons and synchrotrons.

Linear accelerators are commonly used to accelerate x-rays or electrons in an external radiotherapy machine. Linear accelerators shape the beam aiming to reach an energy level that will kill the targeted cancer cells. However, linear accelerators are frequently not powerful enough to be used in proton therapy or with other heavy particles that require high energy to reach deep targets. The alternative accelerators used in proton therapy and heavy particles are synchrotron and cyclotron accelerators, which can reach the necessary energy and intensity levels for proton therapy.

The cyclotron, which was designed to accelerate charged particles to a high energy level of around 200 MeV, was first introduced in 1929. However, the first dedicated cyclotron used in the clinical centre was introduced in 1961 (85). The cyclotron had a helical path that helped increase the particle energy using an electric field to achieve a high energy level (85). Figure 2.6 illustrates the component of the cyclotron and the concept behind it. The cyclotron is designed as an evacuated semi-circular cylinder divided into two sections, and each section is called a dees. The proton starts at the middle point between the two dees, and alternating currents are applied to each. The high-frequency alternating voltage forces the proton to accelerate, and the magnetic field surrounding the dees causes it to travel in a spiral path. Protons are forced to travel from one dee to another by changes in voltage frequency, and each time the proton travels from one dee to another, the energy level increases. The radius of the spiral path increases as the proton energy level increases, and at some point, the accelerator electric field becomes focused preventing particles from diverging from their path. When the proton reaches a maximum energy level, the particle reaches a radius near the inner edge of the cyclotron, and a deflector magnet is used to direct the proton from outside the cyclotron towards the beam transport system (92).

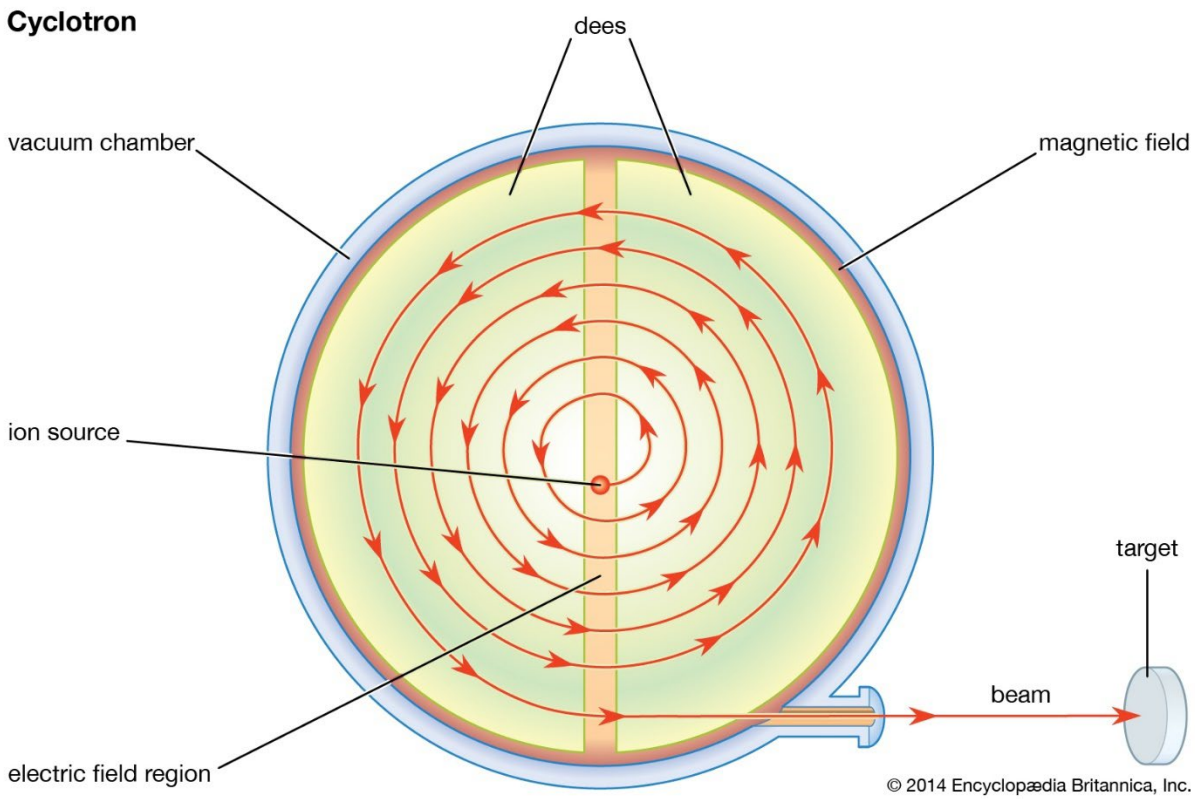

Figure 2.8: Illustration of a cyclotron (93).

A synchrotron is another type of accelerator that is primarily used for charged particles. The synchrotron is designed in a circular shape, with a series of magnets distributed across a specific location. The magnets are the main components that accelerate the charged particles. The cyclotron can accelerate charged particles to reach a maximum energy of 10 MeV using a spiral path and a constant magnetic field. A synchrotron does not necessarily maintain a constant magnetic field, but regulates it. The different techniques and shapes available allow the synchrotron to reach a proton energy level of 10 GeV. As shown in figure 2.7, the proton synchrotron is comprised of a vacuum chamber, with a number of electromagnets are attached to the chamber. The vacuum chamber takes the shape of a doughnut, and at one end, the linear accelerator injects the proton. The magnet field keeps the protons rotating in a circular motion, and changes in radiofrequency force the proton to reach a higher energy level. The strength of the magnetic field and radio frequency increase parallel to the proton energy. The proton continues to circulate until it reaches the required energy level, after which it exits the circular path for clinical use (92,94).

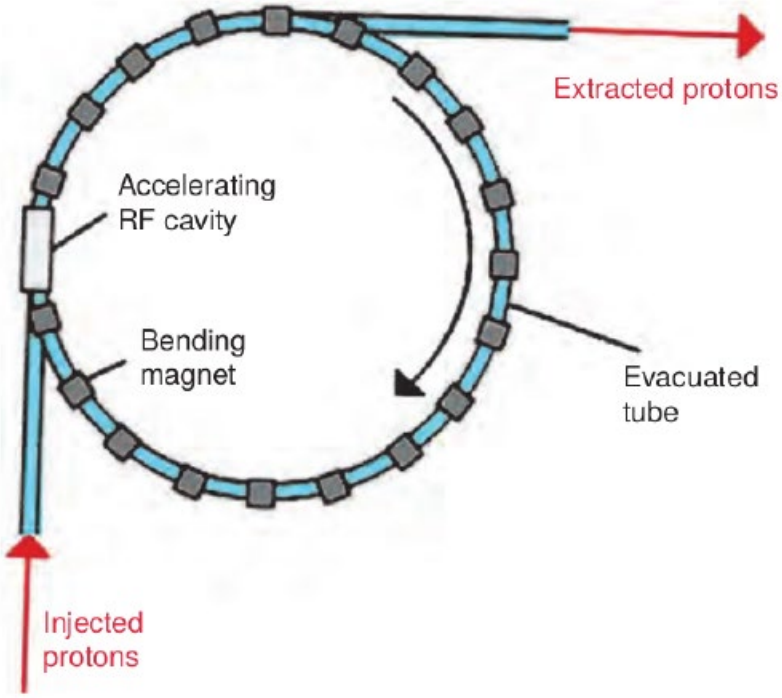

Figure 2.9: Illustration of the proton synchrotron (92).

2.1.2.3 Proton beam delivery system

The proton beam travels through a connection line that runs from the cyclotron or synchrotron to a gantry system. The gantry or beam delivery system is the final step shaping the proton beam to matches the target area. The proton arrives from the connection line as a small pencil beam compared to the target area. Thus, the proton beam requires additional modification to cover the required area, which can be achieved using two different methods. The first method is passive scattering, which uses a sequence of blocks and apertures to achieve dose conformity. The second method, called spot scanning, uses a small pencil beam to draw all over the target area (95).

2.1.2.4 Passive scattering

The traveling proton beam from the connection line must be enlarged to cover the target volume, and this can be achieved by using scattering material in front of the beam. This technique is called passive scattering. In cases of a small volume, a single scatter can produce a broad enough beam to cover the target volume. However, in some cases, where the target volume is large, a second scatter is required to achieve a uniform dose profile. The components used in passive

scattering techniques are the energy modulator, two scattering foils, a collimator, and a compensator. All these components aim to contour the beam to deliver a uniform dose covering the target volume. Figure 2.8 provides a basic illustration of how passive scattering techniques work. The energy level controls the traveling depth of the proton, and the energy modulator's primary role is to ensure the protons have sufficient energy to reach the required depth. The second part of the passive scattering is where the scattering foils spread the narrow beam that comes from the connection line. The beam is too narrow to cover the target volume without double scattering foils. The final shaping component is the collimator, which shapes the beam to mimic the target volume. The final component is the compensator, which helps form the dose distribution at the distal end of the target volume (96,97).

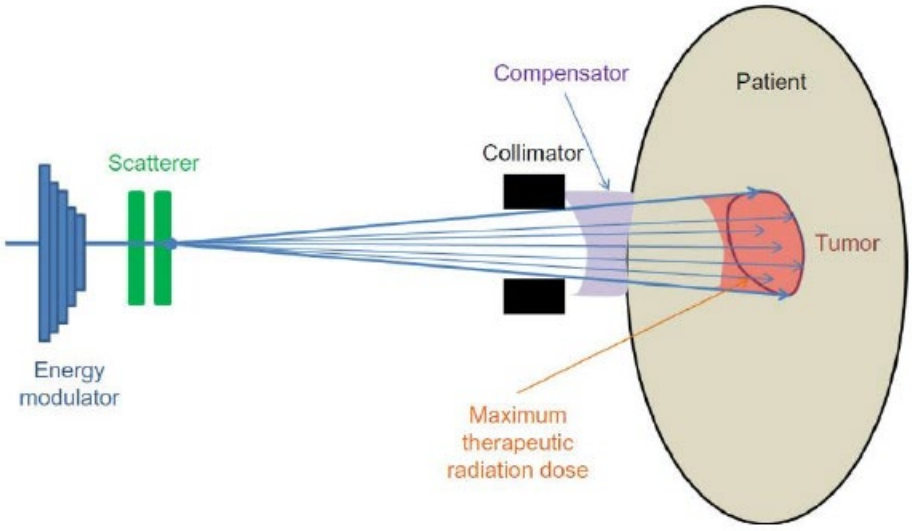

Figure 2.10: Illustration of the passive scattering technique in proton therapy to cover the tumour volume (97).

Spot scanning or active spreading is a technique that uses a scanning magnet to control the proton and shape it, rather than using a scatter foil and collimator. The spot scanning technique uses the advantage of a proton sustaining the Lorentz force, where the proton changes direction when a magnetic field is applied and is accelerated with an electric field (98). The proton arriving from the cyclotron at high speed is interrupted by two magnets. The orthogonal magnet changes the proton's direction by altering the magnets' intensity (figure 2.9). Spot scanning draws small spots around a 10 mm diameter at full width of half the maximum (FHWM) to cover the target volume, creating different layers of equal energy (99). Flexibility when delivering the dose to different

layers allows the delivery of the dose in three dimensions. The dose is delivered to the deepest layer of the target, which requires higher proton energy, and is then moved to the next layer which requires lower energy. Spot scanning stops when the entire target volume is covered, and this technique opens the doors to high intensity modulated proton therapy (IMPT), which is possible in proton therapy. The IMPT gives the radiotherapy oncologist greater freedom to change the intensity of the treatment within the target volume. IMPT can irradiate each pixel at a different intensity.

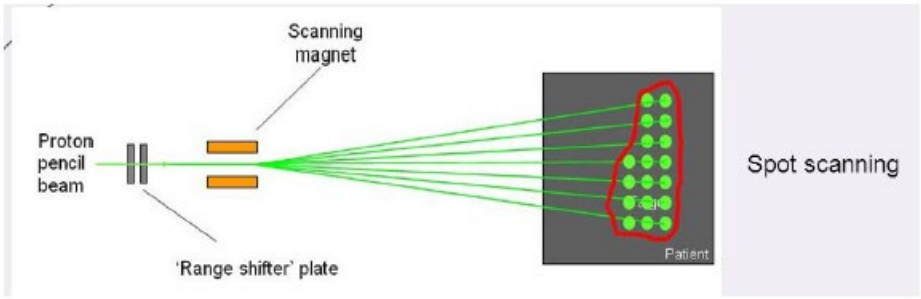

Figure 2.11: Illustration of spot scanning technique used in delivering proton therapy (100).

The spot scanning technique has multiple advantages compared to passive scattering. One of the advantages is that spot scanning results in a lower production of neutrons compared to passive scattering. In passive scattering, the use of a physical compensator prompts increased production of neutrons. Another advantage of spot scanning is that it has a shorter treatment time than other techniques. Furthermore, spot scanning can deliver high and low doses to target regions, which cannot be achieved with the passive scattering method. Therefore, spot scanning is widely used in areas with motion uncertainty, like the lungs. With the help of image-guided techniques, repainting target areas that received a lower dose due to the motion is possible without exceeding the dose to OARs.

2.1.3 Gamma Knife

The Gamma Knife is considered an essential tool in neurosurgery. The concept of the Gamma Knife was introduced by Leksell and Borje Larsson (101). The basic principle of the Gamma Knife remains unchanged, but evolved through the advancement of computers. In 1951 Leksell introduced the idea of bloodless radiosurgery using ionizing radiation (102,103). Initially, use of a proton beam was trialled due to its dosimetric and biological advantages. However, the

experiment failed due to the cost of proton production and challenges using the proton beam. After experimenting with many different prototypes of different sources, cobalt-60 was the chosen energy source, as the gamma emissions produced from cobalt-60 achieved the goals of stereotactic neurosurgery (104). Co-60 is a unstable isotope with a high neutron/proton ratio. Co-60 decays by emitting beta particles with energy 0.32 MeV and neutrinos. These beta particles do not affect the Gamma Knife, and are absorbed by the treatment head. Two gamma photons are released from the recoiled nucleus withs energy of 1.17 and 1.33 MeV, respectively; this is the main component that indirectly ionizes the target tissue (105). High energy gamma is the primary radiation used in the Gamma Knife, which creates a clinical effect through direct ionization of the cellular target (106). The Gamma Knife's components and mechanism differ from radiotherapy, and explaining these will help to establish fundamental grounding for the upcoming chapters.

2.1.3.1 Position of the beam

As mentioned previously, the Gamma Knife uses Co-60 as an active source that cannot be switched off and on like a linear accelerator. Furthermore, the mechanism of the beam positioning differs between the radiotherapy linear accelerator and the Gamma Knife. The Gamma Knife contains multiple arrays that vary between models, such as the 201 array Leksell, or 192 in Perfexion. These sources are aligned with a collimator system, which guides the Gamma Knife to direct the beams of gamma rays to a particular point. The gamma technique uses multiple beams directed at a specific point to ensure a high dosage rate. Furthermore, the cross-firing of gamma beams creates a biological advantage in the case of a small target. These multiple beams lead to the dispersal of energy between the individual beams, because the dose gradient is large outside the desired target area. Additionally, the dose distribution inside and outside the target is fairly heterogonous when compared to dose distribution in radiotherapy. In radiotherapy, fractional dose planning utilizes the biological effect between normal and target tissue. Tissue sparing can be achieved with a steep dose gradient in the Gamma knife single fraction routine (107,108).

2.1.3.2 Collimation system

Improvements to the Gamma Knife in recent years have related not to the source of the energy or the core idea, but to the collimation system. Earlier models' sources were located in five concentric rings inside the central body. The distance between the focal point and the sources is

constant, at 400 mm. The main body contains a pre-collimator and primary tungsten collimator configurated with source assemblies. These sources are aligned with the target area during the treatment and remain stationary. The earlier model includes an external helmet, and the final beam collimation is illustrated figure 2.10.a. The helmet contains a beam channel that can be modified to create a 4,8,14,18 mm beam size field by removing the tungsten alloy. The newer model includes no external helmet, and all components are within the main body. Furthermore, there are eight sources, which are not stationary. The collimator in the newer model contains 192 beam channels, as seen in figure 2.10.b. The sources in the new model are attached to a motor inside the body. Each source contains an independent collimator with a field of 4, 8, and 16 mm. Furthermore, a block shields the radiation when the patient is repositioned, so as to protect the OAR.

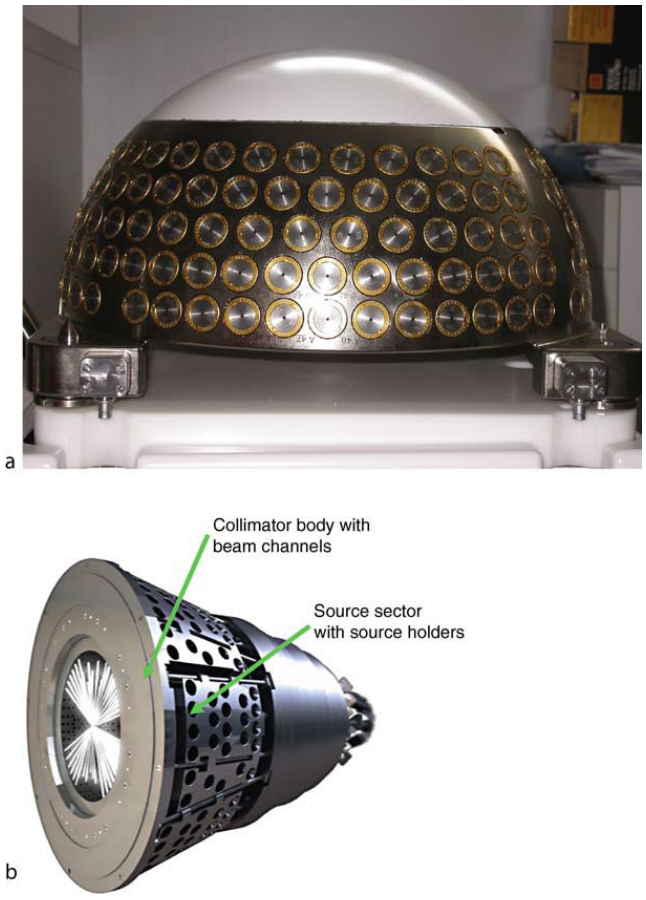

Figure 2.12: Illustration of Gamma Knife. A) collimator helmet. B) the internal sector of the collimator (109).

2.1.3.3 Planning Gamma Knife treatment

The accuracy of the Gamma Knife is one of the main advantages of the treatment, and cannot be achieved without an imaging modality. Radiotherapy and the Gamma Knife both depend on the accuracy of imaging modalities, but the Gamma Knife requires a stereotactic fiducial system for all imaging. The stereotactic fiducial system is a box to which the Leksell frame is attached. This box contains dots that help the treatment planning system identify the location of the anatomy relative to the Leksell space. The primary modality used in most treatment centres is the MRI, because of its ability to visualize soft tissue and solid tumours (110). A T1 weighted sequence is primarily used, although in some cases visualization of the internal auditory canals requires more specialized sequences (111,112). CT, which is mandatory in radiotherapy, is not a Gamma Knife and is not used in many cases. In some cases, if additional information is required for the bone anatomy, the use of a CT image is needed. The delineation of the target and OAR differs between traditional radiotherapy and the Gamma Knife. In radiotherapy, a gross tumour volume (GTV) is contoured and then expanded to create the clinical target volume (CTV), and the CTV creates planning tumour volume (PTV) to ensure the setup error is included in the treatment region (113). In the Gamma Knife, contouring of the target should be as close as possible to the target outline in those images without expanding or adding volume.

The Gamma Knife algorithm used in the treatment planning system needs to account for physics basics to cover the dosimetric perspective. The physics required for the Gamma Knife is photon attenuation, reduction of the dose rate due to interaction with the collimators, the inverse square law, and dose falloff. The planned algorithm used for the Gamma Knife models the brain as a homogenous water equivalent volume, with no built-up region in the surface area. This assumption means the physics required for the algorithm is simple and not time-consuming. However, from a geometric standpoint, each source of cobalt 60 needs to be modelled for accurate dose distribution.

2.2 Overview

This chapter's focus has been to introduce the important external beam modalities and their components. Each modality employed different physics principles with varying advantages and disadvantages. The basic rule of radiotherapy here is to reduce uncertainty as much as possible to

deliver the best possible treatment. Over the past few years, advancements in computer tomography have allowed for better delineation of the OAR, and more accurate data for calculating dose distribution. Furthermore, novel treatment modalities have a digital 2D panel and X-ray tube, which implement cone beam CT to reduce error rates in patients' position during fractions. The linear accelerators are similarly more accurate in alignment (114). One uncertainty here is that the treatment planning system algorithm most likely cannot handle heterogeneity at the treatment site, such as air, bone, or metal implants. The coming chapter will also focus on the MC algorithm, addressing how it provides a solution to resolve the high uncertainty associated with dose distribution in heterogenous areas.

Chapter 3: Monte Carlo

3.1 Introduction

The idea of using the MC simulation for particle transport was introduced during World War II. During the Manhattan Project, a statistical method was required to solve both the neutron diffusion problem and the multiplication issue, and MC helped overcome this. Metropolis and Ulam's first published paper in MC dated to 1949 (115). However, the first article concerning MC and electron transport was introduced by Wilson in 1951 (116). In recent years, MC has become an essential tool in nuclear physics, thermodynamics, quantum mechanics and radiation transport (117). MC is an collection of algorithms designed to indirectly solve the Boltzmann transport equation using a numerical solution (118). MC provides a simulation with the record, and reports particles' interactions with different mediums.

The MC has proven itself to be the most accurate method for calculating dose deposited in a medium and particle interaction. The advantage of MC is that it can calculate dose distributions from the incident beam, without relying on the measured data (119). The MC does not use scaling or conversion for tissue to water dosage to determine effects in heterogeneous areas. MC algorithms use microscopic, rather than macroscopic transport for primary and scatter photons. To simplify the function of MC using random sampling is a method used to approximate answers to an integral or mathematical problem (117). The MC method generates a probability distribution for a quantity under investigation, and statistical uncertainty can be calculated from that distribution (117). For example, the calculation of π for a circle can be achieved with MC; inside the MC algorithm, draw a circle of radius r within a square and throw darts at the square without aiming. The answer for π can be calculated by dividing the number of darts that hit the circle by the darts that hit inside the square equal to the area of a circle, and divided by the area of the square. To achieve a highly accurate answer to any problem, many darts need to be thrown, which then affects the simulation time. In general, a MC simulation is slower to resolve problems than an analytical algorithm. This is because the MC needs to repeat the subprocess multiple times to reduce statistical variance. whilst, an analytical algorithm only needs to resolve a set of equations once (117). The downside of an analytical algorithm is that many obstacles arise when a complex problem arises. However, in the MC, the complexity of the problem need not affect the simulation, because MC does not examine macroscopic complexities. The advantage of MC is that it can use

microscopic physics, which is well understood and simplifies complex problems (figure 3.1) (117,120). The MC method solves a temporal evolution of objects interacting with other objects based on a cross-section, known as a quantum particle in medical physics, providing a numerical solution. MC applies the natural rules of interaction, which are processed randomly and repeatedly. The process continues until a numerical result estimates the means, variance, and quantity of interest. The principle of MC considers a simple approach, and due to the focus on microscopic interactions, complex geometry can be considered easily. MC has an advantage in terms of physical problems with the evolution of five and higher-dimensional systems. Typically, radiotherapy is 6 or 7 dimensions. The human body has a complex geometry, but as explained, this is not an issue with MC. The time needed to solve a complex problem does not differ significantly from a simplified one. Compared to the analytical algorithm, the greater the level of complexity, the more time is required to solve the problem (103).

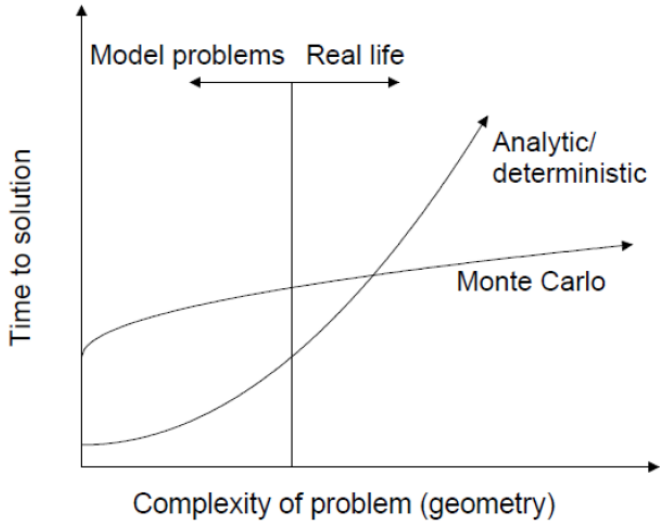

Figure 3.1: Illustration showing the time needed and complexity of the problem to be solved with the MC and analytical algorithm (117).

3.2 Random number sampling

All MC algorithms rely on a random number generator to help solve complex problems. The use of a large random number ensures the random numbers used in any MC simulation are not related and not interdependent. In radiotherapy, some features are required in a random number generator to ensure the results are not false. The first required feature in a random number generator is that the sequence of numbers be large enough to ensure the sequence is not used again,

leading to a correlation in the MC results. In other words, if the sequence of random numbers repeats too quickly, it can lead to inaccuracies or biases in the simulation outcomes. The second important feature is to achieve multidimensional numerical integration. This is because the transport of radiation is complicated, and one-dimensional integration is not adequate to solve the equation. An example is calculating dose in radiotherapy. Here, a multi-compartment equation is necessary for photons and electrons because they are related through Bremsstrahlung, Compton scatter, and photoelectric absorption (121). In radiotherapy, primary particles produce unlimited secondary photons and electrons in an infinite space with parameters. To solve such a problem, some parameters need to be set. A finite space must be used to allow numerical integration and an energy level that stops the simulation once the photon and electron reach that level. Numerical integration works by choosing a sample from the setup dimensional parameter, and from this point a demonstration of the sample is shown by the particle history, which is then created from all secondary particles and daughter particles. These secondary particles and daughter particles are generated from primary particles. Many events are necessary to realize a reliable average value, which can only be achieved through low statistical uncertainty (122). This statistical uncertainty can be reduced by a factor of 2 by increasing simulation events by a factor of 4 (117).

3.3 Monte Carlo radiation transport

The MC method was adapted for the radiotherapy and dosimetry field by describing radiation transport, which can be achieved by solving the Boltzmann transport equation. The Boltzmann transport equation applies the microscopic law of physical interaction between particles and matters in phase space. In a highly complex geometry, such as the patient body, problem solving becomes more complex and cannot be achieved without introducing approximations of the problem. The accuracy of the result provided by MC, however, depends on the accuracy of the geometry, the number of primaries or particles and the cross-sectional data. Due to the nature of the interaction between radiation and matter, which is probabilistic, the MC method is perfectly suited to handling radiotherapy and dosimetry problems (117,123). MC codes for radiotherapy are readily available, and many different codes can be used to model the radiotherapy treatment head or dosimetry. Examples are EGS, PENELOPE, FLUKA, and GEANT4. Each code provides an advantage and some limitations that may not suit the experiment type that needs to be used (117,124). In these two codes, FLUKA and PENELOPE will be used.

3.3.1 Photon interactions with matter

The microscopic physical law particle interaction follows is well-studied and controlled by quantum electrodynamics. The MC algorithm must include the probability with which each interaction may simulate particle transport with high accuracy. Interactions that may occur in conventional radiotherapy are coherent scattering, Compton scattering, the photoelectric effect, and pair production. Figure 3.2 displays possible interactions in each energy range, wherein each interaction dominates a domain. The probability of each interaction changes in terms of photon energy and Z of the medium (125).

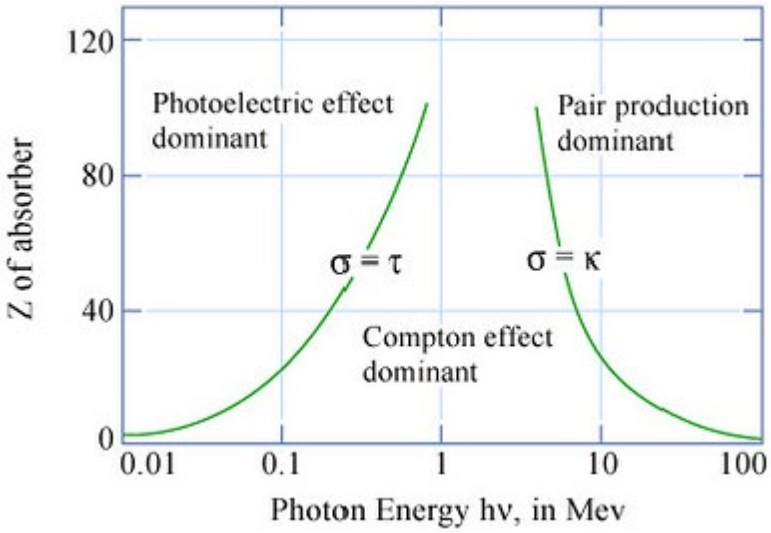

Figure 3.2: The three possible interactions and their relative energy and atomic number (126)

3.3.1.1 Coherent scattering

Coherent scattering can have different names, like Rayleigh scattering or classical scattering. In coherent scattering, a photon interacts without transferring any energy to the target atom. That is, coherent scattering does not convert energy to kinetic energy (figure 3.3), but the photon is deflected. The interaction leads electrons to a temporary vibrational state with frequency equal to that of the incident photon. The electrons then need to return to stable conditions, which can be achieved by releasing electromagnetic radiation similar to that of the incident photon. The effect of coherent scattering can be seen in energy below 100-keV which is mainly used in diagnostic radiology. Coherent scattering at this low level can cause a broadening of the radiation

beam (127). The likelihood of coherent scattering is decreased with the increase in photon energy and low Z material. In radiotherapy and radiation dosimetry, coherent scattering is ignored and seen as a non-significant interaction, because it contributes to less than <10% of the therapeutic energies range.

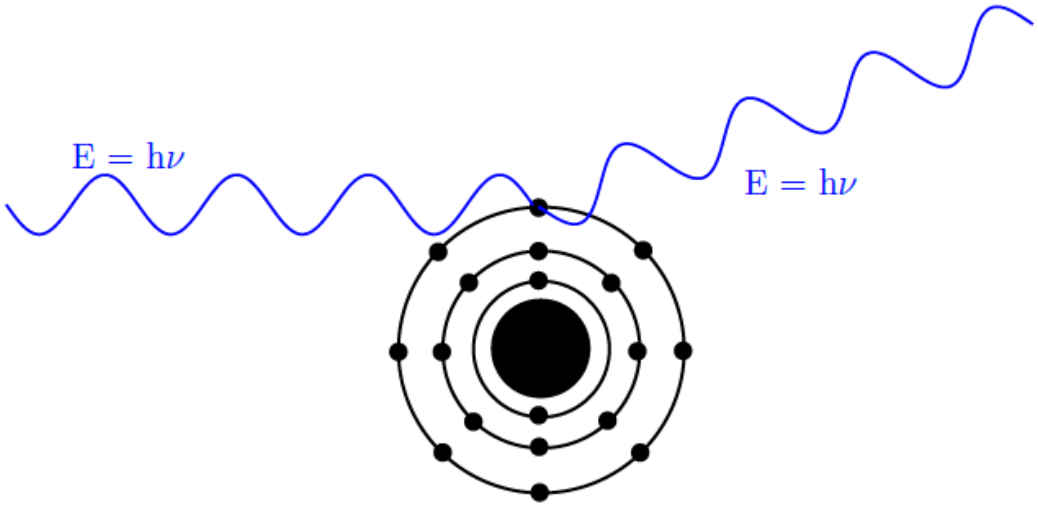

Figure 3.3: Coherent scattering. The interacted photon has an energy of E=hv, and the scattered photon receives the same energy E= hv of the original photon because no energy is transferred.

3.3.1.2 Photoelectric effect

The photoelectric effect describes the dominant interaction at a low energy level. When the photon interacts with the bound electron the incident photon loses all its energy to the electron. The electron then becomes a photoelectron and leaves the atom. The kinetic energy of the photoelectron can be calculated by:

$$E = hv - E_B \qquad (3.1)$$

Where h is Planck's constant, v is frequency, and E_B is electron binding energy. The photoelectric effect cannot occur if the photon energy is lower than the electron binding energy. The atom loses one electron from the inner shell, which needs to be covered by the electron in the outer shell. The process of filling the vacancy in the inner shell leads to the emission of either fluorescence or/and an Auger electron. The photon emitted from filling the inner shell has energy that is equal to the difference between the shells' energy. The possibility of photoelectric interaction reduces with increases in photon energy and increases with an increase in the Z number of the medium. Photoelectric effect is the dominant interaction in the range below 0.1 MeV (127,119).

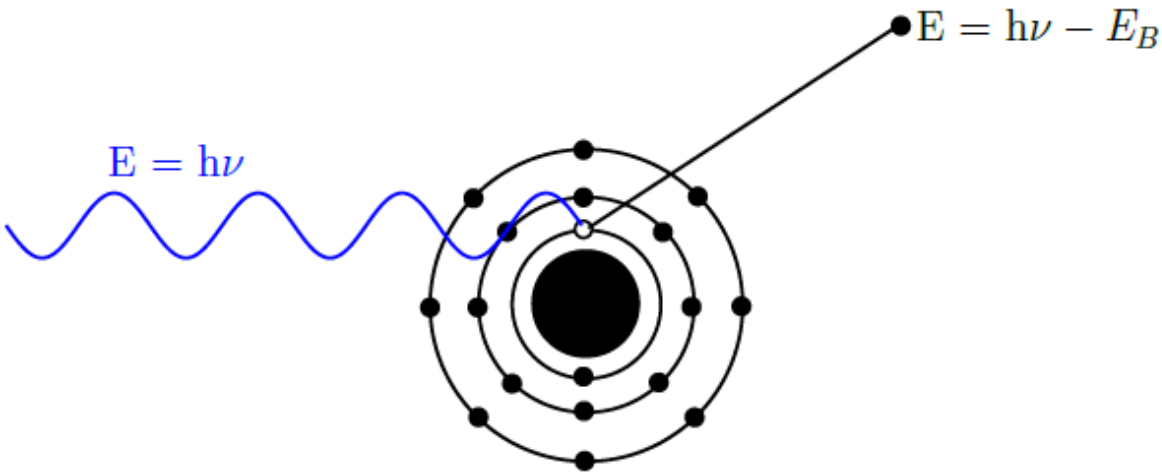

Figure 3.4: The photon electric effect.

3.3.1.3 Compton scattering

Compton scattering (incoherent scattering) occurs when a photon interacts with an electron, leading to a change in the photon's direction, transferring kinetic energy to an electron. Furthermore, kinetic energy transferred from the incident photon frees the electron from the atom. The maximum transfer of photon kinetic energy to the electron occurs when the photon scatters at an angle of 180°, with the result that the electron will be ejected at an angle of 0°. The maximum transferred kinetic energy can then be calculated using a simple equation:

$$hv = hv' + E \qquad (3.2)$$

where hv is the energy of the original photon prior to the collision, the energy of photon after collision with the electron is hv', and E is the energy of the electron. The photon can be scattered from 0 to 360 degrees. Like a photon, the recoil electron can have an angle of 0 to maximise energy transfer. When a recoil electron receives maximum energy, it can transfer energy to another electron within the medium. Compton scattering starts to decrease when photon energy is greater than 10 MeV (127), and the Compton scattering interaction dominates interactions in an energy range of 100 KeV to 10 MeV. Compton scattering is the dominant interaction in radiotherapy because the range of the energy in radiotherapy is between 1 MeV and 10 MeV.

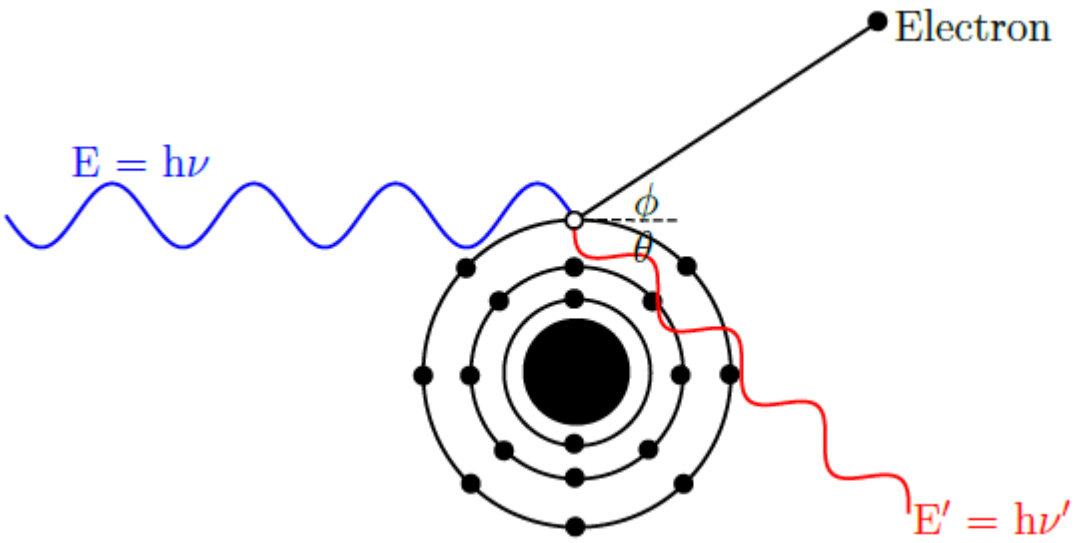

Figure 3.5: Compton scattering.

3.3.1.4 Pair production

When a high energy photon ≥ 1.022 MeV interacts with the nuclear Coulomb field, the incident photon is transferred until all its energy is absorbed. The result of the interaction is electron-positron particles, termed pair production. The threshold of pair production is $E = 2\ mc^2$. Energy higher than the threshold is transferred into both the electron and positron. The pair electron and positron deposit the excess kinetic energy into the medium, and the positron resulting from pair production travels in the medium and loses energy through ionization and excitation. The positron reaches the point where it has lost the majority of its energy and is annihilated by an electron. This annihilation creates two photons with 0.511 MeV, and which travels in the opposite direction. A related process involving pair production is triplet production, which affects the electron's Coulomb field rather than the nucleus's Coulomb field. A pair of electrons and positron is produced, and some energy is then absorbed by the original electron. The threshold for triplet production is higher than for pair production, and requires at least twice the energy as that provided by pair production (125).

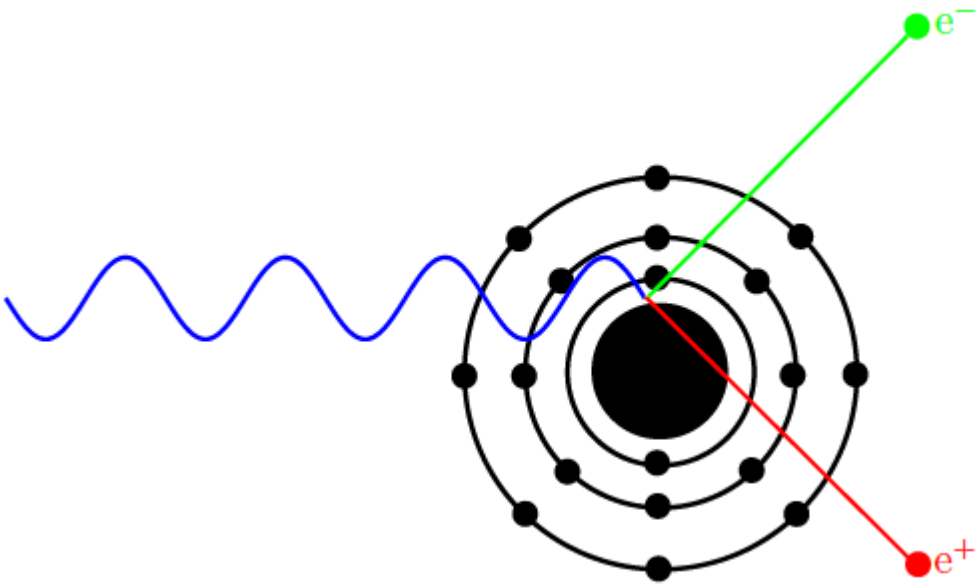

Figure 3.6 Pair production

3.3.2 Electron interactions

3.3.2.1 Inelastic scattering

With inelastic scattering, the traveling electron with the correct mass interacts with an orbital electron of the medium designed to lose most of the electron energy and change the direction. Some electrons travel through a medium close to the atom, but the distance is larger than the atom's radius, leading to transference of the energy to the orbital electrons. The extra energy results in the orbital electron being uplifted to a higher energy state. However, this can only occur if the binding energy is greater than the electron energy. When the traveling electron passes close enough to the orbital electron, the transferred energy can then eject the orbital electron. Due to the ejected electron, the atom becomes ionized. The ejected electron contains sufficient energy to ionize other atoms, called delta rays. The process of creation of the delta ray is called Moller scattering. In Moller scattering, the incident particle can lose half its kinetic energy, which is the maximum energy transferred in each interaction. Inelastic scattering is the primary mechanism of electron energy loss in instances of energies being higher than 10 MeV (128).

3.3.2.2 Bremsstrahlung production

The atomic is surrounded by a strong electric field that can attract electrons as they pass close enough to the field. Due to this, inelastic scattering will occur. The incident electron carrying an electric and magnetic field, which is altered after entering the strong electric field of the nucleus. This adjustment leads to the release of some electron energy in the form of electromagnetic radiation. The energy emitted from the adjustment is called bremsstrahlung radiation, and equates to the difference between electron energy before and after adjustment. The emitted photon energy can reach a level that is equal to the initial electron energy. The traveling electron can then undergo more than one bremsstrahlung interaction (129). The bremsstrahlung interaction increases with a high atomic number and light electron particles $(\frac{z}{m})^2$; for example, electrons. The bremsstrahlung interaction is insignificant in low atomic mediums such as water and tissue and at an energy lower than 10 MeV. The bremsstrahlung interaction contributes to only ~ 3% of the initial electrons interacting with the tungsten target in a radiotherapy machine (125).

3.3.3 Proton interaction with matter

The previous section examined photon interactions with matter as a foundation for the coming chapter. This section goes on to explain proton interactions with matter to add to existing knowledge in the field. Protons interact differently with matter than photons do. Photons usually go through several interactions before depositing their energy. As a result, photons lose their energy on a large scale, and do not have a precise range inside the medium they travel through. On the other hand, protons experience large interactions before they deposit their energy and have a well-specified range in the medium. Protons interaction with matter can be categorised into three different Coulomb interactions: inelastic, elastic, and nuclear coulomb interaction.

3.3.3.1 Inelastic coulomb interaction

Protons are usually positively charged particles with a mass of $1.67x10^{-27}$ kg, and have a mass approximately 1800 times larger than that of an electron. For this reason, in the case of the inelastic interaction, a proton interacts with an electron in the shell, depositing enough energy to eject the electron. This interaction results in the proton losing a small amount of its energy, a free electron and an ionised atom. The energy proton loss that arises due to the interaction with the

electron is minimal, due to the mass difference. In an inelastic interaction, the proton does not significantly alter its direction. The ejected electron is commonly ignored in proton therapy, because it travelled less than 1 mm and deposits its energy locally (130).

3.3.3.2 Elastic coulomb interaction

An elastic interaction occurs when the proton interacts with the atom's nucleus changing its direction. As a result, the nucleus absorbs some energy as a way to conserve momentum. This elastic interaction is the main cause of lateral scatter, as there is a change in the direction of the proton. This elastic interaction does not occur frequently relative to inelastic interaction, which is considered the primary interactive mechanism of proton therapy (130).

3.3.3.3 Nuclear interaction

Nuclear interaction occurs less frequently, at roughly 1%/1cm in water, and only 20% of the protons in the beam undergoes nuclear interaction. The proton is absorbed entirely by the nucleus of the atom. The result of this interaction is the release of neutrons or heavy ions. The protons that escape from the nuclear interaction are called primaries, and the particles that emerge from nuclear scatter are termed secondary (130).

3.4 Statistical uncertainties in patients' dose calculation

Statistical noise describes a level of uncertainty that cannot be avoided in the dose calculation for the MC radiotherapy simulation. Unavoidable statistical noise occurs due to the dose fluctuation in each voxel. The dose fluctuates mainly around its mean value, affecting the isodose and DVH. Variance σ^2 describes the statistical noise, with a lower variance value being preferable. Reaching zero variance is ideal for a simulation, but it frequently cannot be achieved because of the finite amount of time needed.

Efficiency, ε, is the main parameter when evaluating MC performance. Simply, efficiency describes how fast the MC simulation can reach the required variance, which can be calculated using the equation $\varepsilon = \frac{1}{\sigma^2 T}$, where T is the time a central processing unit (CPU) needs to achieve a required variance (131). The recommended level of uncertainty permitted in radiotherapy is less than 2%, which can take a long time to simulate. However, introducing variance reduction techniques helps to minimize the time required to achieve the desired uncertainty level (132).

3.5 Variance reduction techniques

The MC algorithm is considered the gold standard in radiotherapy, but it is generally agreed that the long simulation time is not practical for clinical work. Thus, some techniques have been introduced to reduce the time taken, such as Russian roulette, uniform particle splitting, and range rejection (133).

3.5.1 Uniform particle splitting

One of the basic variance reduction techniques is particle splitting, which can be used with photons and charged particles. As illustrated in figure 3.7, the techniques shows the bremsstrahlung production in a medical linear accelerator. The left side of the illustration simulates one electron producing one bremsstrahlung photon after hitting the target. The production of one bremsstrahlung photon per electron is used here to simplify the illustration and explain the particle splitting technique. The statistical weight of one photon in the simulation is w = 1 to one realistic photon. On the right side of the illustration is the particle split, with a factor of N = 5. One electron will typically produce five independent photons. However, to ensure balance in the statistical weighting, each photon is weighted w =1/N, which means in the case of w = 0.2, with the new weighting distribution, that the total weight of the real photons is preserved. The splitting techniques help increase photon production while reducing the time required to create them, thereby reducing statistical uncertainty and the time taken (134,135).

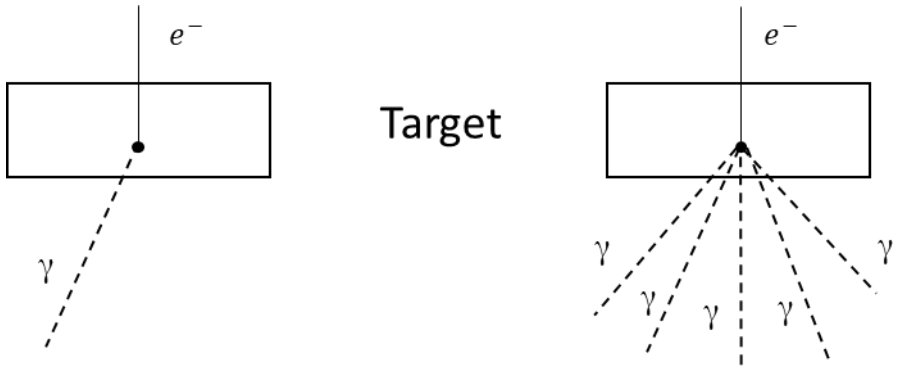

Figure 3.7: Particle splitting technique. On the left side, one electron produces one photon with statistical weight 1. On the right side, applying a splitting factor of 5, one electron produces five independent photons with a weighted statistical factor of 1/N.

3.5.2 Russian Roulette

In most cases, more than one reduction technique is used for an MC simulation. Russian roulette may be used with particle splitting because Russian roulette can be thought of as the reverse technique of particle splitting. When using Russian roulette, a survival probability $P_{survive}$ is defined as $P_{survive} \ll 1$. When applying a threshold, a test carried out with a random number ξ from the distribution uses an interval [0,1]. The particle is expected to survive if it passes the $\xi < P_{survive}$. Otherwise, it will be stopped and then terminated. The statistical weight of the particles needs to remain in parallel with reality, because the statistical weight of the survival particle is increased by the factor $w = {}^{1}/_{P_{survive}}$. An example of combining both reduction techniques involves simulating a LINAC treatment head, in which an electron produces a bremsstrahlung photon after heating the target. The photon created can go in the direction of the collimator, in an interaction termed Compton scattering. The interaction with high Z materials leads to the creation of the Compton electron. The majority of Compton electrons will not produce any secondary electrons and are absorbed in the medium. Simulating these electrons wastes time and resources, because they do not add value to the result. However, if the Compton electron produces a bremsstrahlung photon, a simulation of the photons is essential if the photon is to reach a region of interest. A more advanced technique is then required, so as not to affect the result (134). A study carried out by Rodriguez *et al.* shows using a combination of photon splitting and Russian roulette in the PENELOPE algorithm improves efficiency, leading to lower statistical uncertainty by a factor of 45 (136). Another study compared efficiency using a combination of splitting factors and Russian roulette, in a simulation without using any variance reduction techniques, finding an increase in efficiency of 69 times when using variance reduction techniques (137).

3.5.3 Range rejection

A Compton electron maybe created from interactions with high Z materials, similar to the example in section 2.5.2, and can be stopped using range rejection, which can be used instead of Russian roulette. However, some information is needed before applying range rejection, including describing the distance of the present photon to the boundary, and the maximum distance the photon can travel in the target medium. This technique can only be used in association with a known maximum particle range, and so depends on the particle energy. The photon will be stopped

or terminated if the range is smaller than the range to the boundary, and this will then not affect the interest region that needs to be simulated. The technique is specific because it requires the above information to be provided, and in many simulations, it is not easy to correctly establish the range of the photon (134,138).

3.6 FLUKA MC algorithm

MC simulations have become a highly discussed topic in recent years due to the availability of more algorithms, and the high-accuracy dose calculation. The most frequently used MC codes in radiotherapy fields are EGS, FLUKA, PENELOPE, MCNP and GEANT4. Still, MC codes are not user-friendly, making it more challenging to apply them routinely in a clinical environment. The different MC codes deliver some advantages and disadvantages. FLUKA is used in this study, due to its high accuracy and flexibility with Micro CT and proton simulation (139,140).

FLUKA is an MC code used in multiple applications, such as radiotherapy, shielding, calorimetry, dosimetry, detector design, neutron physics, and cosmic ray simulation (140–142). FLUKA contains more than 60 different particles, producing an interaction result with a high level of accuracy. The range of energy available in FLUKA provides additional options to facilitate the simulation. A photon or electron can be simulated from an energy of 1 keV to 1000 TeV. In hadrons, it can reach 20 TeV. Furthermore, the tracking system in FLUKA can track particles in different environments and those with electric or magnetic fields. FLUKA uses highly accurate, well-known microscopic models to describe the interactions of different types of particles with matter. FLUKA evaluates the interaction model at each step to ensure consistency in a variety of reactions (139,140). FLUKA was checked and benchmarked at the interaction level with experimental data. The underlying physical model used for single interactions can ensure high accuracy in complex cases with absent experimental data, because FLUKA is built to record single microscopic interaction (143). FLUKA works by inputting cards with specific commands, which are written in an American standard code for information interchange (ASCII) format, to execute simulations. The basic structure of an input card is as follows:

- Titles and comments used for the labelling and identification of simulations.
- Identify a particle source.
- Describe the geometry as a voxel for the simulation region.
- Describe the material used in the geometry.

- Describe the material assignments.
- The scoring card, for example scoring of energy, dose and fluence.
- Adding a biasing option.
- Adding any settings for particles not included in the results. For example, cutting any particle with a specific threshold.
- Beginning the random number sequence.
- Adding the number of histories to be used in the simulation.

More cards are available for different purposes, including global cards that need to be used if DICOM files are uploaded to allow FLUKA to handle many voxels. In addition, the user routine is another option designed to create a customized input file, or one that is more advanced that is not available on the standard input card. The latest update in FLUKA allows for the handling of the DICOM series, which is important in radiotherapy because the DICOM series contains a lot of essential information, like the HU of each voxel needed, and the location of each slice (139,144).

3.6.1 DICOM in FLUKA

Exchanging information between different clinical centres is a challenging task. Furthermore, transferring information between different medical equipment manufacturers is complicated. The National Electrical Manufacturers Association (NEMA) created a standard datastore format to establish common ground between all manufacturers. DICOM has become the standard format that simplifies the exchange and transfer of information between different centres (145). DICOM files contains all the requisite information in radiotherapy to create a treatment plan. Furthermore, a treatment plan that includes information on beam energies, gantry angle and region of interest can be saved in DICOM format. The selected DICOM format has been uploaded derived from Python dictionaries, which use a dataset to store information. The DICOM format comprises a collection of pairs of keys and values. The key represents the DICOM tag, and the value is the data elements. The reason for using the Pydicom library is to make the method easily accessible to everyone (146,147). Figure 3.8 provides an example of DICOM dose information and how it is organized. The first column on the left provides a tag number, and the second column an attribute. The third column identifies the value. The fourth column is the value representation and the final column the data length.

Tag	Attribute	Value	VR	Length
(0008,0005)	SpecificCharacterSet	ISO_IR 192	CS	10
(0008,0008)	ImageType	[3] ORIGINAL, PRIMARY, AXIAL	CS	22
(0008,0012)	InstanceCreationDate	20221118	DA	8
(0008,0013)	InstanceCreationTime	171526.040000	TM	14
(0008,0016)	SOPClassUID	1.2.840.10008.5.1.4.1.1.2	UI	26
(0008,0018)	SOPInstanceUID	1.2.826.0.1.3680043.8.691.4.28984515528608.1887.1668605797225.12	UI	64
(0008,0020)	StudyDate	20220831	DA	8
(0008,0021)	SeriesDate	20220831	DA	8
(0008,0023)	ContentDate	20220831	DA	8
(0008,0030)	StudyTime	084110.173000	TM	14
(0008,0031)	SeriesTime	091323.397000	TM	14
(0008,0033)	ContentTime	092301.530000	TM	14
(0008,0050)	AccessionNumber		SH	0
(0008,0060)	Modality	CT	CS	2
(0008,0070)	Manufacturer	Philips	LO	8
(0008,0090)	ReferringPhysicianName		PN	0
(0008,1010)	StationName	HOST-4CE0212317	SH	16
(0008,1030)	StudyDescription	Planning CT Radiotherapy scan with contrast	LO	44
(0008,103e)	SeriesDescription	3MM	LO	4
(0008,1090)	ManufacturerModelName	Big Bore	LO	8
(0010,0010)	PatientName	Pancreas_Stent_1	PN	16
(0010,0020)	PatientID	Pancreas_Stent_1	LO	16

Figure 3.8 Example of DICOM data

A treatment planning system saves and exports the patient's information into different DICOM files; the original DICOM from the CT scan, radiotherapy treatment (RT) structure, RT plan and RT dose. All these files contain the specific information needed to explore or re-simulate treatment in the MC algorithm (147). For example, the DICOM image from the CT scan contains anatomical information concerning the patient. Furthermore, a medical CT scan provides a Hounsfield unit (HU), representing the density of the different organs and tissues in the patient's body. In a two-dimensional array, the HU is stored in the DICOM under the tag name pixel array. The DICOM contains many files, representing a slice in the z-direction. Stacking all the files together produces a three-dimensional grayscale image. Additionally, DICOM files contain the pixel size, patient position, and patient orientation during the imaging. This information is essential to calculate a treatment dose (147,148). The second set of DICOM files is the RT structure created within the treatment planning system. The RT structure contains contouring of the region of interest, such as PTV, GTV, and organs at risk. Contouring means outlining the organ at risk and the targets to guide the radiotherapy plans. In addition, the RT structure contains the contoured region's orientation and the delineated colour lines. The RT structure is essential because DVH cannot be calculated or visualize dose distribution in PTV or organs at risk without it. The treatment planning system exports the second set of information, known as the RT plan, which is essential for re-calculating the plan. The RT plan file contains information about beams, dose

prescription, patient setup, gantry rotation, angles, and isocentre position. This information is essential to mimic TPS treatment using the MC algorithm (147,148). The last file is the RT dose, which contains the calculated dose from the TPS. Furthermore, the RT dose contains other dosimetric information, including the size of the scoring gride, scoring region, and dose distribution in a three-dimensional array, meaning the RT dose contains some pixel array information. Exporting the RT dose file from TPS makes it possible to view each beam dose distribution separately, or view a combination of all beams as the results (147,148). The files exported from TPS cannot be uploaded directly to FLUKA, because FLUKA cannot read all this information. As mentioned, FLUKA uses voxels to describe the complex geometry used in the design or input. Flair is a graphical interface that can be compiled with FLUKA to handle tasks such as uploading DICOM CT images and transferring them to voxels. Voxels from DICOM can be transferred into the FLUKA environment, and recently the new update permits the upload of the RT structure into FLUKA, although some problems need to be solved. Flair provides an option to transfer each voxel HU unit to its density using a default conversion table, or modifying the conversion table to add more elements. However, Flair was unable to handle the RT plan or RT dose until recently. Now, all the information needs to be added manually, or a customized code needs to be written to upload more complex treatment (144,149,150).

3.7 PRIMO MC

PRIMO is another software, which contains the MC algorithm that will be used in chapters 4 and 5. PRIMO can be built using the PENELOPE, PENEASYLINAC and PENEASY algorithms. PRIMO combined all the available components in a friendly graphical interface to support a more friendly radiotherapy simulation. PRIMO can also read a simulated phase-space file using other codes, but must be in an Interactional Atomic Energy Agency (IAEA) binary format. Multiple linear accelerators have been introduced in PRIMO, such as Varian Clinac 2100, and Varian Clinac 2300. Furthermore, two versions of the multi-leaf collimator are available, Millennium 120 and 120 HD. One of the features of PRIMO involves allowing multi-beam simulations with different geometric setups. This feature allows for the simulation of step and shoot and continues on from IMRT. Many parameters can be edited, such as mean energy, focal spot, and beam divergence. Meanwhile, tuning needs to be done to achieve a high percentage of

agreement across the PRIMO simulation and measurements. In chapter four, tuning was done using measurement data from Singleton hospital.

As explained, the PRIMO's main engine is PENELOPE, which was introduced in 1996 by the Nuclear Energy Agency Data bank (151). The first version of PENELOPE can simulate electrons, positrons and photons with complex geometries (151). PENELOPE is written in Fortran 77, and various packages were introduced to fulfil different tasks, such as a materials program to control the material in the simulation. The code's first significant upgrade was introduced in 2001 (152). The physics model used for the electron/positron elastic scattering was the Wentzel model, and this was changed to enable a more accurate angular particle distribution. Furthermore, an update of the bremsstrahlung emission calculation was made. The new version of PENELOPE introduced a more specific K- and L shells fluorescence radiation calculation. A further minor upgrade was undertaken in 2003. All inner shell ionization of electrons was then counted as an independent mechanism to provide a more realistic value (153). This new major upgrade was later introduced in 2008. An improved particle transport algorithm introduced photon polarization and an algorithm to model Rayleigh photon scattering. The PENELOPE algorithm is continually being upgraded with more advanced algorithms, to provide more accurate simulations of different interactions. In 2011, models for a polarizing photon, inelastic collision, and N shells ionizing events were improved. In the latest version, a minor upgrade was made, which involved expanding the cross sectional databases and including radioactive sources (154).

3.8 Comparison of MC and analytical algorithms

3.8.1 Phantom

Many researchers evaluate and compare the use of different TPS with MC to assist in ongoing developments to improve accuracy and decrease the uncertainties associated with photon dose distribution (155,156). An improvement rate of 1% in dose distribution accuracy can lead to an increase of 2% in the early-stage tumour cure rate (157). Researchers report a reduction in the prescribed dose by 5%, where uncertainty in TPS causes 10% to 20% variations in local tumour control probability. This figure can achieve a 30% difference in establishing the probability of normal tissue complications (158). For this reason, increasing the accuracy of radiotherapy is vital

to providing better patient treatment. Throughout the thesis, an analytical anisotropic algorithm currently implemented in the Eclipse system was used. In the analytical anisotropic algorithm, the materials are all treated as water of varying densities. The Hounsfield units were extracted from CT and converted to varying electron densities. However, the medium was still considered water in terms of chemical composition. (159). Han *et al.* studied differences in dose distribution between the analytical anisotropic algorithm (AAA) and MC algorithms using both homogenous and heterogenous phantoms (160). The result reveals an agreement in dose distribution on the homogenous phantom between Varian golden data, AAA and MC. However, dose distribution varies in the heterogenous phantom, especially in the bone area, which reaches 15.4% difference between golden data and MC. The AAA underestimated or overestimated the dose by 8.3% in heterogenous areas compared to MC. The AAA did not meet the 2%/2 mm distance to agreement (DTA) criterion in areas containing air and bones (160). The results from Fogliata *et al.*'s study align with those found in the literature review, which state that the AAA algorithm overestimated the dose in heterogenous areas compared to MC (161). Simulations carried out by Fogliata *et al.* and Bush *et al.* show that in the presence of air or high-density bone, AAA significantly differs in dose distribution, reaching as high as 17.5% (162). Tsuruta *et al*. demonstrate that the greatest difference in dose distribution between AAA and MC is at the boundaries of tissues with different densities (163). Differences in dose distribution are clearly seen in the interface between the two different densities, as shown in the above mentioned studies. The study by Alhakeem *et al*. focuses on the interface dose distribution using a water-air phantom. The results show the differences between TPS and MC in the water-air phantom fall between 5.7% and 12.8% (164). Notably, the study ignores the readings of the first few voxels after the air gap, where the reading is higher, instead focusing on the secondary build-up region.

A similar result was detailed by Kan *et al*., who reported 7.3% using thermoluminescent dosimeter (TLD) readings (165). Stathkis *et al.* obtained a difference of 3%-15% in a similar interface interaction (166). These studies found similar outcomes: TPS shows a significant difference in dose distribution in the interface between different densities using a heterogeneous phantom. A study by Sterpin *et al*. demonstrated a significant dose difference between MC and AAA in a phantom imitating the ribs, bones and lungs using an IMRT technique. A significant dose distribution difference was observed at the border of the rib area (167). Ono *et al.* and Ashfaq zaman *et al.* demonstrated a similar result to that found in the previous study, reporting a significant

difference in dose distribution in the heterogeneous phantom at the border of a high-density materials such as bones (168). The latest study on dose to medium and dose to water recommendation for trials by Kry et al. demonstrated a difference between reporting dose to medium, and dose to water, reaching 10% in dense bone using the slab phantom and 1-1.4% in soft tissue (169). The study shows a difference in medical CT resolution. However, in this thesis a micro-CT data is used when calculating dose distribution using dose to medium. The micro-CT data can provide more in depth information regarding the effect of heterogeneous areas in dose distribution. The distinction between dose to water and dose to medium becomes more pronounced due to variations in interaction cross sections resulting from the diverse material compositions of the media. This dissimilarity in material composition can be accurately captured by Micro CT, which offers superior resolution, revealing certain details that might be absent in medical CT scans. Additionally, this distinction is observable on a macroscopic through factors like mass attenuation, energy absorption coefficient, and electron-stopping power.

The above-mentioned articles mentioned effects associated with high and low density, but focused predominantly on areas with air. However, high-density materials, such as high-density bones and metals, can also result in an overestimation or underestimation of the dose delivered to the target area; e.g., in a prostate patient with a hip prosthesis or a liver patient with a stent. Alhakeem *et al*. simulated a photon beam going through a water-steel phantom and compared AAA and MC. The average difference between AAA and MC is around 5.5%, mainly at the interface between the two different densities (164). AAA underestimates the dose at the interface because there is inaccuracy when simulating lateral and backscatter radiation due to the presence of the high-density materials (164). A similar outcome was observed by Ansbacher *et al*., and a dose peak of 20% at the interface of the metal was present in the MC but absent in the AAA. The dose peak is attributable to electron backscatter events. Furthermore, lateral electron scatter is shown in the MC simulation, but not in the AAA algorithm, leading to a 15% dose peak (170). The previous articles studied the effect of heterogeneity in TPS on the target. However, it did not mention the OAR outside the treatment beam. Howell *et al*. focus on the OAR outside the beam direction, showing a difference between the measurement and the TPS of 40%. The difference in dose increases when increasing the distance from the target (171). A similar outcome was reported by Huang *et al*., indicating that TPS uncertainty increases in OAR (172). The uncertainty in the AAA algorithm increased dramatically in the area with high heterogeneities, due to the limitation

in the interface dosimetry. The inability to handle coupled photon-electron transport at the interface area where backscattered secondary electrons originated from upstream or downstream tissue led to uncertainty in dose distribution, particularly in those areas with significant density variations.

3.8.2 Patients

The uncertainty associated with TPS in heterogeneous areas was noted in the articles mentioned when using a phantom to mimic different human parts. However, a CT simulation of actual patients is crucial to obtain accurate findings. A study by Linthout *et al*. demonstrates that an overestimation in the PTV dose in head and neck cases reaches 12% (173). A similar outcome was seen in head and neck cases in Onizuka *et al*.'s study, in which the difference between AAA and MC was over 7% in IMRT treatment (174). Rana *et al*. carried out a simulation on oesophageal cancer patients, and found AAA presents a difference in dose distribution, reaching 6.2% to the PTV and higher in the OAR (175). The study concluded that AAA either overestimated or underestimated the dose, especially in the presence of heterogeneity in the area (175). In addition, the tumour's location proved critical, because the heart is located within the beam direction. In these cases, reducing uncertainty can decrease the dose delivered to the heart resulting in fewer side effects. The high density of bone can lead to greater uncertainty in dose distribution for TPS, especially if the density of the bone affects the OAR due to the distance. Hughes *et al*. simulates a treatment planning system using the AAA algorithm, where the spinal cord is the OAR. The AAA algorithm shows a difference in the dose reaching 7.4% (176). The high density of the bone increases the level of uncertainty, and the previously mentioned studies show that TPS has higher uncertainty in dose distribution to the OAR than to the target. Another study by Padmanaban *et al*. simulated a treatment plan with VMAT, concluding that a significant dose difference is reported in oesophageal cases for the PTV, heart, and spinal cord (177). The AAA overestimated the dose to the GTV displaying greater uncertainty in the interface of different densities. Additionally, the beam delivery technique was not related to the dose difference between different algorithms (177). The accuracy of the treatment is critical in cases where dose escalation is essential to eliminate cancer cells. However, accuracy cannot be achieved where there is high uncertainty in dose distribution due to factors such as heterogeneity and the algorithm, which cannot handle the complicated interactions.

3.9 Overview

In this chapter, detailed knowledge was built around the MC algorithm, which is known as the gold standard for calculation of dose distribution in radiotherapy. The different interactions between the photons, protons and matter was explored providing essential information for the multiscale chapter. As examined in the above section, MC has a disadvantage given its long simulation time, and many reduction techniques have also been introduced to reduce the time. The chapter continues by demonstrating a different study comparing MC and analytical algorithms in the phantom and the patient. Most of the studies concluded that the MC provides a more accurate dose distribution in heterogenous areas. Given its high calculation accuracy, the MC algorithm will be used in the upcoming chapter as the main algorithm to calculate dose distribution. Before using MC, tuning and validation must be carried out with the Eclipse treatment planning system located in a Singleton hospital. The next chapter describes validation of PRIMO, a MC algorithm.

Chapter 4: MC modelling of the linear accelerator head with Primo

4.1 Introduction

A linear accelerator is composed of different parts, which allow flexibility in shaping the beam in such a way as to imitate the shape of the target. The linear accelerator is designed to deliver a different range of doses. Including all the components of different LINAC models in MC is a challenge. Currently, an advanced code called PENEASYLINAC is available, which works as input to simulate the different designs of the LINAC system. Furthermore, specific detail is included, such as different types of multi-leaf collimators, and the quadric model of the secondary collimator (sempau), which helps to develop a more useful algorithm to be used by both experts and non-experts alike. PENEASY is another program that is necessary to support the main code PENELOPE when preparing for a simulation. PENEASY includes multiple components, such as variance reduction techniques, geometries, tallies, and the voxelisation of the CT images. PRIMO is a MC program that uses the PENELOPE code, which will be used in this chapter. One of the drawbacks of PRIMO is that it does not provide a beam configuration algorithm. To overcome this obstacle, manual tuning must be performed to match the measurement data from the treatment planning system. This is a time-consuming and resource-intensive process; however, valuable experience can be gained by fine-tuning the Linac.

4.2 Objective

This chapter aims to tune and validate the PRIMO MC simulation with the Eclipse treatment planning system located in the Singleton Hospital using simulated and golden beam measurements from Varian.

4.3 Material and method

4.3.1 Tuning and validation of the LINAC model using Primo

The Truebeam linear accelerator model was used for tuning, and contains the target, ionisation chamber, primary collimator, flattening filter, secondary collimator, X jaws, Y jaws and

multileaf collimator, as shown in Figure 4.1. The MC simulation will be divided into three parts using PRIMO to reduce both the uncertainty and the time taken for the simulation. The first part is called the S1, which is the phase space file (PSF). The PSF includes only the upper part of the linear accelerator from the target to the flattening filter, and does not require any patient information. The PSF saves particles energy, type, direction and position, allowing it to be reused for different patients without re-simulating the PSF. However, the PSF file cannot be reused again if the LINAC model changes. The second part is S2, in which the collimator is involved and configured. The final part of the simulation is S3, and involves the phantom or patient's CT. S1 will be simulated separately from S2 and S3, because of the time required to produce a sufficiently rich PSF, so the uncertainty level is less than 2%.

The PRIMO version 0.3.1.1772 was used to simulate a Varian 2100, a Truebeam machine. The nominal energy used was 6 MeV. A fixed field size of $10 \times 10\ \mathrm{cm}^2$ was also used. A phantom was also introduced to tally the dose in a homogenous water phantom, which was created inside the PRIMO with a dimension of $40.2 \times 40.2 \times 31\ \mathrm{cm}^3$. The source to surface distance (SSD) was 100 cm, which is similar to the experimental data. The bin size was set at $0.2 \times 0.2 \times 0.2\ \mathrm{cm}^3$. The experimental data used to configure the treatment plan in Swansea Hospital is golden beam data provided by Varian. The golden beam data was used to configure the treatment planning system during the machine installation in the hospital.. The configuration of the MC simulation was divided into four stages to reach a 95% agreement with the experimental data. Ten million histories were used at each stage to lower the time without affecting the result. The first stage involved configuring the initial energy. The default initial energy was 5.4 MeV, which was used in the first run after which, the simulation was repeated until it reached 6.25 MeV. An increase of initial energy was made for each simulation until it reached the highest level of agreement with measured data using the gamma index passing rate 2%/2mm for the percent depth dose (PDD). Furthermore, all other parameters remained constant. Only in stage one was the PDD curve used for comparison; from stage two until the final stage, a percentage of the lateral dose profile was used for comparison. The second stage used the results of the initial energy input, and changed the focal spot by increasing each simulation by 0.1 mm until 2 mm was reached. The remaining parameters remained constant. Stage three used the highest gamma score for initial energy and the focal spot input and then the FWHM for primary energy distribution. The energy FWHM started at 0 until 0.2 MeV of an increase of 0.05 MeV, and all other parameters were held

constant. The final stage was similar to the first three stages in that the previous input was used and the beam changed divergence from 0° to 3°. After acquiring optimal configuration, a rich PSF file was created to ensure the uncertainty associated with the simulation was less than 2%. MC is a time-consuming process, so in order to reach higher uncertainty without increasing the time, a splitting-roulette was used. Furthermore, simple phantom splitting was used by a factor of 300 to ensure uncertainty was as low as possible in the different stages of the simulation. Among the methods integrated into PRIMO, rotational splitting and splitting roulette have demonstrated notable efficiency. When combined with straightforward dose tallying region splitting, these techniques have proven particularly effective. As a general guideline, for beams with energies below 15 MV, splitting roulette surpasses rotational splitting in efficiency, making it the preferred option. Nonetheless, it's important to note that implementing splitting roulette substantially inflates the size of phase-space files compared to simulations without variance reduction techniques. Parameters governing rotational splitting and splitting roulette are mostly preconfigured to ensure optimal efficiency. One user-adjustable parameter is the specification of the splitting region's size. Determining an appropriate splitting factor often involves trial and error. However, a straightforward approach exists for estimating the initial value of the splitting factor before engaging in trial and error. The steps are:

1- Conduct simulations with an initial splitting factor set at 1.
2- Refer to the achieved average statistical uncertainty from PRIMO as Δ.
3- Define the ratio n = Δ/δ, where δ represents the intended statistical uncertainty.
4- Determine the ceiling value of n^2, denoted as f, which implies $f = n^2$. This value of f becomes the necessary splitting factor for simulating s3.
5- Proceed to perform a new run of s3 employing the calculated splitting factor.

Subsequent adjustments can be made through trial and error to achieve the desired statistical precision without significantly extending the simulation time. Failure to attain the desired uncertainty level may indicate that the phase space file is insufficiently large.

4.3.2 Gamma index analysis method

The gamma index is one of the most commonly used metrics in radiotherapy for the verification of different techniques, such as 3D, IMRT and VMAT (178). Gamma index analysis tools provide a method for comparing two different doses, using criteria that can be altered by the

user. The two input criteria used are dose difference and distance to agreement. Testing point p and dose at point $d_e(p)$, and the gamma index Γ can be calculated by:

$$\Gamma = min\left\{\sqrt{\left(\frac{\Delta d_i}{\Delta D}\right)^2 + \left(\frac{\Delta s_i}{\Delta S}\right)^2}\right\} \quad (4.1)$$

The constant ΔD is the acceptance of dose difference, which is one of the acceptance criteria used for the gamma index tool. The second acceptance criteria is the constant ΔS, which is the distance to an agreement. The Δd_i represents the different doses measured and simulated at a specific point. The Δs_i denotes the different distances between the two points. An example is that if the criteria are 2% dose and 2 mm distance, any gamma index value equal to, or less than 1 is considered to have passed the gamma test (179).

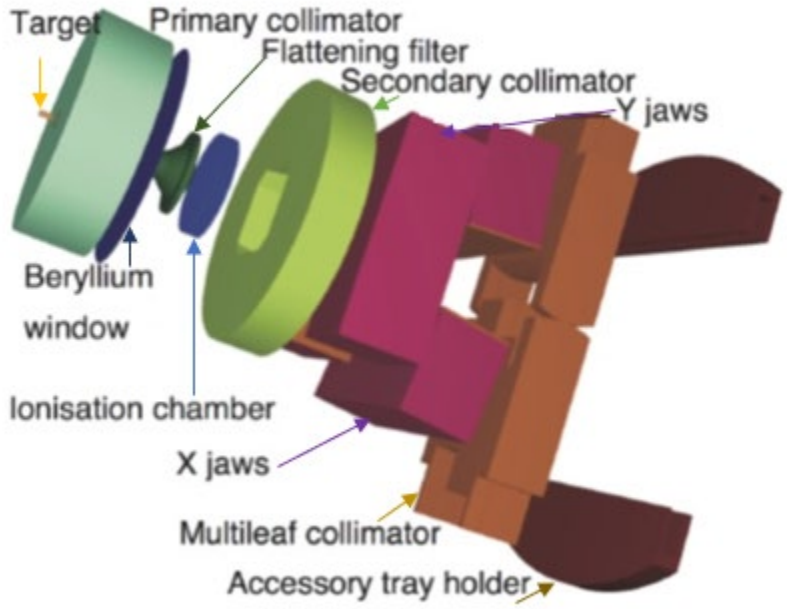

Figure 4.1: Model of the Truebeam target and collimator (180).

4.3.3 percentage of agreement and gamma test

The simulation result was compared with the MC and TPS using both the percentages of agreement and a gamma test. The percentage of agreement is calculated using information from the DVH. The percentage of agreement (PA) formula is:

$$percentage\ of\ agreement = 100\left[1 - \frac{\delta_A}{max\ (A_1, A_2)}\right] \qquad (4.2)$$

The absolute value of the region of $DVH_1\ and\ DVH_2$ is δ_A. The A value is a region in the histogram that represents the DVH of the target.

The demand for high accuracy dose evaluation is increased due to the complexity associated with treatment planning and delivery systems. The main rule for dose evaluation tools is to compare the planned dose and the dose distribution delivered. In 1998, Low *et al.* introduced a quantitative dose analysis called the gamma index (181). Since the introduction of the gamma index, there have been many improvements and upgrades to the algorithm. To date, the gamma index is the most popular method to employ when undertaking dose distribution comparisons. The gamma index combines dose difference (DD) and distance to agreement (DTA) to establish a matrix for each point in the evaluation area. The DTA calculates the distance between two points with an equal dose in the evaluated dose distribution. The DTA and DD are set to ascertain which criteria determine whether a point is passing or failing. These reference points are used to calculate the dose difference, after which the DTA of these points is calculated using a set passing rate criteria. Figure 5.2 simplifies the gamma index calculation.

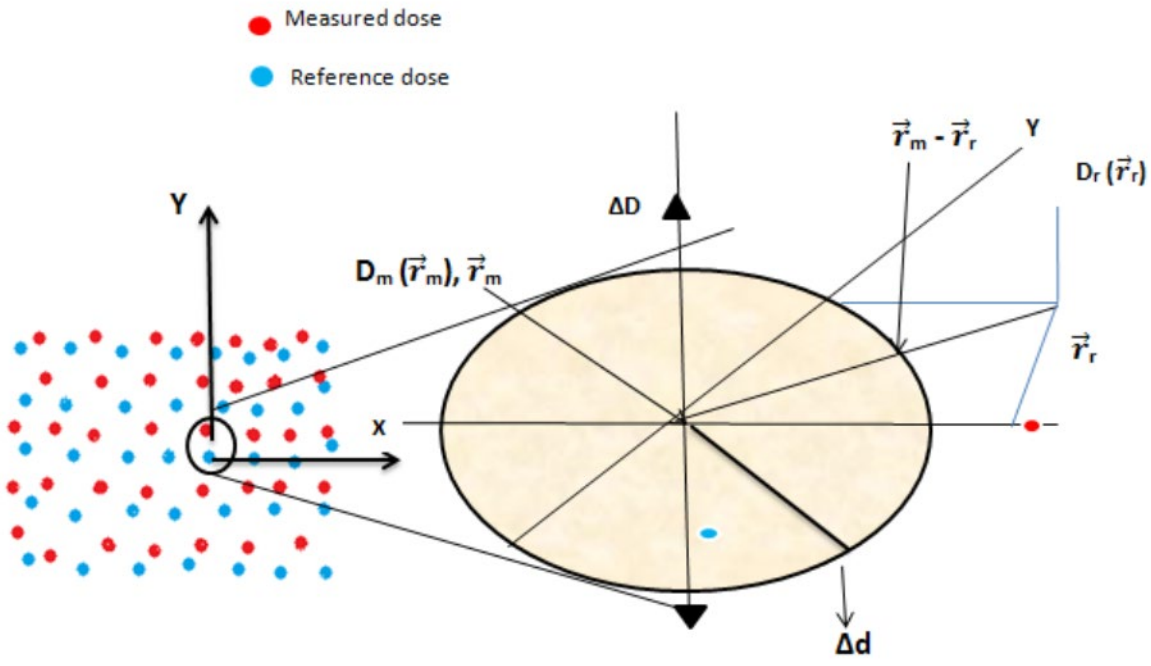

Figure 4.2 The illustration of gamma criteria in 2D dose distribution (182)

The gamma index evaluation equation is:

$$\Gamma\left(\vec{r}_m, \vec{r}_r\right) = \sqrt{\frac{|\vec{r}_m - \vec{r}_r|^2}{\Delta d^2} + \frac{|D_m(\vec{r}_m) - D_r(\vec{r}_r)|^2}{\Delta D^2}} \qquad (4.3)$$

The reference dose distribution is represented as $D_r(\vec{r}_r)$and the measured dose as $D_m(\vec{r}_m)$. The vector, as seen in the figure 5.2, is $\vec{r}_m \; and \; \vec{r}_r$. The DTA is Δd, and the dose criteria are ΔD. The $|\vec{r}_m - \vec{r}_r|$ corresponds to the spatial distance between the two comparison points and $|D_m(\vec{r}_m) - D_r(\vec{r}_r)|$ for the dose difference. Each pixel value within the region of interest in the reference point is subject to calculation. Then a gamma index to a specific point is calculated using the equation. The value of the gamma index ≤ 1 indicates that the point is within the DD/DTA passing value. Meanwhile, a gamma index > 1, which is the evaluated point, fails the passing criteria. The most commonly used criteria is ΔD = 3% and Δd = 3 mm and the some centres use the more relaxed criteria ΔD = 5% and Δd = 5 mm (183). Measurement uncertainty led to some failing points in the gamma evaluation. Overall, the general rule here is that if 95% of the points pass the assigned criteria, then dose distribution passes the gamma evaluation.

4.4 Results and discussion

The simulation to tune the MC model started with the default initial energy of 5.4 MeV, maintaining all other parameters at the default setting. The result was compared with golden beam data and did not pass the gamma analysis tools using 2% / 2mm criteria. The initial energy is the most critical setting affecting the PDD curve. The simulation was repeated by increasing the initial energy until it reached 6.25 MeV. Table 4.1 shows the different initial energy settings, compared with the measured data. As the initial energy increased, the passing rate rose until it reached the recommended level. As the table indicates, the initial energy for 5.8 MeV and above passes the gamma analysis, but reaches maximum agreement with the PDD curve at 6.25 MeV. PDD defined as the absorbed dose in a medium as a function of depth along the beam direction.

Table 4.1: MC simulated data of different initial energy parameters compared with measured data using the three criteria of the gamma analysis for the PDD curve.

Initial energy MeV	Average dose uncertainty	Passing rate 3%	2%	1%
5.40	18.90	99.35	25.10	16.95
5.80	15.80	100	99.81	95.51
6.00	11.92	100	99.68	95.80
6.25	10.90	100	99.74	96.90

The same approach was repeated for the focal spot, using the initial energy from the previous simulation and keeping the remaining parameters on a default setting. The focal spot significantly impacts the lateral dose profile, and is essential to test the effect of changes in the dose profile at different depths. Table 4.2 shows the different MC simulated values for the focal spot compared with the lateral profile of the measured data. The highest score chosen from the 1% gamma analysis was 0.14 cm, and this was used for the next step. The focal spot has a minimal effect on the PDD curve; consequently, the PDD is not used during the comparison.

Table 4.2: MC simulated data for different focal spot parameters compared with the measured data using the three criteria of the gamma analysis for lateral dose profile.

Focal spot (cm)	Average dose uncertainty	Passing rate 3%	2%	1%
0.10	11.8	71.91	52.93	11.24
0.12	10.8	69.41	53.43	19.23
0.13	10.6	97.38	79.28	30.71
0.14	10.4	98.75	86.64	56.93
0.15	9.9	99.63	82.40	36.58

The same steps are duplicated here, but this time using the chosen initial energy, focal spot, and altering the energy FWHM until the higher gamma score was reached. Table 4.3 compares the simulation results and the measured lateral dose profile using different energy FWHM. The highest score was for 0.15 MeV, after which the score declined, indicating further simulation is unnecessary.

Table 4.3: MC simulated data of energy FWHM parameter compared with the measured data using the three criteria of the gamma analysis for lateral dose profile.

Energy FWHM (MeV)	Average dose uncertainty	Passing rate 3%	2%	1%
0.10	11.8	99.25	93.63	33.21
0.14	10.8	99.75	91.01	39.08
0.15	9.4	99.75	96.88	54.43
0.16	10.3	97.75	85.52	50.81
0.20	10.9	98.63	86.52	45.57

The final step was to use the previously chosen parameter to change the divergent beam angle until the highest score for the gamma analysis was reached. Table 4.4 shows the simulation performed at different beam angles to attain the highest gamma passing rate to mimic the lateral dose profile. Beam divergence of 2.5 was chosen due to its high level of agreement with the measured lateral dose profile.

Table 4.4: MC simulated beam divergence parameter compared with the measured data using the three criteria of the gamma analysis for lateral dose profile.

Beam divergence	Average dose uncertainty	Passing rate 3%	2%	1%
1.0	10.5	96.50	88.51	41.45
1.5	10.4	99.38	84.02	31.21
2.0	10.3	90.76	65.17	19.98
2.5	10.5	99.75	95.01	62.67
3.0	10.7	94.13	71.41	47.82

After choosing the configuration with the highest agreement with the measured data, a large PSF file was created using 10×10^8 histories. The simulation time needed for the PSF is 165 hours, which is a CPU-intensive workload. The PSF was used to run a multi-simulation with different field sizes, and was compared with the measured data.

4.4.1 PDD and dose profile comparison

Multiple tests were undertaken to evaluate the MC model configuration, and a comparison of the measured data was undertaken. A PDD curve comparison and lateral dose profile were used to evaluate the MC model. The PSF was created using the configuration chosen from the previous

simulation, to ensure as close a result to the measurement data as possible. The PSF file contains $44x10^8$ photons, $21x10^6$ electrons and $13x10^5$ positrons. Figure 4.2 shows the PDD curve comparison between the measurement and simulated data using a field size of $10 \times 10\ \text{cm}^2$ with the configuration 6.25 MeV initial energy, 0.14 cm focal spot, 0.15 MeV energy FWHM and 2.5 beam divergence.

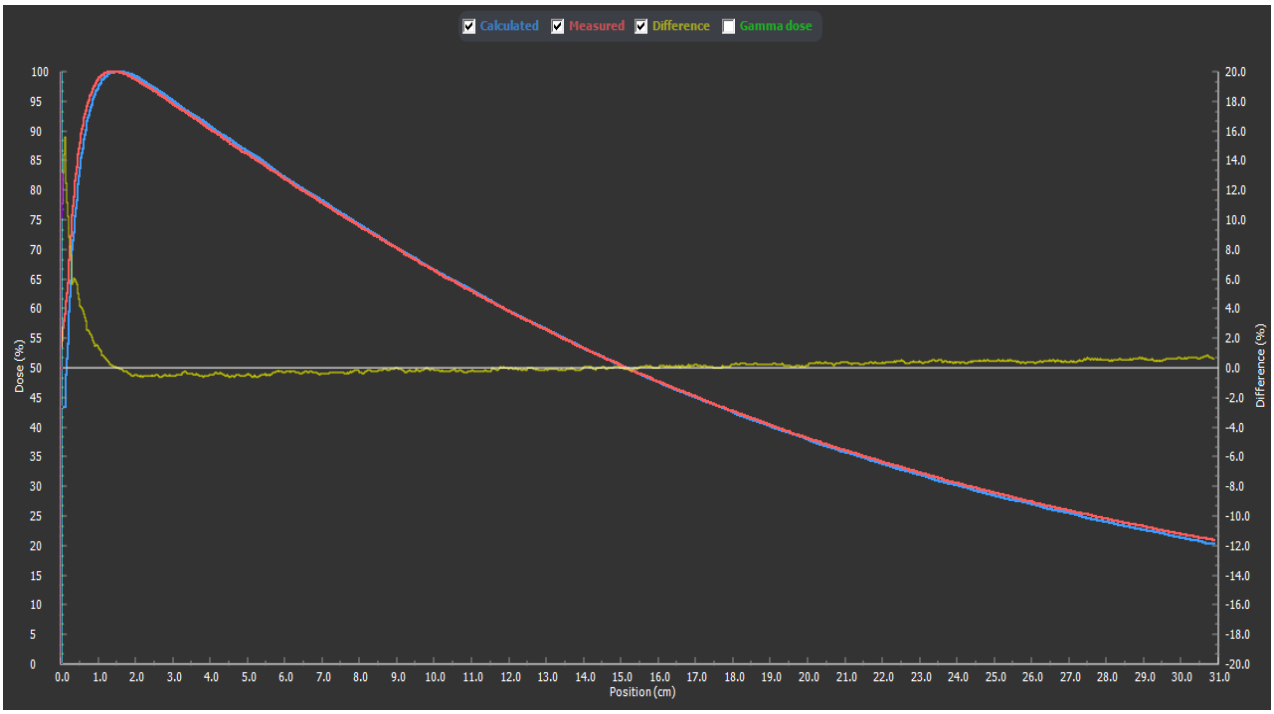

Figure 4.3: shows the PDD curve comparison between measurement and simulated data using a field size of $10 \times 10\ cm^2$ *with the configuration 6.25 MeV initial energy, 0.14 cm focal spot, 0.15 MeV energy FWHM and 2.5 beam divergence. The uncertainty was 0.7%.*

The gamma analysis passing criteria 2%/2 mm score was 99.81%, which exceeds an acceptance level of 95%. The uncertainty level for the simulation was 0.7%. The MC simulated PDD curve for $10 \times 10\ \text{cm}^2$ shows the beginning of the dose was underestimated, starting at 15 cm and reaching maximum at depth 30 cm. However, maximum difference in depth reaches 0.637%, which is considered acceptable (184). Figure 4.3 shows the PDD curve of the MC calculated and compared with data measured using different field sizes. Table 4.5 provides the gamma analysis of the PDD curve for different field sizes. The gamma score for all field sizes passes the minimal score of 95%, which indicates an agreement between the measurement and the calculated dose. The average gamma index before the maximum and after the maximum in all fields was below one, which is within tolerance.

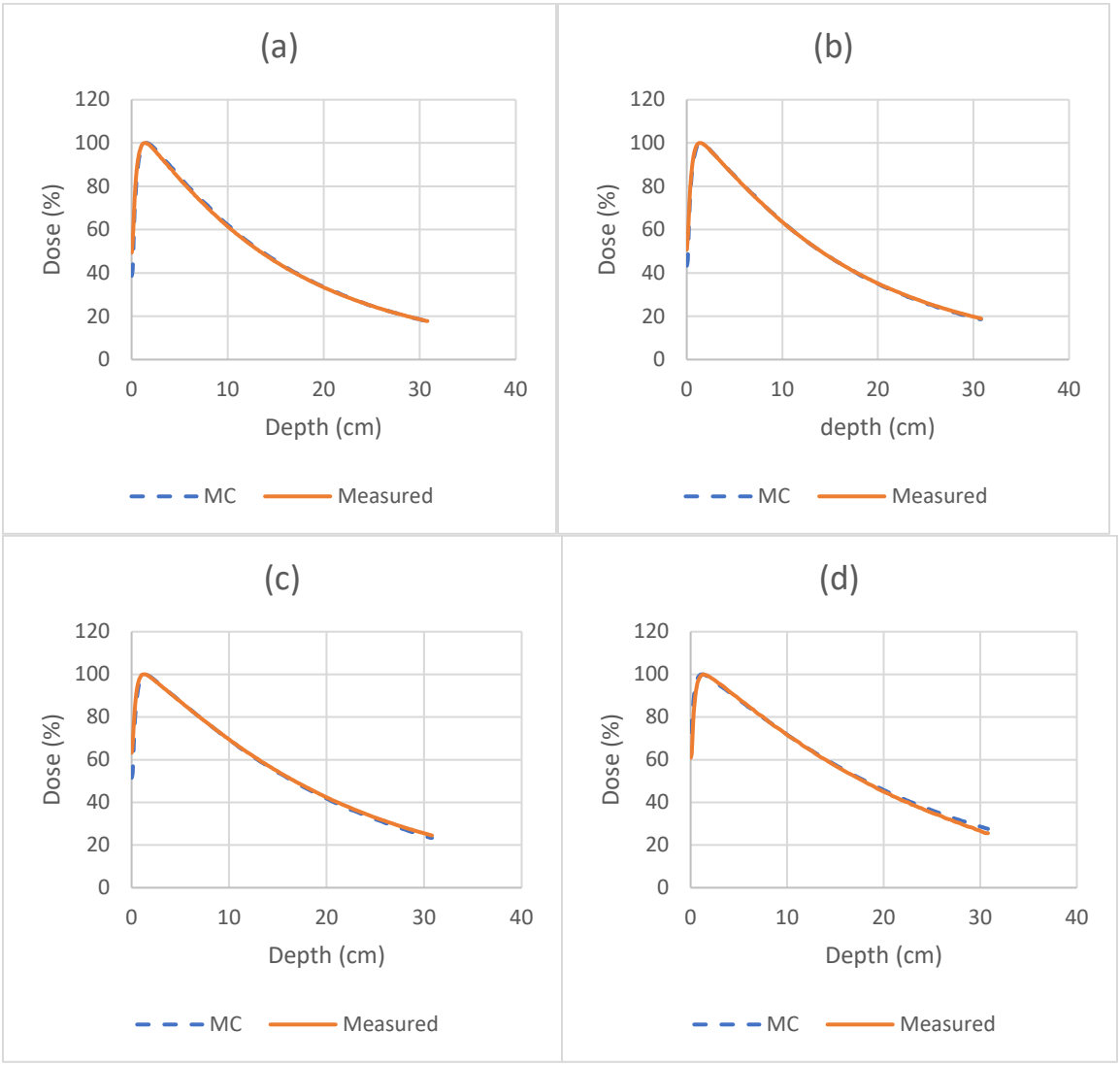

Figure 4.4: The PDD curve for different field sizes: (a) the PDD curve of 4 x 4 cm^2 (b) the PDD curve of 6 x 6 cm^2 (c) the PDD curve of 20 x 20 cm^2 (d) the PDD curve of 30 x 30 cm^2.

Table 4.5: Gamma analysis of the PDD curve for different field sizes.

Field size (cm^2)	Average gamma index before maximum	Average gamma index after maximum	Percentage of points passing the criteria (2%, 2 mm)
4x4	0.46	0.21	99.61
6x6	0.40	0.11	99.68
10x10	0.48	0.16	99.81
20x20	0.58	0.25	99.61
30x30	0.46	0.21	99.68
40x40	0.58	0.35	97.15

Table 4.6: Comparison between the PDD curve measurements at different field size and depth

Field size (cm^2)	PDD (10 cm depth)			PDD (20 cm depth)			Range at 50% dose (cm)		
	Measured	MC calculated	Difference (%)	Measured	MC calculated	Difference (%)	Measured	MC calculated	Difference (%)
4x4	61.54	62.28	-0.74	33.37	33.58	-0.21	13.34	13.57	-0.81
6x6	63.58	63.65	-0.08	35.20	35.12	0.08	14.06	14.11	-0.90
10x10	66.40	66.57	-0.17	38.10	37.96	0.14	15.13	15.18	-0.12
20x20	69.54	69.31	0.23	42.40	41.81	0.59	16.75	16.53	0.66
30x30	70.97	71.38	-0.41	44.53	44.38	0.15	17.59	17.71	-0.22
40x40	71.78	71.65	0.13	45.77	45.03	0.74	18.08	17.92	0.40

Table 4.6 shows the agreement between the PDD curve for different field sizes at 10 cm and 20 cm depth. At the 10 cm depth, the majority of the field size shows a higher simulated result than measured; however, the difference is less than 0.5%, which is within tolerance level. At a 20 cm depth, the measurement becomes higher than the MC simulated result; however, the difference remains within the tolerance level. The results show that the simulated measurement of the PDD curve has achieved the gamma passing rate. The PDD curve is also affected by the initial energy, and the initial energy used in the MC was 6.25 MeV, which shows an agreement with the measurement value. The next step was to evaluate the other setting with different depths in a lateral dose profile in different field sizes. Table 4.7 shows the gamma passing score of varying field sizes at 10 cm depth.

Table 4.7: Gamma analysis for lateral dose profile for different field sizes at a depth of 10 cm.

Field size (cm^2)	Average gamma index inside the field	Average gamma index in the penumbra region	Average gamma index outside the field	Percentage of points passing the criteria (2%, 2mm)
4 X 4	0.26	0.71	0.15	97.49
6 X 6	0.21	0.61	0.26	98.19
10 X 10	0.17	0.65	0.57	98.63
20 X 20	0.25	0.65	0.52	99.72
30 X 30	0.62	0.99	1.17	95.52

The pass rate set was 95%, and it was higher for all the field sizes, as the average gamma index inside the field was below one indicating agreement with the measurement data. The average gamma index outside the field size was within the limit for the different field sizes with the exception of the 30 x 30 cm^2 field, where the score was above one. However, the average score of

1.17 outside the field for 30×30 cm^2 is clinically insignificant, and is due to the physics of the MC. Table 4.8 shows that in a field of 10×10 cm^2 the gamma analytical passing rate for different depths was above 97%, and the average gamma index inside the field was less than 0.18, which indicates high agreement with the measurement data. The gamma score in the penumbra region in Table 4.8 started to increase, but remained within the limit, and the highest score was for the 30 cm depth, due to the mechanism of MC physics. The focal spot, energy FWHM, and beam divergence tuning is important for dose profile. After many trials using different configurations for the setting, the optimal result is given in Figure 4.4.

Table 4.8: Gamma analysis for the lateral dose profile for a field size $10 \times 10\ cm^2$ *at different depths*

Depth (cm)	Average gamma index inside the field	Average gamma index in the penumbra region	Average gamma index outside the field	Percentage of points passing the criteria (2%, 2mm)
1.5	0.17	0.74	0.44	97.75
5	0.15	0.69	0.46	98.38
10	0.17	0.65	0.57	98.63
20	0.15	0.53	0.38	99.27
30	0.17	0.82	0.82	98.51

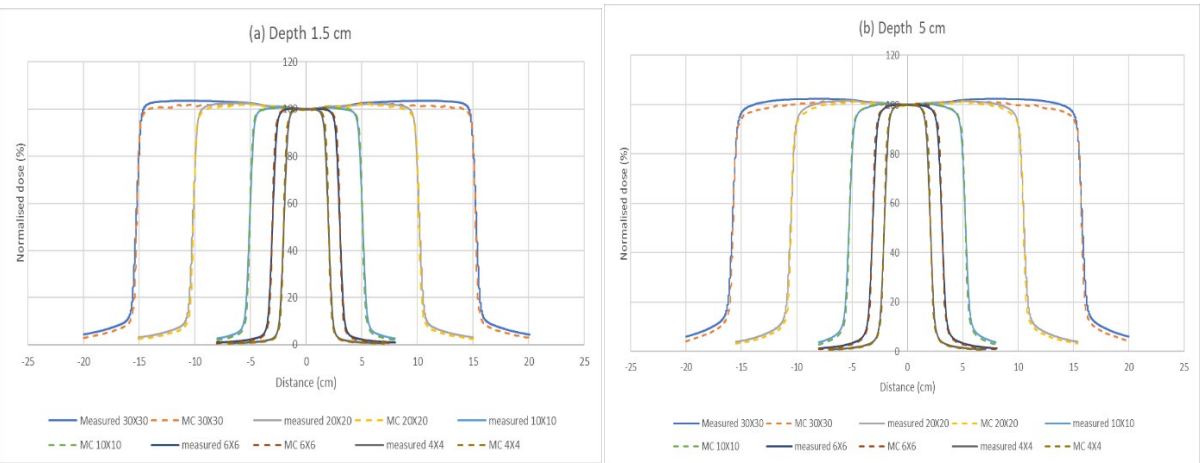

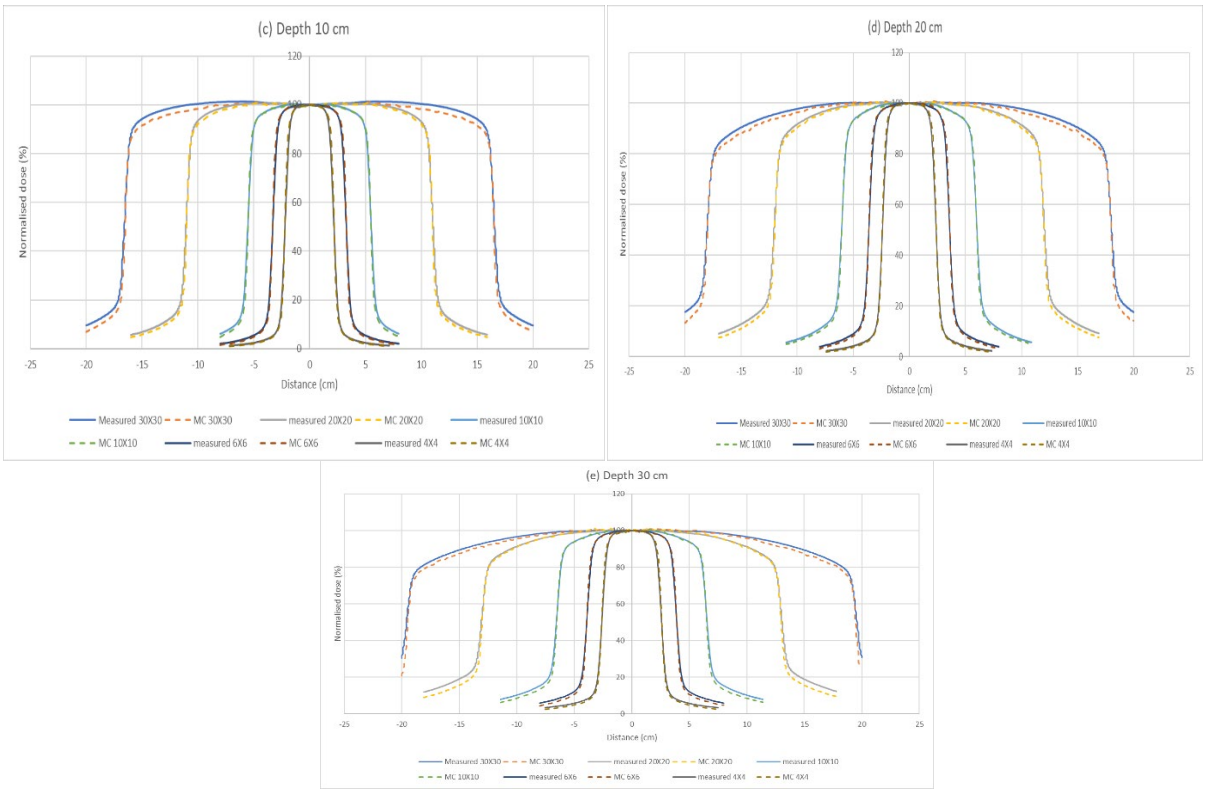

Figure 4.5: A comparison of the dose profiles between measurement and MC simulation at different depths: (a) dose at 1.5 cm depth (b) dose at 5 cm depth (c) dose at 10 cm depth (d) dose at 20 cm depth (e) dose at 30 cm depth

Figure 4.4.a shows the dose profile for different field sizes at a depth of 1.5 cm, revealing agreement between the measurement and the simulated MC passing the gamma analysis. However, in the field size 30×30, the inside field size was within the limit, with a noticeable increase in the penumbra and outside the field; however, the increase was not clinically significant. Furthermore, a large field size is rarely used in VMAT, and two arc rotations are needed rather than one to cover the area. Similarly, at a depth of 5 cm, the passing rate was above 95% for all field sizes. The gamma score inside the fields was less than one for all the sizes, with a non-clinically significant increase in the penumbra region in the 30×30 field size, although the result was still less than one for the gamma score. At a depth of 20 cm, the scores inside the fields and outside the fields were less than one in the gamma score. However, the outside field dose and the dose in the penumbra region in the 30 cm depth began to increase starting with a field size of 10×10. This was not recorded at previous depths but was still less than one in gamma analysis.

Similar steps were undertaken by Bacala *et al.* to tune a PRIMO with golden beam data for the Truebeam machine, and the study concluded that a good match existed between the

measurement and the simulated data (185). However, in the article, the dose profile was performed only for a field size of 10 x 10 cm, which does not support a comparison with a larger field size. The study's conclusion was similar to that reported in this chapter, detailing the steps and results of tuning showing good agreement between the measurement and the MC simulated data (185). Sarin *et al.* performed a study on tuning using the MC model, and included different field size simulations. Their result was similar to that in this study, showing agreement between the measurement and the calculated data (186). Furthermore, the study compared two simulations, one done without using any variance reduction technique and the other using a splitting-roulette. The comparison reveals that there is lower statistical uncertainty and a faster simulation time when using the splitting-roulette variance techniques (186). The results of the tuning in this chapter indicate that PRIMO can be used as a benchmark for the treatment planning system at Singleton Hospital. Sarin *et al.* conducted a further investigation to demonstrate the effect of the reduction techniques used in PRIMO, with the results showing a significant decrease in time and the statistical uncertainty (186). In all the simulations in this chapter and the coming chapter, splitting- and Russian roulette will always be used to ensure the lowest statistical uncertainty and a faster simulation time.

4.4.2 Quality index comparison and output factor

Tissue phantom ratio ($TPR_{20,10}$) is one of the quality indexes employed to describe changes in dose with an increase of depth in tissue. $TPR_{20,10}$ is calculated in a water phantom at 20 cm depth and 10 cm depth in an SSD 100 for the field size $10 \times 10\ \mathrm{cm}^2$. The results for 20 cm and 10 cm cases are used in the formula (187):

$$TPR_{20,10} = 1.2661\ PDD_{20,10} - 0.0595 \qquad (4.2)$$

The result of the measured 6 MV beam TPR was 0.6668, and the simulated TPR was 0.6701. The difference between the simulated and measured results is -0.49%, which is within the tolerance level accepted in this chapter.

The output factor (OF) was compared for a maximum dose at a depth of 1.5 cm for the measurement, and the MC calculated the result for all the fields used when tuning. The agreement

between the actual measurement and that calculated was recorded in all fields. The greatest difference was - 0.083 in the 40 × 40 cm field, which is insignificant because the difference was very low and set within the tolerance level for this study. Table 4.9 shows the OF for the measured and calculated results for the different fields.

Table 4.9: shows the output factor for the measured and calculated results in different field sizes.

Field Size (cm^2)	OF Measured	OF MC calculated
4 x 4	1.000	1.000
6 x 6	1.000	1.000
10 x 10	1.000	1.000
20 x 20	0.999	1.000
30 x 30	0.998	0.999
40 x 40	0.997	0.998

4.5 Conclusion

This chapter focuses on explaining the Varian Truebeam model in PRIMO, and the MC algorithm used. The Penelope code must be tuned with measured data used in the treatment planning system. To match the golden beam measurement data, the tuning focus seeks to determine the optimal configuration for the initial energy, focal spot, energy FWHM, and beam divergence. The fine-tuned parameters for 6 MV were initial energy 6.25, focal spot 0.14 cm, 0.15 MeV, the energy FWHM, and 2.5 beams divergent. After establishing the optimal configuration of the Truebeam model used in the treatment planning system, an investigation was performed to evaluate and validate the MC model. An MC simulation is time-consuming and CPU intensive; therefore, variance reduction tools were used to minimize the statistical uncertainty, and the time required to complete the simulation. The validation of the model was achieved by comparing the simulated PDD curve, dose profile, TPR and output factor with the measurement data for the golden beam. A field ranging from 5 × 5 to 40 × 40 cm was used, and the MC model passed the recommended criteria. Thus, the MC model agrees with the measurement data, and can be used to produce MC clinical plans. The MC model will also be used in Chapter five to compare uncertainties arising due to heterogeneity produced by a stent in pancreatic cancer.

Chapter 5: The effect of a pancreatic stent on photon dose distribution using a new MC model that mimics the actual material of the stent and advanced contouring

5.1 Introduction

Pancreatic cancer is a fatal type of cancer, and is the fourth most prevalent cause of cancer death in the United Kingdom. Approximately 3% of people suffer from pancreatic cancer in the United Kingdom (188). Meanwhile, the use of radiotherapy treatment as a way to combat cancer is subject to ongoing debate in the UK. Conflict arises due to the ambiguous results from the various trials determining the benefits of radiotherapy (189). Huguet *et al.* compared advanced pancreatic cancer patients, who only received chemotherapy, and patients who received chemoradiotherapy, and concluded that radiotherapy improved survival rates by 24.7% (190). In contrast, a study by Chauffert *et al.*, of 119 patients diagnosed with advanced pancreatic cancer, concluded that patients treated with chemotherapy only had a 6% higher survival rate than those treated with chemoradiotherapy (191). Radiotherapy has a limited effect on pancreatic cancer because the delivered dose is insufficient, leading to a poor response rate. Autopsy data shows more than 30% of patients die as a consequence of local disease progression (192). The response rate for doses below 60 Gy varies between 5% and 25% (193). A recent study evaluated dose-escalation to maximize dose response and concluded that a dosage average of 80 Gy can achieve a 50% response rate (193). Another study demonstrated an improved patient survival rate when a high dosage of 70 Gy was administered (194,195). However, increasing the dose can generate a higher toxicity rate, which is the main constraint when treating pancreatic cancer. Pancreatic cancer is associated with many additional unwanted symptoms such as jaundice and poor digestion, which are often treated by inserting a stent into the bile duct to prevent blockage of the bile ducts. The stents used at Singleton Hospital are Cook's evolution biliary stents, consisting of alloy Nitinol (nickel and titanium). Radiation scattered from high-density metals can cause a perturbation of dose distribution within the target area. Much research has been done to examine the effect of the stent within the oesophagus, revealing souring tissues at the stent and the interface of the stent itself, recording either an increase or decrease in the dose (196–200). On the other hand, very few studies have examined the effect of stents on dose distribution and treatments for

pancreatic cancer because of the short duration of survival rates and the low response rate for radiotherapy at a low dosage. However, with the new dose escalation approach, more researchers have become interested in the effect of high doses on the target and OAR (201–203). The affected area contains many radiosensitive organs, which from an increase in dosage, can generate a series of toxicities such as ulcers, haemorrhages, strictures, and perforation (204).

5.2 Objective

This chapter aims to evaluate dose distribution using the gold standard MC algorithm in patients with a biliary stent; modifying stent materials to match the actual components of the stent, as a way to increase the accuracy of the MC simulation and correct for CT artefacts. Furthermore, a new contouring technique is used to imitate the actual anatomy of the stent inside the biliary duct. First, a comparison between standard practice and the new model was made using the one beam plan. Then the second comparison employed a VMAT plan with Singleton hospital parameters to evaluate the differences, and alter dose distribution.

5.3 Literature review

5.3.1 Radiotherapy toxicity from treating pancreatic cancer

As mentioned at the outset of the chapter, the chief constraint when escalating the dose for pancreatic cancer patients is the tolerance of the OAR, such as the upper gastrointestinal (GI) organs and duodenum. For example, Figure 5.1 shows the duodenum, the distance from the OAR, and the proximity to the pancreas. Furthermore, the side effects from radiotherapy can occur in the stomach and small bowel, meaning an increased dosage in the target area can produce a series of toxic effects within the OAR. The gastrointestinal tract constitutes a component of the organ system in humans. Its role encompasses the intake, digestion, nutrient absorption, and eventual expulsion of food in the form of feces.

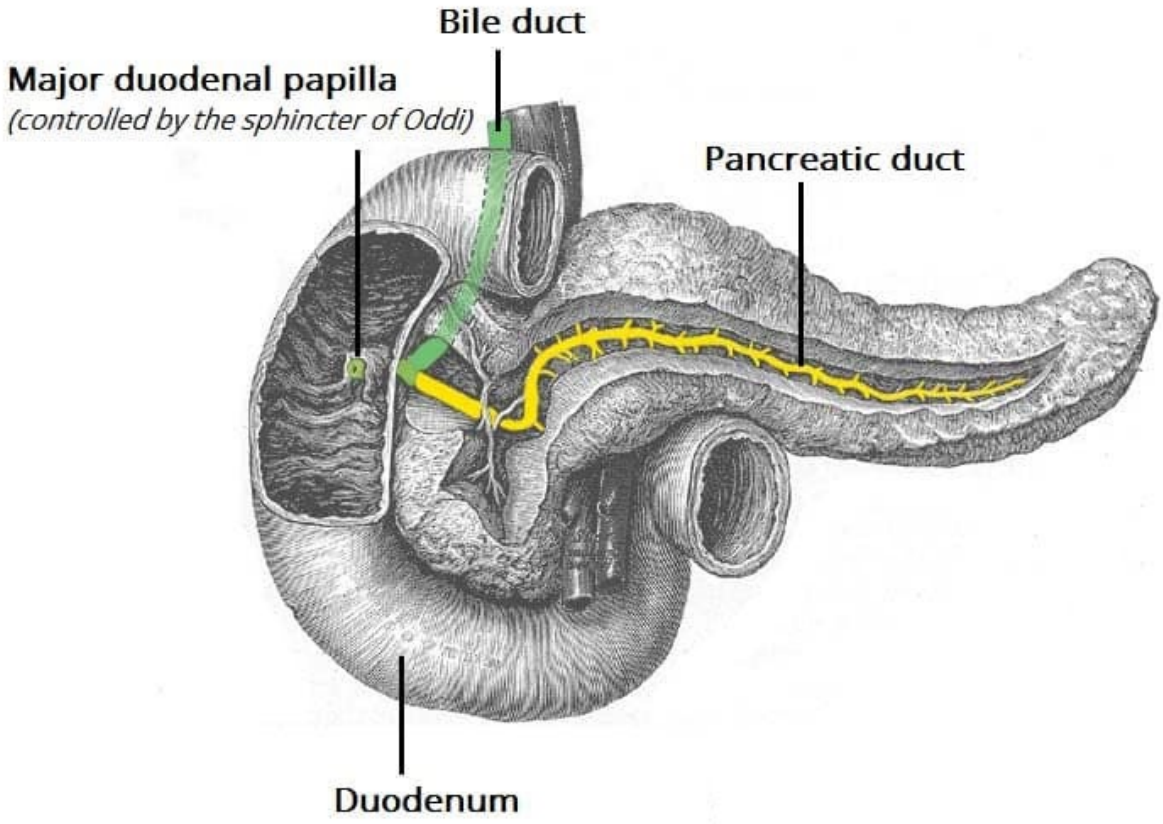

Figure 5.1: Illustration of the pancreas and duodenum (21).

Many researchers have studied the levels of toxicity that occur when increasing radiotherapy dose or when delivering the dose commonly used to treat pancreatic cancer (194,205–208). Nakamura *et al.* studied 40 pancreatic cancer patients treated with chemoradiotherapy. The dose for radiotherapy was 54 Gy in 30 fractions, displaying acute gastrointestinal toxicity for 33% of the patients who suffered side effects including anorexia, nausea, vomiting, and mucositis. Furthermore, 20% of the patients suffered upper gastrointestinal bleeding two months after treatment (209). Huang *et al.* conducted another study, in which the dosage given in each fraction was increased, and concluded identified toxicity effects that included nausea, vomiting, diarrhoea, duodenal ulcer, upper GI bleeding and small bowel obstructions (210). These studies collectively show that increasing the dose leads to higher grade toxicity, due to the high sensitivity experienced in the surrounding organs. Highly accurate delivery and understanding of the effect of the stent in dose distribution may help reduce the dose to any OARs, and increase the dose to the target. Kelly *et al.* followed up with 106 patients with an escalation dose of 70.4 Gy representing a dose-volume

constraint to the duodenum using the IMRT technique. Toxicity to the duodenum was witnessed in 23% of patients. Another study reported toxic effects such as duodenal changes, duodenal bleeding, and duodenal ulcers (211). The side effects of radiotherapy when treating pancreatic cancer are well documented, and dose-escalation is required to achieve a response rate that can positively affect the required survival rate without increasing toxicity to the upper GI organs.

5.3.2 Effect of a stent in the target area

Stent placement is a standard procedure used in pancreatic cancer patients. The stent comes in different shapes and materials, such as a silicon covered stent, a single bare stent, a double bare stent and a large open cell stent. All types of stents can be expanded as they are made of a metal comprised of Nitinol mesh (alloy nickel and titanium) (212). The use of an external beam in radiotherapy treatments can cause some enhancements or reductions in dosage as a result of secondary electrons and scatter; however, in proton therapy, protons interact differently with high Z materials.

Both treatments need to be evaluated to determine the best option for the patient. One of the first studies assessing the effect of a stent on external radiotherapy was conducted by Mayo-Smith *et al.* using an old design stent. They observed no dose enhancement 5 cm away from the stent. However, the stent used in that study is dated, as stents have been modified several times in recent decades. Furthermore, the study used high dose brachytherapy, which was not located at the interface between the implanted stent and the surrounding tissue (213). A more recent study by another group of researchers explored the effect of different stent shapes on dose distribution when inserted inside a phantom, utilizing a film to record the dose. A single beam was used to radiate the phantom containing the stent, and the result proved similar across different stent designs, although with differing intensities. Dose enhancement was recorded between 2.3% to 8.2% on a single beam proximal, left and right to the radiation direction, due to the scattering of radiation from the stent. Furthermore, the greatest enhancement was apparent in the double bare stent, which reached 19.5%. On the other hand, the distal location of the beam source shows a reduction in the dose due to the stent, and the mean dose reduction was between 0.9%-3.6%. The use of multiple beams or VMAT can reduce the effect of radiation scatter from stent materials, and the use of four beams led to dose enhancements between 6.7% and 14.9% in different stent designs. A VMAT plan reveals a better result with an enhancement mean of 4.8%, and a maximum for a double bar

stent of 15.3%. However, VMAT delivery successfully eliminated the cold and hot spots due to dose scattering. Overlapping beams from the different directions can help to control the effect of the stent dose scattering. However, high calculation accuracy is essential, because the radiosensitive organ around the stent does not receive a higher dose than the threshold. Compared to the radiopaque marker, the dose calculated by TPS reveals a 12.8% underestimation of the dose in a proximal location in the single beam simulation. Furthermore, in the distal location, the TPS overestimated the dose by 9.6% (212).

As discussed previously, the stent affects the radiotherapy dose distribution, due to the nature of photons' interactions with high Z materials. However, protons interact differently to photons. Very few articles discuss the effect of dose distribution in the area surrounded the stent during proton therapy (214,215). The majority of studies tested the treatment effects on the stent for oesophageal cancer, and few studies tested the effect on pancreatic stents. Research has been carried out by Sujai Jalaj *et al.* evaluating four different stent materials used for oesophageal cancer on proton therapy (214). The materials used were Nitinol, stainless steel polyester covered with polyurethane, polyester covered with silicone, and polyethene (256). The stents were inserted inside a phantom designed to mimic the oesophageal environment. The phantom was radiated with a proton dose of 2 Gy. The result shows no dose perturbation for a stent made of Nitinol, polyester covered with polyurethane, and silicone. Moreover, the enhancement of the overall dose was minimal, ranging from 0% to 1.2% for the three stent types (256). On the other hand, stainless steel and polyethene stents show dose attenuation and cold spots. The dose decrease in these two stents ranges from 11.6% to 14.5% in cold spots. The large mass of the proton is the primary reason for there being no, or minimal, dose perturbation and little scatter in the stent area. Furthermore, in the case of proton therapy, there is minimal enhancement in the dose at the proximal surface of the stents. On the other hand, the stainless-steel mesh design creates an overlapping metallic area, creating a cold spot due to high Z materials (214). The high number of Z materials will scatter the proton at a large angle when compared to low Z materials, but will have a minimal effect on the proton dose. The study records the dose within the stent surface by using a sheet of sensitive film on the surface, but it cannot record the dose at a distance, because the film cannot cover the entire area. Therefore, the effect of the stent in dose or direction in the context of the greater distance is not measured, which very few studies mention. However, the proton dose measured in this study

was within 5% of the prescribed dose, as required by the international commission on radiation units' measurements (214).

5.4 Method

This chapter focuses on the effect of the stent on dose distribution in pancreatic cancer patients. Two DICOM series were used herein for patients diagnosed with pancreatic cancer, and a stent was surgically inserted into the biliary duct. The stent used by the Swansea Health Board is Cook's evolution biliary stent, made from Nitinol, which is a metal alloy comprised of nickel and titanium. The DICOM series were anonymized to protect patients' privacy. The delineation was carried out by an oncologist. The DICOM series was used in the Eclipse treatment planning system 13.7 to create a treatment plan for the patients. The first plan consisted of one beam to study the effect on dose distribution. The second plan was a VMAT, and the dose was 50.4 Gy in 28 fractions. The constraints used were similar to those used at Singleton hospital, as illustrated in Table 5.1. The DICOM series with radiotherapy plans can be used in the MC algorithm. The MC algorithm used in this chapter was PRIMO.

Table 5.1: The constraints used in radiotherapy in pancreatic cancer patients.

Pancreas (50.4Gy_28#)			
ROI	**Objective**	**Opt.**	**Man.**
PTV1	4788cGy		≥99%
	4990cGy		≥50%
	5090cGy		≤50%
	5292cGy		≤5%
External	5393cGy		D1.8cm³
Liver	Dmean	≤2800cGy	≤3000cGy
	3000cGy		≤30%
Kidney_L	2000cGy		≤40%
Kidney_R	2000cGy		≤40%
Kidneys	2000cGy		≤30%
Cord_PRV	4000cGy		≤0.1cm³

$$percentage\ of\ agreement = 100\left[1 - \frac{\delta_A}{max\ (A_1, A_2)}\right] \tag{5.1}$$

$$\Gamma\ (\vec{r}_m, \vec{r}_r) = \sqrt{\frac{|\vec{r}_m - \vec{r}_r|^2}{\Delta d^2} + \frac{|D_m(\vec{r}_m) - D_r(\vec{r}_r)|^2}{\Delta D^2}} \tag{5.2}$$

5.4.1 New contouring model for a stent

As mentioned previously, the delineation process was carried out by an oncologist. Upon analysing the contouring, the stent appeared to be contoured as one region, but when looking at the CT, a significant difference between the stent and inside the stent HU was apparent. The stent should be hollow, because it is implanted to expand against the walls to prevent blockage. The CT HU inside the stent is at -500, which seems highly unlikely, because the internal material is bile fluid. The low HU inside the stent is due to hardening, which is a CT artifact. Scanning metals produce artifacts such as beam hardening and metal artifacts.

The X-ray beam consists of a range of photon energies. When the beam passes through high-density material, those photons with low energy are absorbed faster than those with high-energy. Due to differences in absorption rates, there is a mean energy increase known as beam hardening (209, 210). Beam hardening can cause dark areas in high-density areas such as bones and metal. Beam hardening can cause a decrease in HU in areas marked by high density, such as inside the stent. Reduction of the HU due to beam hardening is called cupping artifact. One method to reduce beam hardening is to use a higher kV, but this produces lower tissue contrast images which are undesirable in contouring. Furthermore, increasing the kV will increase the radiation dose delivered to the patient, which is not recommended. A metal artifact poses an issue in the case of stents, due to the atomic numbers of metals like titanium and nickel (218). Identifying an artifact is the first step towards increasing the study's accuracy, and the second step in overcoming it. Contouring the whole stent and changing its materials will produce a less accurate simulation, resulting in a larger volume than the average stent size. Furthermore, the effect of the stent will be less accurate, as any difference in HU can enhance the effect by increasing or decreasing the dose. A new model for contouring the stent was implemented by extracting the inner portion, as seen in Figure 5.3.b. The final step involved separating the inner portion from the stent, as seen in Figure 5.3.c. The change in volume of the stent shows a significant reduction from 9.9 cm^3 to 6.8 cm^3, which represents a more accurate model of the stent region.

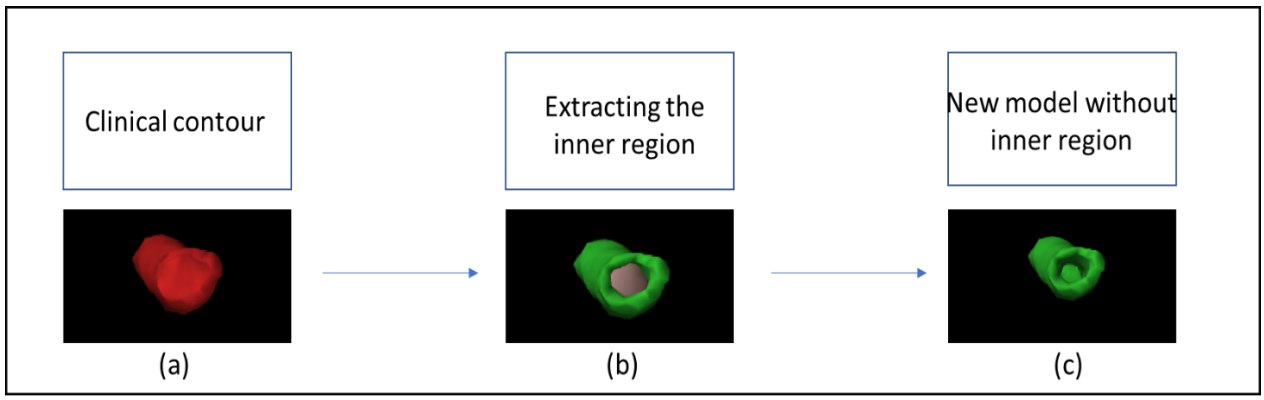

Figure 5.2: The new contouring model extracts the inner region of the stent: (a) the old contouring where the whole region was included; (b) as shown, the inner region was contoured, and separation can be visualized; and (c) the inner region is extracted, and only the stent is included.

5.4.2 PRIMO MC preparation

The Primo MC algorithm using PENELOPE was calibrated using the Varian treatment planning system, as shown in Chapter (4). The calibration indicates a 99% agreement between TPS and MC, allowing for conducting of the MC simulation to proceed with confidence. The Nitinol material file is not included in Primo materials and needs to be added. A pyPENELOPE version 2011 must be used to generate the material file; another version cannot be used because of the different sequences inside the file, which cannot be read by PRIMO. Figure 5.4 shows pyPENELOPE, creating a simulation by adding two materials, nickel and titanium, along with a weighted fraction of 50% for each. Both titanium and nickel are close in atomic number, indicating a similar interaction pattern for photons. For this reason, a 50% contribution from each metal was used to create the Nitinol. The Nitinol has a density of 6.45 g/cm^3. The material file is generated and called Nitinol in .mat format. Adding new material to PRIMO is not straightforward, and a request was made to PRIMO's development team to add Nitinol, which was done in the latest version 03.64.1814 that was released a few months after the request. However, although the developers added the Nitinol, the MC algorithm would allow the flexibility to add any materials the user needs to control the environment, which is impossible in PRIMO. Additional work is required, including the consideration of other materials. It's worth noting that there's a stent brand called Cook's Evolution that contains a platinum core; however, it wasn't included in the study due to the lack of provided specifications regarding the percentage composition of each component by

the company. The higher atomic number of platinum could potentially result in a greater localized enhancement dose.

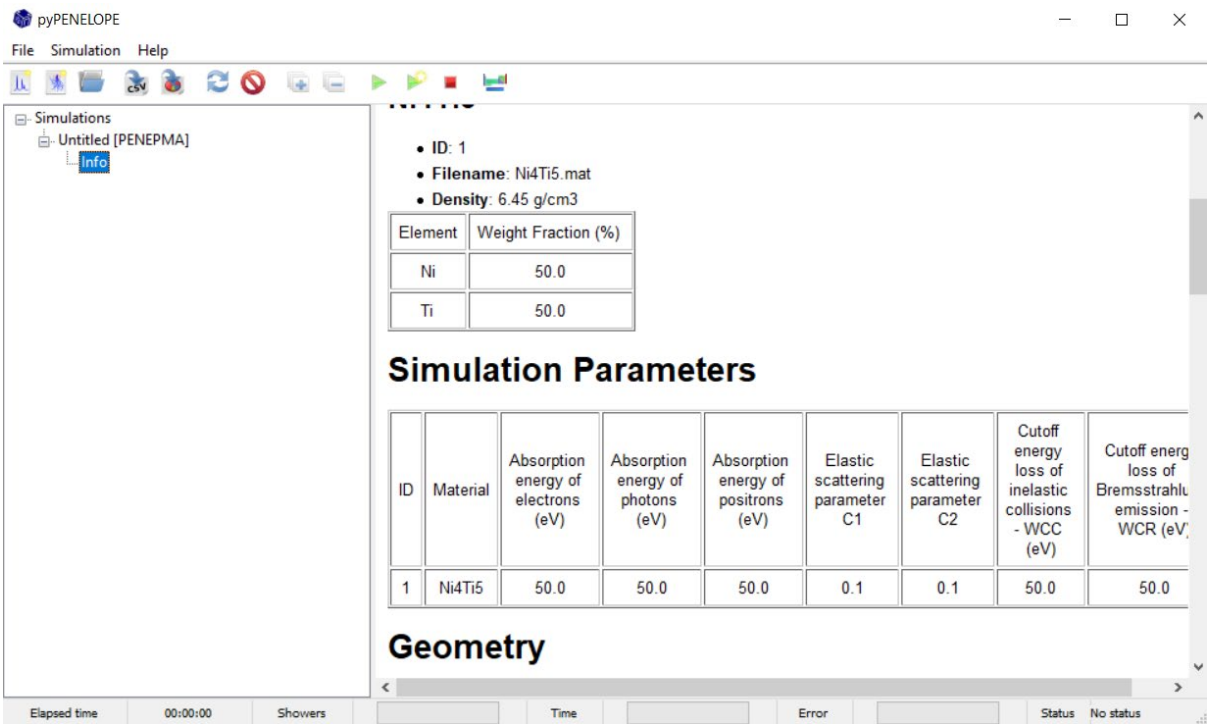

Figure 5.3: pyPENELOPE program used to generate a material file for Nitinol.

The Nitinol file was added to the materials files in the PRIMO algorithm before use. Once PRIMO has read the new material file, a phase space file must be created with sufficient histories to achieve the desired uncertainty percentage ≤ 2%. The phase space file that was created took 340 hours of computer time to complete using the Intel® Core™ i7 Core Processor i7-9700 (3.0 GHz) with a 12MB Cache. Another drawback was reported to the development team; i.e., PRIMO could not work with processors other than Intel. A new study was created, and the phase space was linked to this new study using a linking option. After this, the CT DICOM, RT structure and RT plan were uploaded. When uploading the RT structure, the HU for the stent was modified to 3500 HU, and inside the stent to 1000 HU to change it into water, as shown in Figure 5.5. The scale used in PRIMO is as follows: zero is air. After modifying the HU, a new geometry calibration was conducted, adding the Nitinol material to the calibration curve, as shown in Figure 5.6. After modifying the HU and calibration curve, a splitting ratio of 1000 was used in the DICOM to increase the study's accuracy and minimize uncertainty. The final step was to use a seed and assign cores for the simulation. After this, the simulation environment was ready to be run. The first

simulation was for one beam, and was estimated to take around 28 hours to complete. The second simulation was for the one beam, but this time with addition of stent material information or the HU (using the HU of the CT). The simulation took 28 hours complete. The third simulation was similar to the first, but used a VMAT plan as opposed to one beam. A single VMAT simulation lasted 44 hours. The same steps were repeated for the second patient. A comparison between the results and the TPS was conducted, and a gamma test used for each comparison.

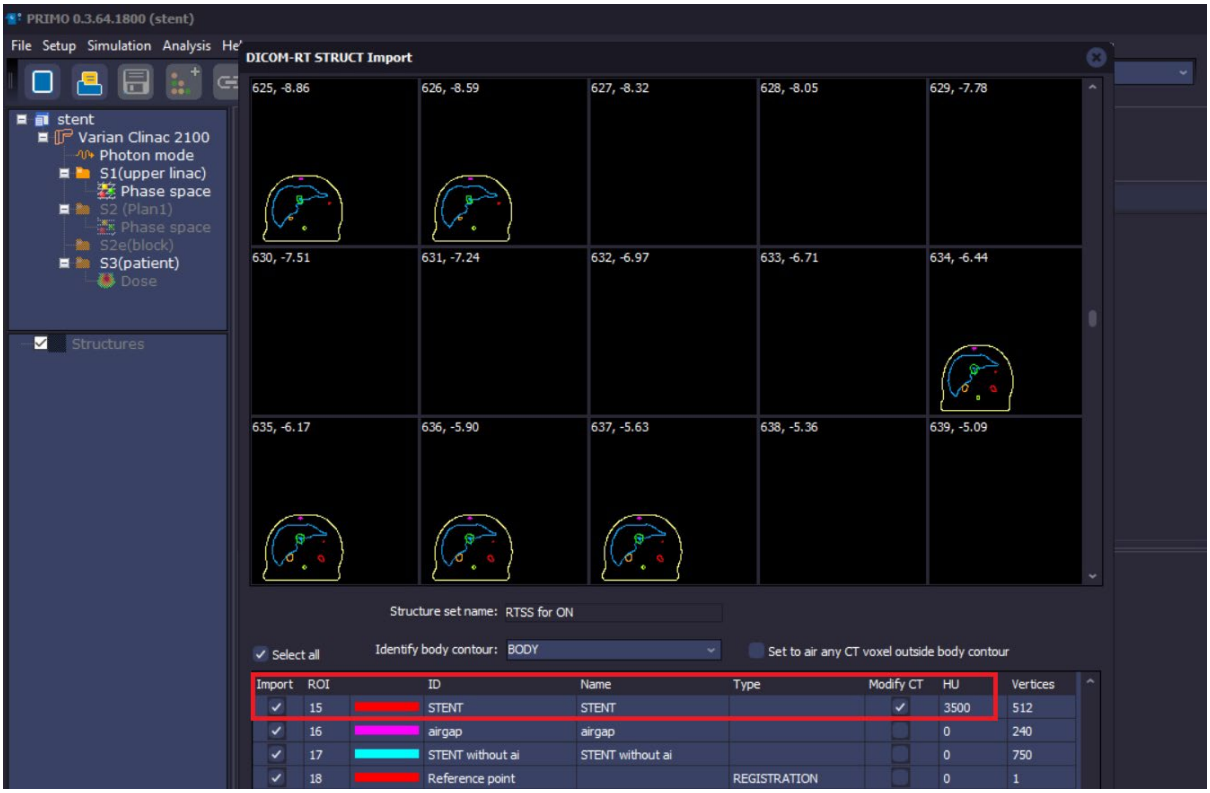

Figure 5.4: A DICOM HU modification of the stent delineation as shown in the red box.

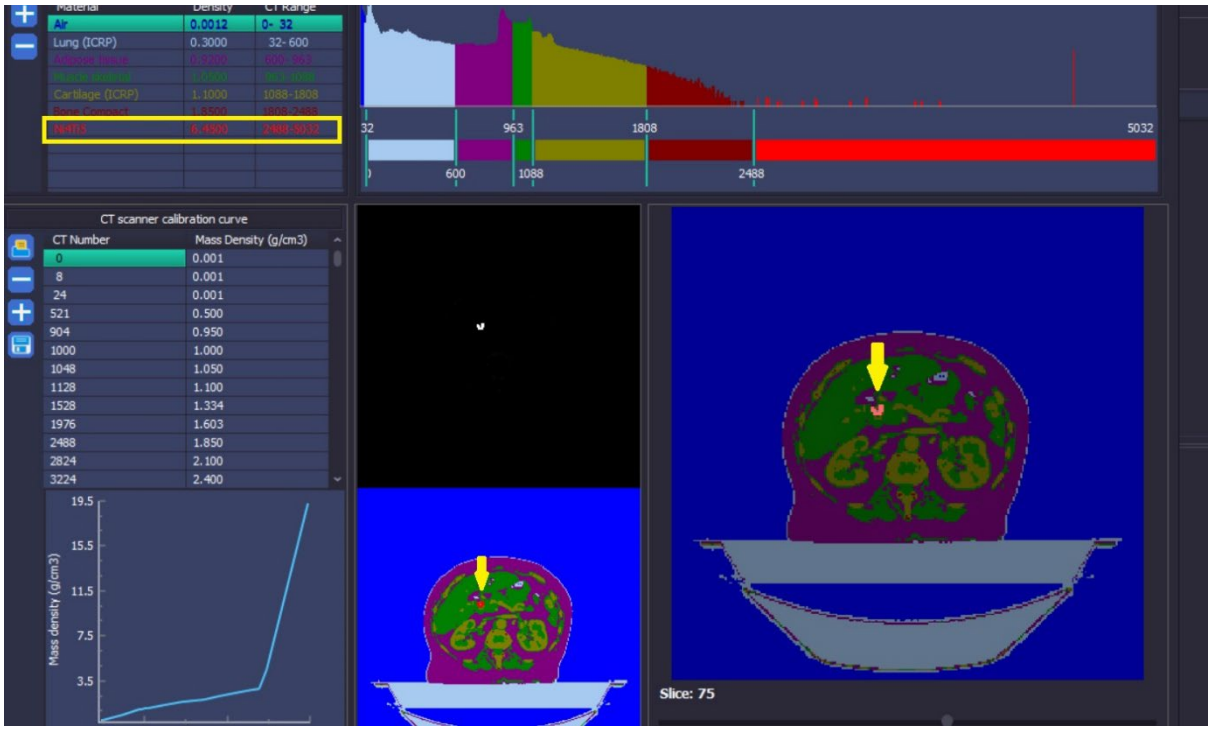

Figure 5.5: introduces the Nitinol material to the calibration curve as shown in the yellow box under the file name Nitinol. The yellow arrow shows the changes in the DICOM series to confirm that MC is updating the files to the new changes.

5.5 Results and discussion

5.5.1 One beam

The simulation of the MC using PRIMO showed an uncertainty of ≤ 2%. In Figure 5.7, the illustration of the MC for the patient with modification of the stent material reports a dose distribution and DVH for the contouring OAR. The beam goes through the PTV and stent, as illustrated in Figure 5.7. Thus, the first comparison was between the MC simulation, with modification of the material of the stent, and without the modification of the stent, as shown in Figure 5.9.

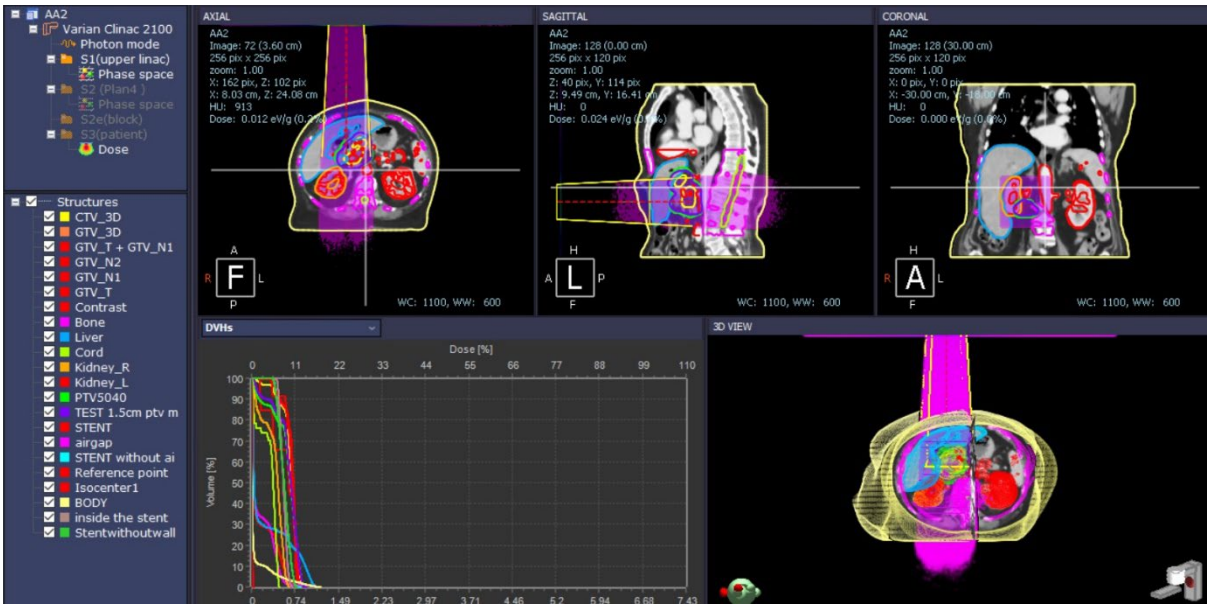

Figure 5.6: Demonstration of the dose distribution of the MC with a new model.

The difference in the dose distribution was evidenced in the distal location from the beam source for both patients. A reduction in the dose was recorded in the MC, with the new model compared to the MC with the old model, attaining a 4.9% difference distal to the source in patient A, and 4.8% in patient B, as seen in Figure 5.9.a. Furthermore, a dose enhancement was observed in the proximal left and right of the stent, with the difference between the MCs reaching 1.8% in patient A and 1.6% in patient B. The increase in the dose is due to scattering electrons from the stent's high-density materials, which were recorded when the correct stent materials were edited. However, in the MC that mimics the TPS, the stent was detected as a bone. A comparison was made for the MC examining the new model and TPS. In patient A, a 4% dose increase was observed at the proximal side, and on the lateral side, a difference increase of 3.4% was noted. On the distal side of the source, a decrease of 6.2% was observed between the MC and TPS, as illustrated in Figure 5.9.c. The dose enhancement for patient B on the proximal side displayed an increase of 2.7%, and on the lateral side, 2.4%. The distal dose shows a decrease of 4%. Patient A's stent location fell within the target area, which could affect the total delivered dose. Furthermore, not all of the stent is within the PTV in patient B, as shown in Figure 5.8. MC can calculate the dose build that occurs resulting from backscatter in high atomic number materials; thus, the TPS cannot calculate this accurately. The simulation used only one beam, and this was not the treatment technique used in pancreatic cancer. The standard technique used is VMAT,

which may reduce the dose reduction in the distal of the source. The single beam simulation was used to explore the effect of the modification of the stent material and new model in the MC to increase treatment accuracy.

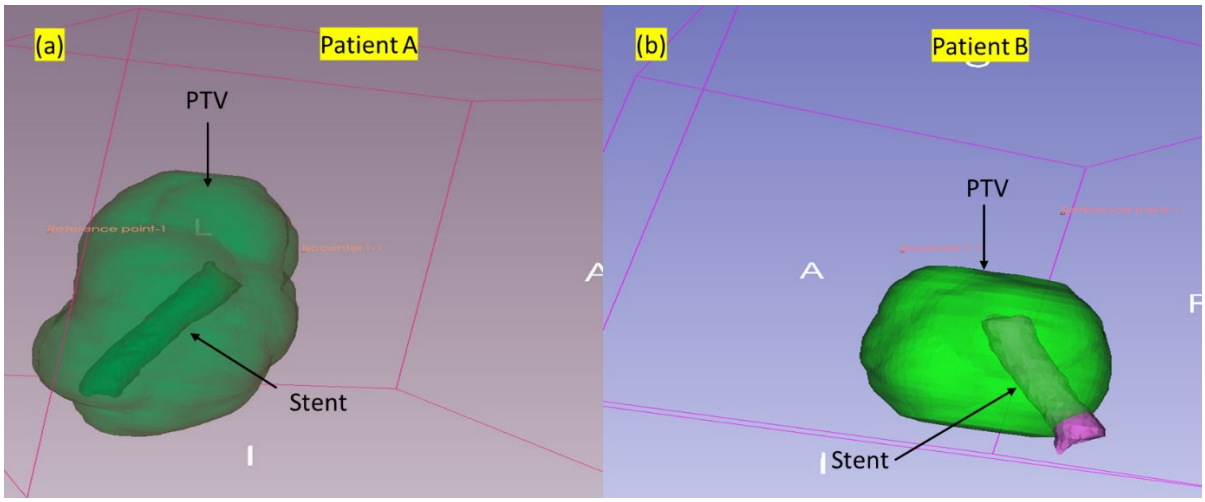

Figure 5.7: Illustrate the stent volume compared to the PTV in patients A and B. Stent in patient A is totally within PTV, but in patient B some of the stent volumes are located outside the PTV.

The main changes in the dose were observed in the stent itself. The percentage of the stent volume occupying the PTV and CTV was calculated to observe the effect in the area without a stent. The stent volume covering the PTV was 2.7% and 7.7% for CTV in patient A. The results from the gamma passing test are shown in Table 5.2, which uses the criteria of 3%/3cm; the MC new model with MC old model, MC new model with TPS, and the MC old model with TPS. The gamma passing rate (GPR) for MC/MC was 99.54% for the entire CT for patient A. As explained, the percentage of agreement (PA) was calculated using the DVH. Furthermore, the comparison of the new and old MC models for patient A showed a PA of 95.5% for PTV and 92.38% for CTV. The percentage of failure is more significant than the percentage of stent volume in PTV and CTV. This indicates that the area outside the stent has a low rate of agreement. The GPR for the PTV was 94.43% and 93.9% for CTV. A significant PA can be noted when comparing the new MC model with TPS. The PA in the new MC model and TPS was 82.78% for PTV and 81.97% for CTV. When comparing the percentage of stent volume in both PTV and CTV, a significant low-rate agreement in the area outside the stent may affect the clinical outcomes of the treatment. However, this was nevertheless till one beam, and the result may differ in the VMAT. The GPR

for the new MC model and TPS was 92.73% PTV, and 88.94% CTV, which were considered unacceptable in the clinical environment.

The final step was to compare the MC old model without modification with the TPS. The PA agreement was high for both the PTV and CTV. Furthermore, the GPR showed a high passing rate in both the PTV and CTV. The same pattern was observed for patient B; however, the covering volume of patient B varied because some of the stent volume was located outside the PTV. The PA for patient B for the new and old MC models was 96.9% for PTV and 94.3% for CTV. This indicated a better agreement for patient A, because some part of the stent was outside the PTV volume. The GPR was 94.49% for PTV and 91.62% for CTV. The following comparison concerns the MC new model with TPS, which followed a similar pattern as that observed in patient A. The PA was 88.51% for PTV and 87.83% for CTV, which indicated that TPS did not handle the presence of the stent very well due to high HU, which created beam hardening due to significant differences in the densities inside the stent and at the wall of the stent. The GPR was 89.8% for PTV, and 88.9% for CTV. The low GPR and PA are considered unacceptable in a clinical environment in an area that is considered homogenous, where the only heterogenous element is the stent. The new trend in pancreatic cancer, which is to increase the dose to produce a better biological response was discussed at the beginning of the chapter. It can increase PA and GPR disagreement. Furthermore, the treatment cannot achieve its target if the disagreement is found to be significantly high. The final comparison is between the old MC model and the TPS, which showed a clinical approval agreement in PA and GRP as illustrated in Table 5.3.

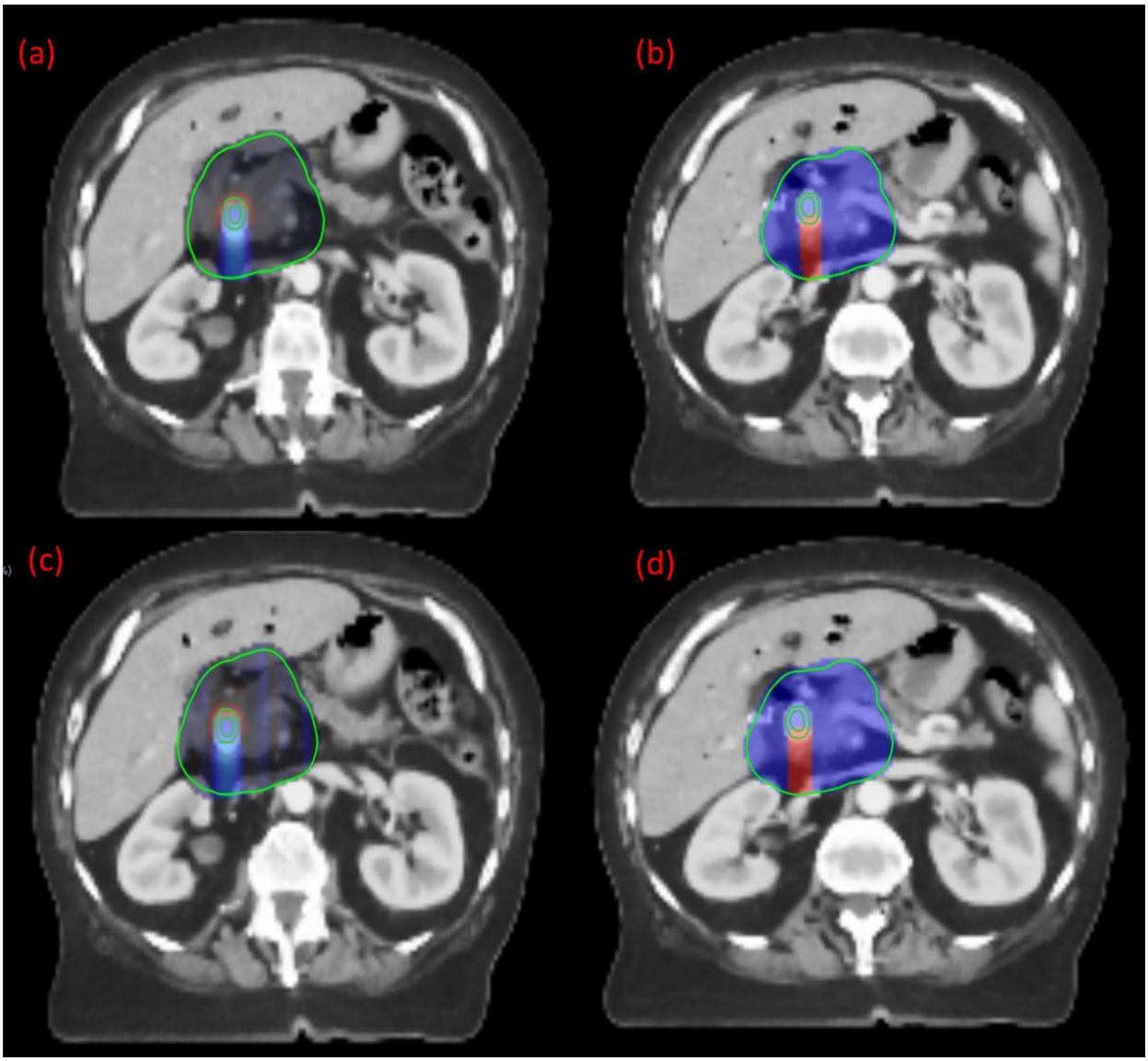

Figure 5.8: Difference between the MC with new model, old model and TPS in patient A: (a) is the difference between the two MCs; (b) the gamma test of the two MCs as the blue area represents where the test passed and the red area represents where the test failed; (c) the difference between MC new model and TPS; and (d) the gamma test between MC and TPS.

Table 5.2: The gamma pass test for MC with modification of the stent material, without modification and TPS. The test for one beam plan using the criteria 3% / 3cm for patient A.

Patient A	Percentage of agreement (PA)	Gamma passing rate (GPR)	Difference %			
Structure MC/MC	%	%	D95%	D50%	D5%	D0%
PTV	95.51	94.43	0.31	-0.76	0.28	-0.35
CTV-3D	92.38	93.9	-53.88	-0.23	0.7	4.29
Structure MC_new model/TPS						
PTV	82.78	92.73	-9.57	-20.2	-18.2	-14.29
CTV-3D	81.97	88.94	-80.48	-19.23	-17.22	-10.14
Structure MC_old model/TPS						
PTV	98.56	99	7.55	0.85	1.55	5.56
CTV-3D	98.64	99	1	1.24	2	4.48

Table 5.3: The gamma pass test for MC with modification of the stent material, without modification and TPS. The test for one beam plan and using the criteria 3% / 3cm for patient B.

Patient B	Percentage of agreement (PA)	Gamma passing rate (GPR)	Difference %			
Structure MC/MC	%	%	D95%	D50%	D5%	D0%
PTV	96.98	94.94	-45.31	0.71	0.21	0.69
CTV-3D	94.33	91.62	-54.25	1.4	1.1	0
Structure MC_new model/TPS						
PTV	88.93	91.9	-31.1	10.84	11.9	15.38
CTV-3D	87.61	90.19	-39	11.44	11.91	15.79
Structure MC_old model/TPS						
PTV	97.88	99	0.28	0.85	2.51	5.71
CTV-3D	97.28	99	0.24	0.93	1.72	7.25

5.5.2 VMAT

VMAT is the standard treatment plan for pancreatic cancer, and figure 5.10.a depicts the use of the VMAT plan in this chapter. The MCs comparison showed an increase in difference, reaching 1.1% in patient A and 1% for patient B, which is considered insignificant. The VMAT delivered mechanism reduces the stent's scatter effect, leading to a lower difference in dose increase. However, the difference in decreased dose achieves a maximum of 6.6% in patient A, as shown in Figure 5.10.b, and 8.5% in patient B. The constraints on maximum dose delivered to OAR, makes it essential to avoid the spinal cord, which then leads to a reduced dosage in the area distal from the beam source. Furthermore, delivering the dose from the posterior of the patient can increase uncertainty due to the presence of compact bone. Therefore, for these reasons avoidance of this is preferable, and reduces the dose in the distal of the stent, which is considered significant. The gamma test between the new and old MC models for the full CT score was 99.24% for patient A and 99.5% for patient B. The percentage agreement for the new MC and old models for CTV is 93.17% for patient A, although the gamma passing rate is low, at 90.92% (Table 5.4). For the PTV, the percentage agreement reaches 94.26%, and the gamma pass rate is 93.19%. The same pattern

is detected in patient B, where PA was 95.7% for PTV and 94.14% for CTV. The GPR was 87.7% PTV and it was 85.4% for CTV.

The gamma test for MC is shown in Figure 5.10.c. In this, the blue area represents where the test was passed and the red area where the test failed. The area that did not pass was concentrated in the stent and surrounding the stent in both patients. In patient A, the percentage of the stent covering the PTV and CTV showed that with the use of VMAT, the PA was reduced in an area other than the stent, as the stent only covers 2.7% of the PTV. Furthermore, the VMAT reduced the scattering effect to an insignificant level, but disagreement with regard to the dose was clinically effective. Comparing the MC new model with TPS reveals a difference in dose enhancement, reaching 0.8% near the stent in patient A, and 0.7% in patient B. Furthermore, a decrease in the dose reached 7.1% for patient A, and 7.8% for patient B. The whole CT passing rate for the gamma test was 95.61% between the new MC model and TPS in patient A, which remains lower than the MC passing rate. As shown in Table 5.4, the PA was 85.48% for CTV and 87.54% for PTV in patient A. A similar outcome is apparent in patient B: the PA is 88.5% for PTV and 87.3% for the CTV decrease in dose, due to the inability of TPS to handle high-density materials effectively. The PA for the CTV was significantly low, even with the extraction of the percentage of the stent volume, and the PTV presenting a similar pattern in patient A. Nevertheless, the equivalent for patient B was not calculated, because some of the stents were located outside the PTV. VMAT reduces the scatter effect significantly, but due to the threshold, it was not possible to overcome a decrease in the distal area. Furthermore, the new model adds greater complexity and artifacts like beam hardening, which TPS struggles to handle. In patient A, when comparing the MC new model and TPS, the score for the GPR of PTV is 91.97% and it is 87.4% for CTV. The GPR percentage is not clinically acceptable. In patient B, the GPR is 89.9% for PTV, and 88.9% for CTV. Both patients A and B show agreement and clinical approval when comparing the old MC model with TPS, as shown in Table 5.4.

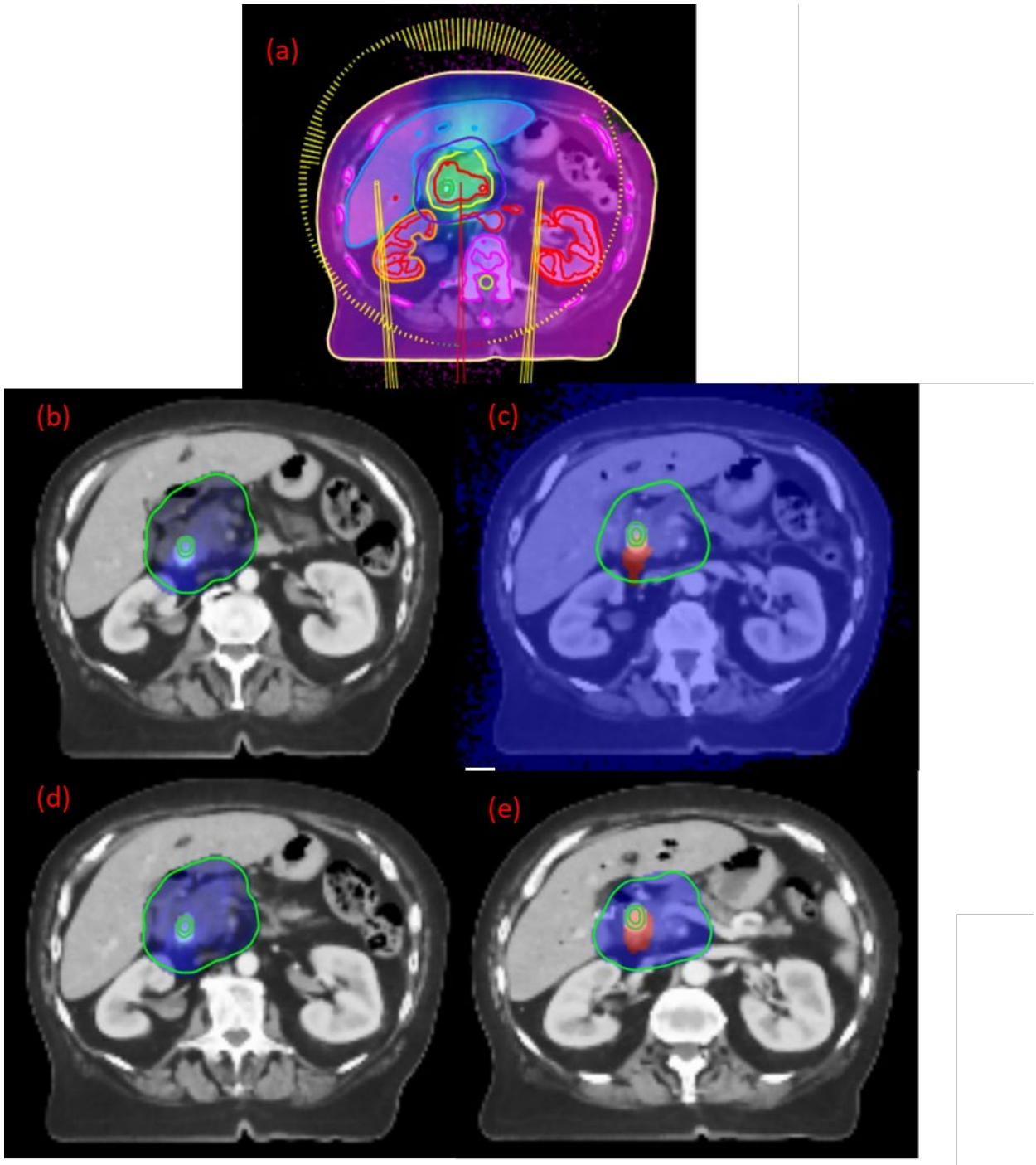

Figure 5.9: Details the VMAT plan and treatment comparison between the MC algorithm and TPS: (a) VMAT plan; (b) dose difference between MC with the modification of stent material and without; (c) gamma test for the MCs; (d) dose difference between MC with modification and TPS; and (e) gamma test for MC and TPS. The blue in the gamma test indicates where the test has been passed, and the red indicates the test has failed.

Table 5.4: The gamma pass test for MC with modification of the stent material, without modification and TPS. The test for VMAT plan using the criteria 3% / 3cm.

	Percentage of agreement (PA)	Gamma passing rate (GPR)	Difference %			
Structure MC/MC	**%**	**%**	**D95%**	**D50%**	**D5%**	**D0%**
PTV	94.26	93.19	-3.28	-3	-1.21	-0.3
CTV-3D	93.17	90.92	-4.81	-4.6	-1.34	-1.2
Structure MC_new model/TPS						
PTV	87.54	91.97	1.2	3.31	4.06	8.91
CTV-3D	85.48	87.4	-0.14	0.73	4.42	7.44
Structure MC_old model/TPS						
PTV	98.19	99	0.73	2.59	1.65	5.93
CTV-3D	98.16	99	0.81	1.51	2.14	5.15

Patient B	**Percentage of agreement (PA)**	**Gamma passing rate (GPR)**	**Difference %**			
Structure MC/MC	**%**	**%**	**D95%**	**D50%**	**D5%**	**D0%**
PTV	95.74	87.75	-8.96	-3	-0.93	0
CTV-3D	94.14	85.41	-19.18	-4.57	-2.84	-3.38
Structure MC_new model/TPS						
PTV	88.51	89.81	-5.6	0.49	4.55	6.85
CTV-3D	87.83	88.99	-17.55	-1.36	2.1	2.53
Structure MC_old model/TPS						
PTV	97.44	96.07	1.85	2.19	4.24	5.62
CTV-3D	97.47	95.98	0.1	1.86	3.56	4.86

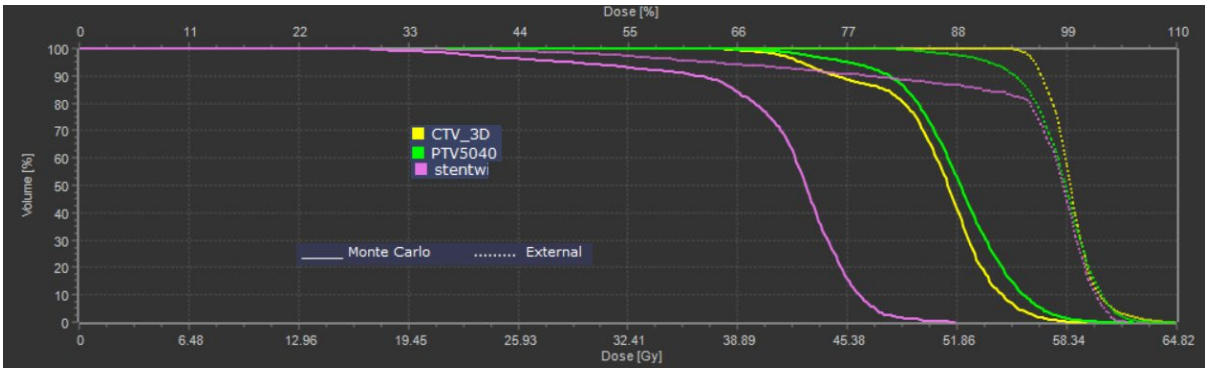

Figure 5.10: DVH for patient B comparing MC new model with TPS. The solid line represents the MC new model and the dots represent the TPS.

The study of the effect of the biliary stent on dose distribution was not discussed thoroughly, and very little research was carried out. A study by Lee Ho *et al.* reports a range of increased doses between 2.3% to 8.2% in the proximal area of the stent using one beam, and showing a minor magnitude increase of 1.8% (212), which is similar to the outcome of the MC simulation completed in this study. The reduced dose in this research study was 0.9% to 3.6%. However, the MC simulation outcome was observed to be 4.9% higher in the MC simulation when comparing the new MC model to the routine practice. In addition, a comparison between the new MC model and TPS shows greater difference through a decreased dose reaching 6.2%. Lee Ho *et al.* indicates that VMAT reduced the dose enhancement and reduction in the distal area (212). In

the MC simulation, dose enhancement was reduced significantly in the distal area, but remained significant. The difference in the result is that Lee Ho *et al.* used a phantom with a stent inside it that did not contain any OAR or constrain the OAR. In this study, a DICOM series and routine clinical constraints were used. The constraint forced the planner to use the patient's anterior portion, whilst avoiding the posterior. Using a phantom provided information, but was not found to be directly related to the clinical environment. In this study, more actual data were used to relate the results to the daily routine in radiotherapy department. The TPS significantly overestimated the dose in the distal region of the stent, and underestimated the dose in the proximal area of the stent when compared to the MC. Lee Ho *et al.* reported a similar outcome compared to the TPS. The use of the MC alone without any correction was not sufficient to provide an accurate estimate, as shown in the result of the MC simulation. Using the new model provided in this chapter increases the accuracy of dose distribution by overcoming the artifact of CT, due to the hardening effect and correction of the stent materials, so as to produce accurate results that can be used to increase dose to the target area without delivering high doses to the OAR.

5.6 Conclusion

The new model tested in this chapter offered an alternative approach to increasing the accuracy of dose distribution in the presence of stent in pancreatic cancer patients; doing so is essential for managing dose escalation. The new model uses the correct materials for the stent and a better contouring technique than in previous studies. Three different scenarios were tested. The first scenario used TPS without the addition of any other changes. The second scenario used the MC algorithm, without altering any other factors. The final scenario used an MC with a new model. The results revealed PA and GRP agreement between the MC and TPS, whereas the new MC model showed a significant difference in dose distribution. Unless we edit the material or overcome the hardening effect, the MC will not show any significant improvement from TPS. A VMAT technique was found to reduce dose enhancement but did not alter the dose of radiation delivered to the distal area. The new model aims to reduce uncertainty surrounding the treatment of pancreatic cancer patients with a stent to make it possible to increase the dose based on an accurate calculation of dose distribution. As uncertainty decreases escalation in dose can be achieved with better estimates of the side effects of radiotherapy treatment. The model utilized in this study demonstrated the potential for adjusting the stent's materials to achieve both enhanced

and reduced dosages. It's important to consider that the inclusion of a platinum core would further amplify the effect, thanks to its higher atomic number in comparison to nickel and titanium. Moving forward, the next steps involve incorporating the precise components of the stent and their respective proportions. This information can be sourced either from the manufacturer or through the utilization of specialized equipment capable of analysing the stent's composition for example, scanning electron microscopy, and energy dispersive X-ray spectroscopy. As mentioned in the literature review, dose escalation can produce better outcomes for patients, and the new model can increase the accuracy of dose distribution to avoid impacting the OAR as much as possible.

Chapter 6: Multiscale modelling of photon distribution

6.1 Introduction

Radiotherapy, whether administered with or without chemotherapy, plays an important role in the treatment of patients with head, neck, or brain tumours. Tumours of the head, neck and brain are considered to be within the most heterogonous areas of the body. Furthermore, in the head, neck, and brain area, there are many OAR that are affected by treatment. These affect the quality of life of the patient directly, particularly those that are related to parts of the body like the cochlea and hippocampus. Increasing the dose to OAR can cause a decrease in the patient's quality of life, and an increase in the side effects of the radiotherapy treatment. One solution for ensuring the target receives the prescribed dose is to increase the margin of the target delineation, known as 'planning target volume'. However, an increase in the margin can cause an increase in the dose that reaches the healthy tissue. One solution for avoiding an increase to the margin is increasing the accuracy of the treatment using new techniques, such as VMAT. Alternatively, the MC simulation can decrease the dose to the normal tissue, due to its ability to lower the uncertainty of the dose distribution. Furthermore, selecting the optimal setting for the treatment area in the treatment planning system (TPS), for example dose to water, or dose to medium, is essential for optimizing the treatment. In addition, understanding the photon behaviour in the heterogenous areas is essential for decreasing the error involved in delivering the dose to the target. However, due to the limited clinical CT resolution, many details of the heterogeneous area of the anatomy are missing, and can only be seen in higher CT resolution, such as Micro CT. This chapter presents a novel MC simulation using a patient's Micro CT DICOM series to study dose effects in the complex temporal bone area. The approach overcomes clinical CT limitations and provides insights into dose distribution, offering a basis for comparing dose to water and dose to medium in treating the temporal bone and cochlea. The objective of this chapter is to explain in more detail in the section 6.3.

6.2 Literature review

The TPS is the main algorithm used to create a radiotherapy plan, due to its rapid, clinically acceptable accuracy. The new TPS can employ two modes: dose to water, or dose to medium, although the optimal mode for use is a subject of significant debate. Before comparing the different modes of reporting, both modes must be explained, with the advantages and disadvantages of each

considered thoroughly. In radiotherapy, the recorded dose absorbed in water is not equal to, and does not correspond to, the dose absorbed in various tissue. A TPS reports the dose to water by collecting information regarding the attenuation and the scatter of different tissue densities, then displaying the result as dose to water at each location. Applying the information regarding different densities to a water medium overcomes the different effects of the densities in the dose absorbed. In contrast, the MC report directory considers dose to medium to be the impact of the different chemical structure of each tissue and their density, and do not need to address any types of conversion. The various facets of the debate regarding the best mode for use are supported by ongoing research, and dose to water is currently the mode most used in reporting for two main reasons. First, dose to water has been used in clinical planning for the last decade, and many dose limitations have been established through this mode. Furthermore, all of the knowledge acquired regarding dose effects is based on this method. Secondly, all calibrations are built using dose to water as the reference. MC alone cannot be used in calibration, as it uses the CT number, based on the human body's composition, and employs the approximation function of this to model the chemical composition of various tissues. This approximation works in biological material, but performs poorly in non-biological materials, causing problems, for example to the phantom used in quality assurance. If the TPS were to be based on dose to medium, it would be necessary to introduce a conversion step to convert the dose to medium to dose to water (219). The study conducted by Siebers *et al.* introduced Bragg Gray Cavity theory to demonstrate that conversion between the two modes can be conducted. However, the study demonstrated that there is a significant difference in the result in areas that contain cortical bones that exceed 10% (220). Meanwhile, Dogan *et al.* explored the idea of calculating the dose to medium before transferring the measurement to dose to water, in order to overcome possible uncertainties, due to the calibration. However, the conversion between the two modes introduced a systematic error that reached 8% in hard bone areas (221). Many previous studies agreed that in areas with low heterogeneities, the difference between dose to medium and dose to water is less than 2%, which is not clinically significant (212, 215, 216). However, in areas of different densities, especially in the presence of bone material and air, the difference can reach 10% (212, 215, 216). To simplify the effect of the heterogeneous area in both calculation algorithms, the variation in density does not change the dose because the dose is a measure of absorbed energy per unit mass. Both values impact proportionately with the change of density. The difference between dose to water and dose

to medium rises because of the difference in interaction cross sections due to the material compositions of the media. Furthermore, the difference can be observed at a macroscopic level in the mass attenuation, energy absorption coefficients and electron stopping power (159). This chapter uses a microscopic structure with a Monte Carlo algorithm to provide data that can help answer the debate on which dose reporting can provide a better outcome for the patients. In the study discussed in this chapter, the target area of the temporal bone and inner ear was considered to be one of the most heterogenous areas, given its high density and the presence of soft tissue and air. Furthermore, the cochlea is sensitive to radiation after a patient receives chemotherapy. The problem arises because of the differences between the two modes of planning that affect the dose distribution, plan evaluation, dose verification, and dose reporting. The reporting mechanism must be evaluated carefully in clinical situations when an alternative mode to dose to water is chosen. Further, a deep evaluation must be conducted to identify the most accurate mode for use in the target area for providing the treatment with the best treatment plan (219). The study by Kry *et al.* demonstrated the percentage difference between the different reporting systems using a slab phantom of different density (169).

The current study used micro-CT data to provide more details of the dose distribution in heterogenous areas that the aforementioned report did not provide. Meanwhile, Radojcic *et al.* found that there is a significant difference between dose to water and dose to medium when reporting the dose distribution of the cochlea (224). The study also revealed the presence of a lower dose to the cochlea after using the dose to medium mode; two areas demonstrated a significant difference in the dose distribution, namely the cochlea and the mandible. The cochlea is surrounded by a bone labyrinth and the mandible consists of bones (224). The study concluded that any bone or high-density area will produce a lower dose using the dose to medium method than in the dose to water method (224). Meanwhile, Accuros XB reported that the use of dose to medium produced a 10% higher dose in the cochlea and 13% higher in the mandible when using dose to water calculation, compared with dose to medium, in the same TPS (225). The study of 10 head and neck patients conducted by Dogan *et al.* that employed an MC in an IMRT treatment produced a systematic error when the dose to medium was converted to dose to water, thus affecting the DVH of the target and the OAR. Such systematic errors can reach 5.8% in the target and 2.7% for the OAR (221). One noticeable difference between dose to water and dose to a medium was the relative isodose lines of 70.8 Gy and 60 Gy (221). In a plan that uses dose to water, the two isodose

lines are stretched into the mandible. Alternatively, in a dose to medium plan, the two isodose lines do not reach the mandible, and are safely distanced from it (221). The issue occurs because of the presence of bone material, especially high-density bones. In Micro CT, images of the bone show blood and some air cavities that may affect the distribution of the dose that do not present themselves in a normal CT resolution, as shown in Figure 6.1.

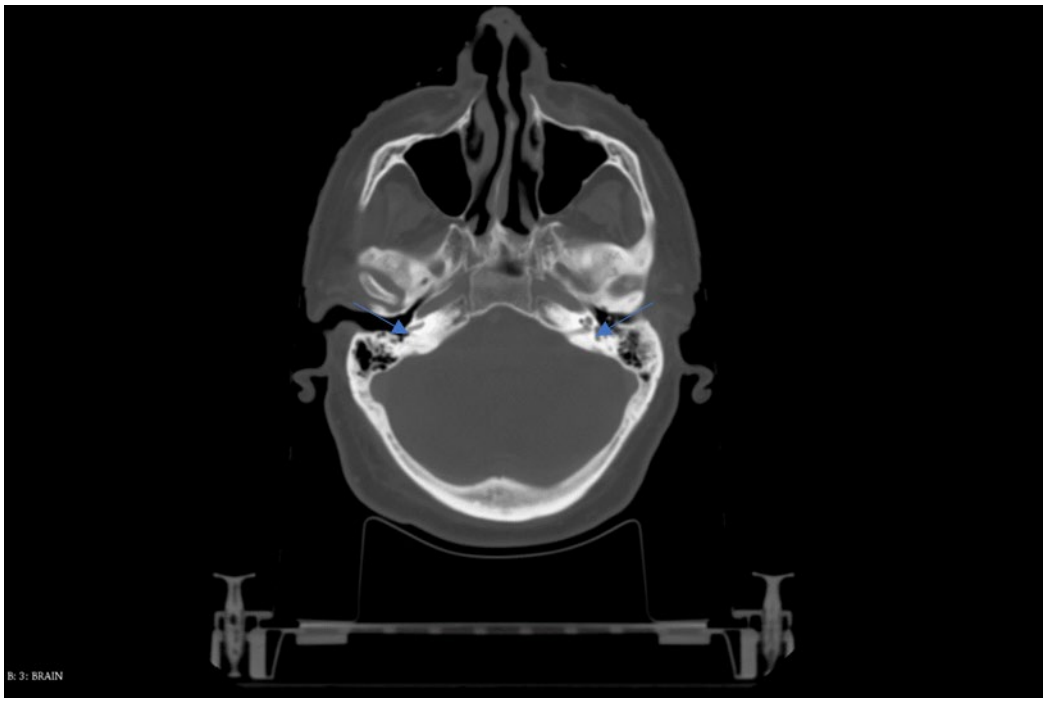

Figure 6.1: Clinical CT resolution of the brain. The arrows indicate the right and left cochlea.

In radiotherapy, bones have traditionally been considered to be solid units, but with the advent of more advance techniques, this concept is evolving. For example, the spongiosa bone marrow contains a radiosensitive cell type called red bone marrow that consists of haematopoietic stems cells that form a portion of the whole bone marrow. Spongiosa is located in numerous places, including the spine, mandible, cranium, pelvis, ribs, and long bones. Furthermore, the trabecular bone, which surrounds the spongiosa, is covered with osteogenic cells called 'bone surface cells'. The thickness of the bone surface cells is 10 μm (226). The study conducted by Walter *et al.* of bone marrow phantom receiving a dose of photons using a MC and TPS found that there was a clinically significant difference of > 5% between dose to water and dose to medium in the cranium area. This was the highest difference between the two reported modes of all the areas tested regarding the dose to red bone marrow and bone surface cells. It is not possible to visualize the small cells in normal CT scans, and they can only be estimated with a micro-CT data. Dose to

medium versus dose to water is an estimator of dose to sensitive skeletal tissue, and more studies are required to support the optimal mode for the head and neck area, especially given the availability of high accuracy treatment techniques.

6.3 Objective

In this chapter, an MC simulation was conducted in the area of the temporal bone, an area that contains the middle and inner part of the ear, as well as the cochlea. The simulation was executed using a Micro CT DICOM series which, to our knowledge, was the first time a real patients Micro CT DICOM series has been used to study the effect of an area of high heterogeneity under different energy levels of dose deposition, using the MC simulation. The purpose of using Micro CT was to overcome the limited resolution of the clinical CT that do not show the different densities in a heterogeneous target. Therefore, this study sought to aid understanding of the dose distribution in a heterogeneous area, using the gold standard MC with a Micro CT simulation tool. The results helped to build a fundamental base to connect to the clinical environment to evaluate whether there is a significant difference between dose to water and dose to medium in the dose distribution in the temporal bone and cochlea area in an actual patient treatment plan.

6.4 Materials and methods

6.4.1 The cochlea and temporal bone Micro CT

The open-access DICOM series used for the purpose of this study was a Micro CT of the temporal bone that contained the resected cochlea tissue. The DICOM series is available for download for research and commercial use, provided the content is referenced appropriately. In comparison, the study in coming Chapters 7 and 8 were more clinical-oriented, and detailed the side effect of high dose distribution to the cochlea and the sensitive area within the cochlea. The micro-CT series was obtained from OpenEar library (227). The article by Sieber *et al.* uploaded to the OpenEar library, detailed the steps conducted to create the Micro CT series of the temporal bone (227). A specimen of temporal bone was immersed in phosphate buffered saline, after which the specimen was epoxy embedded. As advised in the aforementioned article, 0.1% Acid Fuchsin was added to enhance the contrast between the soft tissue and the embedded epoxy. The voxel size of the micro images was 0.125 mm. Reconstruction and registration of the Micro CT was conducted using the open-source programme, 3D slicer version 5.0.2 (227). The registration

involved an alignment of the Micro CT with a cone beam, as in CT. Figure 6.2 shows the 3D segmentation from the Micro CT and the different slices, prior to cropping.

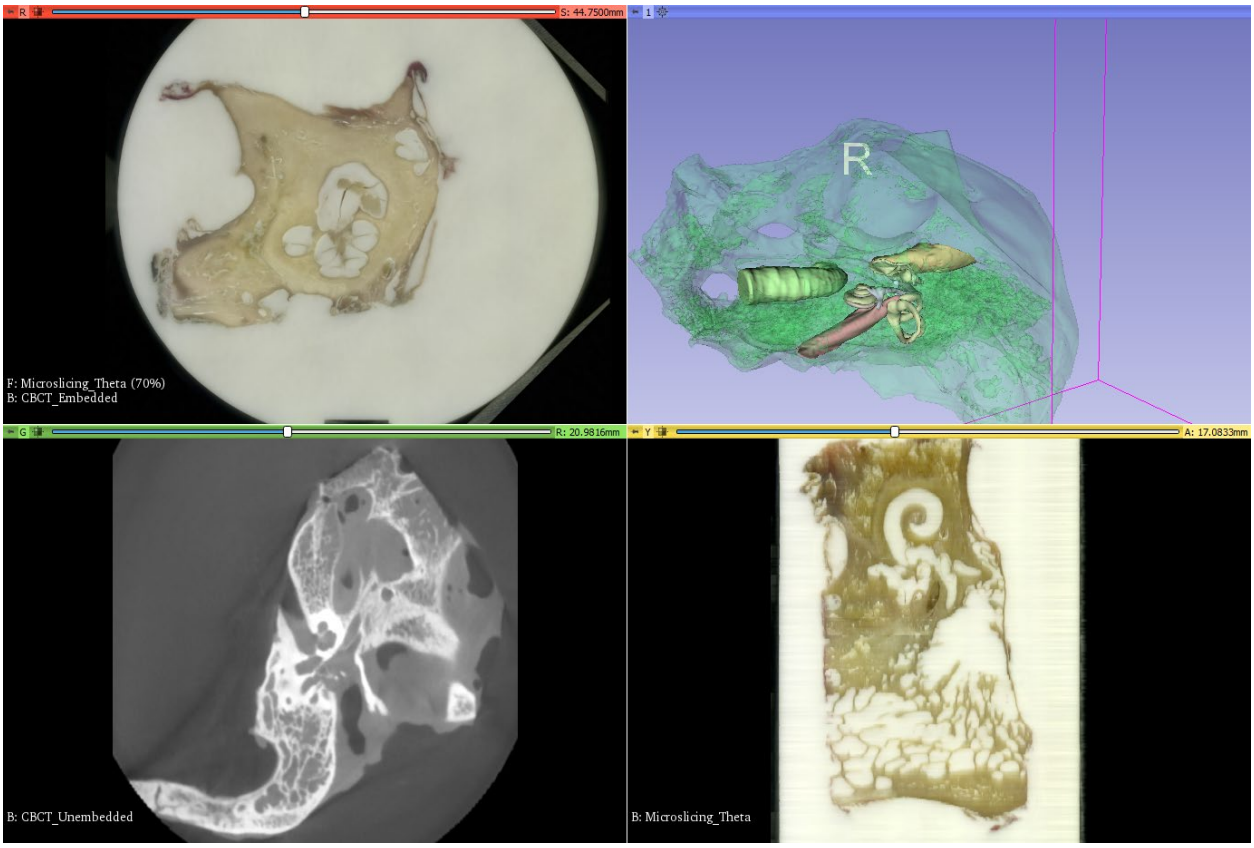

Figure 6.2: 3D segmentation and slices of the Micro CT of the temporal bone and cochlea.

6.4.2 Handling Micro CT DICOM using MATLAB

CT images are essential for radiotherapy planning, as they provide two points of key information that facilitate an effective planning system for use in radiotherapy treatment. First, CT provides a geometry of the target and OAR; the contouring of the target and OAR is conducted using CT and, in some locations the fused images of other modalities, such as MRI can be used. Second, CT creates a map of electron density information for all organs that is required for the calculation of the dose to be applied. The CT images are taken from different angles, and from these images a computer can generate a grayscale to reflect the tissue density. The Hounsfield unit (HU) is a quantitative scale that relates to the CT radiodensity. The HU reveals the electron density for different organ types; for example, air has a value of – 1000 in HU, and is shown as black in

the grayscale, while dense bone has a value of +2000 in HU, and presents as clear white in the grayscale. A downside of using Micro CT is that it does not contain HU similar to those of medical CT. In order to overcome this problem, the Micro CT voxel values were changed from grayscale to HU via a relevant linear transformation equation. This is possible as the x-ray attenuation coefficient is related directly to the grayscale in Micro CT. The equation is

$$HU = (Grayvalue)*slope + intercept \qquad \text{(Equation 6.1)}$$

In medical CT, the slope and intercept are available in the DICOM header information, but in the DICOM series used in this simulation, the header did not contain the slope and intercept. Subsequently, the slope and intercept required calculation, and this was conducted via MATLAB. The first step for calculating the slope and intercept was to upload the DICOM series to MATLAB, enabling the modification of the DICOM. In the MATLAB, a histogram was created from the value of the voxels to identify the peaks that represented the highest frequencies of the grayscale on the voxel.

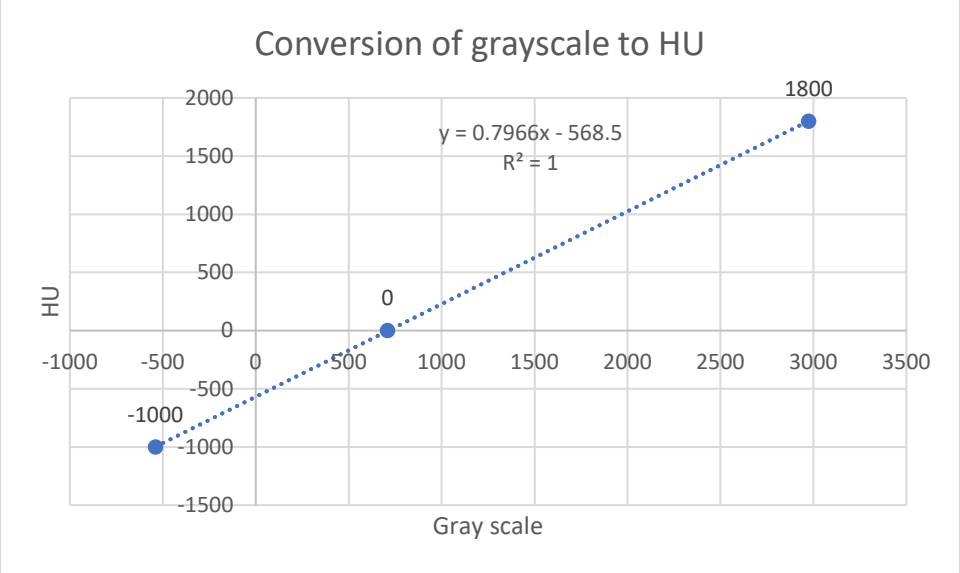

Figure 6.3: The three points chosen that represent air, water, and bone.

The histogram showed high peaks in the area of – 538, 709, and 2974. Upon comparing these values with the voxel location of these peaks, the results showed that -538 was air, 709 was soft tissue, and 2974 was bones. In creating a Micro CT sample, the air was extracted, but in the MATLAB processing, air was found in the sample. As show in Figure 6.3, three specific points were plotted and fitted with a polynomial to generate an equation. Only these points were chosen because this study was concerned with heterogeneity, and these points represented these heterogeneities. The soft tissue displayed a very similar value to water in a medical CT, and was the material used by the present study. A visualization test was conducted to ensure that the number imported from the DICOM was correct, and that no error had occurred. Figure 6.4 shows the different points chosen from the Micro CT to evaluate the different tissues and their ranges.

(a)

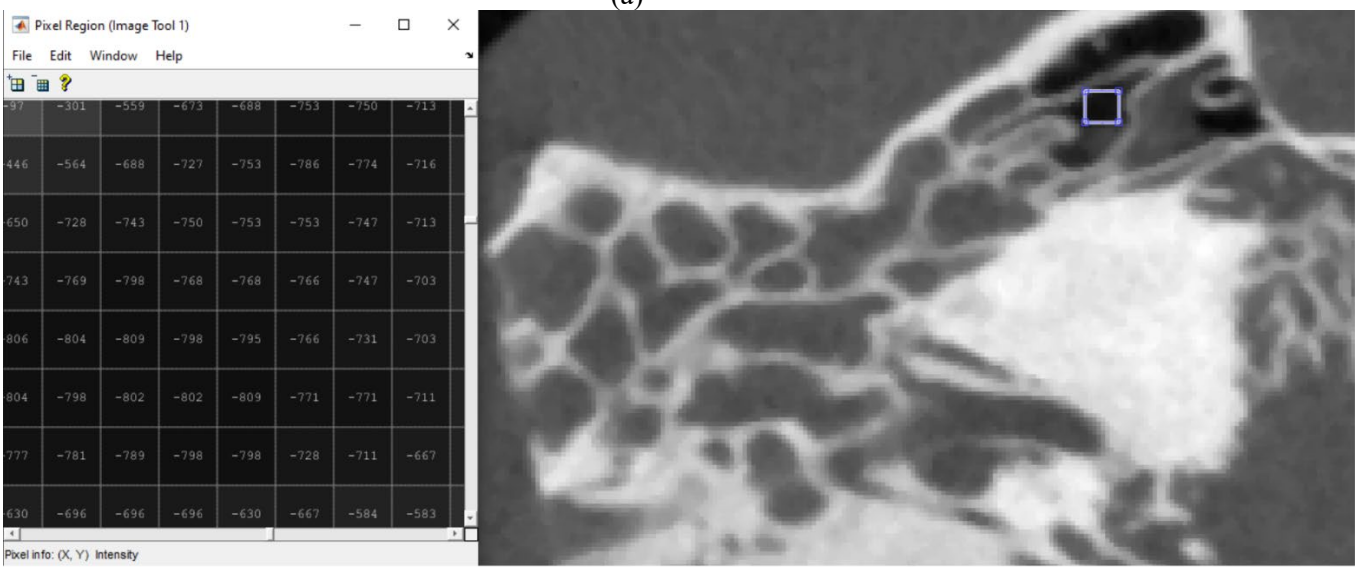
Pixel Region (Image Tool 1)
File Edit Window Help
-301 -559 -673 -688 -753 -750 -713
-446 -564 -688 -727 -753 -786 -774 -716
-650 -728 -743 -750 -753 -753 -747 -713
-743 -769 -798 -768 -768 -766 -747 -703
-806 -804 -809 -798 -795 -766 -731 -703
-804 -798 -802 -802 -809 -771 -771 -711
-777 -781 -789 -798 -798 -728 -711 -667
-630 -696 -696 -696 -630 -667 -584 -583
Pixel info: (X, Y) Intensity

(b)

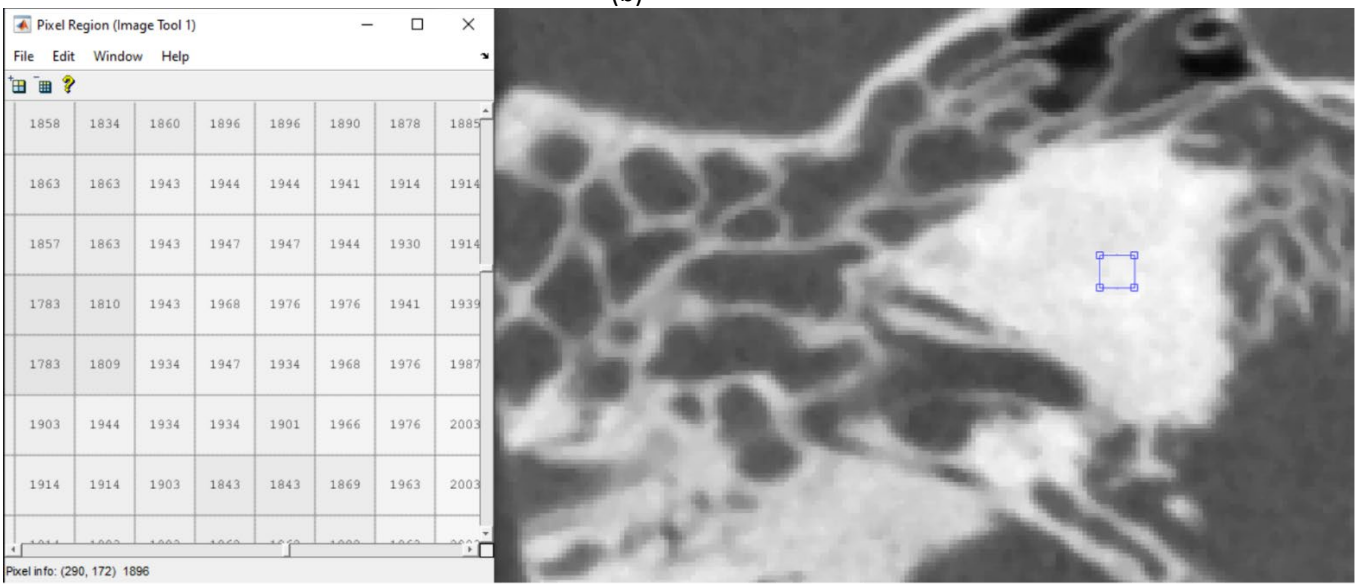
Pixel Region (Image Tool 1)
File Edit Window Help
1858 1834 1860 1896 1896 1890 1878 1885
1863 1863 1943 1944 1944 1941 1914 1914
1857 1863 1943 1947 1947 1944 1930 1914
1783 1810 1943 1968 1976 1976 1941 1939
1783 1809 1934 1947 1934 1968 1976 1987
1903 1944 1934 1934 1901 1966 1976 2003
1914 1914 1903 1843 1843 1869 1963 2003
Pixel info: (290, 172) 1896

(c)

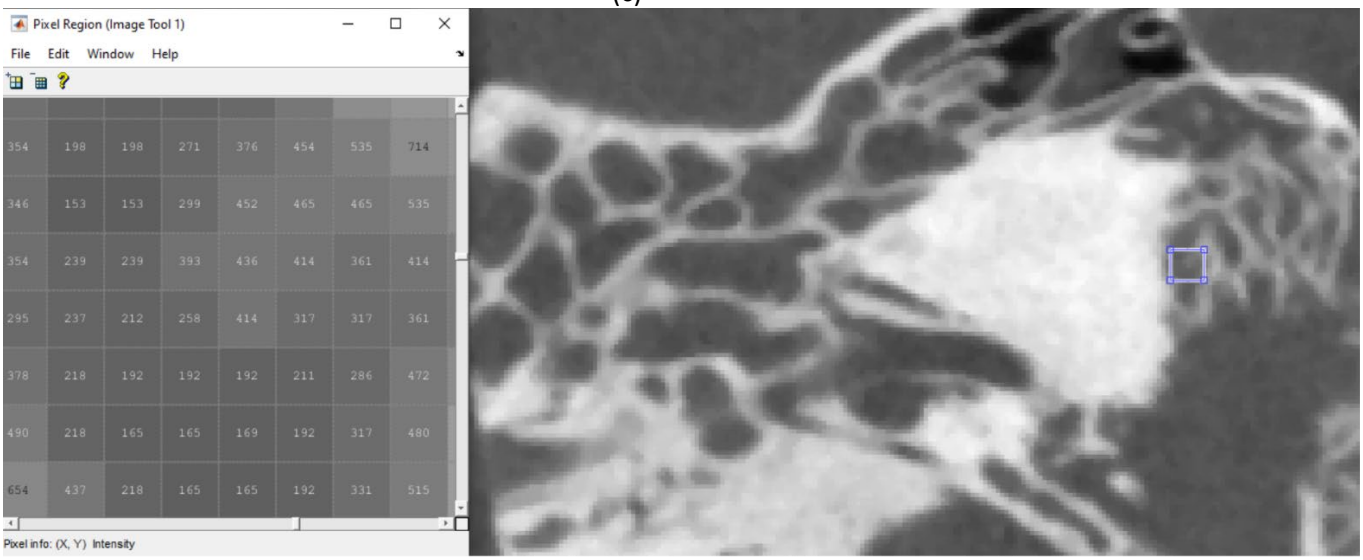

(d)

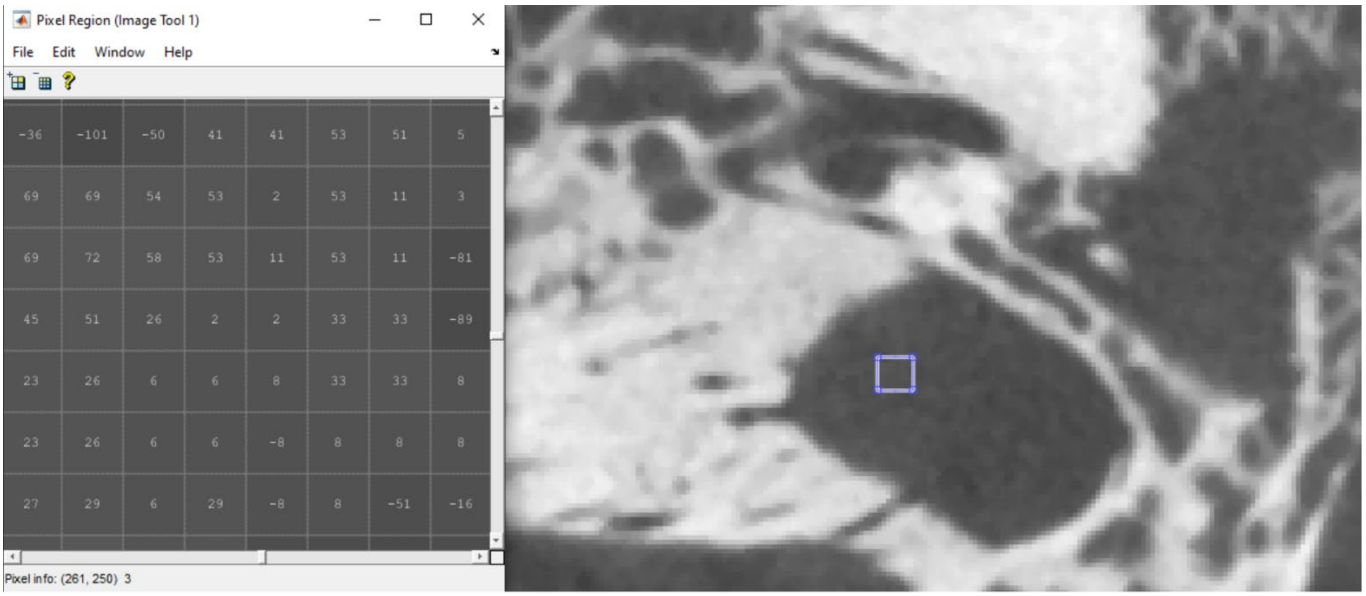

Figure 6.4: The points chosen in the Micro CT: (a) air, (b) bone, (c) soft tissue, (d) another soft tissue.

The three points were fitted in a polynomial scale to create an equation that was used to transfer the grayscale of the Micro CT to HU. The equation used was

$$HU = ax^2 + bx + c \qquad \text{(Equation 6.2)}$$

The value obtained from the polynomial equation was used in the MATLAB code to transfer each voxel to HU. Figure 6.5 shows the code used to transfer the grayscale in each pixel to HU, and to save the outcome as a DICOM series.

```
clear
image_list=dir('IM*.dcm');
[slice_no,y]=size(image_list);

for i=1:slice_no
AA_ct=dicomread(image_list(i).name);
image_stuck(:,:,i)=dicomread(image_list(i).name);
imgHdr = dicominfo(image_list(i).name);

AA_ctd_hu = min(max (0.7966*AA_ct -568.5, -1000),4096);
AA_ctd_huu = int16(AA_ctd_hu);
dicomwrite(AA_ctd_huu, ['Micro' num2str(i) '.dcm'], imgHdr,'CreateMode','Copy')

end
```

Figure 6.5: The MATLAB code used to transfer the grayscale to HU.

The final step consisted of a comparison between the value of the HU of the Micro CT with the value of the medical CT in the same area, to ensure that the conversion represented a value that was very close to the real medical CT. The Micro CT was then similar to the medical CT, in terms of the HU. However, the DICOM data could not be used in FLUKA, due to the information missing from the header. In medical CT, the header contains information about the DICOM series, such as slice location and the series number that are not found in a Micro CT. In order to fill the header with the relevant information, without corrupting the sequence of the DICOM or the location of each slice, a MATLAB code was used to provide the particle information in the header. It was important that this information was readable in FLUKA, or in other code if needed. The first element of information added was the spacing between the slices, which was 0.125 mm. The second element was the slice location, which was calculated by using two values: the slice number, and the distance between slices. The following remaining information was added without using any calculations: the series number, pixel spacing, rescale slop, and acquisition number. Figure 6.6 shows the code used to prepare the DICOM series for adaptability to different MC codes. After editing the header of the DICOM data, the final edited version of the Micro CT was saved, and the data was deemed to be ready for use in the MC simulation code.

```
clear
imagelist = dir('M*.dcm');
[slices,nn] = size(imagelist);
for i = 1:slices
    Jimages = dicomread(imagelist(i).name);
    Jinfo = dicominfo(imagelist(i).name);
    copyinf = dicominfo(imagelist(i).name);
    copyinf = dicominfo('T (5)');
    copyinf.BitDepth = Jinfo.BithDepth;
    copyinf.FileMetalInformationGroupLength = ...
        Jinfo.FileMetalInformationGroupLength;
    copyinf.MediaStorageSOPClassUID = Jinfo.MediaStorageSOPClassUID;
    copyinf.SOPClassUID = Jinfo.SOPClassUID;
    copyinf.MediaStorageSOPInstanceUID = Jinfo.MediaStorageSOPInstanceUID;
    copyinf.SOPInstanceUID = Jinfo.SOPInstanceUID;
    copyinf.SpacingBetweenSlicess =
    copyinf.PixelSpacing = 0.125;
    copyinf.SliceThickness = 0.125;
    copyinf.SeriesNumber = i+1;
    copyinf.AcquisitionNumber = i+1;
    copyinf.SliceLocation = 0.125*i+1;
    copyinf.ImagePositionPatient = copyinf.SliceLocation;
    copyinf.PixelSpacing = [0.125;0.125];
    copyinf.RescaleSlope = 1;
    dicomwrite(Jimages, ['MicroFinal' num2str(i+1000) '.dcm'], copyinf,'CreateMode','Copy')
end
```

Figure 6.6: The MATLAB code used to fill the information missing from the Micro CT header to be used in the MC simulation.

6.4.3 MC simulation using FLUKA

The MC simulation engine used in this study was FLUKA version 4-0. FLUKA interface FLAIR version 3.0 enables the creation of different geometrical shapes. The input cards are the command that controls the simulation environment, and basic input cards were used in this case. However, some customization of the input cards was conducted to allow the import of the DICOM series. FLUKA possesses the capability to oversee the initiation of geometry-dependent arrays by designating provisional memory spaces prior to acquiring knowledge about the precise dimensions of the issue. The unutilized portions within these spaces are later reclaimed after the complete input has been processed. Nevertheless, when confronted with an extensive quantity of regions (exceeding 1000), it becomes essential to notify the program to expand the magnitude of these

provisional memory spaces. This pivotal data must be provided immediately, utilizing the "GLOBAL" card. A GLOBAL card was added to allow a high number of regions to be simulated. It is necessary to use a GLOBAL card when DICOM data is used in a simulation. Further, the DICOM data must be converted to voxel geometry, to allow readability by FLUKA. The DICOM tab enabled the DICOM files to be uploaded, and as the DICOM data contained 481 slices, with a high number of voxels in the data, the simulation was long. In order to reduce the time needed to complete the simulation, it was necessary to crop the data; this was conducted within the FLAIR interface. However, since the crop in the Z direction did not work, due to the presence of a bug in the code, it was conducted manually, outside of the FLAIR interface. The original dimension was $481 \times 481 \times 481$ mm, reduced to $193 \times 121 \times 391$ mm after cropping, which was conducted in the slice tab. Next, the information tab was used to read the new dimension; the voxel tab was used to create a voxel geometry, and USBIN was used to cover the voxels. In total, two essential files were required to create the voxel card: material.inp and head.mat. The head file contained information used as a conversion ramp that was essential for mapping the DICOM materials, and the material file contained the material compound card. After loading both files, FLAIR created voxel region numbers and organs, as well as a USBIN for the region to cover all the voxels. In the input card, two USBINs were used: one to record energy, and a second for the dose.

The DICOM series used in the simulation was very thin, and required a phantom to allow the interaction to be recorded. A phantom of water was created, and the Micro CT was implemented inside the phantom. A BEAMPOS card was used to control the position of the beam, and a FLOOD option was used to allow uniform fluence within the target, similar to isotopic distribution. A range of energies was used in this run, from 0.0175 MeV to 5.5 MeV. The range of the energies was calculated using the fluence in water taken from the article by Hugtenburg *et al.* (228). An EMFCUT card was used to control the energy level of the electrons to be included in the run. The first 23 runs of any electron energy below 10 KeV were not included, which meant that the simulation allowed the electrons to be included, as most of the electrons produced had energy of above 10 KeV. Due to this option, the simulation took a longer time to execute. The second 23 runs of electrons with energy below 11 MeV were not included, therefore the simulation did not contain any electrons produced from interaction with matter. The runs without electrons were faster and required less time to be produced. For example, the simulation of energy 2.5 MeV

with electrons took 33 hours to complete, with 32 CPU and using multi thread technology. In contrast, the same run without electrons took five hours to complete. Each run contained five cycles, in order to reduce the statistical uncertainty.

The aim of the simulation was to reduce the uncertainty to lower than 2%; this could be achieved by increasing the number of histories in each voxel. The spawn option was able to reduce the time, and to increase the histories number via simultaneous multiple runs, achievable using the multi-thread CPU technology. The first attempt was conducted using the Google Cloud Service to create a virtual machine with many CPU. However, due to the high costs involved, it was not possible to employ this method in the cloud. It was calculated that it was more cost effective to build a high-performance computer with 32 CPU and multi-thread technology, providing 64 threads, than to use cloud technology. Building a high-performance computer became the first option, due to the lockdown measures taken by the UK government during the COVID-19 pandemic. Furthermore, the Kuwait State government issued an emergency evacuation for all medical staff and students in the UK. The FLOOD option produced a uniform distribution within the radius of the beam, and to ensure that the uniformity was within the acceptance limit, a uniformity test was conducted. The setting of the uniformity test replaced the voxels from the DICOM CT with water, where the same simulation for 2 MeV energy would be run, taking into consideration the dominant one in the beam.

6.5 Results

The demand for high accuracy treatment to reduce the side effects of radiotherapy has increased in recent years, due to the advancement of treatment techniques and TPS. The new TPS can use a MC code, which outputs dose to medium, rather than dose to water, but there remains debate regarding the optimal mode for use. All of the techniques concerned raise the question, in a heterogenous area with micro-CT data, regarding whether interactions of varying energy levels differ from the current medical CT resolution, or if a correction is required.

In this study, the MC simulation provided high accuracy, but at the cost of a very long simulation time. The drawback of the long simulation time affected this project significantly, as many simulations were required. Furthermore, all of the simulations were required to have a statistical error of less than 2%. The first attempt was conducted using cloud technology provided by Google to deliver as many CPUs as possible, but this method was cost-inefficient, and thus was

not recommended for this project. The project required many simulations and trials to correct the error and experimental model, which would have cost thousands of pounds if cloud technology was used. Cloud technology might be employed in future if the cost is reduced, as no hardware is needed, which will be more cost effective for small radiotherapy units. However, the optimal option for this project was to build a supercomputer containing 32 CPUs with a multi-thread capacity to allow for 64 simultaneous, parallel simulations using spawn in FLAIR.

The MC simulation required a low uncertainty percentage to produce data that did not contain a high percentage of statistical error. Consequently, all of the simulations conducted by the project achieved an uncertainty of less than 2% by using spawn, and total uncertainty of less than 1%. It was essential to achieve the uncertainty target to rule out any statistical error in the result that may have affected the DVH. Within the FLAIR interface, the different spawns could be combined to produce one file containing all the histories of the spawns. Table 6.1 shows the uncertainty percentage of each run, with and without electrons.

Table 6.1: The uncertainty, FWHM, and resolution of each run, with and without electrons.

Energy (MeV) with electrons	Uncertainty	FWHM	Resolution	Energy (MeV) without electrons	Uncertainty	FWHM	Resolution
0.0175	3.00%	3.52%	4.36E-11	**0.0175**	2.97%	3.49%	
0.025	2.02%	2.37%	2.43E-10	**0.025**	2.05%	2.41%	2.47E-10
0.035	1.25%	1.47%	3.46E-10	**0.035**	1.28%	1.51%	3.57E-10
0.045	1.26%	1.48%	3.97E-10	**0.045**	1.31%	1.54%	4.11E-10
0.055	1.34%	1.58%	4.04E-10	**0.055**	1.42%	1.67%	4.25E-10
0.07	1.24%	1.45%	4.43E-10	**0.07**	1.56%	1.83%	4.18E-10
0.09	1.50%	1.76%	3.75E-10	**0.09**	1.64%	1.93%	4.07E-10
0.125	1.46%	1.71%	3.93E-10	**0.125**	1.61%	1.89%	4.31E-10
0.175	1.43%	1.68%	4.91E-10	**0.175**	1.60%	1.88%	5.54E-10
0.25	0.96%	1.13%	4.72E-10	**0.25**	1.18%	1.39%	5.88E-10
0.35	1.20%	1.41%	8.61E-10	**0.35**	1.77%	2.08%	3.56E-07
0.45	0.86%	1.02%	7.91E-10	**0.45**	1.52%	1.79%	1.40E-09
0.525	0.79%	0.92%	8.54E-10	**0.525**	1.56%	1.84%	1.70E-09
0.605	0.72%	0.85%	8.99E-10	**0.605**	1.61%	1.90%	2.01E-09
0.73	0.64%	0.76%	9.53E-10	**0.73**	1.69%	1.98%	2.45E-09
0.9	0.51%	0.60%	9.21E-10	**0.9**	1.59%	1.87%	2.87E-09
1.125	0.45%	0.53%	9.81E-10	**1.125**	1.68%	1.98%	3.66E-09
1.375	0.44%	0.51%	1.13E-09	**1.375**	1.67%	1.96%	4.32E-09
1.75	0.32%	0.37%	1.00E-09	**1.75**	1.69%	1.98%	5.32E-09
2.5	0.32%	0.38%	1.32E-09	**2.5**	1.71%	2.01%	6.89E-09
3.5	0.30%	0.35%	1.56E-09	**3.5**	1.61%	1.89%	8.27E-09
4.5	0.32%	0.38%	2.01E-09	**4.5**	1.58%	1.86%	9.75E-09
5.5	0.30%	0.35%	2.14E-09	**5.5**	1.60%	1.88%	1.14E-08
Sum	0.98%			**Sum**	1.65%		

Figure 6.7 presents the dose distribution produced using FLUKA. The FLUKA simulation produced files that were not compatible with MATLAB, and it was therefore necessary to convert them to ASCII format, which is readable in MATLAB. This conversion was conducted within the FLAIR interface. Each run produced two ASCII files, one for the dose and one for energy. Editing was then required to remove the headers and non-necessary information within the files. The removal of the header was conducted in the Linux command line for each file, after the header was cropped to make the files readable within MATLAB, which was the primary platform used for analysing the data discussed in this chapter. This was because there was significant information of

around nine million points in each file, and programmes such as Excel cannot handle this level of data without crashing.

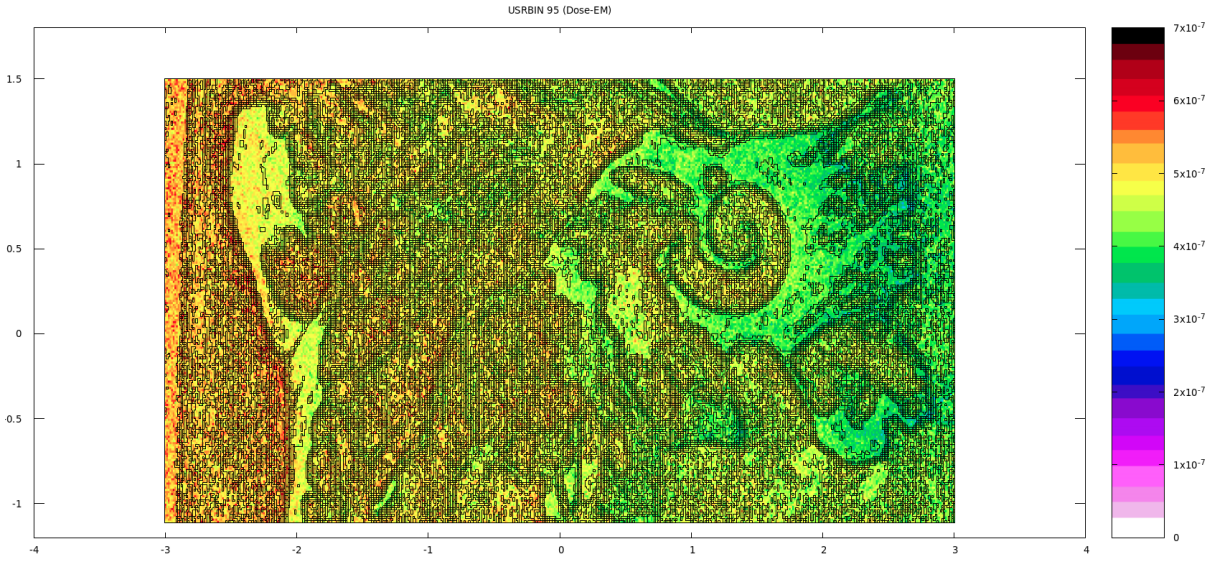

Figure 6.7: The FLUKA run and dose distribution in the target.

The first step was to ensure that the FLOOD option produced a uniform field within the target. The uniformity test files were loaded onto MATLAB, after which the line was taken from the middle in a different direction by fitting a quadratic polynomial to calculate the uniformity, as shown in Figure 6.8.

```
clear
files = dir('p*.asc');
numfiles = length(files);

for i=1:numfiles
    load(files(i).name);

end

photonDR1095=reshape (photon1095',1,[]);
photonDR1098=reshape (photon1098',1,[]);

test = reshape([photonDR1098 0 0 0],193,121,391);
figure(24);imshow(test(:,:,200),[]);

plot (test(:,60,200));
plot (squeeze (test(100,60,:)))
plot (squeeze (test(100,:,200)))
```

Figure 6.8: The code used to create a line through the water phantom to fit a polynomial curve.

The plot in Figure 6.9 displays a cross-section with a polynomial curve fit, with two points taken from the middle and edges. The test was conducted for both simulations concerned, namely with and without electrons. The polynomial equation was used, and the uniformity was found to be approximately 99% for both, indicating that the dose distribution was uniform within the target area. The uniform distribution of the dose was essential to mimic the VMAT distribution in the target area.

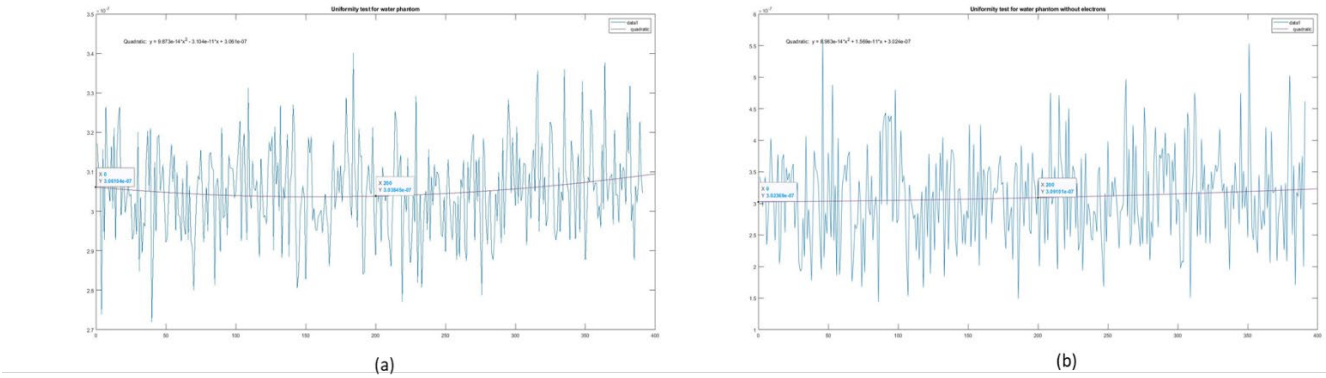

Figure 6.9: Plot of a cross-section of the water phantom with quadratic polynomials fit: (a) cross-section of simulation with electron interaction, (b) cross-section of simulation without electron interaction.

The uniformity test was conducted within the required limit, which facilitated the continuation to the next step. The next step involved the processing of the simulation data in MATLAB, the first element of which was to load all the files, a time-consuming process given the vast amount of data. Following this, the data was reshaped using a transpose reshape to create different graph types, taking into account the space dimension of the result. Each energy was then multiplied by a weighting factor to reveal the contribution of that energy to the total beam energy in the treatment situation. The weighted factor was calculated using the data from the energy distribution in water, as cited in Hugtenburg *et al.* (228). The weighted factor was calculated for three different field sizes: 10×10, 20×20, and 30×30. The last step totalled the energy, enabling the commencement of an analysis of the data.

A density histogram of the DICOM series Micro CT was created, as shown in Figure 6.10, which produced three distinct density areas. The highest peak, which covered the range from 0 to 1.25 g/cm^3, represented normal tissue (density of 1 g/cm^3 is water). The second peak started from

> 1.75 gm/cm^3, and was considered to be high density, such as compact bone. The third density ranged from 1.25 to 1.75 gm/cm^3, appeared with the micro-CT data, and denoted soft bone.

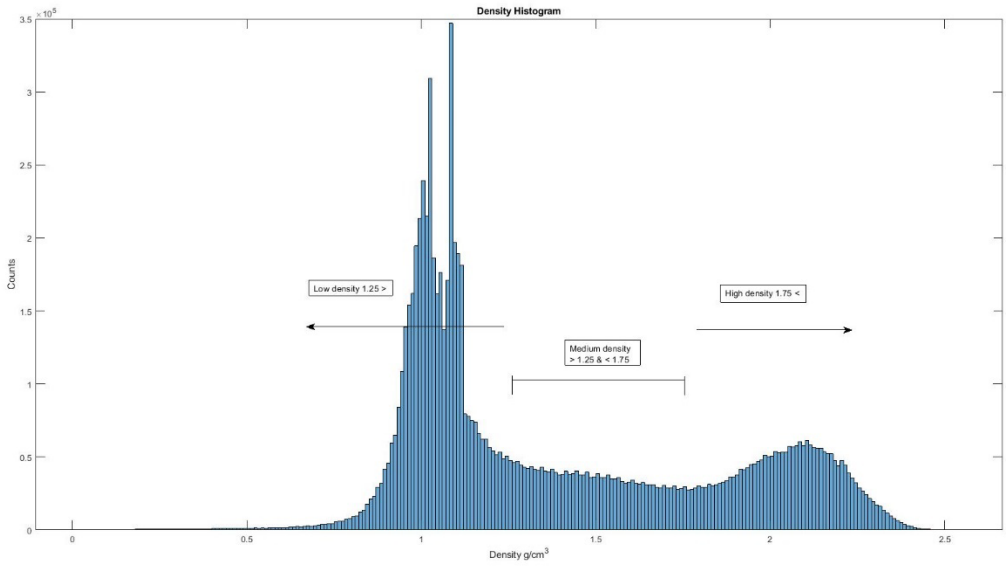

Figure 6.10: Histogram of the density of the DICOM series.

6.5.1 Individual beam energy

As mentioned previously, the simulations of the different energies were conducted in two scenarios: one with electrons, and one without electrons. The first step was to evaluate each energy level alone, in order to observe the effects of the heterogeneous micro level. A pattern was detected from the 23 energies chosen, and their behaviour in the Micro CT level occurred over three different field sizes: 10 × 10, 20 × 20, and 30 × 30 cm. From 0.025 MeV, the highest deposited energies were in the high density, then in the medium density. The deposit ratio began to change in the beam energy of 0.07 MeV, and the highest deposited area was of a high-density, followed by a low-density as the second most deposited area.

The second change in the pattern was present in the beam energy of 0.125 MeV: the low density received the highest ratio, followed by the high density, and then the medium density. After 0.45 MeV, the ratio of the dose deposition became similar, with the majority of the dose ratio deposited in the soft tissue, such as in the energy of 2.5 MeV, where the ratio of dose deposition was 55.2% for low energy, 19.66% for medium energy, and 25% for high density. Table 6.2 shows the change in the ratio level between the different densities.

Table 6.2: The dose distribution in the different energy levels.

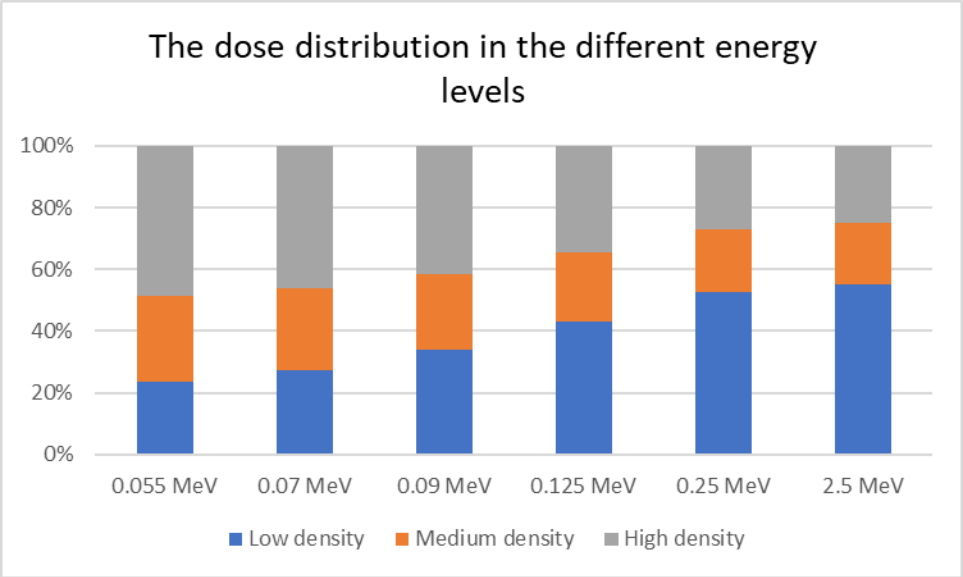

Figure 6.11 shows the individual beams' energy, and the behaviour of each beam towards the three density levels. The low energy, 0.045 MeV, showed higher dose counts in high density (49.26%) than in the low density (22.2%) and the medium density (28.3%). Furthermore, the separation between the low and high density dose deposition was clear: the dose peak in the soft tissue was 1e^-10, and in bone was 4.8e-10. The electron effects revealed low energy, and in this energy range the photoelectric effect was the dominant interaction. In the 0.07 MeV beam, the dose distribution peaks began to change in shape and become more Gaussian, but still revealed a similar outcome in the lower energy. Further, in the energy of 0.09 MeV, a shift in the disruption began to occur, as the higher dose counts began to build up in the low density (33.8%). Concurrently, there was a reduction in the dose counts of the medium density (24.65%) and the high density (41.55%). Alongside an increase in the beam energy, the shift was increasingly evident, with increased dose deposits in the soft tissue. The difference between the low-density curve and the high-density bone was almost 50%. This notable difference was due to the photoelectric effect, which was affected by the high Z materials, as shown in Figure 5.11(b).

In energy 0.125 MeV, the deposition of the dose was higher in the low density (42.9%) and the high density (34.59%). The high-energy individual beam had a similar shape and distribution, in terms of the dose, to the final sum of the beam. As shown in Figure 6.11, in the 2.5 MeV photon, the dose distribution showed a shift, namely a less deposited dose in the high Z material than in

the low-density material. The difference between the two was around 10%, due to the dominant Compton interaction in this energy level that was dependent upon the electron density. In terms of the percentage change between the dose deposition in the different energies and different densities, the soft bone dose deposition change was the smallest; there was a 26.9% change in the soft bone between the energy levels of 0.055 MeV to 2.5 MeV, compared with 48.28% in the hard bone, and 54.87% in the soft tissue.

(a)

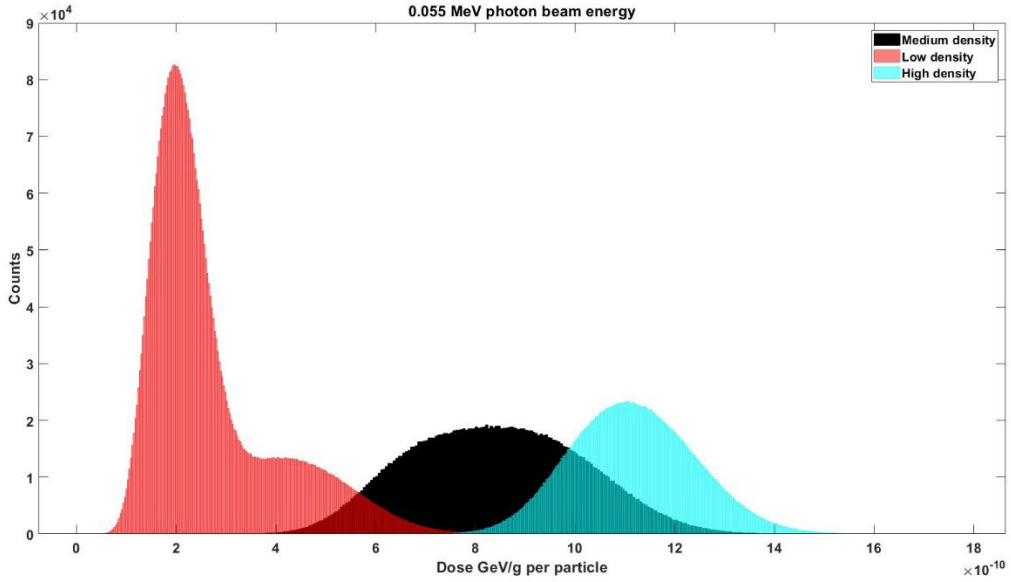

(b)

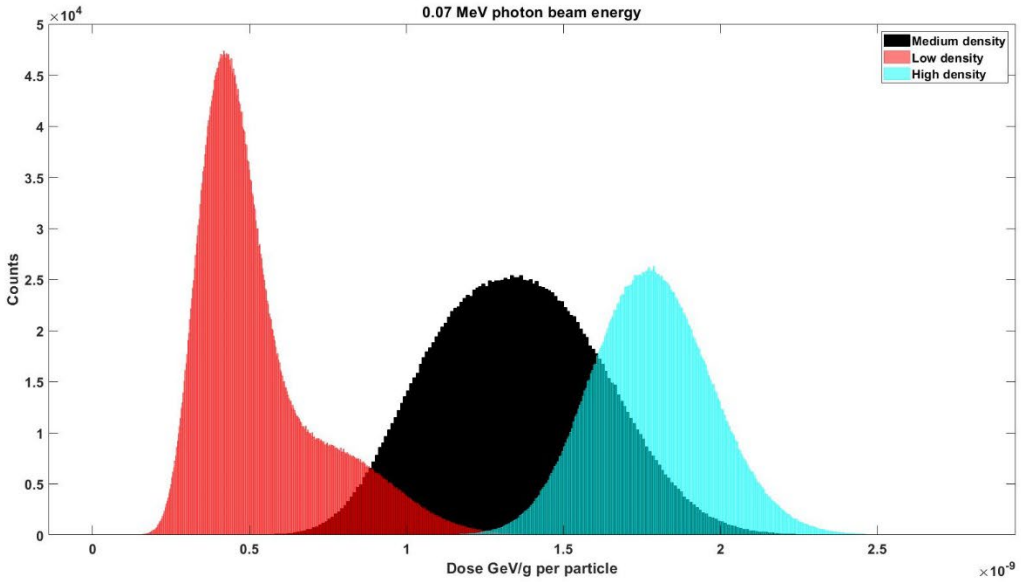

(c)

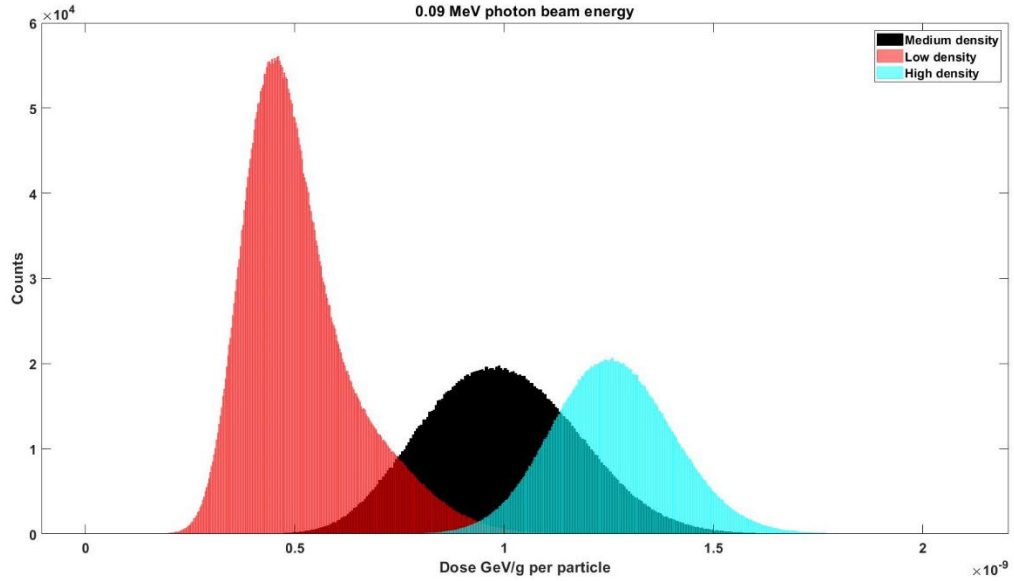
0.09 MeV photon beam energy
×10^4
Medium density
Low density
High density
Counts
Dose GeV/g per particle
×10^-9

(d)

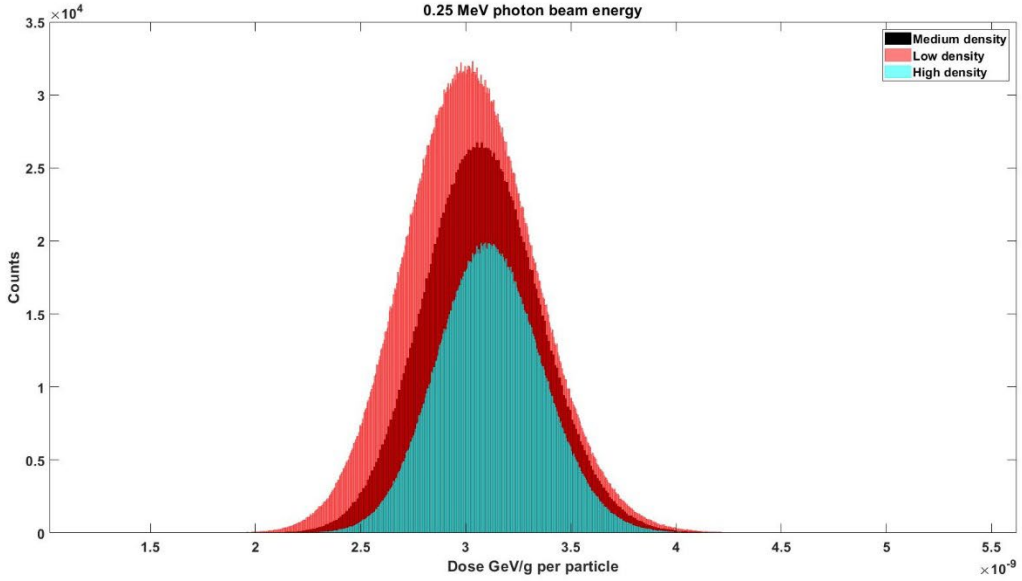
0.25 MeV photon beam energy
×10^4
Medium density
Low density
High density
Counts
Dose GeV/g per particle
×10^-9

(e)

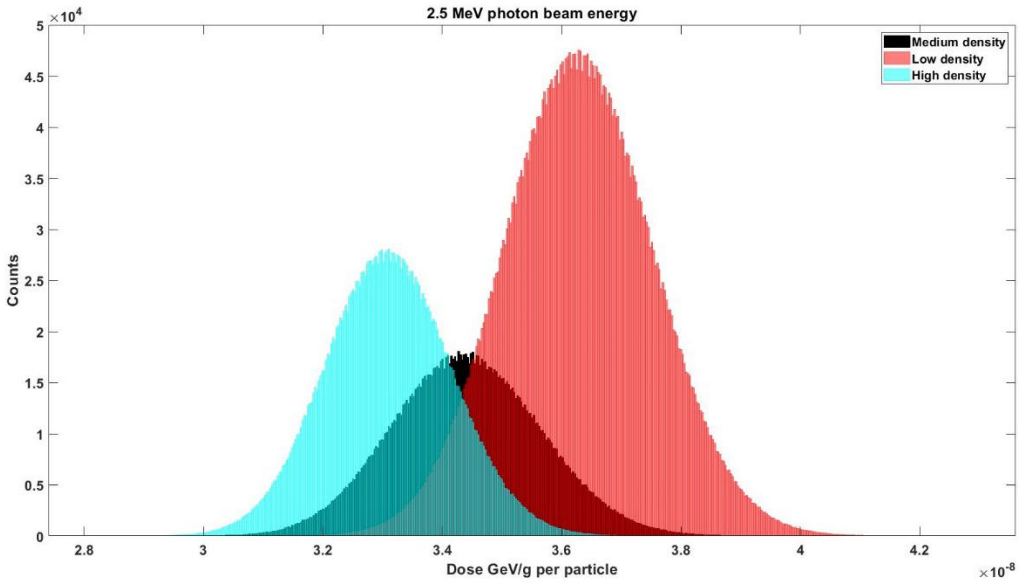

Figure 6.11: The different dose volume distribution levels in the Micro CT heterogenous area: (a) 0.055 MeV photon energy, (b) 0.07 MeV photon energy, (c) 0.09 MeV photon energy, (d) 0.25 MeV photon energy, and (e) 2.5 MeV photon energy.

6.5.2 Beam summation

Assessing individual energy levels provides the means by which the dose deposition in heterogeneous areas can be understood. Moreover, understanding the summation of energy level behaviour is essential for clinical work. The summation of all of the beams in both of the scenarios discussed above, with the addition of the separation of the three density levels, is provided in Figure 6.12(a), while Figure 6.12(b) presents the final sum of all of the simulated beam energies, without electrons overlaps, covering a dose range from $1.76\ e^{-7}$to $2.925e^{-7}$GeV/g for the low-density tissue.

The low-density tissue had the broadest range of all three densities; the dose range of the high density was between $1.857e^{-7}$to $2.634e^{-7}$GeV/g. However, while the majority of the primary doses were deposited in the low-density tissue, a high percentage of the count was located in the high-density area. Further, the middle range density received the lowest dose when the simulation contained only the primary photons, and cut off the electrons. Figure 6.12(b) shows the sum of the beam energies with electrons, illustrating the distinction between the deposit of energy of the three-density range, namely they did not overlap. In addition, there was a noticeable increase in the low-density counts, a result of the inclusion of electrons, and a decrease in the high density counts. The

medium density count changes were not significant when electrons were added. The change in the top of the peak value in the high and low densities was an indication of the electron transport effect in a heterogeneous area. The difference in the dose distribution between the low density and the high density was around 10%, which was similar to the single beam of 2.5 MeV. In the high energy, the pattern did not change significantly, due to the dominant interaction in this energy range the Compton interaction.

(a)

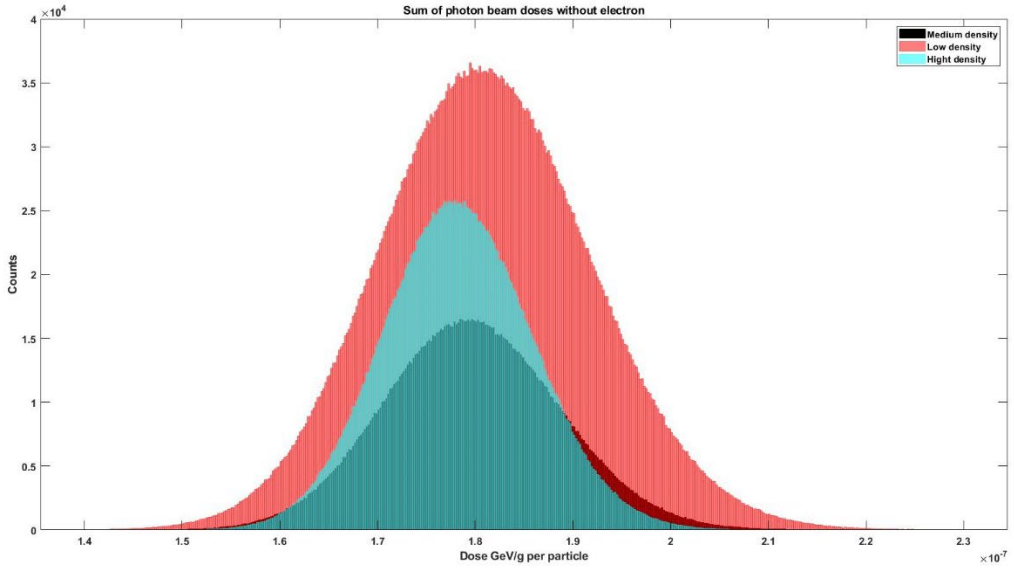

(b)

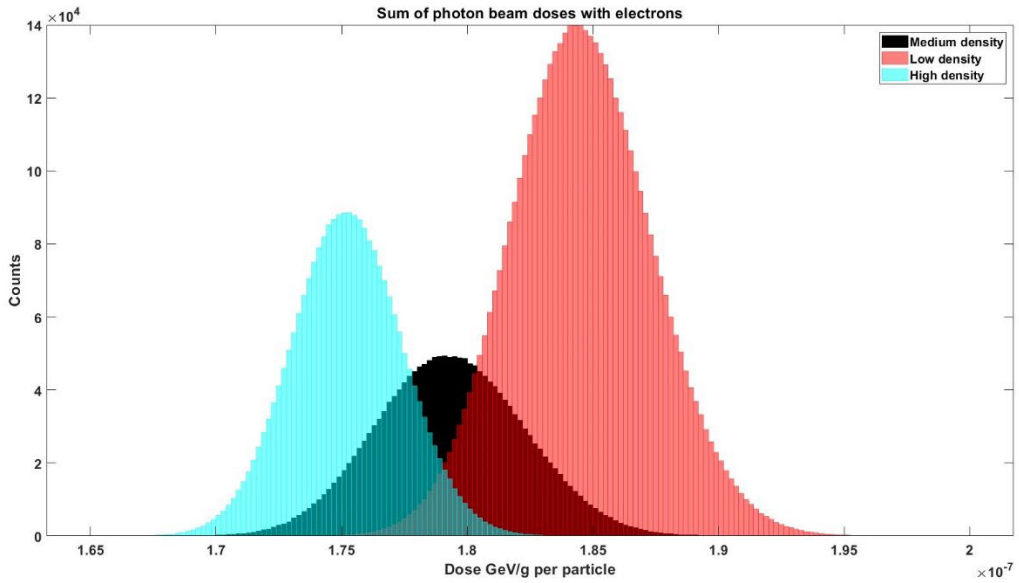

Figure 6.12: Sum of the photon beam energies, with three divisions of density levels (a), including the sum of the photon beam with and without electrons (b).

The assessment of these graphs provided a means by which the effect of the heterogeneous area in dose distribution could be understood, analysing a relative dose-to-dose distribution revealed more information. Table 6.3 shows the calculation of the FWHM related to the dose for a sum of the beam energies. The FWHM fraction of the dose for the simulation without electrons was wider than the fraction with electrons, and the distribution around the target area was uniform, as shown in Figure 6.9 for both simulations. However, the starting condition and scatters were not a proportion of the density. The HU was not equal, even to an area with a high-density region, like the cochlea. In terms of the total energy with electrons, the highest FHWM was for the medium density area, which cannot be detected in the standard CT resolution used in radiotherapy. The electrons in the simulation worked as a filter for the outliers in the beam energies that were evident when compared with the simulation without electrons.

Table 6.3: The FHWM of the total of the beam energies, with and without electrons.

File	Mean value	Relative mean	SD	FWHM	Relative FWHM	FWHM fraction of dose
Final sum with electron	2.29E-07		8.09E-09	1.90E-08		0.083
Low density	2.35E-07	1.028	3.79E-09	8.91E-09	0.469	0.038
Medium density	2.25E-07	0.985	4.21E-09	9.89E-09	0.520	0.044
High density	2.19E-07	0.955	2.80E-09	6.59E-09	0.347	0.030
Final sum without electron	2.28E-07		1.36E-08	3.19E-08		0.140
Low density	2.31E-07	1.013	1.48E-08	3.47E-08	1.085	0.150
Medium density	2.26E-07	0.993	1.21E-08	2.85E-08	0.892	0.126
High density	2.23E-07	0.979	1.02E-08	2.40E-08	0.750	0.108

6.6 Discussion

It was not a straightforward task to analyse the data produced for this project, because a micro-CT data provides more details than a clinical CT. Furthermore, previous studies regarding the effect of the heterogeneous area in dose deposition, and the difference between the results of dose to medium and dose to water, primarily used phantom or medical CT. Medical CT records the temporal bone area as hard bone, soft tissue, and air, as in the study by Radojcic *et al* (224). However, anatomical details were missing in a clinical CT resolution, as seen in the results, and soft bone is not detectable in the clinical CT resolution. The high resolution of the Micro CT introduces a more detailed and distinguishable density between the cortical bone and soft bone, which contains the red marrow cells that are considered to be sensitive to radiation (229). One of the limitations of this is that the Micro CT of the temporal bone does not contain air, due to the injection of gel that has a density of water; however, there is a small area in the DICOM that contains air, and is used in the calculation of the HU scale.

The photoelectric effect is the dominant interaction in low-level energy. In the present study, the increased dose in the high density and medium density, which was considered to be bone material, may have been due to the photoelectric effect that increases with higher density materials. The high heterogeneous area with irregularities in soft bone and hard bone shape increases the dose to the edge, revealing a higher deposition in a high-density area. However, the contribution of the low-level energy to the total beam was small compared with the higher level

energies, and the build-up factor in the low energy level was negligible. The build-up factor decreases with the increase of the material density for any depth penetration in energies of 1.5 MeV and lower (230). The beam energy increased, and the dominant interaction shifted to Compton scatter, which does not correlate with density. The low-density tissue, which in a real scenario is considered to be the white or grey matter of the brain, received a higher dose than the bones, yet there remained the presence of deposited dose in the high density areas, including the cochlea, a site that is sensitive after chemotherapy. Furthermore, the build-up factor in the low z material, such as the white and grey matter, was high in terms of energy level to the extent that a Compton scatter was the dominant interaction. The build-up factor contributed to the dose in the soft tissue when increasing the energy level. The soft bone containing red marrow cells received a dose that did not change significantly, even with increases in energy levels. The density level of the soft bone is not distinguished in a medical CT, and the dose received is ignored.

The results of the project discussed in this chapter demonstrated that the high energy dominated the behaviour of the treatment beam. Furthermore, the behaviour of the dose distribution started to shift from 0.125 MeV, and the soft tissue dose deposition did not change significantly. These result can be used as a base to connect to different modalities, for example radiotherapy treatment using VMAT and Gamma Knife. The next chapter tests the effect of the findings of this chapter on the clinical routine.

6.7 Conclusion

The study of the behaviour of the dose distribution in the micro-level heterogeneous area can contribute to the creation of a treatment plan with lower toxicity levels in the inner ear and cochlea. The use of a micro-CT data introduced a normal tissue, soft bone and hard bone rather than a normal tissue and hard bone, as medical CTs showed. The soft bone contains sensitive cells that can be damaged by high radiation exposure. A Monte Carlo FLUKA used with FLOOD option was used to allow uniform fluence within the target, similar to isotopic distribution. The photoelectric effect in low energy beams did not add a significant dose to the soft bone, depositing most of the dose in a high-density bone. However, the weighting factor of the low energy was small, compared with that of the high energy. The relative dose to FWHM of the final sum beam showed that the highest rate between the three densities was the medium density that contained the soft bones. The findings of this project were not sufficient to answer whether the use of a

micro-CT data and a more accurate dose distribution algorithm would impact the clinical routine significantly. The next chapter addresses this question by focusing on the connection between the results of the dose distribution in MC, using a micro-CT data and a clinical routine.

Chapter 7: Connecting multiscale outcome with brain cancer VMAT treatment

7.1 Introduction

Cancers of the brain, head, and neck affect almost 12,000 people around the UK, annually. One type of brain tumour is known as glioma, and the rate of people diagnosed with gliomas in the UK has increased by 39% since the 1990s. Brain, head, and neck tumour treatment consists of surgery, chemotherapy, and radiotherapy (231). Improvements to treatment, and its effectiveness, has engendered increased survival rates: the survival rate between 1982 and 1986 was 52.7% for head and neck cancer, increasing to 65.9% between 2002 and 2006 (232). This improvement was due to multiple factors, including higher accuracy treatment in radiotherapy, and its combination with chemotherapy. The high accuracy delivery system of radiotherapy helps to increase the dose delivered to the tumour, without increasing the dose to the OAR (232). Radiotherapy is the standard care for most head, neck, and brain cancer cases. Understanding the limitations, and improving the accuracy of dose distribution in radiotherapy can help to provide a better quality of life for patients.

The treatment of head, neck, and brain cancers is complex, due to the number of OAR in the vicinity. Radiotherapy treatment can cause certain side effects, as it damages healthy tissue. Limiting the dose to different, normal tissues and organs can prevent permanent damage. For example, 50% of nasopharyngeal, and 53% of parotid gland cancer patients treated with radiotherapy develop sensorineural hearing loss (SNHL), due to the close proximity of the area affected to the cochlea, that causes an overdose to the cochlea (233). The cochlea is a small, bony part of the body located in the inner ear, with an average volume of 0.6 mL, and contains fluid to help transform the different levels of frequency into neural signals (234). Damaging the cochlea can cause hearing loss in one, or both, ears. Before exploring this matter in depth, it is necessary to understand the different toxicity scales, dose limitation to the cochlea, delineation setting, types of tumours that can cause hearing loss, and the chemotherapy that can affect such hearing loss.

7.2 Literature review

7.2.1 Hearing loss

The damage that causes hearing loss can be categorized as conductive hearing loss, SNHL, and a combination of conductive and sensorineural hearing loss. In conductive hearing loss, the damage occurs in the middle ear, and treatment is available, while SNHL affects the inner ear, and cannot be treated (235–237). To date, the process that causes SNHL has not been fully discovered, or supported with evidence. However, a pattern was noticed between the missing hair cells in the organ of Corti in a patient treated with radiotherapy (231, 232). A study by Oh *et al.* sought to identify the connection between the loss of hair cells in the organ of Corti, but was unable to support the claim as no functional hearing test was conducted on the patient concerned (239).

Having defined the categories of hearing loss, it is essential to understand the methodology that defines ototoxicity. The American speech-language-hearing association uses a threshold shift > 20 dB in one frequency, or 10 dB > at two or more frequencies. However, the standard terminology criteria version 4.03 uses threshold shift > 15 dB in at least two or more frequencies (240). The grading scale used in ototoxicity of 2 to 4 indicates severe or permanent damage (241). A follow-up study of 294 patients by was conducted 4.5 years after their final session of a radiotherapy course for nasopharyngeal carcinoma, and the study concluded that the participants' hearing loss continued to increase, even with extended follow-up (242). Furthermore, the study indicated that a short follow-up was not sufficient for assessing the damage to the patients' hearing after the radiotherapy treatment effectively and comprehensively (242). Increasing familiarity with the cochlea, ototoxicity, and different hearing tests can help with setting the thresholds required in contouring, and the dose limit to the cochlea.

7.2.2 Cochlea delineation and effect of chemotherapy

Delineation of the target and OAR is essential in any treatment plan. High delineation accuracy can reduce the side effect to healthy tissue, due to the radiation, and can increase the accuracy of the dosimetric dose calculated. Contouring a small size structure, such as the cochlea, with a high accuracy delineation, requires a small slice thickness of < 2.5 mm or less, a CT scan, and a proper level of bone window setting (230, 234, 236–238). Further, given the small size of the cochlea, the use of a dose-volume analysis is impractical, because of the limitation of the

cochlea's contouring. By using a dose-volume analysis, a mean dose can be ascertained to evaluate the dose to the cochlea (230, 234, 236–238). The dose limit to any structure is crucial, as it can decrease the side effects of radiation. However, many other factors can affect the dose limit, such as age and chemotherapy. In the case of hearing loss, the factors that can cause, or increase, the chance of hearing loss are cisplatin treatment, age, and radiation dose to the inner ear (233, 236, 238, 239).

Cisplatin is a treatment type that falls under the category of cytotoxic chemotherapy, and is combined with radiation therapy to treat different types of cancer, including head and neck cancer, brain cancer, oesophageal cancer, neuroblastoma, and lung cancer. One of the main side effects of cisplatin is ototoxicity, and it can cause damage to the hair cells and organ of Corti. Furthermore, combination treatment with radiotherapy can increase the chance of SNHL. In order to reduce the side effects of cisplatin, a protection agent, such as an antioxidant agent, can be used. However, the agents are ineffective when a high radiation dose is used with chemotherapy (233, 239). A phase III trial was conducted to evaluate the effect of chemoradiation therapy against radiation treatment alone on hearing loss for patients with a nasopharyngeal carcinoma (247). The trial demonstrated that the hearing loss percentage was higher in patients treated with chemoradiation than with radiotherapy alone. After the treatment plan, age is a pivotal factor in hearing loss, including SNHL, and most previous research agreed that children under the age of five, and elderly patients, face an increased risk (246). A group of patients aged under 45 who received a radiotherapy dose of 48.1 Gy showed a 50% risk of SNHL (245), while another group of patients aged 45 and above treated with a dose of 39.44 Gy showed an increase in the risk of SNHL of 64% (245). Due to the factors that impact the loss of hearing directly, different-dose limits must be established for children and adults treated with only radiotherapy or with chemoradiotherapy.

7.2.3 Dose limit to the cochlea

Currently, on-going research contests the dose limit to the cochlea, and different dose limits are recommended. The data gathered from 78 children treated with radiotherapy, and no cisplatin chemotherapy, showed that a mean dose of less than 35 Gy to the cochlea should minimize the risk of hearing loss within five years of follow-up (227, 241). For children treated with a combination of radiotherapy and cisplatin, the dose limit to the cochlea suggested is less than 10

Gy (227, 241, 242). In an adult, the dose limit suggested differs according to centre, and there is currently no universal agreement concerning the dose limit to the cochlea. However, many studies agreed that doses of higher than 45 Gy cause acute hearing loss, without cisplatin agents (227, 230, 234, 237, 238). For example, Pan *et al*. conducted a study of 31 adult patients diagnosed with head and neck cancer, and treated only with radiotherapy. The patient dose was >45 Gy, and all of the patients were diagnosed with hearing loss (250). Meanwhile, Van der Putten *et al*. recommended that doses of higher than 45 Gy should be avoided, supporting this claim with data gathered from 52 patients treated only with radiotherapy, who were all diagnosed with SNHL (241, 244). The study conducted by Vieira *et al*. concluded that any dose to the cochlea of below 40 Gy caused very little hearing loss in patients treated only with radiotherapy, and that the threshold of a patient treated with cisplatin and radiotherapy was as low as 10 Gy (249). Moreover, Cheraghi *et al*. concluded that a dose of less than 30 Gy to the cochlea would hardly cause any hearing loss (245), and Bhandare *et al*. suggested that, in order to minimize damage to the cochlea, the dose administered should be below 35 Gy. Since there is currently insufficient data to create an SNHL threshold, it is therefore argued that the dose to the cochlea should be reduced as much as possible (243).

Lee *et al*. demonstrated that a 33.46 Gy mean dose to the inner ear produces tinnitus, another precursor to hearing loss (241). The study concluded that a dose of less than 32 Gy can minimize the side effect of grade two tinnitus, or higher, to less than 20%, and that a dose of below 46 Gy can reduce SNHL to 50%, which is still considered to be a high percentage. Meanwhile, Mosleh-Shirazi *et al*. concluded that there is no statistically significant difference in hearing loss between patients treated with chemotherapy and patients treated without chemotherapy (236). However, the follow-up in this study was brief; it was conducted 30 days after the treatment, and employed a CT slice thickness of 3 mm, which was higher than the 2.5 mm recommended, to create the delineation of the cochlea. Indeed, many previous studies conducted a follow-up after only a short period of time, which is insufficient when studying the long-term effects of radiation in the inner ear that are likely to cause hearing loss. Since hearing loss can occur as long as five years after treatment, the follow-up period recommended is two to four years (226, 233, 242). A phase two study of 45 children diagnosed with medulloblastoma, and treated with proton therapy, found that there were no hearing problems at the baseline of their hearing test. However, three

years following their treatment, 12% hearing loss was observed in the children, a figure that increased to 16% at five years following their treatment (252).

Although there is sufficient evidence that radiation, with or without cisplatin, can cause hearing loss that affects patients' quality of life, particularly that of younger patients, in the standard daily routine of radiotherapy, there is no dose constraint to the cochlea; this does not help to avoid SNHL (226, 246). In most of the extant literature, the hearing loss concerned was found to occur primarily in the high-frequency range located in the basal area of the cochlea. The high frequency range starts at 2000 Hz, and is essential for speech discrimination and accurate speech analyses (237, 238, 241, 246). A possible explanation for the sensitivity of the high-frequency area in the cochlea is that there are three outer cells in a row on the basal area, compared with four outer cells in a row in the low-frequency area (247).

The factors discussed above, and the threshold of the cochlea, are essential for establishing sufficient knowledge to enable the investigation of different techniques for reducing the possibility of SNHL and the rule of MC, in the improvement of the quality of life of the patient.

7.2.4 Treatment techniques for treating head, neck, and brain tumours

Many existing techniques, such as IMRT, VMAT, and proton therapy, can treat head, neck, and brain cancer, each of which has unique characteristics. In the case of the cochlea, it is important to compare between different techniques, in order to reduce the dose as much as possible, without compromising the dose to the target. An example of this can be seen in a medulloblastoma patient who suffered from hearing problems after receiving radiotherapy treatment, due to the radiation exposure to the cochlea (249,254). In the past, a two parallel lateral field beam plan was used for radiating posterior fossa, after which 64% of patients developed ototoxicity at grades 3 and 4. More advanced techniques have been used in recent years, including IMRT, VMAT, and proton therapy (255). The data gathered from 29 patients treated with three-dimensional conformal radiation therapy reported that 51% of them developed SNHL, with the follow-up study conducted six months after the treatment (245). In another study, nine patients received a Cisplatin, and 77% developed an SNHL; the dose for the chemoradiation group was 30.7 Gy, and for the remaining patients was 51 Gy (245). The study concluded that the cochlea can increase tolerance up to 50 Gy, however, it did not provide details regarding the CT slice thickness, and the follow-up period was short.

The dose given to patients can be reduced by using more advanced techniques, such as IMRT or VMAT. Many previous studies reported a high percentage of SNHL when using 2D or 3D radiotherapy treatment. In the case of parotid cancer, a 43% incidence of SNHL was recorded when using 3D, and in other studies, the incidence reached 85% with the use of chemotherapy (256). Meanwhile, IMRT has a lower incidence rate of SNHL, at 16% (256). These incidence reports suggested that the use of IMRT can reduce the dose to the cochlea. However, Hitchcock *et al*. noted a limitation of IMRT, namely that it engenders a higher mean dose to the cochlea than 3D conformal treatment, as no dose constraints are used in the cochlea (253). A study of 15 patients diagnosed with medulloblastoma conducted by the Texas children's hospital revealed a 13% incidence of SNHL after IMRT treatment, although the 11 patients treated with conventional RT showed a 64% incidence (249). The study did not mention whether a chemotherapy treatment was used, or if a special sparing treatment in proton therapy was employed in the treatment plan.

Meanwhile, the multi-centre trial COSTAR investigated the sparing of the cochlea in a patients diagnosed with parotid cancer by comparing IMRT and conventional radiotherapy with the aim of reducing hearing loss (257). The treatment consisted of 65 Gy doses in 30 fractions, and the median dose to the cochlea was 56.2 Gy in 3D-CRT, and 35.7 Gy in IMRT. The follow-up was designed for 60 months, and although most of the patients involved did not complete the process, 12 months after the last fraction 39% of the 3D-CRT patients were found to have developed SNHL, as had 35% of the IMRT patients. The study concluded that there was no clinically significant difference between the two techniques. In the COSTAR trial, the cochlea tolerance used was 40 Gy to 45 Gy, a high figure, and it has been argued that these levels can still lead to the development of SNHL. Furthermore, the trial did not mention if the patients used any chemotherapy; patients treated with a combination of chemoradiation must receive a lower threshold dose to the cochlea. The cochlea is close to the PTV in parotid cancer, which engenders a 50 Gy dose to the cochlea (257), and a 3 mm addition to the margin to cover any uncertainty can increase the dose to the cochlea further. Use of the MC simulation can help to reduce the uncertainty and increase the accuracy of the dose, which can cause a smaller margin to be used. When there is a close range between the PTV and the cochlea, proton therapy can play a major role in reducing the dose to the cochlea, given the advantage of the Bragg peak.

Only a small number of previous studies compared advanced techniques, such as VMAT or proton therapy, with MRI Linac that uses VMAT or IMRT, although without exploring their

full potential. For example, Ali *et al*. compared the dose to the cochlea when using two different techniques, IMRT and VMAT, using a slice thickness of 3 mm, which is not considered to be optimal for contouring the cochlea (258). The dose to the cochlea when using VMAT was found to be 16.7 Gy, while it was 17.9 Gy when using IMRT. While there was therefore no clinically significant difference between the doses, the reduction of the monitor unit (MU) revealed a significant difference between VMAT 465 MU and IMRT 1228 MU. Furthermore, the treatment time for the VMAT was 2.89 minutes, compared with 7.13 minutes for the IMRT; a reduction in time can reduce the motion uncertainty of the patients (165). The combination of VMAT and MC can reduce the dose further, by lowering the uncertainty involved in treatment planning.

Another comparison of VMAT and IMRT was conducted by Gao *et al*., who found that both plans delivered a high dose to the cochlea of patients treated for nasopharyngeal carcinoma: 47.8 Gy for the IMRT and 43.8 Gy for the VMAT (259). The 2.5 mm used by the study increased the accuracy in contouring the cochlea and the other OAR, helping to provide a more accurate dosimetric outcome. The differences occurred in the monitor units and the delivery time, supporting the finding of Ali *et al.* (258), with the VMAT delivering 15% less in terms of monitor units and 56% less in treatment time (259). The study did not mention that hearing tests were conducted with the patients involved, or whether any constraints were used in the cochlea, because the dose delivered was high, and the advantages of using IMRT or VMAT cannot be fully utilized without the use of dose constraints in the cochlea.

The use of a proper constraint for the cochlea, and increasing the accuracy as much as possible via advanced techniques like MC, can create a more accurate treatment plan to help to avoid SNHL. Further investigation is required to evaluate whether the proton therapy outperforms the VMAT and IMRT, in terms of reducing the dose to the cochlea for both patients treated with chemoradiotherapy and those treated with radiotherapy alone. The evaluation should include an assessment of whether the difference is clinically significant, due to the high cost of proton therapy, and the lack of availability of the proton centres.

The study by Zhang *et al*, attempted to minimize the dose to the cochlea by employing tighter constraints, and by increasing the protective weight (237). The result was a reduction of the dose to the cochlea by 23%. Furthermore, the study attempted to divide the cochlea between the high and low region dose, to reduce the dose to the cochlea as much as possible. A reduction of the dose to the cochlea was noticeable after the division, as a higher constraint was used in high

dose area. In order to divide the cochlea into two regions, a slice thickness must be below 2.5 mm, and should be fused with an MRI to ensure the accuracy of the delineation. However, the accuracy of the contouring of the high and low areas in the cochlea is questionable, given of the small volume of this area. Furthermore, dividing the cochlea into two regions is insufficient if the treatment plan has a low accuracy, particularly in the head and neck regions, which are considered to be highly heterogenous. While the division of the cochlea was a promising approach, the study did not cover the protocol necessary to achieve this. A better form of division would be to mark the high-frequency region as a low dose region, given its higher radiation sensitivity; alternatively, the low-frequency region might be used as an area of high radiation. Through this approach, a higher area of the cochlea might be spared from the radiation and chemotherapy.

For the cochlea of medulloblastoma patients, proton therapy can deliver a dose that is 25% lower than that prescribed, compared with 75% of the dose prescribed when using 3D RT (233). However, the comparison is imbalanced between the two modalities, because IMRT or VMAT can reduce the dose further than 3D RT. Moreover, the percentage of the proton therapy dose to the cochlea can be reduced further by increasing the accuracy of the treatment planning by using MC to overcome the uncertainty of the proton range, due to multi coulomb scatter. In their study, Paulino *et al*. compared between passive scattering proton treatment and IMRT in 84 patients treated for medulloblastoma. The median follow-up for the audiogram was 66 months, which is considered to be a medium- to long-range follow-up. The mean dose to the left ear for the proton therapy was 31.6 ± 8.5 Gy, while for the photon it was 37.5 ± 5.8 Gy (255). For the right ear, the corresponding figure was 31.4 ± 7.3 Gy, while it was 37 ± 5.1 Gy for the photon. While the proton therefore delivered a lower dose to the cochlea than the IMRT, the grade 3 and 4 ototoxicity was found to be at similar levels in both modalities (255). In total, 9.3% of the patients developed ototoxicity, while 9.9% developed ototoxicity when using the Brock system. The study concluded that proton therapy can spare other areas, such as the endocrine system, but in the case of the cochlea no significant difference was found in the development of grade 3 and 4 ototoxicity (255).

The location of the tumour is an important factor when selecting the technique that will spare the cochlea most. For example, in the case of low-grade gliomas, proton therapy can provide an advantage in sparing the cochlea, while IMRT can spare the cochlea by applying a tight constraint. While a low dose path has been recorded in the beam directions (260), the study by Paulino *et al* (255). found that there was no significant difference in the percentage of hearing loss

between the two modalities. However, passive scattering proton therapy is not the latest proton therapy; techniques such as scanning beam proton therapy and IMPT also exist, with varying benefits. In passive scattering proton therapy, cochlear sparing is not implemented, while the scanning beam can apply cochlear sparing techniques. A comparison of the sparing technique of IMRT with a passive scatter proton therapy, which does not have a sparing model, is unbalanced, and does not show the full benefit of proton therapy. One way to reduce the dose to the cochlea is to choose the optimal technique for delivering the treatment. According to previous studies, proton therapy is a promising modality that can spare the cochlea, while VMAT produces the same outcome, also sparing the cochlea. Further investigation is required to determine which is the best treatment technique for avoiding a high dose to the cochlea. Most of the previous studies concluded that IMRT, VMAT, and proton therapy are superior to 3DRT, in terms of sparing the cochlea and other OAR in the areas affected by head and neck cancer. In order to enhance the technique, a high accuracy algorithm, like MC, should be selected to provide the best conversion option in the region, such as dose to water, or dose to medium.

7.2.5 TPS compared with MC in brain, head, and neck cases

While MC code is considered to be the most accurate simulation in radiotherapy, its long simulation time, and the computer power required for one simulation are drawbacks for the daily use of the treatment. Nevertheless, MC can be used to create a model, or to understand the effect of heterogenous area in the dose delivered to a target. The study by Onizuka *et al.* found that there was a 7% dose difference between TPS and MC when using VMAT and IMRT (152); the significant difference in the head and neck dose between TPS and MC was due to the air cavity and bone within the soft tissue. While the study calculated the dose difference between TPS and MC in the field of treatment planning, some of the OAR were located outside the treatment planning field, which may have caused an overestimation or underestimation of the dose to that organ.

The study by Shine *et al.* evaluated the accuracy of TPS in an area out of the treatment plan, demonstrating that TPS underestimated the dose in IMRT and VMAT for OAR located outside the field by 20-50% (162). Meanwhile, the study by Wang *et al.* explored dose distribution in actual cases of head and neck cancer treated using the IMRT technique (261). The DVH comparison between the TPS and the MC demonstrated that there was a maximum difference of

10% in the area of air cavities and bones. Furthermore, the MC showed that the target was underdosed, compared with the TPS. The study did not use the latest technique of VMAT that is more desirable for head and neck cases, as discussed in the previous section. The MC demonstrated a higher accuracy than the TPS, but revealed a drawback in the increased length of time that was taken to simulate a treatment plan. The use of the MC in complicated cases is therefore one means of increasing the accuracy of the TPS.

In recent years, some TPS have contained a light version of a MC simulation that is able calculate the plan within an acceptable timeframe. However, the new TPS that contains MC is not widely available in radiotherapy treatment centres. Furthermore, the TPS that uses MC operates on a dose to medium mode, as opposed to the traditional dose to water mode, which highlights a much-debated topic concerning this treatment regarding the best mode of use. The second aspect of the treatment that engenders increased accuracy is the selection of the most suitable mode in an area with high heterogeneity. As discussed in Chapters 3 and 5, many previous studies demonstrated the significant dose difference between TPS and MC in heterogenous areas. However, none of these cases used a multiscale model with micro-CT data to observe the effect of different density in brain cases, especially in the temporal bone and cochlea.

7.3 Objective

The project discussed in this chapter applied the previous result, discussed in Chapter 6, to the clinical environment, in order to compare the TPS and MC using micro-CT data. The comparison helped to evaluate the difference in the dose distribution, in order to reduce the uncertainty in the dose distribution in the heterogeneous areas in the brain. Applying the result to different scenarios using an advanced model mimicked the clinical routine that enabled a comparison of the dose distribution to the cochlea.

7.4 Method

The cochlea model created in the previous chapter constituted a basic model. The intention of the model was to facilitate the study of a different scenario at the micro-level by using a depth of 15 cm that increased the scatter events. The simulation involved was executed using small beam energy boundaries to record each change in each energy level accurately. While the results

obtained from the basic model could be used to study more complex models, it could not be used in the clinical environment, due to different in-depth dimensions and scatter events involved. Therefore, a more complex model was required to apply the MC Micro CT simulation results to the clinical environment and other modalities, such as Gamma Knife. The complex model would help to calculate the normal tissue complication probability (NTCP) for the cochlea, using micro-CT data in a MC simulation.

The current Southwest Wales cancer centre protocol for treating brain tumours consists of VMAT, with either a non-coplanar arc or a coplanar arc. The location and size of the tumour affect the plan chosen. There are two cochlea delineations, one the real cochlea fit, and the second which increases the size by 5 mm in all directions to overcome any uncertainty. It was important that the complex model designed included the primary beam of the VMAT and scatter events that reached the cochlea. Furthermore, the distance between the PTV and the beam differs in each beam location and patient. Considering all the variables in the VMAT, a fixed universal model was challenging to achieve, but a semi-universal model could be created.

7.4.1 Model

The advanced model developed, based on the results of the basic model, consisted of two main parts. The first part was the primary, which covering approximately one-third of the arc, as seen in Figure 7.1. The field size used was 10×10 cm^2 at-depth 1.5 cm. The edge of the arc covered two-thirds of the beam, and the distance to the target was 15 cm. Adding these two main parts covered both the primary and scatter events to the cochlea. It was possible to extract a formula from the model to calculate the weighting factor used to obtain the dose to the cochlea in the clinical environment. The fluence data in a study by Hugtenburg *et al.* was used to calculate the weighted factor (228). The first step was to calculate the fluence of the model for each case separately using the following equation:

$$\frac{1}{3}(A)_{1.5\,cm} + \frac{2}{3}(B - C)_{15cm} \qquad (7.1)$$

A is the primary beam, which used a 10×10 cm^2 at a depth of 1.5 cm. B is the distance from the target to the arc at a depth of 15 cm. Finally, C is the distance between the target and

cochlea, at a depth of 15 cm. Data obtained from the cancer imaging archive was used to apply the advanced model to different scenarios.

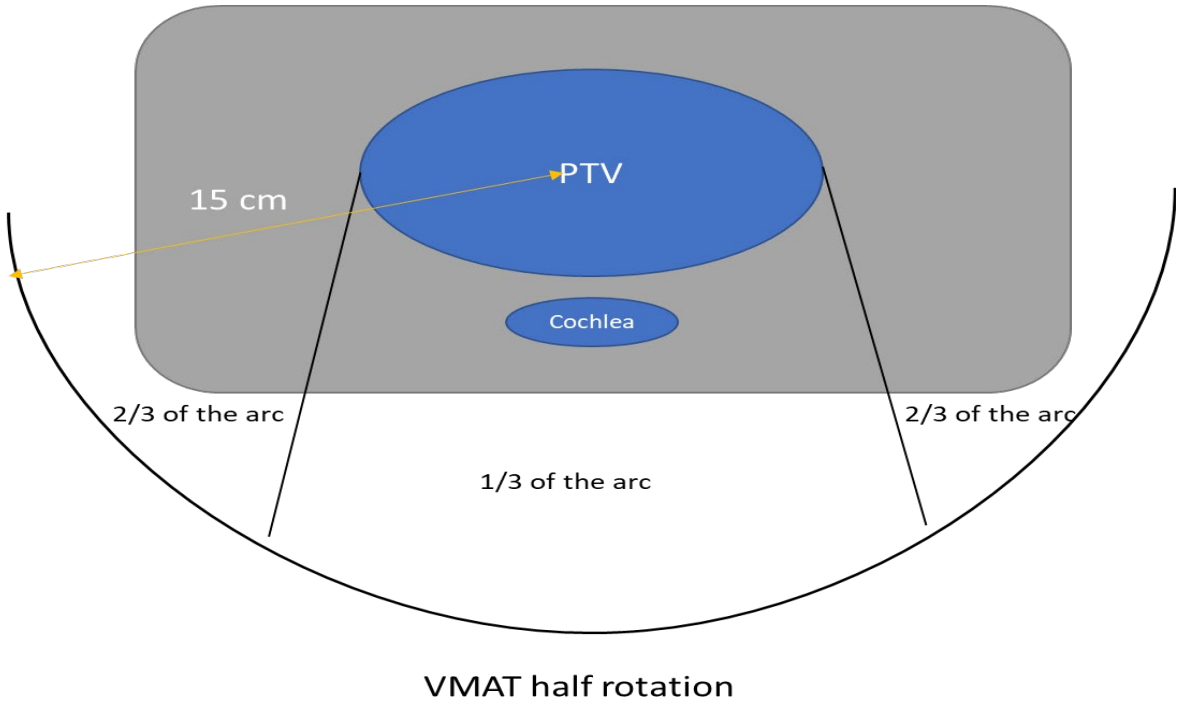

Figure 7.1: The advanced model.

7.4.2 Creating the treatment plan and processing technique

In total, 230 cases of glioblastoma and low-grade glioma were used to extract a different scenario to apply the result of MC in the clinical routine. A 3D slicer was used to calculate the distance in each case, and to record the volume of the target and cochlea. From the data, 11 different scenarios were founded, as shown in Table 7.1. The points from the different scenarios were applied to the equation, and energy fluences were calculated for each case.

Table 7.1: The 11 cases extracted from the data, with different scenarios and points for application to the advanced model equation.

		Points in the equation	
	A (cm)	B (cm)	C(cm)
Case 1	5.64	5.64	1.30
Case 2	5.64	11.28	1.30
Case 3	5.64	16.93	5.64
Case 4	5.64	11.28	5.64
Case 5	5.64	16.93	1.30
Case 6	5.64	16.93	11.30
Case 7	5.64	11.28	11.28
Case 8	5.64	22.57	1.30
Case 9	5.64	11.20	2.80
Case 10	5.64	16.93	2.80
Case 11	5.64	22.50	2.82

The next step was to apply fluence to calculate the weighting factors for each case. The weighted factor calculated was applied to MATLAB code. The result obtained from applying the weighted factors to the MC result was not sufficient to demonstrate the effect in a clinical routine, therefore it was necessary to create a DVH format to allow a better demonstration and connection with the clinical data. The DVH contained information concerning the minimum, maximum, and median doses. Furthermore, the DVH illustrated the dose distribution around the median dose. The more significant dispersion in the DVH was due to non-uniform dose distribution. The use of an MC flood technique showed a high uniformity of dose distribution (Figure 6.9). A DVH comparison could not be made without creating a treatment plan for each case. A Southwest Wales cancer centre protocol was used for the dose constraint in each case, and the protocol for a treatment plan at the centre was the protocol used for all of the cases. A coplanar arc was chosen for all of the cases with dose constraint, as shown in Table 7.2. An Eclipse system was used with an AAA to create all of the plans.

Table 7.2: Dose constraints used in the treatment plan.

ROI	Objective	Opt.	Man.
PTV			
	5400cGy		≥99%
	5700cGy		≥95%
	5940cGy		≥50%
	6060cGy		≤50%
	6300cGy		≤5%
	6420cGy		≤2%
Cord	Dmax		≤4600cGy
Brainstem	Dmax	≤5400cGy	≤6000cGy
Chiasm	Dmax	≤5000cGy	≤6000cGy
OpticNerve	Dmax	≤5000cGy	≤6000cGy
Eye	Dmax		≤4500cGy
Lens	Dmax		≤1000cGy
Hippocampus	Dmean	≤2500cGy	
Pituitary	Dmax	≤2500cGy	≤6000cGy
Cochlea	Dmax	≤2500cGy	≤5000cGy
External	6420cGy		≤1.8cm³

A DVH from a TPS was created and converted to a text format readable by MATLAB. The last step in processing the data was to create and compare both DVHs; this was not a straightforward task, given the different scales of both DVH. The intention was to rescale the MC result, and then to use the convolution theorem to create the DVH that combined both datasets. The final step was to compare the DVH obtained from the convolution theorem and the DVH from the TPS. Figure 7.2 illustrates the concept of the convolution theorem in creating the DVH.

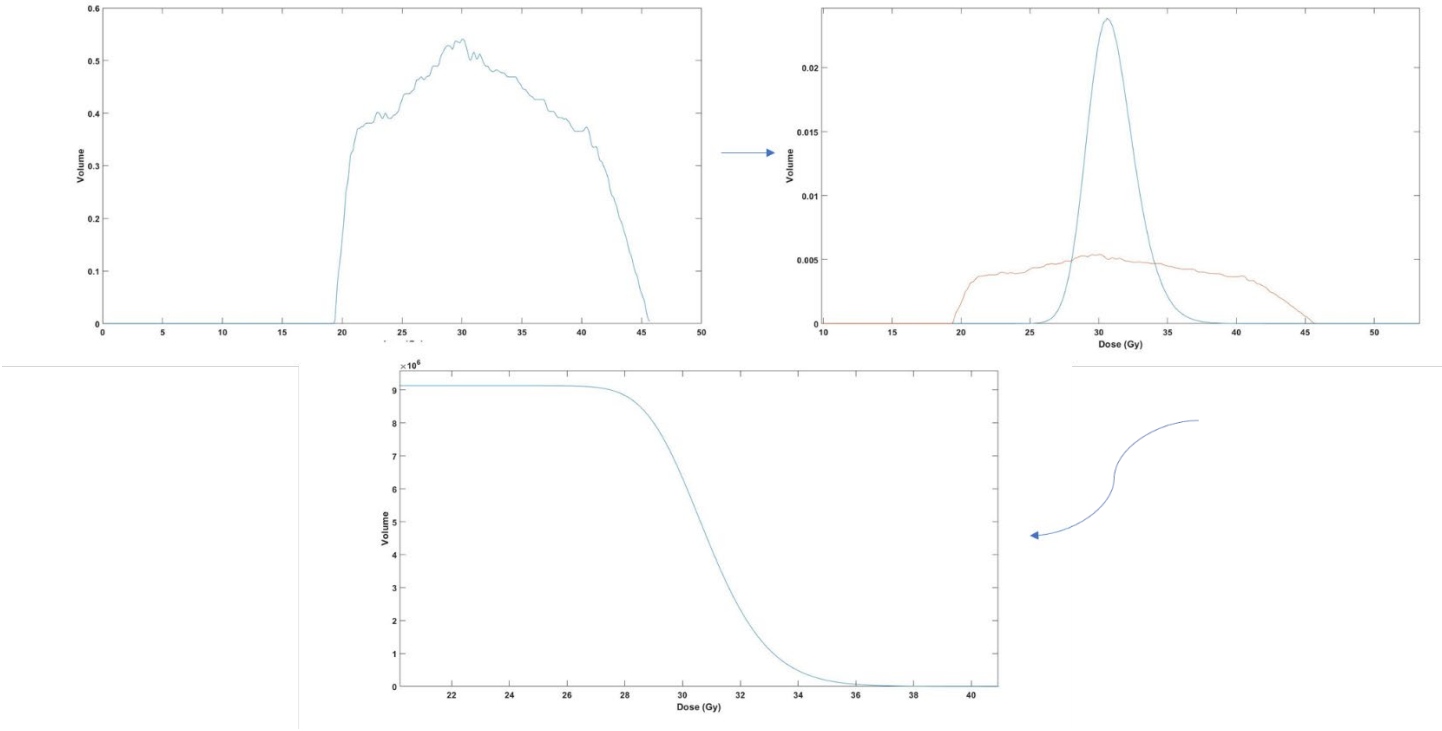

Figure 7.2: The process of creating the DVH using the convolution theorem.

The code used for creating the DVH is shown in Figure 7.3. The first step was to remove the headers from the DVH file, and then to load the file to MATLAB. The dose was represented in column one in the DVH file, and column three represented the volume. The second step was to plot the DVH using columns one and three, as seen in the first line of the code in Figure 7.3, then a gradient function was applied and plotted, but it was necessary to add a minus sign before the gradient in the plotting, because the result needed to be inverted. Next, a mean of the TPS was calculated for application in the MC DVH to rescale. Once both datasets had the same scale, a convolution function was used, as shown in the code. Finally, the new DVH was plotted using the code (r,sum(h)-cumsum(h)), and was converted to DVH format. The last few lines of the code plotted both the DVH of the TPS and modified the DVH for comparison.

```
load RC7.txt
plot (RC7(:,1),RC7(:,3)); % DVH of the treatment plan
gp17=gradient(RC7(:,3));
plot (RC7(:,1),-gp17);

mean = sum(RC7(:,1).*-gp17)/sum(-gp17);
[h r]=hist(finalsumEDW./finalsumDW*mean,0:0.1:120);
plot (r,h/9131020)
hold on
plot (RC7(:,1),-gp17/100);
c = conv(-gp17/100,h/9131020);
plot (-mean:0.1:((length(c)-1)*0.1-mean),c)
figure ; plot(r,sum(h)-cumsum(h))


plot (RC7(:,1),RC7(:,3)/100);
hold on
plot(-mean:0.1:((length(c)-1)*0.1-mean),sum(c)-cumsum(c))
```

Figure 7.3: MATLAB code for creating the DVH comparison, using convolution theorem.

7.4.3 Overview of NTCP modelling

Toxicity is one of the drawbacks of radiotherapy, and hearing loss and grade two tinnitus are two of the main toxicities caused by depositing a high dose to the cochlea. In order to evaluate and compare the calculated dose volume of the TPS with the MC simulation, in other words to quantify the clinically significant, it was necessary to calculate the NTCP for the cochlea and to use it as a biological endpoint parameter (262). The NTCP is a tool used to describe the probability of complication in an organ or structure, due to the use of radiation during treatment, and to the consideration of the specific biological cells of the structure (93). The Lyman-Kutcher Burman (LKB) model is used to calculate the NTCP for clinical cases, and was the primary model used in the extant literature. The LKB model was created through multiple steps, illustrating the difficulty possibilities for uniformly irradiated organ volume (262). Since the model was deemed to be incomplete, because the normal tissue was rarely uniformly irradiated, Kutcher and Burman proposed the conversion of the heterogeneous dose distribution into a uniform dose distribution (263). The proposal employed a DVH reduction algorithm that used an effective volume method. A new version of the LKB model created by combining both models is currently the most common model used to calculate the NTCP (264–266). The equation for the model is as follows:

$$NTCP = \frac{1}{\sqrt{2\pi}} \int_{-\infty}^{t} e^{\frac{-t^2}{2}} dt \qquad (7.2)$$

Where t is

$$\mathrm{t} = \frac{\mathrm{EUD} - \mathrm{D}_{50}(\mathrm{v})}{\mathrm{mD}_{50}(\mathrm{v})}$$

And

$$\mathrm{EUD} = \left[\frac{1}{\mathrm{N}} \sum_{\mathrm{i}=1}^{\mathrm{i}=\mathrm{N}} \mathrm{D}_{\mathrm{i}}^{1/\mathrm{n}}\right]^{\mathrm{n}}$$

In the model, the parameter equivalent uniform dose (EUD) is equivalent to a non-uniform dose distribution to the cochlea OAR. D50 is the tolerance dose for the whole organ, and v represents the partial volume fraction, with 50% of patients expected to experience toxicity within five years. The slops of the NTCP is m, and NTCP is a sigmoid curve. D_i, the volume effect parameter, represents the dose at voxel, and the total number of voxels is N. The volume effect parameter is represented as n.

7.4.4 Selecting of LKB model parameter

While the connection between tinnitus toxicity, SNHL, and radiation dose to the cochlea is well recognized, it is inadequately quantified (262)**.** The quantitative analyses of normal tissue effect in the clinic (QUANTEC) does not establish a guideline to avoid hearing loss or tinnitus. However, it recommends delivering a mean dose of less than 45 Gy to the cochlea to avoid after-treatment side effects (238, 258). Furthermore, there are currently no established specific NTCP parameters for the incidence of tinnitus toxicity and SNHL, an absence that causes a lack of current dose constraints to help in preventing high-grade tinnitus (241). The review of the extant literature produced only one set of parameters for grade two tinnitus, and two sets for SNHL. The study by Lee *et al.* addressed the NTCP model for grade two tinnitus, which was tested using various validation tools, such as the scaled Briere score that assesses the difference in the score between the prediction and the actual outcome (241). The validation and calibration of the NTCP model were found to be within the expected ranges, and the NTCP model was designed with a 95% confidence interval. The study used two tolerance dose (TD20%) and TD50% in the NTCP model,

concluding that in order to retain grade two tinnitus <20%, the dose should be below 32 Gy, and for <50%, the dose should be below 46 Gy (241).

As mentioned previously, in QUANTEC the recommended dose for avoiding SNHL is below 45, which is the dose constraint used in most centres. In the extant literature, the constraint recommended was between 45 and 70Gy. The parameter set by Lee *et al.* was used in this project, with minor modifications: the 32 Gy was used to evaluate the tinnitus, and 46 Gy for SNHL was used (241). One of the obstacles in creating the NTCP model was the small cochlea volume and the constraints related to its delineation. The LKB uses a dose-volume analysis that previous research demonstrated is unsuitable for the cochlea (241,243). The mean dose should replace the dose-volume relation when creating the NTCP; as shown in Table 7.3, the value used for a by the present study was one. A value is extracted from the observed dose-response data, and the model uses the mean dose if it is used as a value (245). One of the reasons the model developed by Lee *et al.* was chosen for this study was because it used the mean dose, rather than the dose-volume analysis, providing more accurate results (241). While the study by Cheraghi *et al.* tested different NTCP models for the cochlea, the only model involved that was selected for the present study was LKB (259). Therefore, in total, two models were chosen (Table 7.3). Although the first model employed a dose-volume analysis, which a number of previous studies noted is not best suited for the cochlea, this study used the model to validate the use of the mean dose, in order to produce a more accurate outcome than a dose-volume analysis in the cochlea. The second model used the resulting mean dose, but the TD50% was higher than the constraint used in the plan created, and modifications were added, namely 45 Gy, rather than 51 Gy, was used (245).

Table 7.3: The four NTCP models chosen for the endpoint of tinnitus and SNHL.

LKB model parameter	Endpoint	Reference
TD20%= 32.82, m= 0.35, a=1	2+ tinnitus	Lee *et al.* (241)
TD50%=46.52 , m=0.35 , a=1	SNHL	Lee *et al.* (241)
TD50%=45 , m=0.11 , a=11.1	SNHL	Cheraghi *et al.* (267)
TD50%=45, m=0.14 , a=1	SNHL	Cheraghi *et al.* (267)

The LKB model was calculated using a computational environment for radiological research (CERR), built on MATLAB. In total, two calculations were required for this study: first, the NTCP for the TPS, and second the calculation for the MC simulation. The calculation of the TPS NTCP was straightforward and involved uploading the DICOM and entering the parameters. However, the MC simulation data could not be uploaded directly, and some MATLAB code needed to be modified to a readable format for CERR. Figure 7.4 shows the modification to the CERR code to allow the data to be uploaded by adding a few lines, as shown in Figure 7.5, to build the connection between the MC data and the CERR code. It was necessary to update the modification for each case, due to the changes in the files within the DICOM series.

```
EUDv = linspace(0,100,100);
if ~isempty(structNum) && ~isempty(doseNum) && ud.eudChanged
    ud.doseBinsV = planC{1, 10}(6).DVHMatrix(:,1); %changed by AAA
    ud.volsHistV =  planC{1, 10}(6).DVHMatrix(:,2);%changed by AAA
    ud.EUD = calc_EUD(ud.doseBinsV, ud.volsHistV, n);
    ud.maxDose = max(planC{indexS.dose}(doseNum).doseArray(:));
    ud.eudChanged = 0;
elseif isempty(structNum) && isempty(doseNum)
    ud.EUD = [];
end
```

Figure 7.4: The modification to the CERR code, in order to use the MC DVH data in the calculation of the NTCP.

```
newdvh =[-meann:0.1:((length(c)-1)*0.1-meann); c]';
planC{1, 10}(6).DVHMatrix =[ DVH(:,1), -gpl7];
planC{1, 10}(6).DVHMatrix = newdvh;
```

Figure 7.5: The command needed to recall the DVH from the MC for each case.

7.5 Results

The energy fluence for the cochlea were calculated for each case and plotted in Figure 7.6. For example, the original data from the MC of the basic model, as shown by the black line in Figure 7.6, was assumed to be a base line scenario. In all, five cases showed a higher fluence, indicating a higher variation of dose distribution in low energy levels.

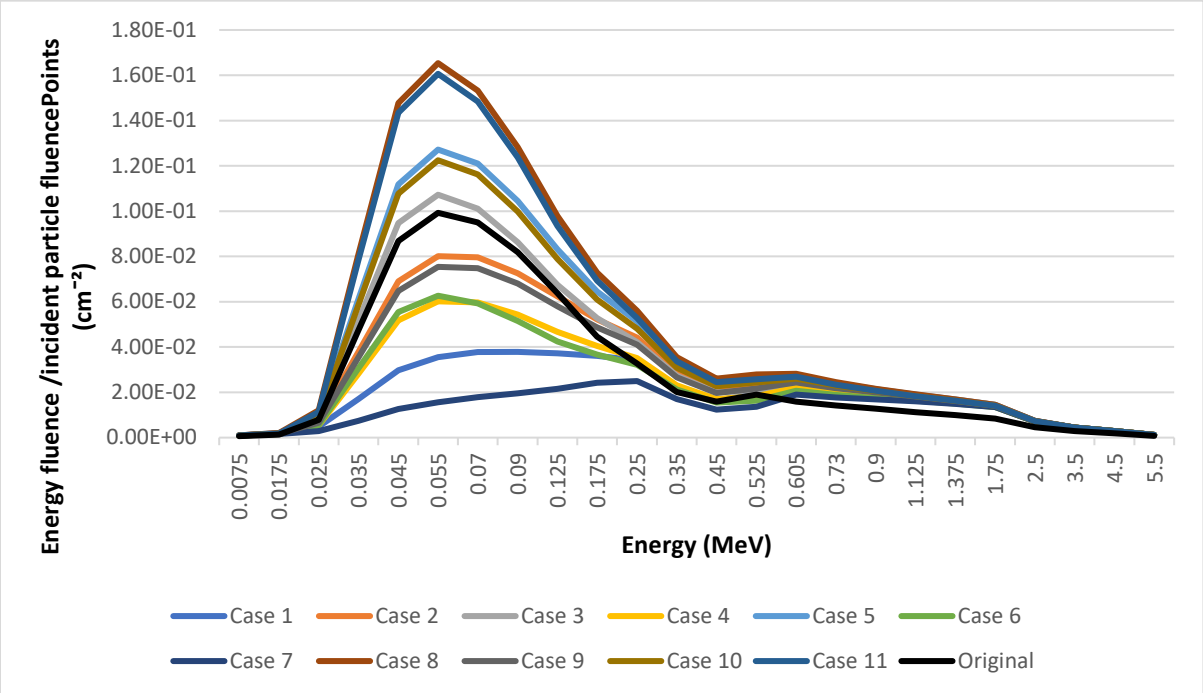

Figure 7.6: Photon energy fluence of the different scenarios using the advanced model of the cochlea.

The higher energy fluence indicated a higher percentage difference in the dose distribution in the low energy levels. The distance between the cochlea and the PTV was a main factor that indicated the dose deposited in the cochlea, and the uniformity of the dose. Table 7.4 shows details of the cochlea and target volume for each case.

Table 7.4: The volume of both the cochlea and the PTV for each case.

	Volume (cm^3)		
	PTV	**R cochlea**	**L cochlea**
Case 1	333.40	0.08	0.08
Case 2	287.50	0.10	0.10
Case 3	162.00	0.28	0.22
Case 4	156.80	0.12	0.11
Case 5	362.00	0.13	0.11
Case 6	184.86	0.16	0.13
Case 7	148.80	0.09	0.08
Case 8	495.00	0.12	0.12
Case 9	470.70	0.28	0.28
Case 10	391.00	0.01	0.18
Case 11	267.30	0.10	0.11

Table 7.5 shows that the proportional size between the cochlea and the PTV was significant, and also includes the minimum and maximum distance between the PTV and the cochleae. The distance can be essential for indicating the dose deposited in the cochlea, due to the different scattering events involved.

Table 7.5: The distance between the cochlea and the PTV for each case.

	Right cochlea to PTV			Left cochlea to PTV	
	Minimum (cm)	**Maximum (cm)**		**Minimum (cm)**	**Maximum (cm)**
Case 1	0.69	9.0		3.50	11.0
Case 2	0.65	9.6		4.60	12.3
Case 3	7.50	12.1		3.50	11.4
Case 4	6.30	11.1		2.98	9.9
Case 5	3.60	11.5		0.06	8.5
Case 6	6.70	12.2		7.30	12.7
Case 7	7.00	12.5		6.30	11.8
Case 8	2.70	11.8		0.86	10.6
Case 9	1.70	11.3		4.20	12.6
Case 10	1.90	11.5		4.20	12.0
Case 11	5.39	10.8		1.10	9.7

The next step was to evaluate each case and to calculate the DVH, in order to understand the effect of the scattering events in the micro-CT data. The cases were divided into two groups, one with an energy fluence lower than the original data, and the second with an energy fluence

higher than the original data. After evaluating the cases in both groups, extra cases chosen from a similar database were introduced, in order to study the effect in the cases with a high dose distribution to the cochlea. The distance between the cochlea and target was required to be below 1 cm, in order to ensure uniform distribution to the cochlea that increased the difference between the MC and the TPS. In all, 12 cases were chosen and divided into three categories.

7.5.1 Group A

In Group A, six of the 11 cases had a fluence energy distribution that was lower than in the original data. The distance between the cochlea and the PTV was an essential factor in determining the dose deposited in the cochlea, and the uniformity of the distribution. In all, two of the six cases had a distance < 1 cm, while the rest were > 1 cm. The comparison between the TPS and MC dose distribution showed a similar pattern in Group A, which generally demonstrated a higher dose distribution in the TPS than the MC, with the exception of Dmax, where the MC reported a higher distribution. Furthermore, the Dmin of Group A showed a significant difference that reached a maximum of 12.5%. In contrast, cases one and two showed a significant difference only in Dmax that reached 7.6%. The mean doses of the Group A cases did not show a significant difference. The difference range of the mean doses was 1.5% to 3.5%. Table 7.6 shows the dose calculation of the four cases, excluding cases six and seven, because the mean dose was below 1 Gy. Due to the similarity of Group A, a closer examination of each case was essential for understanding the elements affecting the dose distribution.

In case one, the location of the right cochlea was near the PTV 0.69 cm, with a huge PTV target. A high deposited dose was predicted, and uniform distribution occurred, due to the short distance from the PTV. A significant difference was evident in volumes 99% and 98%, in which a TPS overestimated the dose, compared with the MC that did not. Furthermore, the 95% volume was on the borderline, which was a considered to be a significant difference. The maximum dose exceeded the constraint limit, and required re-evaluation to assess if the dose could be reduced without affecting the dose distribution to the target. Reducing the dose to the cochlea was desirable in this case, in order to avoid a complication like tinnitus or SNHL. The second case in Group A had a higher energy fluence distribution. The target was close to the cochlea at 0.65 cm, but the PTV volume was not as large as in the first case. A similar pattern to that of case one of 99% and 98% demonstrated more than a 5% difference in dose. The dose to the cochlea was within the

limit. The first two cases in Group A had a higher dose deposited in the cochlea than the remaining case, in which the low dose deposited in the cochlea would not affect the clinical decision. The remaining cases had low doses deposited in the cochlea, due to the distance between the PTV and the cochlea. Although there was a difference in the Dmin, it would not affect the clinical decision. The distances were 1.7 cm, 2.98 cm, 6.7 cm, and 6.3 cm for cases nine, four, six, and seven, respectively. The doses deposited in the cochlea in these cases were below 3.5 Gy. Due to the low dose to the cochlea, applying an advanced model would not affect the treatment outcome, and would not provide beneficial information for choosing the patient's optimal plan.

Table 7.6: The Dmin, Dmax, and Dmean of Group A, and the difference in the doses.

	TPS (Gy)	MC (Gy)	Difference %
Case 1			
Dmin	37.69	33.50	12.50%
Dmax	53.13	56.00	5.10%
Dmean	46.98	45.50	3.30%
Case 2			
Dmin	17.55	15.80	11.10%
Dmax	38.09	41.21	7.60%
Dmean	27.75	27.11	2.40%
Case 4			
Dmin	1.17	1.10	6.40%
Dmax	1.63	1.65	1.20%
Dmean	1.38	1.36	1.50%
Case 9			
Dmin	3.00	2.70	11.10%
Dmax	4.28	4.37	2.10%
Dmean	3.55	3.43	3.50%

(a)

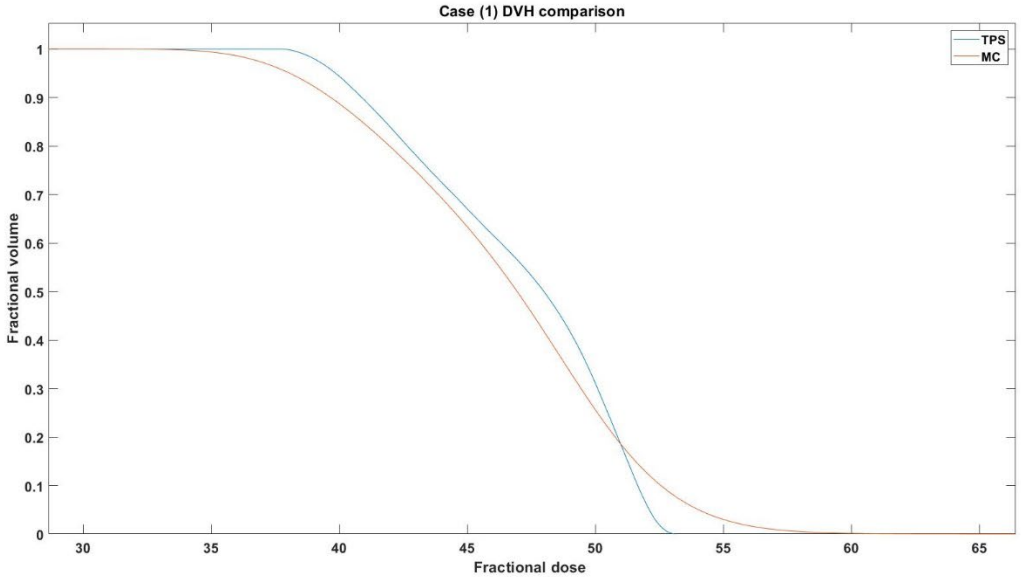
Case (1) DVH comparison
TPS
MC
Fractional volume
Fractional dose
0
0.1
0.2
0.3
0.4
0.5
0.6
0.7
0.8
0.9
1
30
35
40
45
50
55
60
65

(b)

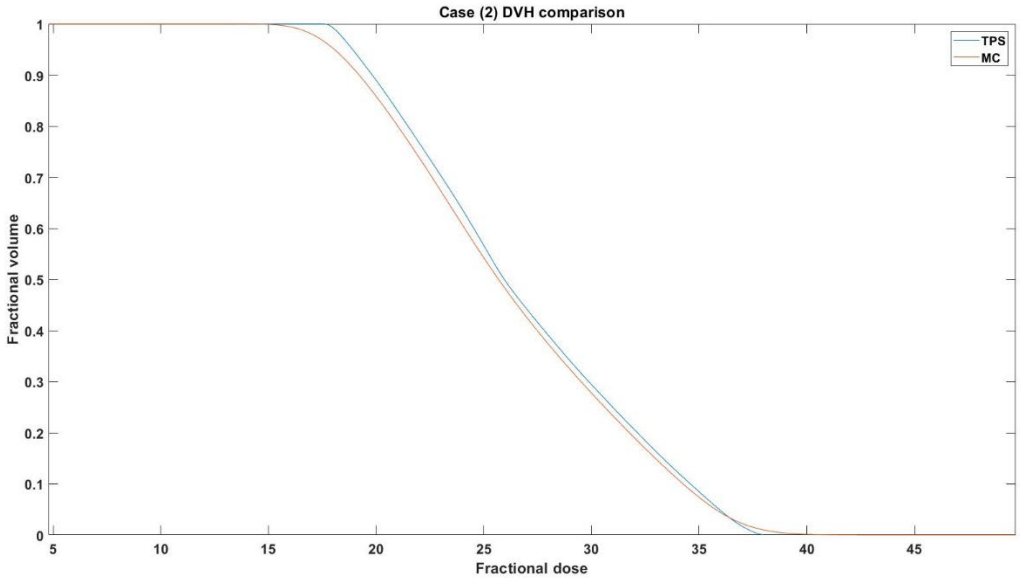
Case (2) DVH comparison
TPS
MC
Fractional volume
Fractional dose
0
0.1
0.2
0.3
0.4
0.5
0.6
0.7
0.8
0.9
1
5
10
15
20
25
30
35
40
45

(c)

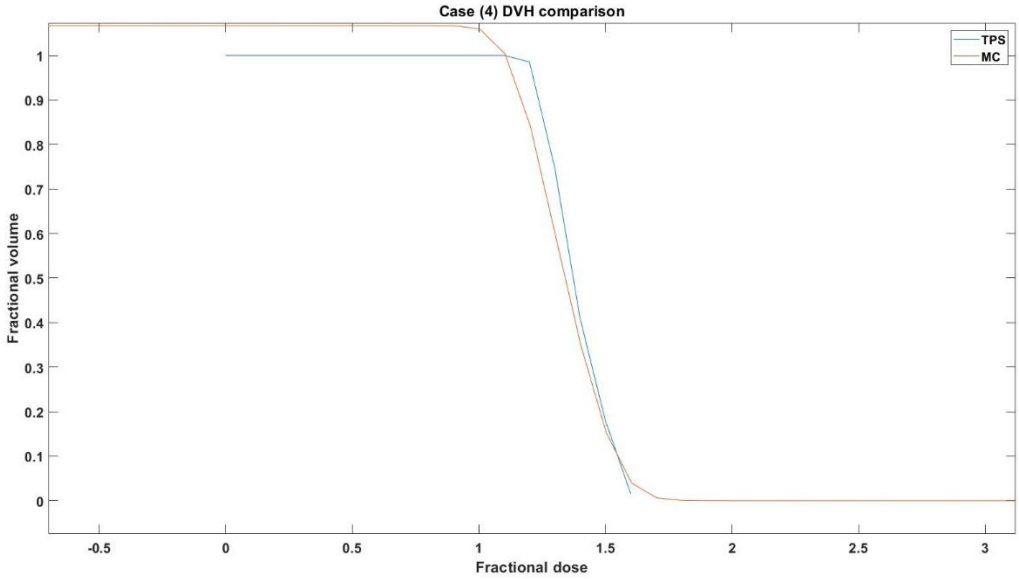

(d)

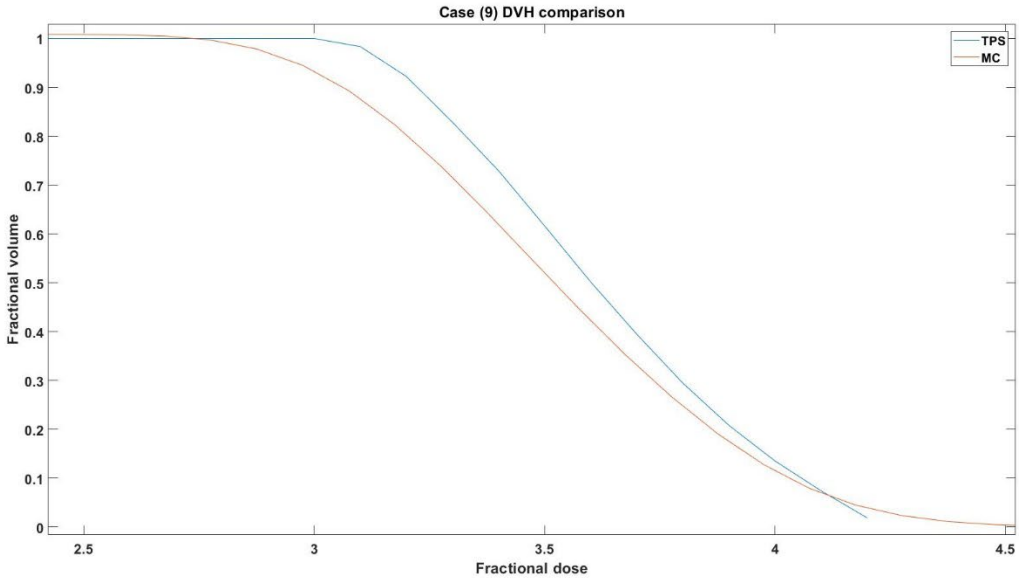

Figure 7.7: DVH comparison of Group A: a) case one, b) case two, c) case four, and d) case nine.

7.5.2 Group B

Group B was comprised of the remaining five cases with a fluence energy distribution that was higher than that of the original data. The group included two cases, cases 5 and 8, with a distance between the target and the cochlea of less than 1 cm. As shown in Table 7.7, the cases in Group B shared some similar outcomes to those in Group B. The significant difference was in the

mean dose, Dmax, and Dmin. Group B showed a significant difference in mean dose from group A, but a significant difference in the dose means does not always impact the clinical decision, and other factors must be considered. Case three was not included in the table, because the dose distribution to the cochlea was less than 1 Gy, which, as mentioned previously, would not affect the treatment outcome. The range of the Dmin difference in the cases in Group B was 10.3% to 17.3%, and for the Dmax, 6.2% to 9.6%. Due to the similarities in Group B, more details of each case were required to ascertain whether or not any further differences may impact the clinical decision.

Cases three, 10 and 11 had a similar pattern, namely a low dose distribution to the cochlea that did not affect the clinical decision, due to a distance between the target and the cochlea of more than 1 cm. In case three, the volume of the PTV was small, compared with that of the other cases. In addition, the distance between the left cochlea and the PTV was 3.5 cm, which was considered to be a considerable distance. VMAT reduces the dose to OAR, and allows a better dose distribution control. Due to the high accuracy of the treatment, a low dose was delivered to the cochlea. Although there was a high energy fluence, the clinical effect was negligible, due to the low dose of the cochlea. A similar outcome was evident in case 10. The distance between the cochlea and the target was 1.9 cm, but a low dose was still deposited in the cochlea, as shown in Table 7.7. The significant difference in the dose deposited was recorded in minimal, maximum, and mean doses. Despite the significant difference between the algorithms, the case was considered to be insignificant in terms of clinical routine, due to the low dose distribution to the cochlea. Case 11 was 1.1 cm from the cochlea to the target, but the dose deposited in the cochlea was 11.2 Gy, producing a low-risk probability of hearing loss. Case 11 demonstrated the advantage of VMAT of delivering a high accuracy treatment to the target and reading the dose to the OAR. The last two cases had a distance of less than 1 cm between the cochlea and the target, in which a higher, more uniform dose was delivered to the cochlea.

In case five, the distance between the left cochlea and the PTV was 0.06 cm, and the volume of the PTV was enormous. The difference in the mean dose was 8%, which was significant. The minimal dose difference reached 10.3% between the two algorithms, and the maximal dose exceeded the clinical constraint to the cochlea in both algorithms. Given the small distance between the cochlea and the target, the plan required re-evaluation to determine whether the dose could be reduced, without affecting the dose to the target. Case eight revealed a similar outcome

to case five, and had the highest maximal dose difference in Group B. In case eight, the plan passed all the constraints, with use of a TPS. However, if an advanced model were to be used, the plan would require re-evaluation, due to the constraints in the cochlea. The high accuracy algorithm with Micro CT showed the advantage in this case, with the constraint within the borderline.

Table 7.7: The Dmin, Dmax, and Dmean of Group B, and the difference in the doses.

	TPS (Gy)	MC (Gy)	Difference %
Case 5			
Dmin	57.00	51.70	10.30%
Dmax	60.50	64.00	5.50%
Dmean	60.00	55.58	7.90%
Case 8			
Dmin	19.43	16.90	15.00%
Dmax	45.74	50.60	9.60%
Dmean	31.58	29.90	5.60%
Case 10			
Dmin	3.20	2.90	10.30%
Dmax	4.12	4.50	8.40%
Dmean	3.60	3.38	6.50%
Case 11			
Dmin	4.47	3.81	17.30%
Dmax	24.75	26.50	6.60%
Dmean	11.20	10.29	8.80%

(a)

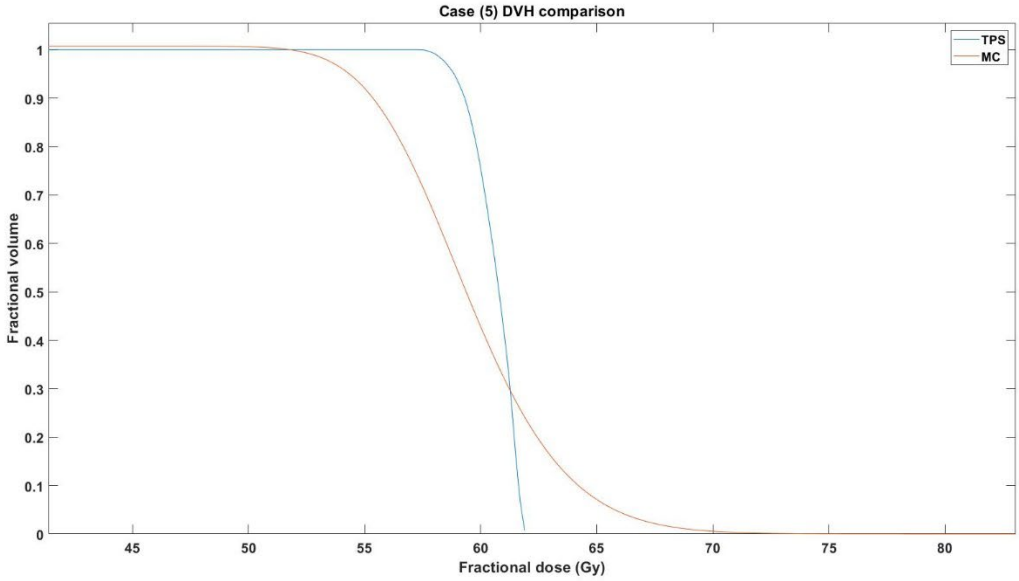
Case (5) DVH comparison
TPS
MC
Fractional volume
Fractional dose (Gy)
0
0.1
0.2
0.3
0.4
0.5
0.6
0.7
0.8
0.9
1
45
50
55
60
65
70
75
80

(b)

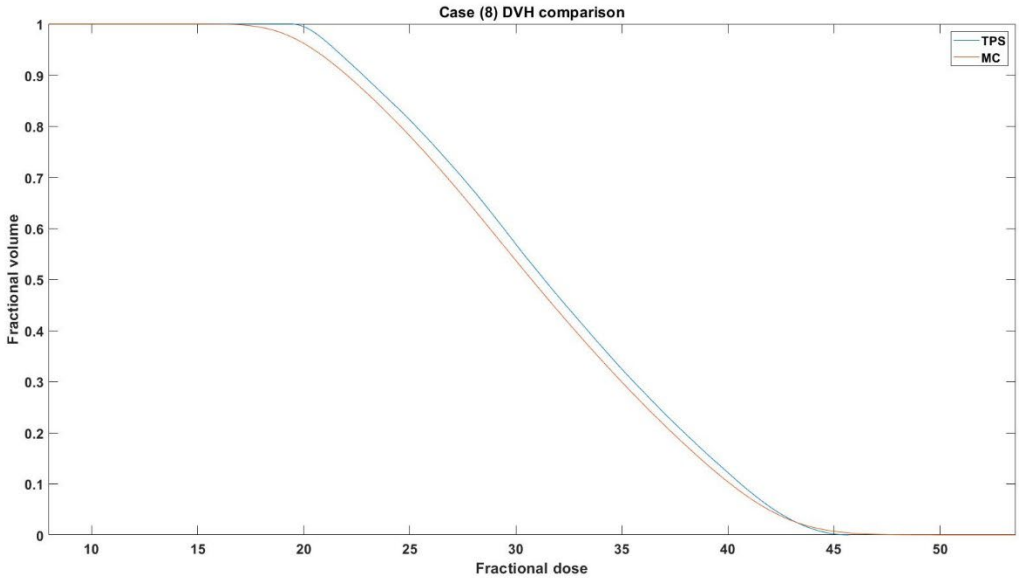
Case (8) DVH comparison
TPS
MC
Fractional volume
Fractional dose
0
0.1
0.2
0.3
0.4
0.5
0.6
0.7
0.8
0.9
1
10
15
20
25
30
35
40
45
50

(c)

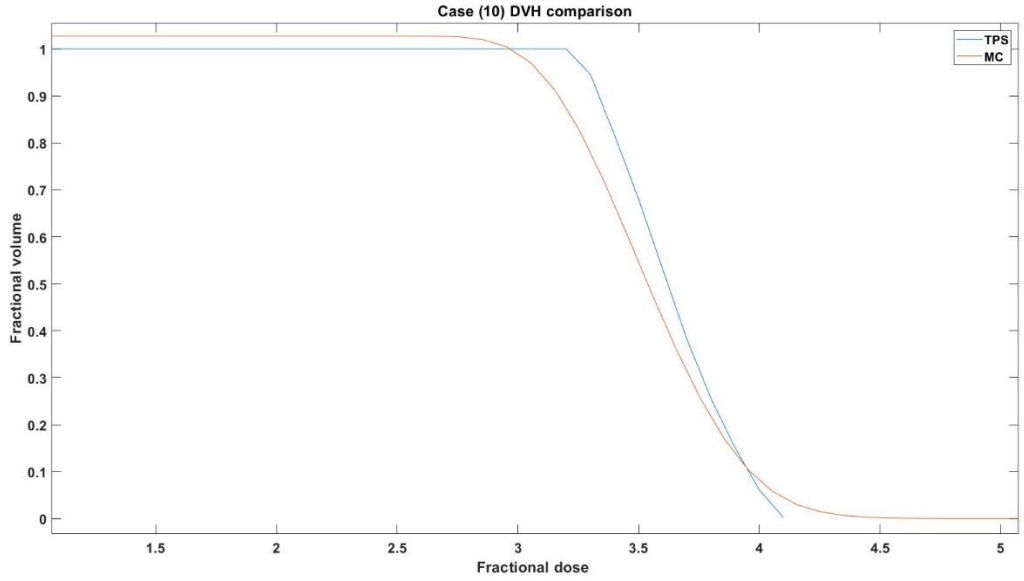

(d)

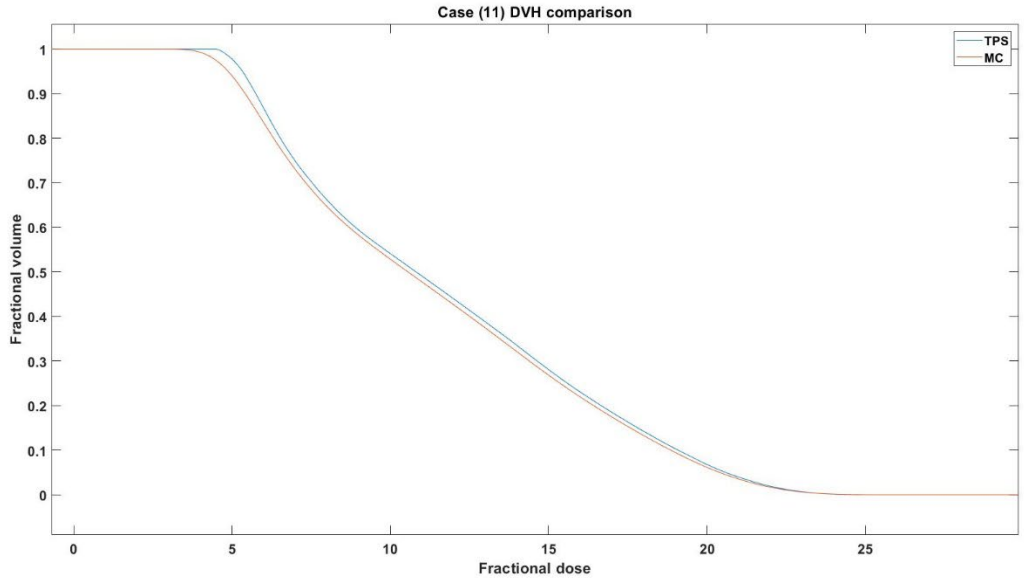

Figure 7.8: DVH comparison of Group B: a) case five, b) case eight, c) case 10, and d) case 11.

7.5.3 NTCP comparison

As mentioned previously, a different NTCP model was adapted for this study. The first NTCP model concerned grade two tinnitus, and the second model SNHL.

7.5.3.1 NTCP model for grade two tinnitus

The first section of the analysis concerned the model for grade two tinnitus; the results for both groups are shown in Table 7.8. While many of the cases demonstrated a significant percentage difference between the TP and the MC, the difference would not impact the clinical decision significantly. In Group A, cases six and seven showed a significant difference in the NTCP model for grade two tinnitus, but the NTCP value was small. Further, both cases had low doses to the cochlea, due to the distance between the cochlea and the target being more than 3 cm. The NTCP difference in both cases was significant, but this was due to the number of points in the DVH for comparison, which increased the percentage of statistical uncertainty. In addition, the low dose distribution to the cochlea marked the case as non-clinically significant, and would not affect the planning decision. The remaining cases in the group showed an insignificant difference between the MC and the TPS in the NTCP calculation for grade two tinnitus. The highest value was found in case one, and was due to the high dose deposited in the cochlea.

In Group B, all of the cases showed a significant difference between the TPS and the MC, although it was not clinically significant, due to the low dose distribution. In the cases with a low dose distribution, such as case three which had a high energy fluence distribution. The NTCP difference reached 11%, which was significant, but due to the low dose distributed to the cochlea (1.6 Gy), would not make the overall case significant as a clinical decision. The low dose to the cochlea was due to the long distance of 3.5 cm between the cochlea and the target. The two cases that showed a clinically significant difference in both the dose distribution and the NTCP model for tinnitus were cases five and eight. Case five demonstrated a significant difference that reached 5.3%, and the MC NTCP was lower than the TPS NTCP by a significant percentage. The mean dose was above the threshold of tinnitus, and the energy dose distribution was higher than the worst-case scenario anticipated. Due to the short distance between the target and cochlea, a uniform dose distribution in the cochlea had most likely occurred that increased the percentage of difference, due to low energy distribution in the different density levels that the TPS found challenging to track. Case eight had a high energy fluence distribution, with a TPS mean dose that was close to the threshold of tinnitus, but with a lower MC mean dose. The NTCP difference was significant at 8 %. Case eight was considered to be clinically significant in the NTCP model, with an endpoint of tinnitus.

Table 7.8: NTCP model for grade two tinnitus, using LKB parameters TD = 32.82, Gy, m = 0.35, and a = 1. The top table is for Group A and the second is for Group B.

Group A	NTCP TP	NTCP MC	Difference %
Case 1	0.884	0.855	3.28%
Case 2	0.308	0.296	4.06%
Case 4	0.003	0.003	0.00%
Case 6	0.003	0.003	8.93%
Case 7	0.002	0.002	13.22%
Case 9	0.005	0.005	0.64%
Group B			
Case 3	0.003	0.003	10.73%
Case 5	0.600	0.568	5.33%
Case 8	0.474	0.437	7.83%
Case 10	0.006	0.005	7.27%
Case 11	0.033	0.030	9.92%

7.5.3.2 NTCP models for SNHL

The second NTCP model's endpoint was SNHL. Previous studies discussed the fact that using the dose-volume analysis method in a small structure like the cochlea produces inaccurate calculations and higher uncertainty. Therefore, for the purpose of the present study, two NTCP models used mean dose for the calculation, as seen in a = 1, and only one NTCP model used a dose-volume analysis to test the idea that a dose-volume analysis is not the option recommended for the cochlea.

The results of the three models for the cases in Group A are shown in Table 7.9. The Lee *et al.* parameters differed significantly in cases six and seven, but the NTCP values were low (241). The similar outcome found in the tinnitus NTCP model for these two cases may have been due to the low information in the DVH that was likely to have produced a higher statistical uncertainty. The remaining cases showed an insignificant difference between the TPS and the MC. The second NTCP models demonstrated an insignificant result in case one, but a significant result in case two. The low case two values could be overcome in the clinical routine, due to the low probability of hearing loss. The second model, which used the mean dose of Cheraghi *et al.*, and the Lee *et al.*

model, showed increased sensitivity to cases with a low dose distribution to the cochlea (233,259). The last dose volume analysis model showed an amplified difference between the TPS and the MC in case two. Furthermore, the value of the NTCP in case one was the highest of the three models. A similar result to that of the Cheraghi *et al.* parameter was the lowered sensitivity to the cases with a low dose distribution to the cochlea (259).

TD50% =46.52 Gy ,m=0.35 ,a=1			
Group A	NTCP TP	NTCP MC	Difference %
Case 1	0.48	0.5	4.17%
Case 2	0.116	0.111	4.31%
Case 4	0.00278	0.00276	0.72%
Case 6	0.00264	0.00239	9.47%
Case 7	0.0023	0.0021	8.70%
Case 9	0.00419	0.00417	0.48%

TD50% =45 Gy ,m=0.14 ,a=1			
Group A	NTCP TP	NTCP MC	Difference %
Case 1	0.559	0.58	3.76%
Case 2	0.0022	0.002	9.09%
Case 4	0	0	0.00%
Case 6	0	0	0.00%
Case 7	0	0	0.00%
Case 9	0	0	0.00%

TD50% =45 Gy ,m=0.11 ,a=11.1			
Group A	NTCP TP	NTCP MC	Difference %
Case 1	0.757	0.782	3.30%
Case 2	0.0078	0.006	23.08%
Case 4	0	0	0.00%
Case 6	0	0	0.00%
Case 7	0	0	0.00%
Case 9	0	0	0.00%

Table 7.9: The NTCP models for the cochlea, with the endpoint being SNHL for Group A. Two models used a mean dose, a= 1, and one model used a dose-volume analysis.

While Group B demonstrated more significantly different results from Group A, as shown in Table 7.10, the cases with a low dose distribution with minimal DVH points had a higher statistical uncertainty that might cause significant differences, as in the cases in Group A. Cases three, 10, and 11 had a low dose distribution to the cochlea, although there was a difference in the NTCP endpoint for the SNHL using the Lee *et al.* model (241). Therefore, the result was not considered to be clinically significant. The Lee *et al.* parameters showed a significant difference in cases such as five and eight, which were clinically significant, due to a higher dose deposition than in the other cases (241). The mean dose of Cheraghi *et al.* was employed to show a significant difference in only two cases, but this was amplified in case eight (259). In contrast, the NTCP value for case eight was low. The last NTCP model used a dose-volume analysis and demonstrated a magnified result in two cases, but no value for the remaining cases.

TD50% =46.52 Gy ,m=0.35 ,a=1			
Group B	NTCP TP	NTCP MC	Difference %
Case 3	0.00289	0.00266	7.96%
Case 5	0.75899	0.7122	6.16%
Case 8	0.187	0.1702	8.98%
Case 10	0.0041	0.0038	7.32%
Case 11	0.016	0.0145	9.38%

TD50% =45 Gy ,m=0.14 ,a=1			
Group B	NTCP TP	NTCP MC	Difference %
Case 3	0	0	0.00%
Case 5	0.651	0.611	6.14%
Case 8	0.02	0.013	35.00%
Case 10	0	0	0.00%
Case 11	0	0	0.00%

TD50% =45 Gy ,m=0.11 ,a=11.1			
Group B	NTCP TP	NTCP MC	Difference %
Case 3	0	0	0.00%
Case 5	0.598	0.7379	23.39%
Case 8	0.105	0.0697	33.62%
Case 10	0	0	0.00%
Case 11	0	0	0.00%

Table 7.10: The NTCP models for the cochlea with the endpoint being SNHL for Group B. Two models used a mean dose, a= 1, and one model used a dose-volume analysis.

7.5.4 Additional cases

The 11 scenarios extracted from the data showed a significant difference in some cases in both the mean dose and NTCP. However, not all of the significant differences would be considered necessary in the clinical routine if the dose to the cochlea was low, and the risk of side effects was minimal. In this scenario, the case was considered non-significant, despite the difference between the NTCPs. The distance between the target and the cochlea is critical for evaluating whether or not the cochlea would receive a high dose. In cases 1, 2, 5, and 8, the distance was less than 1 cm, and the cochlea received a considerable amount of radiation that a difference in NTCPs would consider to be clinically significant. Cases nine and 10 had a distance of less than 2 cm, with low radiation to the cochlea that was far from the threshold. Meanwhile, the remaining cases had a distance of more than 2 cm, and the cochlea received a very minimal dose that was considered to be non-significant in the clinical routine.

The next step addressed the cases with a distance of less than 1 cm between the cochlea and the target, in order to evaluate the MC model better. The rationale for the extra cases was that when the dose to the cochlea is uniform, which can only happen if the cochlea is close to, or within, the target area, the difference in dose distribution can be the highest of all distributions. The additional cases were chosen from the same dataset of 280 cases of glioma. The cases were filtered using the distance between the cochlea and the target, which was required to be less than 1 cm. The search produced three scenarios, categorized into three categories. The first two categories followed the same pattern as Group A in cases one and two. The last category was case five in Group B. None of the other scenarios were found in cases with short distances between the cochlea and the target in the data used. In total, four cases were chosen for each category. A VMAT plan was created for each case, and an MC modification was conducted. The last step was to calculate the NTCP using different model parameters for SNHL and tinnitus.

7.5.4.1 Category one

The first category contained four cases: 14, 17, 18, and 20. Category one received a similar energy fluence distribution to case one. The TPS plans were then compared, in order to modify the MC. Similarly to the previous cases, the energy fluence distribution was low, compared with the other cases. Figure 7.9 shows the DVH comparison with modified MC, demonstrating

that the four cases showed a similar pattern that differed significantly in the Dmin and Dmax. However, the mean dose difference was insignificant, as shown in Table 7.11.

Table 7.11: The Dmin, Dmax, and Dmean of the four cases in category one, and the difference in the doses.

	TPS (Gy)	MC (Gy)	Difference %
Case 14			
Dmin	31.15	27.26	14.00%
Dmax	49.44	58.60	16.00%
Dmean	43.23	41.41	4.00%
Case 17			
Dmin	46.90	40.10	17.00%
Dmax	58.10	60.00	3.00%
Dmean	53.96	51.90	4.00%
Case 18			
Dmin	15.48	13.40	16.00%
Dmax	46.00	49.80	8.00%
Dmean	31.00	29.70	4.00%
Case 20			
Dmin	12.50	9.44	32.00%
Dmax	42.80	46.32	8.00%
Dmean	27.75	27.10	2.00%

(a)

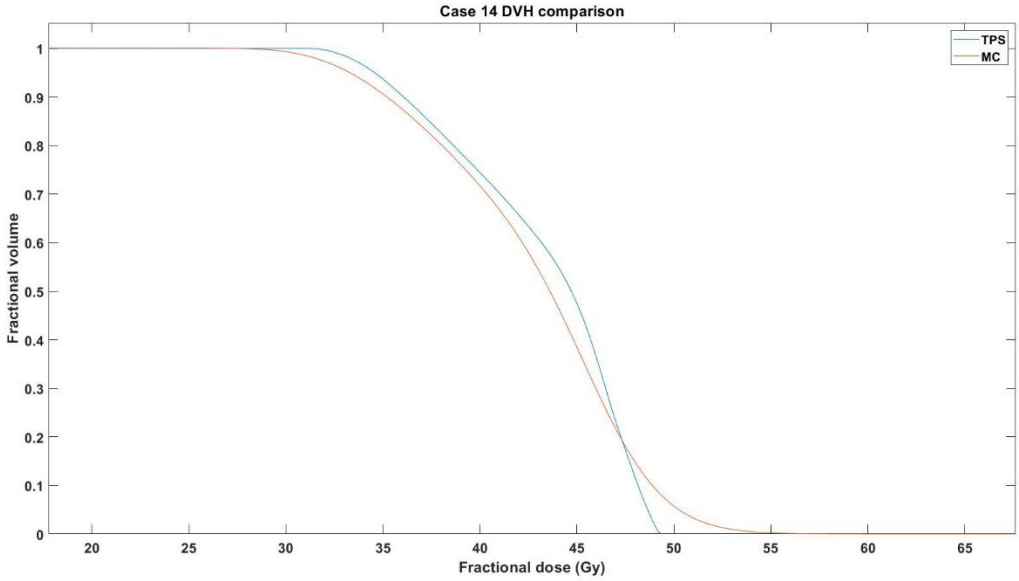
Case 14 DVH comparison
TPS
MC
Fractional volume
Fractional dose (Gy)

(b)

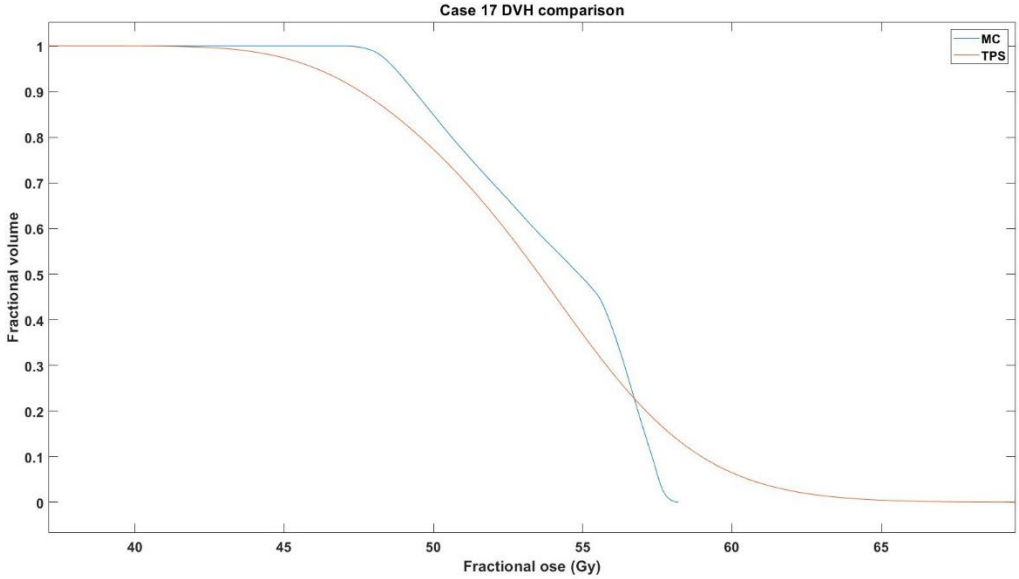
Case 17 DVH comparison
MC
TPS
Fractional volume
Fractional ose (Gy)

(c)

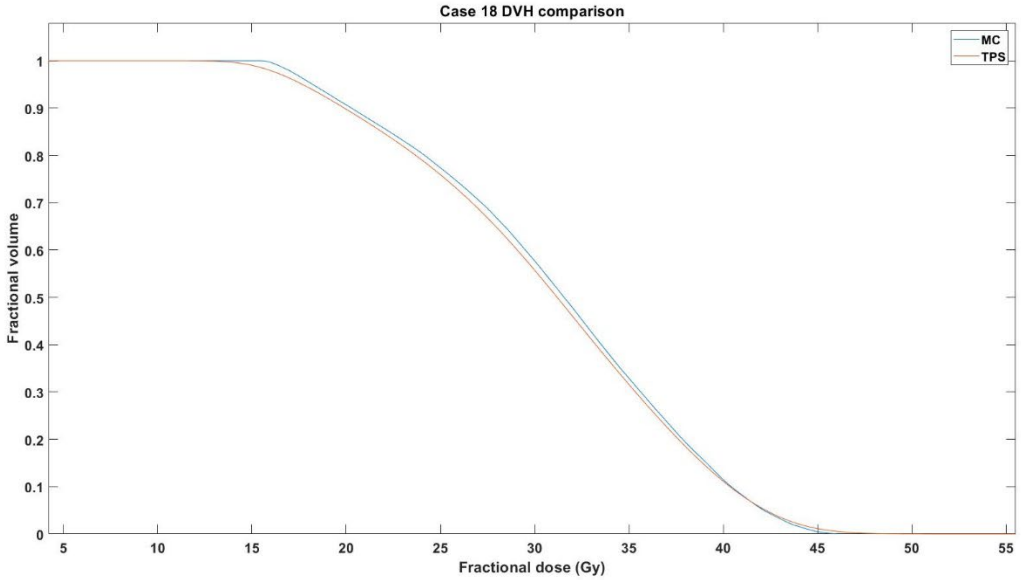

(d)

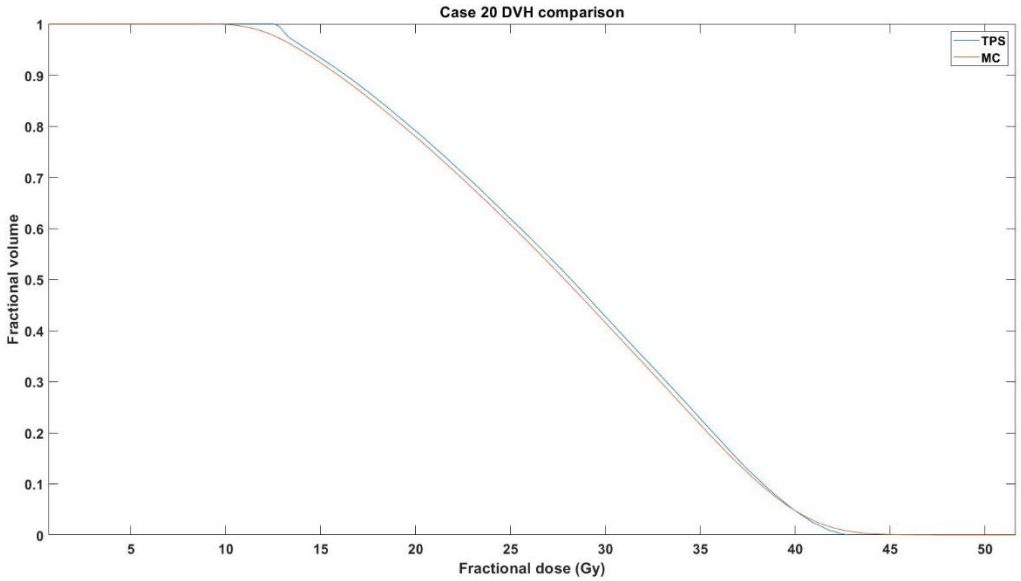

Figure 7.9: The DVH comparison of the four cases of category one, a) case 14, b) case 17, c) case 18, and d) case 20.

The NTCP was calculated using similar parameters to the previous cases (Table 7.12). All of the cases demonstrated that the parameters of Lee *et al.* showed no significant difference in both models for the endpoint of tinnitus and SNHL (241). Furthermore, the parameter set by Cheraghi *et al.,* using mean dose, produced a similar result, namely no significant difference (259).

However, the last dose-volume analysis model demonstrated amplified results that reached a 200% difference, which was considered to be an outlier result. The 200% difference illustrated the inaccuracy of the dose-volume analysis in small structures like the cochlea, producing unreasonable results.

Table 7.12: The NTCP calculated for the category one cases using different models' parameters for SNHL and tinnitus.

	NTCP TPS	NTCP MC	Difference %
SNHL parameter	TD50%=46.52 Gy, m =0.35, a= 1		
Case 14	0.400	0.410	2.40%
Case 17	0.657	0.665	1.20%
Case 18	0.168	0.170	1.20%
Case 20	0.129	0.124	3.60%
SNHL parameter	TD50%=45 Gy, m =0.14, a= 1		
Case 14	0.364	0.365	0.27%
Case 17	0.900	0.910	1.10%
Case 18	0.013	0.013	4.58%
Case 20	0.004	0.003	4.23%
SNHL parameter	TD50%=45 Gy, m =0.11, a= 11.1		
Case 14	0.550	0.530	3.77%
Case 17	0.970	0.980	1.02%
Case 18	0.079	0.043	84.58%
Case 20	0.046	0.015	200.97%
Tinnitus parameter	TD=32.82 Gy, m =0.35, a= 1		
Case 14	0.807	0.800	0.88%
Case 17	0.961	0.963	0.21%
Case 18	0.433	0.438	1.29%
Case 20	0.342	0.329	3.95%

7.5.4.2 Category two

The second category had an energy fluence distribution that was similar to case two. The cases in this category were 13, 16, 22, and 23. The fluence distribution was close to the estimated worst-case scenario. As shown in Table 7.13, the difference in the mean dose in all of the cases was insignificant. However, the difference in the Dmax was significant and was higher than in category one. The difference in the distribution in the Dmax area was due to low photons.

Table 7.13: The Dmin, Dmax, and Dmean of the four cases in category two, and the difference in the doses.

	TPS (Gy)	MC (Gy)	Difference %
Case 13			
Dmin	8.80	7.49	17.50%
Dmax	14.29	15.39	7.10%
Dmean	11.41	10.95	4.20%
Case 16			
Dmin	29.10	25.10	15.90%
Dmax	52.40	60.00	12.70%
Dmean	41.70	39.90	4.50%
Case 22			
Dmin	35.70	31.00	15.20%
Dmax	48.00	56.10	14.40%
Dmean	42.75	41.10	4.00%
Case 23			
Dmin	18.80	15.67	20.00%
Dmax	47.30	52.00	9.00%
Dmean	33.30	31.90	4.40%

(a)

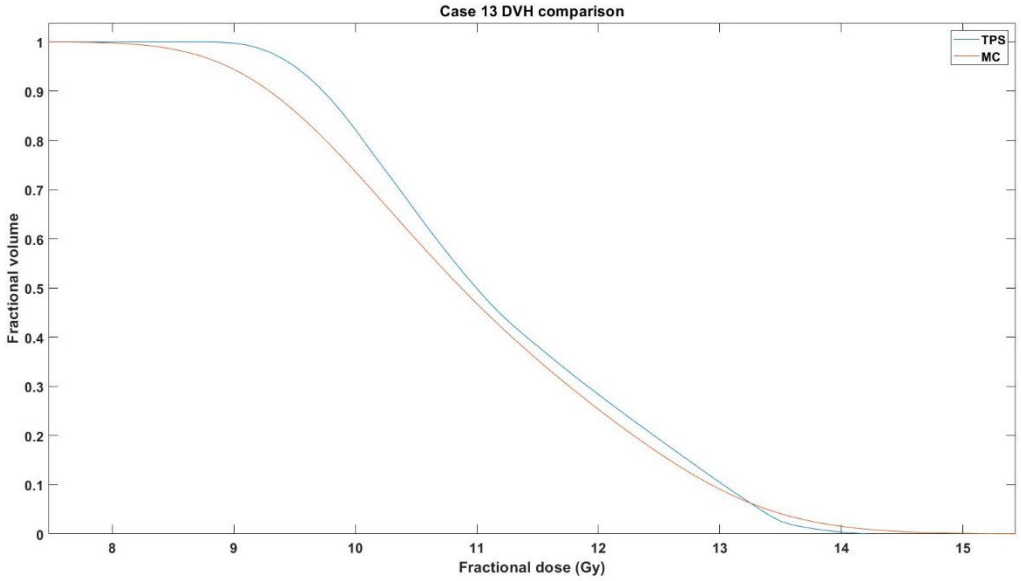
Case 13 DVH comparison
TPS
MC
Fractional volume
Fractional dose (Gy)
0
0.1
0.2
0.3
0.4
0.5
0.6
0.7
0.8
0.9
1
8
9
10
11
12
13
14
15

(b)

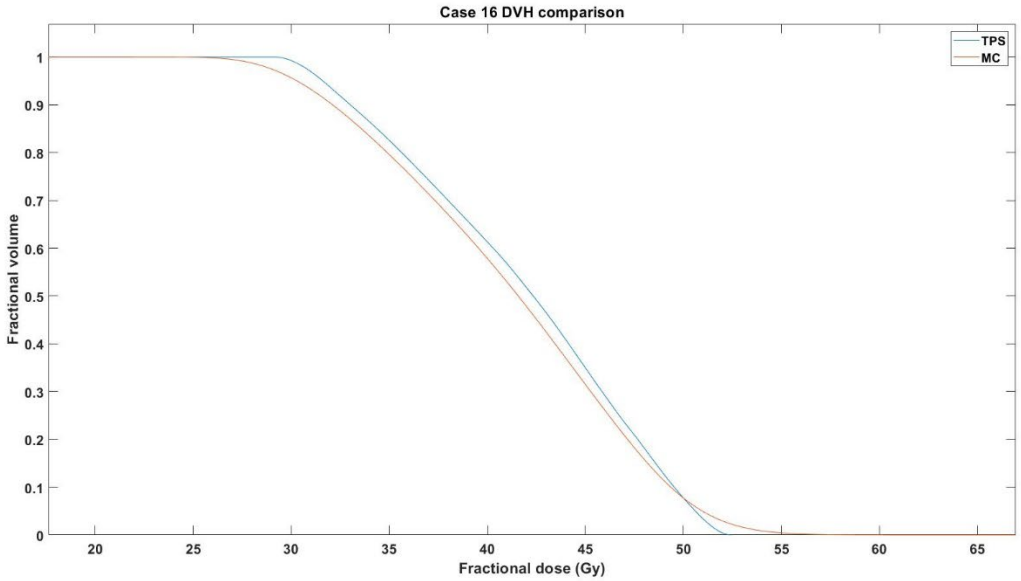
Case 16 DVH comparison
TPS
MC
Fractional volume
Fractional dose (Gy)
0
0.1
0.2
0.3
0.4
0.5
0.6
0.7
0.8
0.9
1
20
25
30
35
40
45
50
55
60
65

(c)

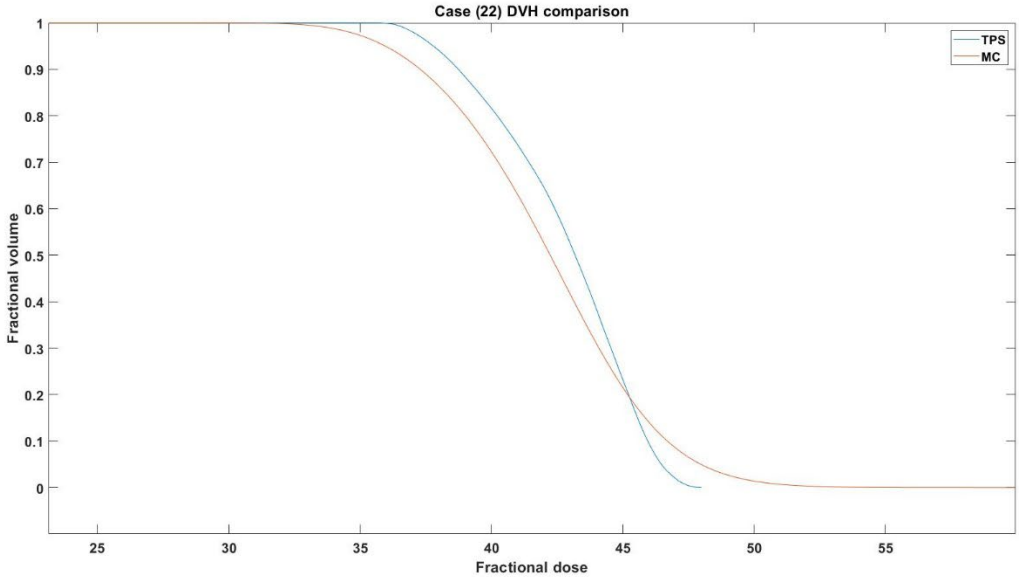

(d)

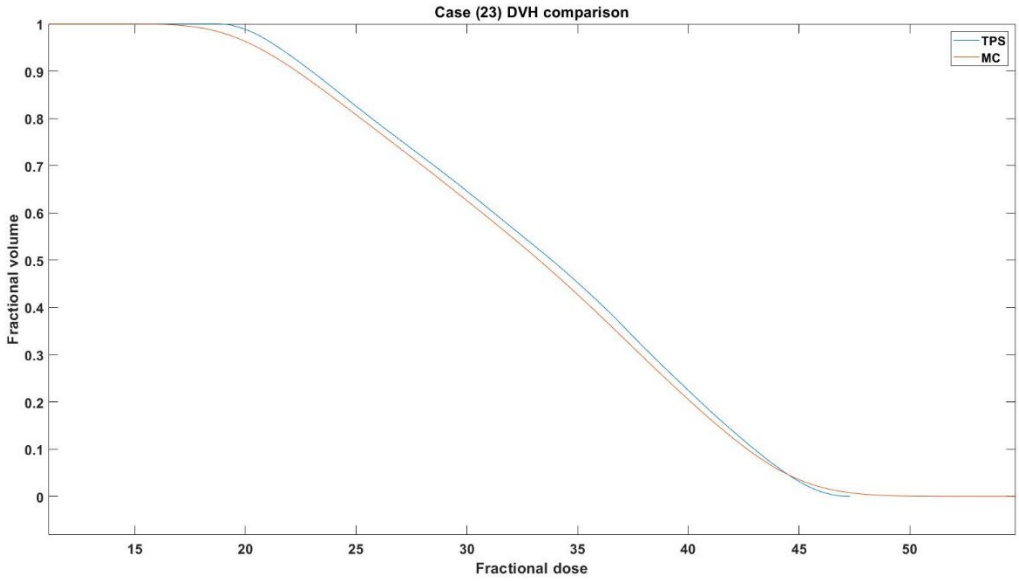

Figure 7.10: The DVH comparison of the four cases in category two: a) case 13, b) case 16, c) case 22, and d) case 23.

The NTCP models that used a dose-volume analysis demonstrated an overestimated value that was considered to be inaccurate. The tinnitus model showed a significant difference in all cases but, due to the low dose distribution in case 13, was considered to be clinically non-significant. The low dose in case 13 illustrated a minimal probability of future complications. The NTCP values for the TPS were higher than for the MC in all cases. Case 23 had a TPS mean dose

that was over the recommended threshold for tinnitus, but was within the threshold for the MC. In addition, the NTCP model for tinnitus showed a difference of 8.7%, which might change the treatment plan decisions. In the study by Lee *et al.*, all of the cases showed a significant difference that must be considered when evaluating the plan of each case (241). The study by Cheraghi *et al*. demonstrated a similar outcome, but was less sensitive to low value dose distribution, such as in cases 13 and 23 in the present study, where the NTCP calculation was zero (259).

Table 7.14: The NTCP calculated for the category two cases, using different models' parameters for SNHL and tinnitus.

	NTCP TPS	NTCP MC	Difference %
SNHL parameter	TD50%=46.52 Gy, m =0.35, a= 1		
Case 13	0.015	0.014	7.10%
Case 16	0.380	0.361	5.30%
Case 22	0.400	0.377	6.10%
Case 23	0.200	0.188	6.40%
SNHL parameter	TD50%=45 Gy, m =0.14, a= 1		
Case 13	0.000	0.000	0.00%
Case 16	0.300	0.272	10.29%
Case 22	0.360	0.333	8.11%
Case 23	0.000	0.000	0.00%
SNHL parameter	TD50%=45 Gy, m =0.11, a= 11.1		
Case 13	0.000	0.000	0.00%
Case 16	0.620	0.512	21.09%
Case 22	0.400	0.300	33.33%
Case 23	0.177	0.000	100.00%
Tinnitus parameter	TD=32.82 Gy, m =0.35, a= 1		
Case 13	0.030	0.028	6.79%
Case 16	0.780	0.730	6.85%
Case 22	0.800	0.730	9.59%
Case 23	0.500	0.460	8.70%

7.5.4.3 Category three

The final category consisted of cases with a higher fluence distribution than that of the original data. As shown in Table 7.15, the dose distribution demonstrated a significant difference in terms of Dmin, Dmax, and mean dose. Category three also demonstrated a higher percentage of

difference in the Dmin and Dmax than the other categories. Furthermore, the only category with a mean dose difference was category three. A TPS showed a higher dose distribution in most DVH only Dmax, whereas the MC showed a higher dose distribution.

Table 7.15: The Dmin, Dmax, and Dmean of the four cases in category three, and the difference in the doses.

	TPS (Gy)	MC (Gy)	Difference %
Case 12			
Dmin	19.10	16.44	16.20%
Dmax	44.00	50.40	12.70%
Dmean	33.46	31.82	5.10%
Case 15			
Dmin	12.00	10.30	16.50%
Dmax	40.00	44.70	10.50%
Dmean	24.90	23.40	6.40%
Case 21			
Dmin	42.20	36.90	14.40%
Dmax	50.80	60.00	15.30%
Dmean	47.49	44.90	5.80%
Case 24			
Dmin	38.70	34.00	13.80%
Dmax	51.50	60.00	14.20%
Dmean	45.20	42.90	5.40%

The calculations of the NTCP models for both tinnitus and SNHL are shown in Table 7.16. Case 12 demonstrated a mean dose that was within the threshold of tinnitus, and the TPS showed a higher distribution to the cochlea than the MC. Furthermore, the NTCP for tinnitus showed a significant difference that indicated that the probability of tinnitus side effects would be lower than that of the predictions calculated using TPS. A similar outcome was evident in cases 21 and 24, with the TPS dose not within the threshold of QUANTEC. However, the MC was within the threshold, and a significant difference was noted in both of the SNHL NTCP models. Therefore, the advantage of the advanced model was demonstrated in the similar cases in category three, where the plan was above the recommended threshold. While the plan may require re-evaluation, it lay within the recommended threshold in the MC. Furthermore, the NTCP models of the SNHL showed a significant difference, and were lower in the MC than in the TPS.

(a)

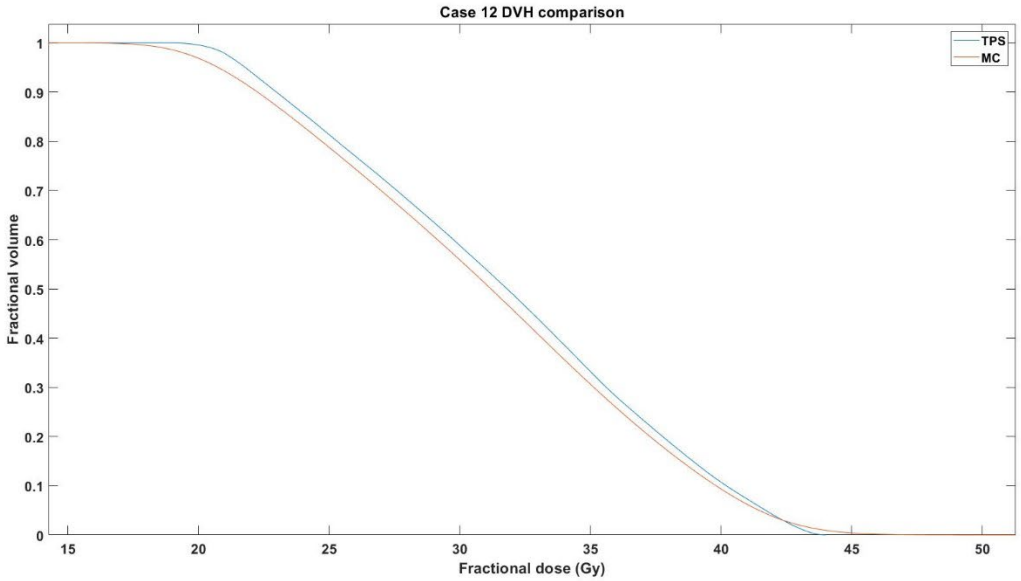
Case 12 DVH comparison
TPS
MC
Fractional volume
Fractional dose (Gy)
0
0.1
0.2
0.3
0.4
0.5
0.6
0.7
0.8
0.9
1
15
20
25
30
35
40
45
50

(b)

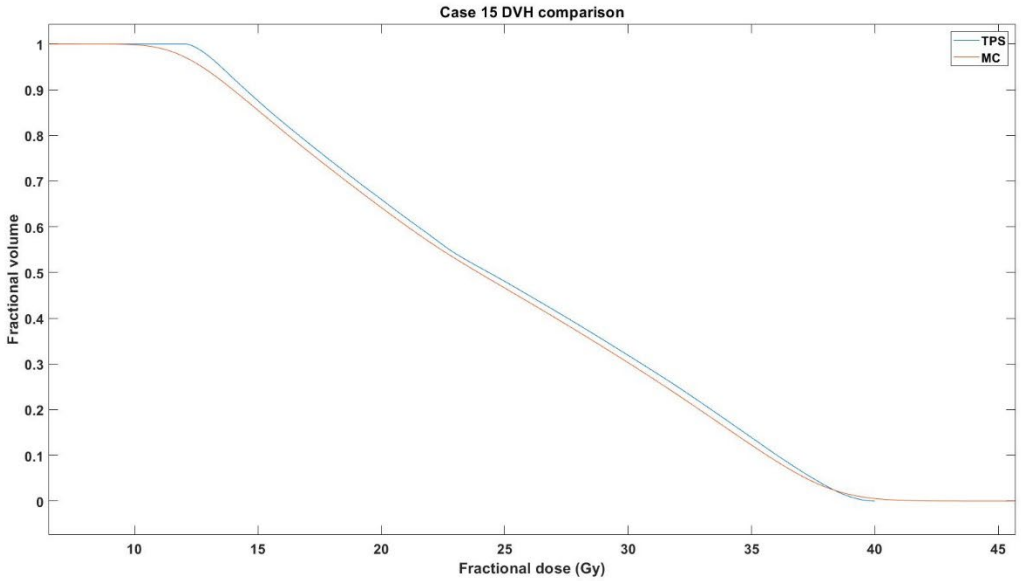
Case 15 DVH comparison
TPS
MC
Fractional volume
Fractional dose (Gy)
0
0.1
0.2
0.3
0.4
0.5
0.6
0.7
0.8
0.9
1
10
15
20
25
30
35
40
45

(c)

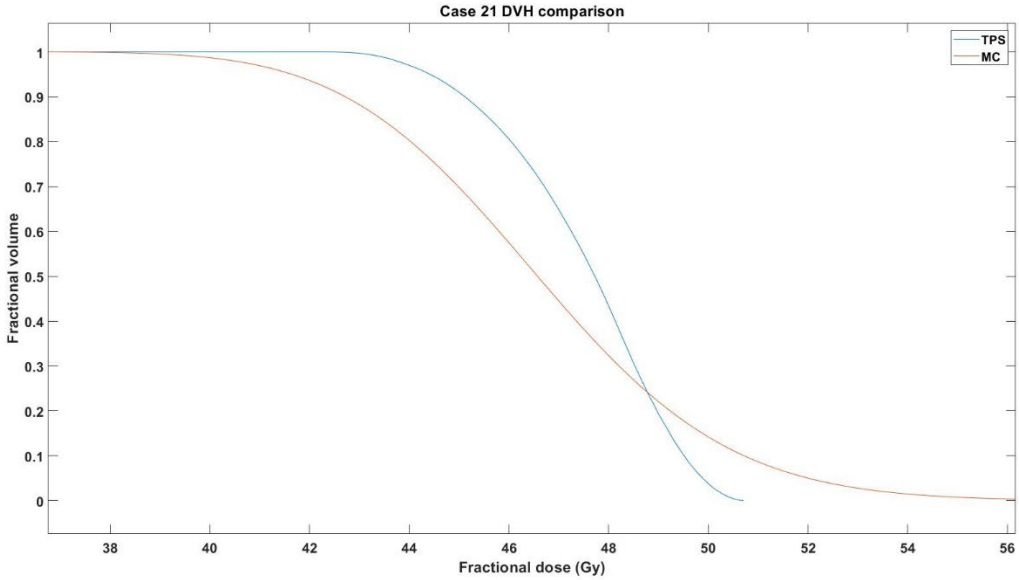

(d)

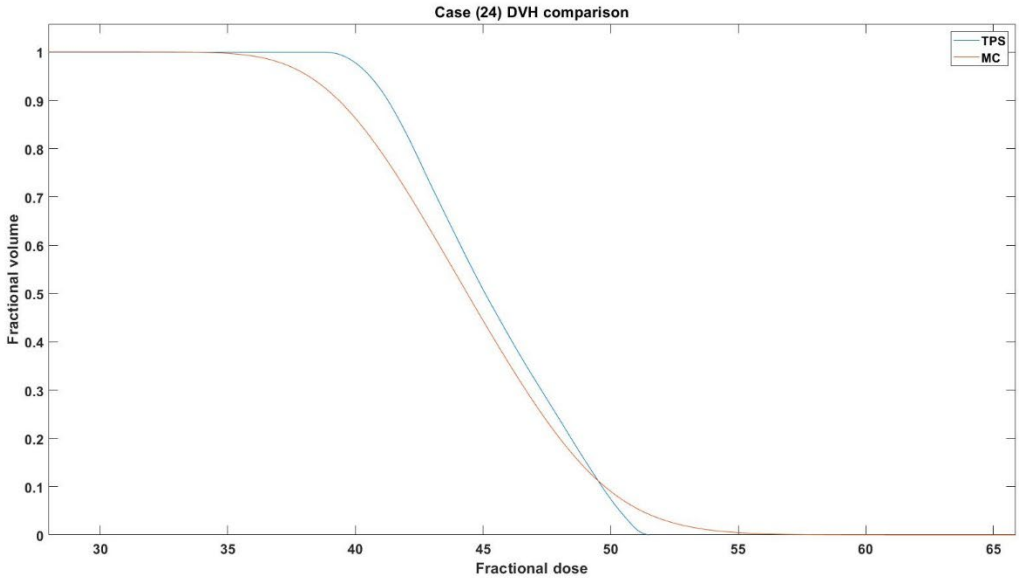

Figure 7.11: The DVH comparison of the four cases of category three: a) case 12, b) case 15, c) case 21, and d) case 24.

Table 7.16: The NTCP calculated for the category three cases, using different models' parameters for SNHL and tinnitus.

	NTCP TPS	NTCP MC	Difference %
SNHL parameter	TD50%=46.52 Gy, m =0.35, a= 1		
Case 12	0.180	0.171	5.30%
Case 15	0.099	0.092	7.30%
Case 21	0.525	0.495	6.10%
Case 24	0.470	0.440	6.80%
SNHL parameter	TD50%=45 Gy, m =0.14, a= 1		
Case 12	0.017	0.014	23.29%
Case 15	0.001	0.000	100.00%
Case 21	0.652	0.600	8.67%
Case 24	0.518	0.471	9.98%
SNHL parameter	TD50%=45 Gy, m =0.11, a= 11.1		
Case 12	0.036	0.035	3.31%
Case 15	0.018	0.004	300.89%
Case 21	0.721	0.710	1.55%
Case 24	0.600	0.600	0.00%
Tinnitus parameter	TD=32.82 Gy, m =0.35, a= 1		
Case 12	0.459	0.437	5.22%
Case 15	0.260	0.245	6.12%
Case 21	0.898	0.850	5.65%
Case 24	0.861	0.812	6.03%

7.6 Discussion

In the treatment of cancers of the brain, head and neck, the increased demand to deliver a higher dose to the target reduces the dose to the OAR. This improves the accuracy of the treatment plan by reducing the side effects of treatment. A minimal increase of only 1% in the accuracy of the treatment can improve the cure rate of early-stage tumours by 2% (157). Moreover, Chetty *et al.* found that a decrease in the dose in the steepest region of the DVH, and a change of 5% in the local dose can produce a 20% change in local tumour control (158). Additionally, a change in typical tissue complications can reach up to 30% (158). The most accurate algorithm currently

available is MC, which is considered to be the gold standard. The limitations of the MC were discussed in detail in Chapter 3, and include the long simulation time. Applying the result of the MC simulation to an advanced model, in order to study the dose distribution in micro-CT data can help to increase the accuracy of the treatment.

The cases in this study were divided into two groups. The first group showed a lower fluence distribution than that of the original data, and the second group showed a higher energy fluence than that of the original data. Both groups had similar points, as well as certain differences. Both of the groups demonstrated that an Eclipse TPS equipped with AAA reported a higher mean dose to the cochlea than MC. This concurred with the finding of the study by sterpin *et al.* that the TPS that uses the AAA algorithm overestimated the dose in the area containing bones through the use of a phantom (167). Moreover, the study by Onizuka *et al*. found that there was an overestimated dose in the bone area compared with the MC when using a phantom (174). Both of these studies employed a phantom for the comparison, but a real patient's CT was used and enhanced using micro-CT data in the cochlea region. Furthermore, the focus of this chapter was the cochlea and temporal bone. The cochlea is small, but highly heterogeneous, and can only be distinguished in micro-CT data. In all cases, the TPS significantly overestimated the dose in low-dose regions, like Dmin, by 7% - 17.5%.

The findings of the study of breast and lung cancer cases by Hasenbalg *et al.* were similarities to those of the present study, demonstrating that the TPS involved in both cases overestimated the dose in Dmin, while the MC did not (268). However, the current study employed micro-CT data in the area considered to have the highest heterogeneity, with different scenarios of energy fluence. The enhanced resolution provided by the Micro CT is a novelty not generally used in temporal bone and cochlea areas. In the DVH, a noticeable trend was evident in the curve of the TPS that began to underestimate the dose at the end of the curve in most cases. Nevertheless, in most cases, the TPS overestimated the dose. Meanwhile, the maximum dose was underestimated in most cases, with some reaching a clinically significant level. Overall, these findings aligned with those of Radojcic *et al*., namely that the dose distribution at the cochlea differs between the TPS and MC; indeed, Radojcic *et al.* reported a significant difference that reached 10% (224). The cochlea cases in the present study also showed a difference in dose distribution, some of which were significant. The lower percentage difference identified in the present study may have been due to the extraction of the air in the Micro CT in reserving the sample, and its replacement with

material similar to water. Including the air in the sample can increase the difference in the densities, but the percentage of air is small and cannot differ significantly in the outcome. The difference was not clinically significant in some cases, although it is a factor that can alter the TPS, increase the chance of sparing the cochlea, and increase the dose to the target, as the MC-deposited dose was lower than in the TPS.

Other cases in the present study demonstrated a significant difference, and exceeded the constraint that requires re-evaluation if a cochlea sparing can be achieved in cases with a short distance between the cochlea and target. One reason for the difference in the dose distribution was the bone labyrinth surrounding the cochlea, and the different densities concerned. This difference in densities could be distinguished in the Micro CT, in which a dose deposition of each layer was recorded, as discussed in the previous chapter. The difference between the TPS and MC occurred at the interface of the heterogeneous area, particularly if the mix of bone densities was within the material of the heterogeneous area. The TPS could not handle the photon-electron across the interface, such as backscatter photons, or backscatter secondary electrons that initiate from other tissue. These phenomena can be noted in interfaces with large density differences. The noticeable factor between the groups in the present study was that the distance between the cochlea and the target affected the dose distribution dramatically.

The study by Zhang *et al.* concluded that a distance of over 1.53 cm between the cochlea and the target is sufficient to spare the target, but that a distance of less than that of a significant dose delivered to the cochlea, and a higher accuracy, is required to spare the cochlea and reduce the side effects (269). The present study found that any distance above 1 cm can be enough to spare the cochlea, deliver a dose below the threshold, and produce a low probability of tinnitus and SNHL. In Group A, the energy fluence distribution that was below that of the original data showed a non-significant difference in both the mean dose and the NTCPs models. Conversely, Group B showed a significant difference, and the two cases concerned were clinically significant. It was therefore important to employ an advanced model to improve the cochlea sparing in the cases with short distances. Case eight exemplified the benefit of using an advanced model, with MC and micro-CT data as the TPS, and showed a dose below the constrained level. Nevertheless, in MC the cochlea still received a higher dose in the maximum dose, indicating the potential development of increased hearing side effects in the future. An advanced model showed that the plan should be re-evaluated to enable the reduction of the dose in the cochlea to reduce the dose

as much as possible. An NTCP model that used dose-volume analysis produced an enlarged result in both groups A and B. Furthermore, the extra cases amplified the results of the NTCP, causing the difference to reach over 50% in some cases.

The three categories in this study had a distance of less than 1 cm, which should have allowed a uniform dose distribution to the cochlea. Among them, two categories demonstrated a non-significant difference in the mean dose distribution and SNHL NTCP models. The last category showed a clinically significant difference in both the mean and the NTCP models. The study by Zhang *et al.* did not use multiscale, and did not connect to the clinical routine (260). The advanced models employed by the present study demonstrated that not all of the differences presented were clinically significant. Furthermore, the cases that were below the level of original data in terms of energy fluence distribution did not show a clinical significance.

7.7 Conclusion

In summary, the advanced model developed by this study connected the MC data that used Micro CT to the clinical routine, in order to evaluate the difference between the MC with a micro-CT data and the TPS clinical resolution. In total, 11 different scenarios were identified from a database of 280 cases of gliomas, and the 11 scenarios were divided into two groups. The first group had an energy fluence distribution that was lower than that of the original data, and the second group had a higher fluence distribution than that of the original data. An overall finding of both groups was the difference in dose distribution between the advanced model and the TPS in all scenarios. Most of the scenarios were not clinically significant, but some showed clinical significance in both the mean dose and the NTCP models. For example, Group A was found to be non-clinically significant, but Group B showed clinical significance in some cases. The distance between the cochlea and the target was identified as a major effect on dose distribution; a short distance of less than 1 cm allowed a more uniform dose distribution, producing a higher difference between the MC and the TPS. Extra cases were selected to test the advanced model further, all of which had a distance of less than 1 cm. The extra cases were divided into three categories, two of which had a lower energy fluence than that of the original data, and were not clinically significant in both dose distribution and NTCP models. However, the third category, which had an energy fluence that was higher than that of the original data, showed a clinically significant difference in dose distribution and NTCP models. Some cases of the advance models therefore presented a

difference that could affect the probability of hearing loss in patients, due to a higher uncertainty of the TPS when dealing with highly heterogeneous areas.

Chapter 8: Gamma Knife

8.1 Introduction

The Gamma Knife is an evolving treatment modality that is increasingly used at various tumour sites. The Gamma Knife is a precise treatment with few side effects, and is considered to be an effective, first option for the treatment of many tumours, including vestibular schwannomas (VS), arteriovenous malformations, brain metastases, and acoustic neuromas (270–273). The first Gamma Knife was introduced in the UK in 1985 at Weston Park Hospital, Sheffield, with more units installed around the country since then (265, 266). The Gamma Knife planning systems are simple and fast. Using data from the standard beam set, the dose distribution is calculated by totalling the number of beams used in the treatment. The system assumes that the target is a homogenous area, like water, and does not consider the heterogeneity and scatter dose contributions in calculating the dose distribution (267, 268). An example target area is the brain, which consists of areas with different densities, such as sinus cavities, the head bone, and hard connective tissues like the dura mater and cochlea. Assuming the target area is homogenous raises the question of the effect of heterogeneity in the treatment. This present study employed MC to study the effect of heterogeneity in the Gamma Knife. Some researchers concluded that heterogeneity does not affect the dose distribution significantly, while others found that there was a significant effect (270). The topic is therefore a matter of considerable debate in the radiotherapy community (277), particularly concerning the effect of heterogenous areas on Gamma Knife dose distribution, although the primary focus concerns dose distribution at the target, not the OAR.

8.2 Objective

This project employed uses the data discussed in Chapter 5 in an advanced model designed for the Gamma Knife, in order to calculate the scatter dose and dose distribution in the OAR using micro-CT data and MC calculation. A schwannoma case was used, because the OAR in this case was the cochlea.

8.3 Literature review

8.3.1 Schwannomas and the side effect of treatment using Gamma Knife

Vestibular schwannomas are benign tumours located near the cochlea. Previously, schwannomas have been treated via microsurgery, but with the introduction of the Gamma Knife in 1969, the treatment has shifted to an alternative approach that is considered to be safe, efficient, and non-invasive. Data documenting the many years of Gamma Knife use to treat schwannomas justify the Gamma Knife as the primary treatment for this type of tumour. The typical dose for the treatment is between 12 to 17 Gy, and it is recommended that the dose should be reduced as much as possible, without compromising tumour control. Due to the tumour's location, many organs, nerves, and vessels are exposed to radiation. Therefore, a highly accurate dose distribution is essential to avoid any complications. The main concern in treating the schwannoma is the side effect of hearing loss, due to the treatment. A reduction in the side effects of the treatment can only be achieved by reducing the dose to the OAR as much as possible by increasing the accuracy of the treatment. The development of Gamma Knife technology, such as the automatic positioning system involved, decreases the uncertainty in dose distribution to help reduce the OAR dose (278).

While the Gamma Knife has replaced microsurgery in the treatment of schwannomas, certain complications have arisen that are due to the radiation delivered to OAR, which must be reduced as much as possible to increase patients' quality of life. Examples of the side effects of treating schwannoma include hearing deficiencies, facial palsy, and brain stem damage (278). Hearing deficiencies arise due to the high dose distribution to the cochlea, and there is no established threshold for the cochlea dose. The study by Regis *et al.* found that a 60% hearing preservation rate was achieved after three years of follow-up in patients who received less than 4 Gy to the cochlea (279). Numerous other studies, including that by Tamura *et al.,* agreed that a dose of less than 4 Gy to the cochlea would preserve patients' hearing (270-274). An accurate calculation is required to ensure that the cochlea receives less than 4 Gy; this cannot be achieved when the TPS does not include heterogeneity's effect appropriately.

8.3.2 Gamma Knife dose distribution in the homogenous and heterogenous area

The Gamma Knife planning system calculates the dose distribution by assuming the head have to be a homogenous density, such as water. However, this assumption can cause an

underestimated or overestimated dose, due to heterogeneity in the target area, or the area around the target, such as bone and air (281). As the Gamma Knife treatment consists of a single high dose, ignoring the heterogeneity can affect the tumour control in some cases, as well as the OAR. The electronic equilibrium and secondary scattering must be calculated adequately to reduce the uncertainty in the treatment. In their study, Solberg *et al.* used a phantom to compare MC and Gamma Knife planning systems, and found a notable disagreement in the dose distribution within the target (282). Similarly, Cheung *et al.* found that the difference in the dose distribution between MC and Gamma Knife planning reached 25% (283). Meanwhile, the study by Dagli *et al.* that used a water phantom and heterogenous phantom to mimic the brain, and calculated the dose distribution using a Geant4 and gamma planning system, also noted the presence of a significant difference, observing that the difference arose from the effect of the inhomogeneity in the target area (277). The study employed a phantom, and focused on the target dose, therefore differing from the focus of the present study, which addressed the cochlea as the OAR. The data used in this study, which was obtained from a simulation conducted on actual patient data, used micro-CT data, and was compared with a schwannoma case. Most previous studies focused on the target area and did not calculate the dose to the OAR, with consideration of the heterogeneity. For instance, Al-Dweri *et al.* compared the dose distribution between the MC and the gamma planning system on a target with bone density, concluding that up to a 12.2% reduction of the dose to the target area with bone density could be achieved (276). The study demonstrated that heterogeneity in the target area can affect the dose distribution significantly, a matter that is addressed appropriately in the Gamma Knife TPS. However, the previous studies in this field neither mentioned nor evaluated the effect of the dose distribution on OAR, such as the cochlea, in cases of schwannoma. The project discussed in this chapter therefore addressed the scatter dose distribution at the cochlea that the Gamma Knife TPS simulates improperly.

The Gamma Knife TPS is fast, due to its simplicity and effectiveness, as shown by the previous treatment data. However, changing the TPS algorithm is not straightforward, because all the information concerned is gained using Gamma Knife simple TPS. Some previous articles compared the convolution algorithm used in the photon TPS with the classic Gamma Knife system, in order to evaluate the difference in dose distribution. For instance, Peters *et al.* simulated a case in which the target was located in a heterogeneous area, in order to compare the convolution algorithm with a classic Gamma Knife TPS (284). The study found that there was a significant

difference in dose distribution to the target area. Moreover, a significant difference of between 14% to 39% was found in the cochlea (284). The study by Boari *et al.* reported a similar outcome, namely that the dose distribution in the cochlea differed significantly between the two algorithms; the convolution algorithm considered heterogeneity, but required an additional CT scan to calculate the dose distribution (285). Further, Xu *et al.* found that there was a clinically significant dose distribution between the convolution algorithm and classic Gamma Knife algorithm in the target area, in the presence of dense bone and air (286). However, the study did not address the effect in the OAR. The study by Osmancikova *et al.* produced a similar outcome, with the cochlea dose distribution difference concerned reaching 15.6% (287). Furthermore, the study suggested that a target located near the heterogeneities was most affected by ignoring the effect of different densities, such as in a vestibular schwannoma case. These studies demonstrated the effect of using an algorithm that includes the effect of the heterogeneity in dose distribution, and reveal that MC remains the most accurate dose distribution tool. Since clinical CT resolution cannot distinguish between the different densities in the cochlea and temporal bone, micro-CT data was used in the simulation in the present study.

8.4 Method

Schwannoma treatment can cause the deposition of some dose in the cochlea, due to the proximity between the target and the cochlea, increasing the side effects of Gamma Knife treatment. The Gamma Knife delivery system differs from that of radiotherapy, as explained in the previous chapter. This study created an MC model to calculate the weighted factor of the scatter dose deposit on the cochlea, using the Micro CT data. As shown in Figure 8.1, the advanced model consisted of three areas: the brain, the tumour, and the cochlea.

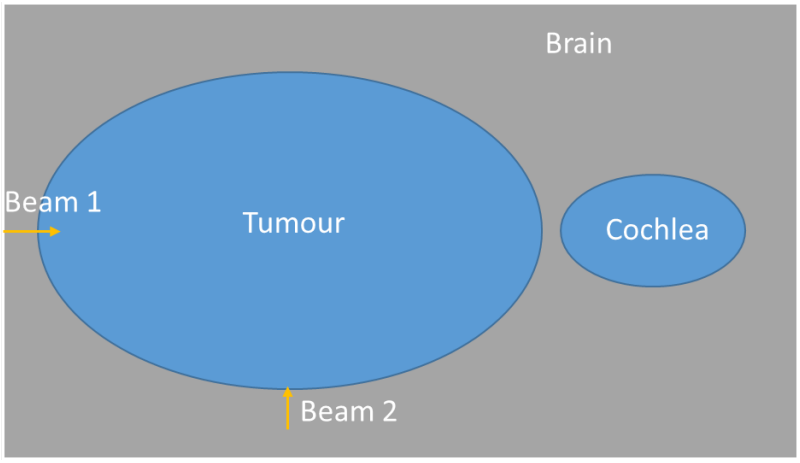

Figure 8.1: The basic model used to calculate the weighted factor for scattering events in Gamma Knife.

The cochlea and tumour size mimicked an anonymised case of a patient diagnosed with a schwannoma. The distance between the cochlea and the tumour was 0.8 mm, measured using Slicer3D. The material of the three parts was water, because the treatment planning algorithm of the Gamma Knife assumes the target and brain are homogenous. In the MC, two energies were used: 1.17 MeV and 1.33 MeV. The first simulation employed beam direction, as shown in Figure 8.1, which began in the target and passed through the cochlea, and was termed 'Beam 1'. The second beam direction did not pass through the cochlea, as seen in the model, and was called 'Beam 2'. The scoring card used was the USRTRACK, which records the track length fluence. The maximum energy recorded was 1.5 MeV. The statistical error was below 2%, by using 500 million histories, dividing the work through 50 CPUs. After the simulation, the results were processed within flair and then saved in ASCII format to enable their reading by MATLAB. The data file was uploaded first into an Excel sheet to calculate the weighted factor for the scatter event for each energy. The weighted factor was then calculated using the Micro CT calculation boundaries, and each fluence from a specific boundary was totalled. Finally, the weighted factor of the scatter events of the 17 different energies was calculated, and the result was used in MATLAB processing.

In total, 34 cases of schwannoma were used in this study, all of which were collected from the cancer archive (288). In all cases, CT and MRI were conducted to increase the accuracy of the

delineation of the target and OAR. The data was then displayed on a 3D slicer, in order to export the DVH data to a format readable by MATLAB. Following this, a dose distribution of gamma treatment planning was extracted. After the data extraction, a degree of editing of the files was required to ensure their compatibility with MATLAB. The final step was to create the DVH using the convolution theory. Finally, the DVHs of the dose distribution in the cochlea calculated using MC were compared with the DVH from the Gamma Knife TPS.

8.5 Results and discussion

In the cases of schwannoma in this study, there was a short distance between the cochlea and tumour (Figure 8.4). The dose distribution of the TPS showed that a significant dose was deposited in the cochlea, as shown in Table 8.1. The lowest difference in the mean dose to the cochlea was 0.2%, and the highest was 8.3%. The average difference across all cases was 3.1% (Figure 8.3).

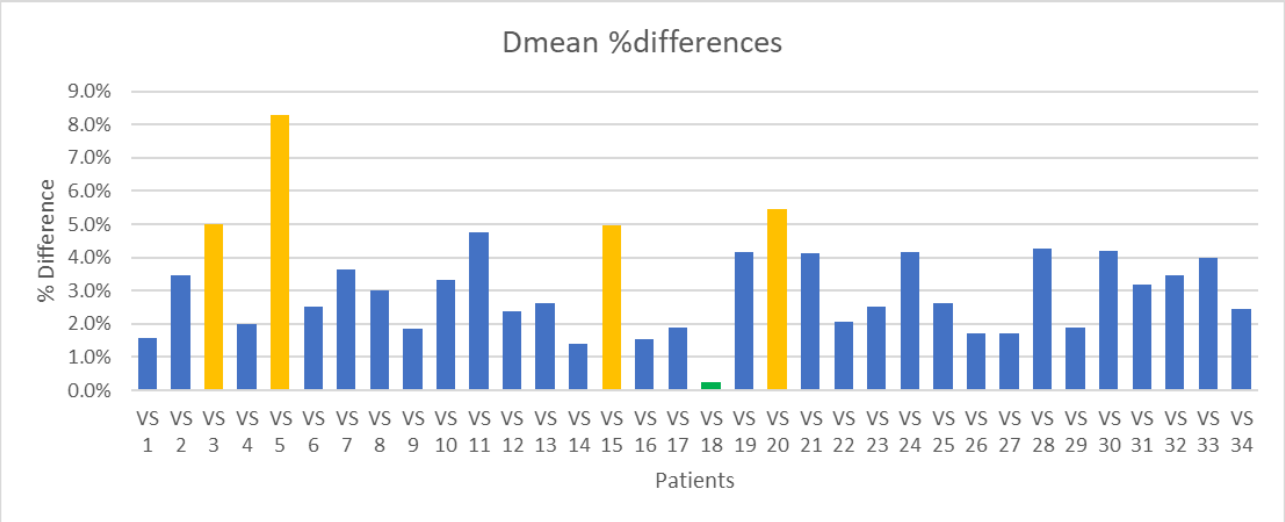

Figure 8.2: The percentage difference of the mean dose distribution in the 34 cases. The yellow bar is the maximum difference recorded, and green bar is the minimal difference. Vestibular schwannomas (VS).

The majority of the cases demonstrated a similar outcome when comparing the TPS and MC in the dose distribution in the cochlea; the majority of the cases had higher doses deposited in the MC than the TPS, and the differences varied between the cases. As discussed in the literature review, the recommended threshold of the dose deposited in the cochlea is less than 4 Gy. In total,

15 cases had a TPS dose higher than the threshold, and the MC reported a higher dose than the TPS. The advanced model provided a lower uncertainty regarding the dose distribution, and helped to provide the best treatment option for the patients concerned. The difference could not be ignored, and should be included to clarify any uncertainty. The difference arose due to having ignored the effect of heterogeneity in the cochlea and the surrounding area. Furthermore, the TPS ignores the effect of secondary scattering and electronic in equilibrium. The results of the simulation were similar to the outcome of the study by Al-Dweri *et al.,* although the difference between the MC and the TPS was lower in this simulation (276). It should be noted that the focus of the present study was the dose distribution to the cochlea, which was considered to be the OAR, while previous studies addressed the heterogeneity in the target area. Additionally, the results obtained by the present study agreed with those of Boari *et al.*, Peters *et al.*, and Osmancikova *et al.*, namely that the dose distribution in the cochlea displayed a significant difference that reached 15%, although in the present study only four cases showed a significant difference in the dose distribution, due to its heterogeneity and the improper handling of heterogeneity in the cochlea by the classic Gamma Knife algorithm (277, 278, 280).

Using MC and micro-CT data decreases the uncertainty of dose distribution in the cochlea, which can help to provide a more accurate treatment, in order to improve the quality of life of the patient concerned. The simulation employed by this study was unique, due to the more complicated calculations regarding the OAR. By using the MC algorithm, micro-CT data, and real patient data, this simulation was closer to the clinical routine than it would have been if it employed a phantom. Although some previous studies used the convolution algorithm, MC offers the highest accuracy available in calculating the dose distribution. Furthermore, the enhanced resolution showed details that are not available in a routine CT, as discussed in Chapter Six.

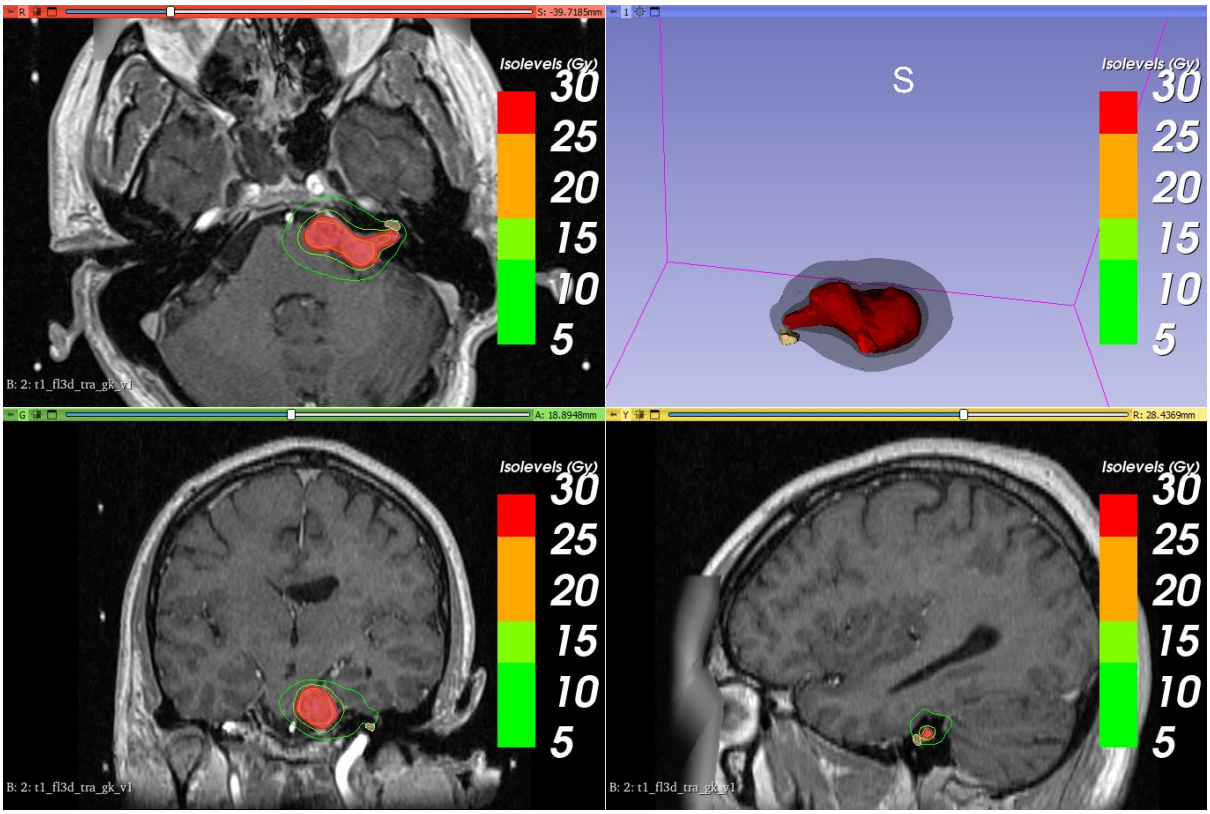

Figure 8.3: Dose distribution of case three from the TPS. The top right is a 3D image of the tumour and cochlea.

(a)

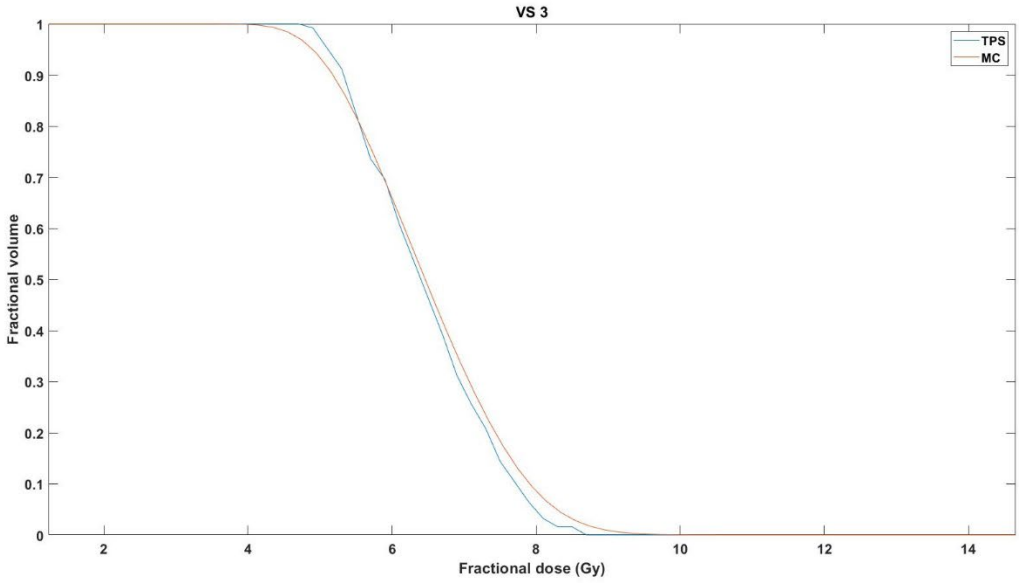

(b)

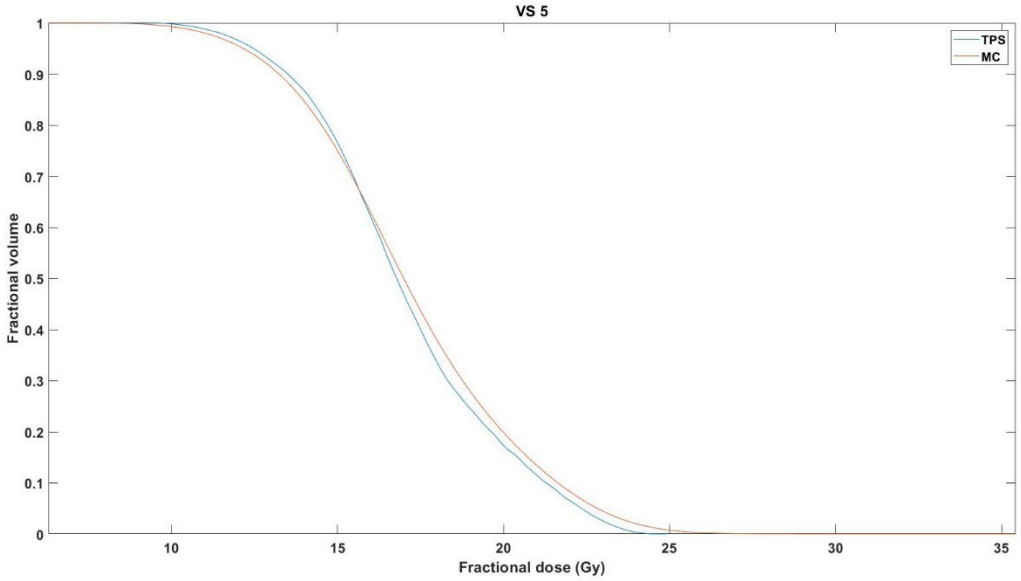
VS 5
TPS
MC
Fractional volume
Fractional dose (Gy)
0
0.1
0.2
0.3
0.4
0.5
0.6
0.7
0.8
0.9
1
10
15
20
25
30
35

(c)

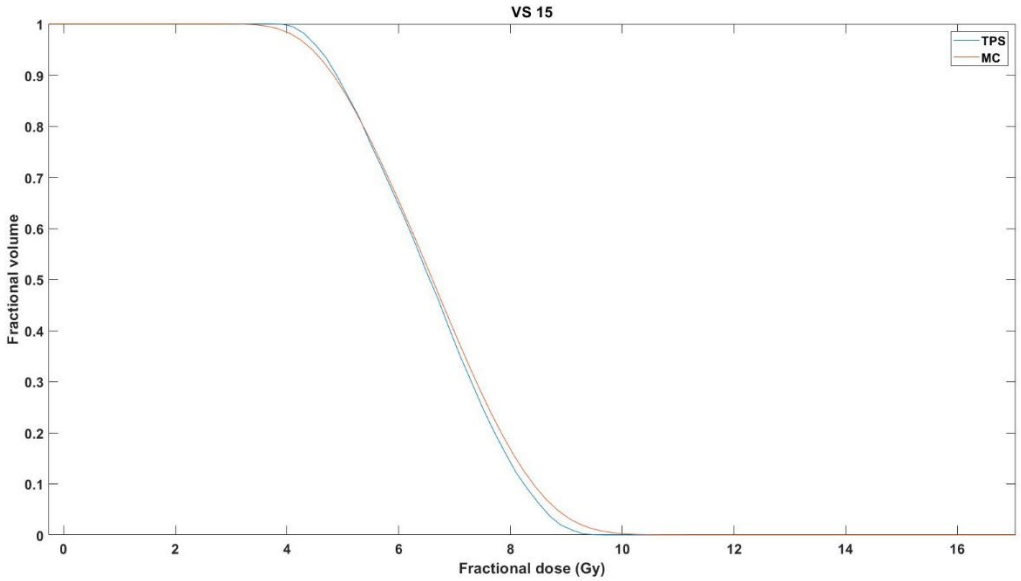
VS 15
TPS
MC
Fractional volume
Fractional dose (Gy)
0
0.1
0.2
0.3
0.4
0.5
0.6
0.7
0.8
0.9
1
0
2
4
6
8
10
12
14
16

(d)

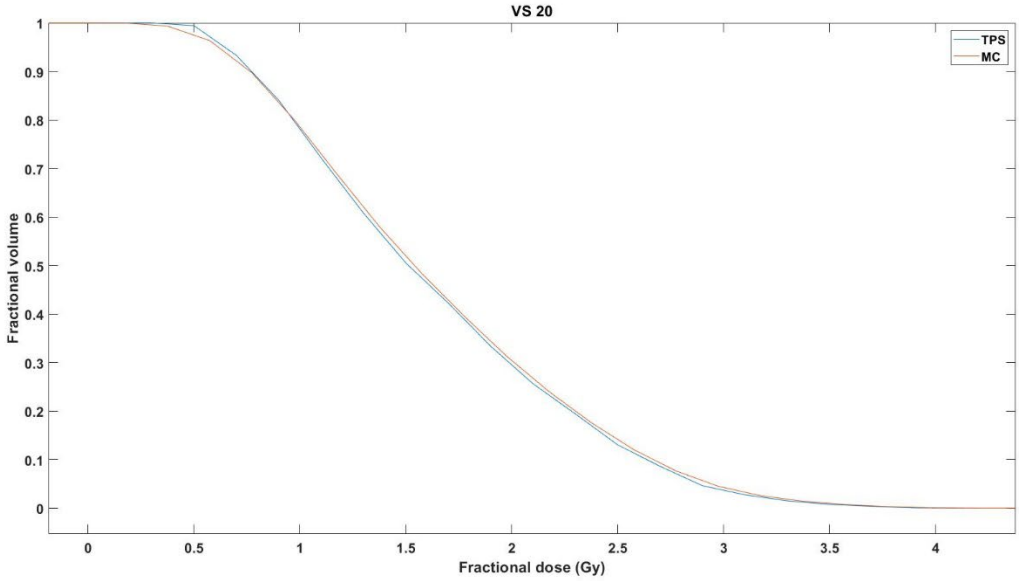

Figure 8.4: The DVH of both the MC and the TPS for the four cases (a-d). The blue line is the TPS, and the orange line is MC.VS3, VS5, VS15, and VS20.

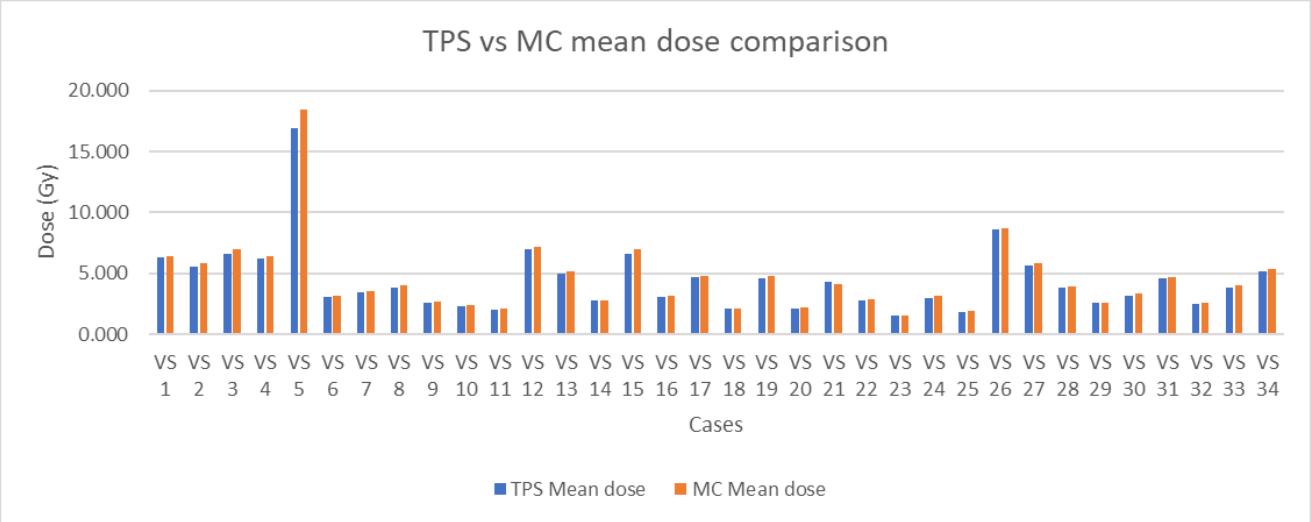

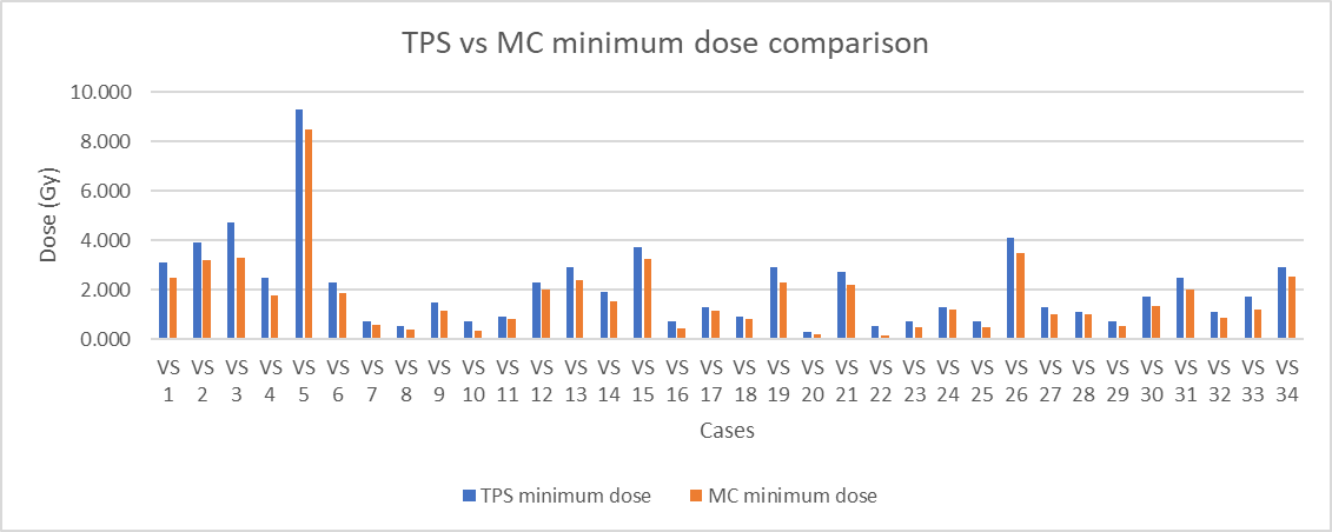

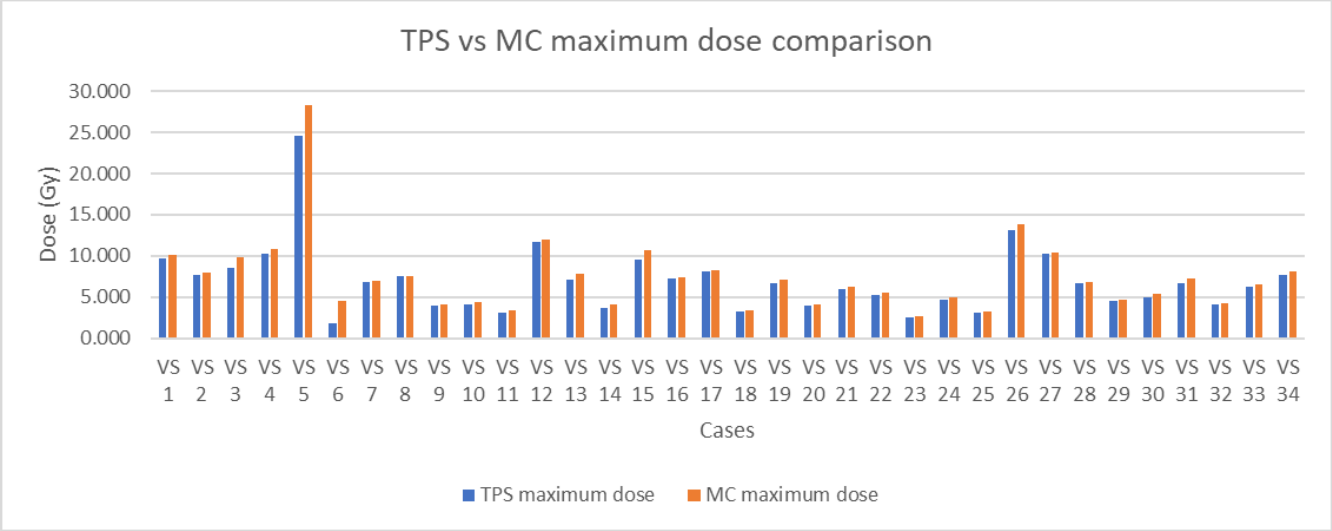

Figure 8.5: A comparison between TPS and MC for Schwannomas cases

8.6 Conclusion

In this study, an advanced model was created to calculate the weighted factor for the scattered dose to the cochlea, in order to connect the data obtained from the micro-CT data of the previous chapter to the clinical routine of Gamma Knife treatment. The Gamma Knife TPS was deemed to be inappropriate, due to the effect of the heterogeneity in the dose distribution on the OAR. The advanced model's simulation of 34 schwannoma cases showed a clinically significant dose difference in four cases, compared with those of the TPS. The TPS underestimated the dose for the majority of the cases, compared with the advanced model, which reached 8.3%. Furthermore, some of the cases had a higher cochlea dose than the suggested threshold, both in the advanced model and the TPS. The difference in the dose distribution was due to the fact that the

effect of secondary scattering and electronics in equilibrium were ignored, which can increase the dose distribution uncertainty, particularly in dense, soft, and air-filled areas. The advanced model decreased the dose distribution uncertainty, which may help to increase the dose to the target, as well as preventing overdosing the cochlea.

The findings from this chapter provide evidence that there are differences in dose distribution within the cochlea between the Monte Carlo simulation and the treatment planning system. Micro CT offers higher resolution than medical CT, which can decrease uncertainties in dose distribution, particularly for the gamma Knife, where high doses are delivered. The outcomes of this chapter highlight the significant uncertainties in dose distribution within the treatment planning system used for gamma knife procedures. The current treatment planning system for the gamma knife is relatively simple and could benefit from an upgrade to a more sophisticated algorithm, similar to the one employed in photon therapy. However, transitioning to an advanced treatment planning system could incur additional costs, as the existing system doesn't require CT scan images; MRI images suffice for dose distribution calculations. In contrast, a CT scan image is necessary for the photon therapy treatment planning system. Nonetheless, the extra cost could prove advantageous for patients by reducing uncertainties in dose distribution, consequently aiding in minimizing radiation exposure to nearby organs at risk (OARs). The enhanced model presented in this chapter has the potential to evolve into a universal model for the cochlea. Further testing with a larger patient sample could facilitate the development of guidelines aimed at minimizing uncertainties in dose distribution when utilizing gamma knife treatment for schwannomas.

Chapter 9: Multiscale modelling of proton dose distribution

9.1 Introduction

Proton beam therapy is a cancer treatment modality that uses charged particles to eliminate cancer cells. It is a treatment whose availability has increased in recent years. The concept of proton therapy is to allow a controlled proton to travel to a specific depth, as a result of energy input, in order to deposit the maximum energy to a target. The physics behind proton and photon therapy differs in all aspects. Photons penetrate the material and continue to lose their energy, even after reaching the target, because the therapy delivers high doses to normal tissue beyond the target area. In contrast, proton therapy increases the dose when it penetrates the material and deposits maximum energy in the target, while nothing is deposited beyond the target. The physics of proton therapy engenders a reduction in the dose to normal tissue beyond the target area. Despite the drawback of the therapy is that it is costly, compared with photon therapy, its advantages mean that there has been a worldwide increase in the number of centres offering this treatment in recent years. The deposit of the maximum dose in the target area requires a high accuracy treatment plan that considers how heterogenous areas may affect the beam. The smaller the margin of uncertainty in the treatment, the fewer side effects are seen.

9.2 Literature review

Radiotherapy and proton therapy aim to achieve a high dose to the target, and a minimal dose to the OAR, in order to reduce any side effects. The TPS can produce a highly accurate treatment in homogenous areas, but there is increased uncertainty in a heterogeneous area. A heterogeneous medium can affect the dose falloff advantage in proton therapy, and the penetration and lateral scattering can be distorted, due to density changes. When creating a proton treatment plan, it is essential to account for the heterogenous area in the target volume or beam direction when considering the coverage and range of volume. Patient selection for proton therapy is the primary key to successful treatment, and the ideal choice for proton therapy is a patient who may experience a high dose to the OAR surrounding the target area. However, proton therapy is not ideal if a large volume of heterogenous material is within the beam path. Major uncertainties can occur in patient positioning, intrafraction organ motion, or physiological instability during the treatment course. In these scenarios, photon treatment can achieve a better outcome than proton

therapy. The effect of the heterogeneous area can differ in different clinical cases, and the clinical situation can be categorized into three different scenarios. The first scenario is that heterogeneity covers the entire beam direction. The second is that heterogeneity is in one part of the lateral direction of the proton beam. The third is the case of a small complex structure with high heterogeneity in the proton beam.

Understanding the effect on the proton beam in the first scenario, with heterogeneity located in the beam direction, can help to decrease the uncertainties within the treatment plan. The mechanism of proton loss energy is similar in an area with a close density range, but the energy loss differs in high Z elements, and in highly hydrogenous substances. The primary method of proton loss energy is through electromagnetic interactions with electrons. Here, a proton loses a minimal amount of its energy after interaction with an atomic electron, due to the differences in mass, as the mass of a proton is approximately 1800 times larger than the mass of an electron. Furthermore, the proton is deflected in a non-significant amount in each interaction, which can be ignored. The chances of nuclear interaction increase with rising proton energy, and although this interaction does not impact the therapeutic energy range significantly, it does impact the shape of the Bragg peak. Nuclear interactions produce secondary particles that decrease the intensity of the proton beam. The secondary particles have a higher relative biological effectiveness value that is essential from a biological point of view. However, the secondary particles are negligible in their impact on the dose distribution. The large heterogeneous area in the beam direction primarily affects the beam range, and does not alter the shape of the depth dose in volume distal to the heterogeneity.

The second scenario occurs when heterogeneity crossing the proton beam is restricted to the boundary between two media. Here, the beam's penetration is altered in the heterogenous area, and decreases when the heterogenous density introduced is higher than the density of the medium that the proton beam passes through. The introduction of a volume with a density that differs from the surrounding medium can alter the part of the beam that intersects with the heterogenous material, but does not alter the part that does not intercept with the heterogenous material. The boundary region is where there is a difference in the multiple Coulomb scattering between the two densities, and it can cause a hot spot in a low-density area, or a cold spot in a high-density area. The most extreme alteration in the dose can be observed in the interface between air and tissue, reaching a figure as high as 50%. The presence of air on one side is considered to be the worst

case scenario, but if both sides do not contain air, there are still different scattering powers, and so the perturbation will decrease. For example, if bone and tissue are the two interfaces, the dose perturbation is around 9% compared with air, which is reduced significantly.

The last scenario occurs frequently in clinical situations in which small, complex heterogeneities cross the beam direction. One of the most complicated cases involves the base of the skull. In the skull base, the proton must travel through extended bone surface, or a complicated heterogenous region. Due to the complex heterogeneity, a significant increase in the range uncertainty occurs, and multiple Coulomb scattering causes dose nonuniformities.

The study by Urie *et al.* evaluated the effect of the complex heterogeneity in a proton beam, and found that multiple Coulomb scattering was the primary source of Bragg peak degradation, and that using the stopping power of the heterogenous material to calculate the Bragg peak degradation was not possible (289). Furthermore, the study indicated that increasing angular divergence can resolve the Bragg peak degradation and widen the lateral falloff. Meanwhile, Sawakuchi *et al.* conducted simulations to understand the causes of increasing distal falloff width, concluding that high complex heterogenous volume was the primary reason (290). Furthermore, the study agreed with Urie *et al.* that the Bragg peak degradation was caused mainly by multiple Coulomb scattering (289). The simulation concerned demonstrated that nuclear scattering had a small effect of 5% on the distal falloff of the Bragg peak. In the study, a TPS that operated on the analytical model could not comprehend the effect that caused uncertainty in the distal edge, and the uncertainty of the highly complex heterogeneity region was approximately ± 1mm in distal edge degradation. However, an MC algorithm had the potential to report a more accurate dose deposition in proton therapy than an analytical TPS. Meanwhile, in their study, Yamashita *et al*. identified the presence of a significant difference between MC and TPS in the distal falloff in the spread-out Bragg peak, due to complex heterogeneity in the proton beam path (291).

Uncertainties in dose distribution and range increase in the presence of heterogeneity. Further, the need for high accuracy dose distribution is higher in proton therapy, because of the maximum level of deposition in the target. High accuracy is essential in reduced target volume, because small lesions are treated with a small number of fields and a high single fraction dose; an error in one field cannot be covered by other fields, causing a reduced dose to the target. The size of the field is essential for determining the magnitude of the dose uncertainty in the treatment. The number of pencil kernels is required for the calculations related to the field size. Smaller pencil

kernels are required for small field sizes, which means that each pencil kernel's magnitude of dose inaccuracies is greater. Moreover, two factors can increase the dose uncertainty in proton treatment planning: first, the difference in modelling that occurs before the proton reaches the patient, and second, the heterogeneity inside the patient from different scattering scales. The first factor is out of scope, as it occurs before it reaches the patient, and is due mainly to aperture and range compensator. In recent years, with advancements in computing power that have enhanced the availability of MC algorithms, increased focus has been assigned to the second factor. The study by Paganetti *et al.* evaluated the effect of heterogeneity in proton treatment plans for patients with small lesions and recorded cold and hot in the target volume, as a result of scattering in a heterogeneous area (292). Furthermore, it identified a degradation in the range of the beam. The study also found that while the difference in range and dose distribution was less than 3%, which was not clinically significant, for individual beams, the difference reached 8.6%.

Many previous studies agreed that the complexity of the heterogenous area has a significant effect on proton therapy, and that the TPS cannot predict the dose in these scenarios correctly (216, 284). For instance, Paganetti *et al.* (294) assessed various patients with different levels of heterogeneity, concluding that the more complex the heterogeneity, the higher the difference in dose between the TPS and the MC. The difference reached 5.4% in the target of one patient, and the TPS overestimated the dose to target, temporal bone, and cochlea. The difference was as low as 1% in the area of low heterogeneity. Additionally, the tolerance of single fields exceeded the accepted limit of the treatment plan, which was highlighted when comparing it with the MC result. The multiple fields treatment was within the clinical limit.

Most previous studies demonstrated that a TPS creates a more clinically acceptable plan in a homogenous area than MC, and in some cases in a heterogeneous area. However, the difference was higher between the TPS and the MC, and differed by the treatment site. A higher dose was recorded in the TPS than the MC in low homogenous areas of the liver and breast, with a difference of less than 2%, while the highest difference recorded in the head, neck, and lung reached an average of 4%, a figure that was below the acceptable limit of the clinical tolerance of 5%. However, the difference reached more than the tolerance level in some cases. In addition, the tumour control probability difference could reach up to 6% in some head and neck patients (223,293–297).

9.3 Objective

In the study discussed in this chapter, an MC simulation of proton therapy was conducted around the temporal bone, an area that contains the middle and inner part of the ear, and the cochlea. The simulation was executed using the Micro CT DICOM series, and sought to evaluate the effect of heterogeneity in proton beam dose distribution using a micro-CT data.

9.4 Material and methods

The DICOM series used by the project discussed in this chapter was similar to that used in the study discussed in the previous chapter, and no changes were required to the CT, because all of the necessary steps were applied in the previous chapter. Specifically, the HU and header information were modified in the last chapter, and were therefore ready for use in this project. The MC code used in this study was FLUKA, although certain modification were required to mimic the proton therapy in clinical practice. It was necessary to add the global card to allow FLUKA to comprehend the high number of voxels in the DICOM series. The simulation time was one of the main issues of the MC simulation, therefore to ensure a realistic simulation time, a HADROTHrapy card was used. This card also increased the accuracy of the simulation. The EMFCUT was employed to allow more control than the default option in the minimal energy of the electrons. Following this, the beam card was changed to the proton, and the HADROTH option was added in the default card. Furthermore, the FLOOD option was used to ensure equal distribution. In the card sheet, momentum was chosen to ensure gaussian distribution. The DICOM series was uploaded using the FLAIR option, as in the study in the previous chapter, and a water phantom was added around the target. After adding all these cards, the simulation model was ready, and only the number of histories and energy was changed each time. FLUKA contain different atomic physics models that are used to comprehend the different scenarios, such as continuous energy loss, delta ray production, and Coulomb scattering. The acceptable uncertainty level was <2%, requiring a high number of histories to reach that level, although it was a smaller number of histories than photons.

9.4.1 Modification of the energy

An MC simulation requires input energy for the proton beam, and in the study discussed in this chapter, multiple energies were used. The deposited energy used in the simulation was

extracted from the TPS of the head and neck plan, information that can be found in the RT and RD files generated by the TPS. The information was calculated for the initial energy at the surface, not the cochlea located 4 cm from the skull. The depth of the cochlea was measured during the treatment planning stage, and a roller was used to measure the depth of the cochlea from the skull. Then, a two-step modification of the energy deposition was conducted for the new location. The first used the NIST PSTAR database to collect the stopping power of different energy levels, and a natural logarithm of energy and stopping power was calculated. The natural energy was plotted, preventing the power algorithm from calculating a regression line equation. This first step was essential to acquire the slope and intercept value for the new energy deposition calculation model in 4 cm. The equation used was as follows:

$$logS = logE * M + C \tag{9.1}$$

$$A = 10^{C}$$

E is the energy and S is the stopping power from the NIST database. The intercept value C is 5.6, and the slope value M is 0.7832. A is calculated at 270. The second step was to create the calculation model, which was as follows:

$$\int_{Emin}^{Emax} \frac{DE}{S(E)} \quad where\ S(E) = AE^{-\Delta} \tag{9.2}$$

$$= \int_{Emin}^{Emax} \frac{dE}{A} E^{\Delta}$$

$$\frac{E_{max}^{\Delta+1}}{A(\Delta+1)} - \frac{E_{min}^{\Delta+1}}{A(\Delta+1)} = D$$

$$E_{min}^{\Delta+1} = \left(\frac{E^{\Delta+1}}{A(\Delta+1)} - D\right) A(\Delta+1)$$

The D value is the distance to the cochlea, 4 cm. The delta is the slope value from the regression line equation 0.7832. Table 9.1 shows the calculation results to obtain the energy level at 4 cm for the simulation.

Table 9.1: The energy level at the surface, and the calculated energy at a depth of 4 cm.

The energy at the surface (MeV)	The energy at 4 cm (MeV)
81.70	37.59
86.39	45.72
90.81	52.73
95.02	59.00
99.05	64.73
102.92	70.04
106.66	75.03
110.29	79.76
113.83	84.28
117.31	88.65
120.73	92.88
124.11	97.01
127.47	101.06
130.83	105.07
134.20	109.05
137.59	113.02
141.02	117.00
144.49	121.01
147.83	124.83

After calculating the energy required for the simulation, a FLUKA cards environment was established for each energy. The only change between each MC simulation was the energy, and every other card was consistent. The final step before data analysis was to calculate the weighted factor for each energy level that modelled the ion chamber response as a function of energy. The weighted factor was calculated using information obtained from the DICOM and NIST databases. The slope and intercept from the fitting curve of the natural log of energy and stopping power were used to calculate the modified weighted factor using the following equation:

$$Weighted\ factor = number\ of\ proton\ X\ E^{-1/2}$$

The new modified weighted factor is shown in Table 9.2, and was used to analyse the data.

Table 9.2: The new calculated weighted factor for the target.

Beam energy	Weighted factor (from DICOM)	New weighted factor
147.83	29.26	6.01
144.49	9.57	1.93
141.02	7.84	1.55
137.59	6.05	1.18
134.20	4.91	0.94
130.83	4.08	0.76
127.47	3.47	0.64
124.11	3.03	0.54
120.73	2.69	0.47
117.31	2.44	0.42
113.83	2.26	0.38
110.29	2.12	0.35
106.66	2.02	0.32
102.92	1.94	0.30
99.05	1.89	0.29
95.02	1.85	0.27
90.81	1.82	0.26
86.39	1.79	0.25
81.70	1.78	0.23

9.5 Results and discussion

The toxicity of radiotherapy treatment is a core topic that was much discussed by previous studies. Radiotherapy treatment aims to achieve a high dose to the target, and as low a dose as possible to the OAR. Proton therapy can deliver a high dose to the target and a very low dose to the OAR, because of the physical property of the proton. However, uncertainty has a higher impact in proton therapy, particularly in small fields, as multiple errors can be found that cause a reduced dose to the target. Understanding the interaction of the proton with an area of high heterogeneity by adding a correction factor to the TPS can be beneficial. Furthermore, studying the effect of the heterogeneity at the micro level is a new approach that can help to decrease the uncertainty. The simulation of proton interaction should be conducted in the gold standard algorithm, namely MC, in order to achieve a high trust result. The code used in the simulation in this study was the MC FLUKA code, and the uncertainty of the simulation was <2%. The total time required to complete the MC simulation was around 180 hours. The number of CPUs used in each simulation was 60.

The total uncertainty was 0.75%. Table 9.3 shows the energy, the number of histories used, and the uncertainty achieved in each simulation.

Table 9.3: The energy and number of histories used in each simulation to reach the uncertainty level desired.

Energy (MeV)	Total histories	% uncertainty	FWHM
37.59	6.00E+07	2.35%	2.76%
45.73	9.00E+07	2.42%	2.84%
52.74	1.50E+08	2.55%	2.99%
59.01	1.50E+08	1.85%	2.17%
64.73	1.80E+08	1.35%	1.59%
70.05	3.00E+08	0.93%	1.10%
75.03	6.00E+08	0.42%	0.50%
79.77	9.00E+08	0.26%	0.31%
84.29	9.00E+08	0.23%	0.27%
88.65	1.50E+09	0.17%	0.19%
92.88	1.20E+09	0.18%	0.21%
97.01	9.00E+08	0.21%	0.24%
101.07	9.00E+08	0.20%	0.24%
105.07	9.00E+08	0.21%	0.24%
109.05	9.00E+08	0.20%	0.24%
113.02	9.00E+08	0.21%	0.25%
117.01	9.00E+08	0.22%	0.25%
121.02	1.50E+09	0.18%	0.21%
124.83	2.10E+09	0.15%	0.18%
	Sum	0.75%	0.88%

The tolerance level of the statistical uncertainty was achieved in all of the MC simulations for the proton, which increased the data confidence. The second step conducted a uniformity test to evaluate the FLOOD option and to ensure uniform distribution. Figure 9.1 shows the uniformity test and the quadratic fit. The uniformity was 99%, showing a high uniformity within the target area. The MC simulation passed the tests, therefore the data could be analysed.

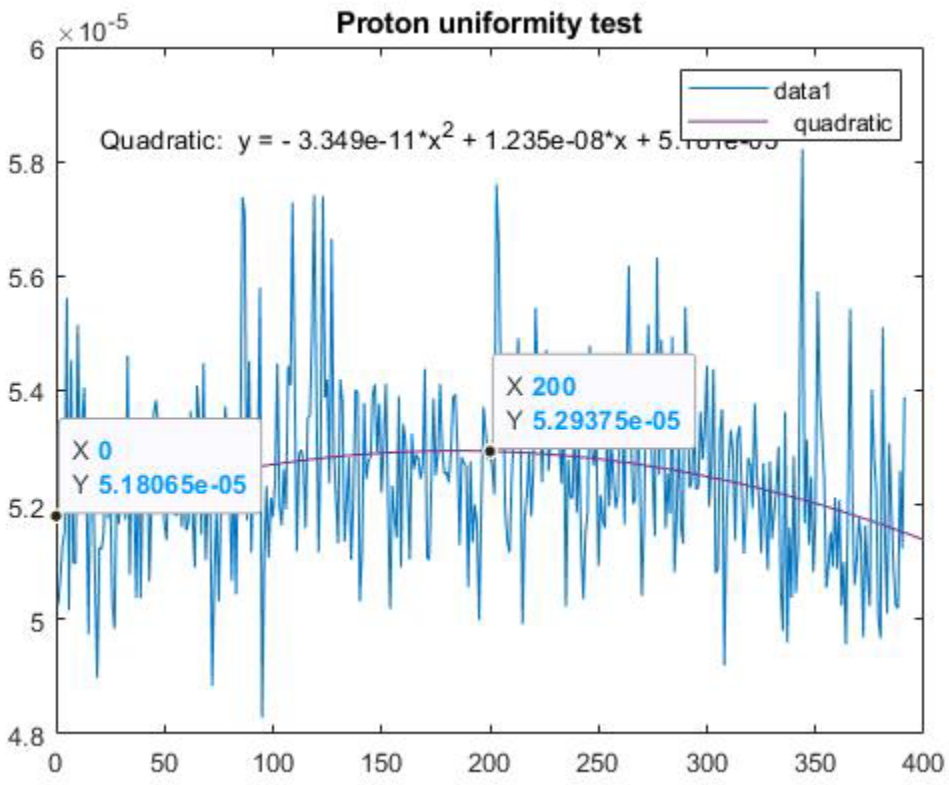

Figure 9.1: A cross-section of the water phantom with quadratic polynomials fit to test the uniformity within the target.

9.5.1 Individual beam energy

The simulation was conducted for the beam energy levels extracted from the TPS. Each energy beam was simulated to test their behaviour and effect at the micro level. In all, 19 energies were used in the simulation, after depth modification. Each energy was simulated, and their deposit behaviour was recorded for the three-level density. The dose distribution between the three densities did not change significantly between the different energy levels. The proton interaction behaviour also did not change when the proton energy was increased or decreased. The micro interaction in different density levels differed between the photon and proton, as there was a significant change in the deposition behaviour in the photons, but no change in the behaviour in the protons. Most of the proton deposition dose was in a low-density region, and the second-highest dose was in a high-density region. However, the medium density received a consistent dose over the different energy levels. Table 9.4 shows the dose deposition at the different density levels.

Table 9.4: Different energy levels and their distribution.

Energy (MeV)	Low density	Medium density	High density
37.59	54.86%	19.75%	25.39%
45.72	55.06%	19.69%	25.25%
52.73	55.14%	19.76%	25.10%
59.00	55.12%	19.56%	25.33%
64.73	54.92%	19.54%	25.54%
70.04	54.62%	19.71%	25.67%
75.03	54.50%	19.77%	25.74%
79.76	54.48%	19.78%	25.74%
84.28	54.21%	19.84%	25.95%
88.65	54.16%	19.85%	25.99%
92.88	54.16%	19.84%	25.99%
97.01	54.12%	19.84%	26.04%
101.06	54.15%	19.86%	25.99%
105.07	54.16%	19.83%	26.01%
109.05	54.22%	19.77%	26.01%
113.02	54.16%	19.81%	26.03%
117.00	54.17%	19.82%	26.01%
121.01	54.15%	19.79%	26.07%
124.83	54.21%	19.79%	26.00%

The percentage dose deposition of proton in the three different density layers did not change with increasing energy. The stability of the percentage of the dose in the three layers gave the proton an advantage in an area with a density change, because the pattern could be predicted by excluding the proton behaviour in the air. The difference between the weighted factor of the highest energy level, 124 MeV and 121 MeV, was significant, increasing approximately four times. The significant increase indicated that the highest energy was the dominant beam in the summation, and the main contributor to the final sum beam. As shown in Table 9.4, the dose distribution between the three-density levels did not change significantly after the energy level of 88 MeV. Figure 9.2 shows the histogram of the dose distribution of the 97 MeV, which did not have a gaussian shape, due to the low energy that contributed only 3% of the final sum weighted factor. From the energy of 105 MeV, the histogram began to take a Gaussian shape, and the deposition at the low-density levels was much higher than at the other two densities. However, the proton interaction did not rely on material density, therefore the distribution of the dose did not change significantly between the low and high energy level of the proton. The proper separation

between the dose deposition and the three-density levels was shown in energy 113 MeV and above (Figure 9.2). The highest four energy levels of the beam contributed 62% to the weighted beam factor, and the 124.8 MeV proton energy alone contributed to 35% of the beam.

Assessing the highest proton energy dose distribution histogram clarified the final histogram shape and distribution in the Micro CT data. The highest weighted factor for one photon energy level was 10.12%, which was significantly lower than the highest weighted factor for proton. For the photons, the lower-level energy still contributed significantly to the final beam from 0.9 MeV. The contribution of the weighted factor was 56.34%, and the remainder was for high energy. The difference between a proton and photon is that a proton beam is weighted heavily in high energy, but low energy can affect the final beam distribution in a photon. As shown in the histogram of the individual energy levels of a proton beam in the Micro CT data, the density change did not alter the proton's interaction with the materials significantly. Furthermore, the dose distribution and energy deposition were approximately stable between all of the proton energy levels. The energy and dose deposition changed significantly between the density and photon energy level, compared with the photon.

(a)

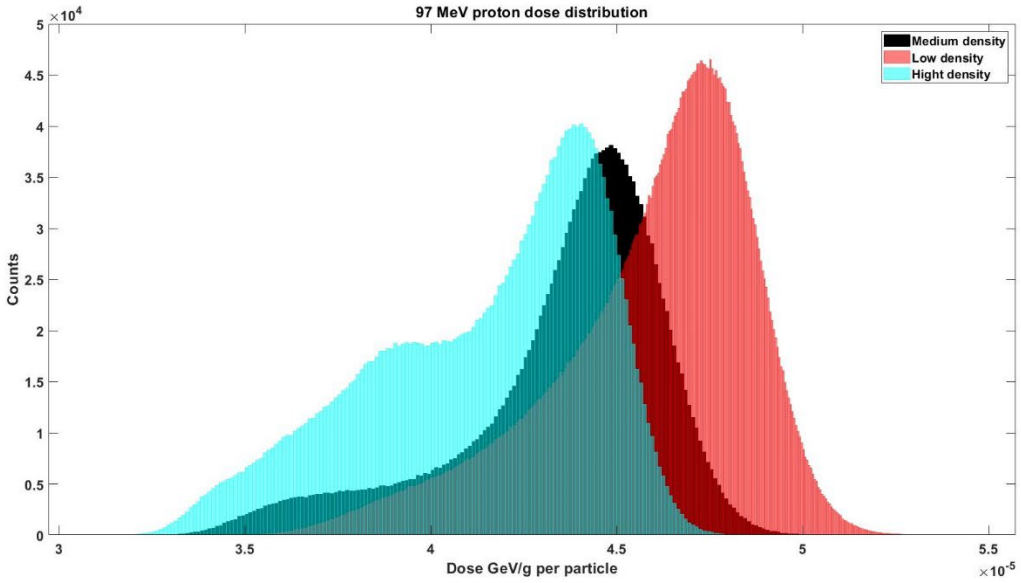
97 MeV proton dose distribution
×10^4
Counts
Dose GeV/g per particle
×10^-5
Medium density
Low density
Hight density

(b)

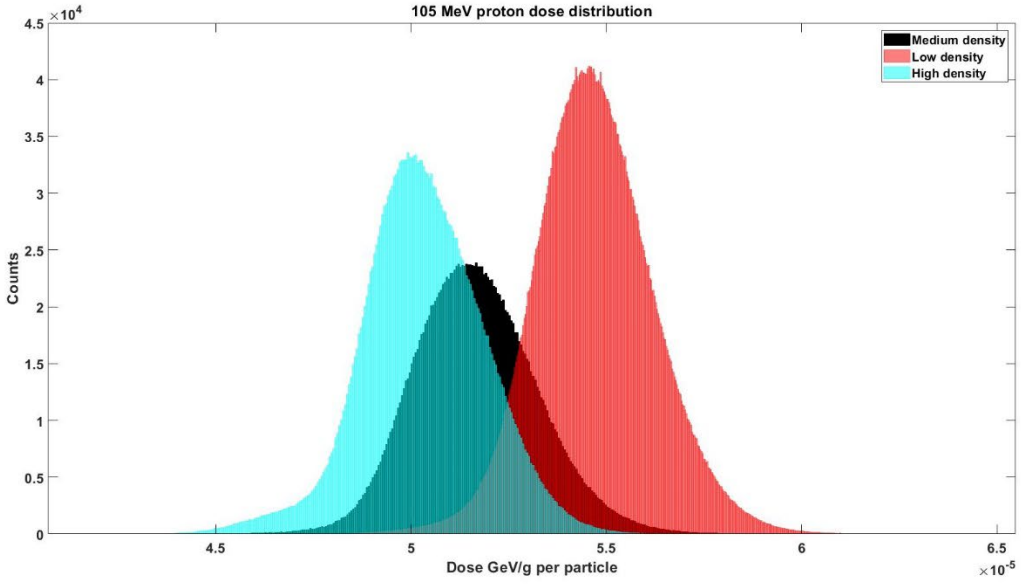
105 MeV proton dose distribution
×10^4
Counts
Dose GeV/g per particle
×10^-5
Medium density
Low density
High density

(c)

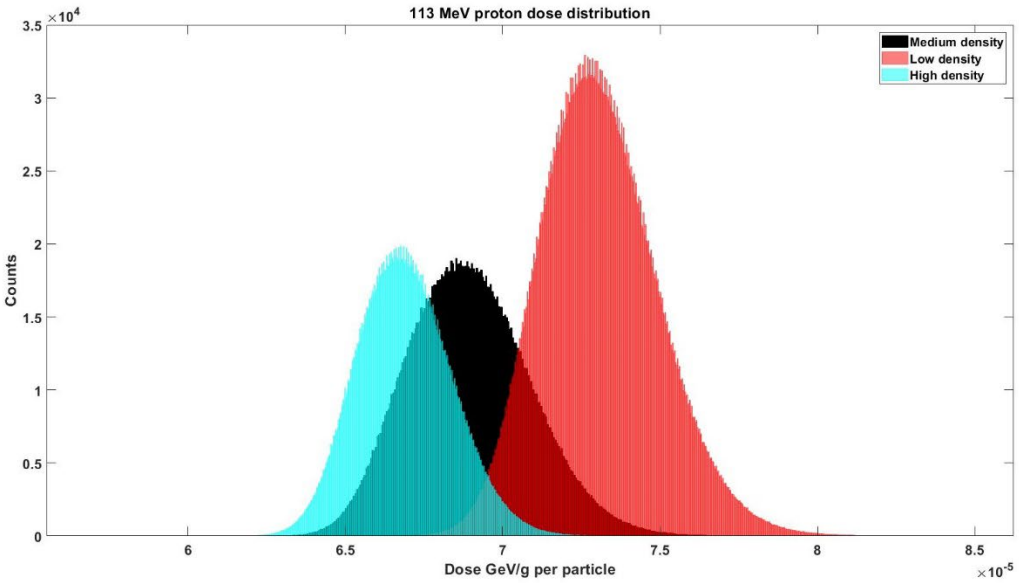
113 MeV proton dose distribution
×10^4
3.5
3
2.5
2
1.5
1
0.5
0
Counts
Medium density
Low density
High density
6
6.5
7
7.5
8
8.5
Dose GeV/g per particle
×10^-5

(d)

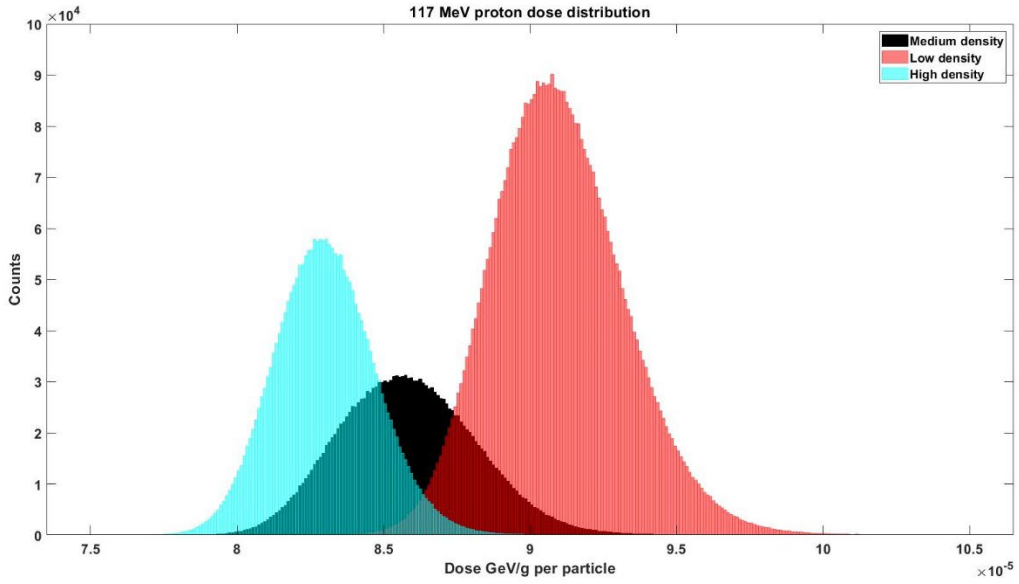
117 MeV proton dose distribution
×10^4
10
9
8
7
6
5
4
3
2
1
0
Counts
Medium density
Low density
High density
7.5
8
8.5
9
9.5
10
10.5
Dose GeV/g per particle
×10^-5

(e)

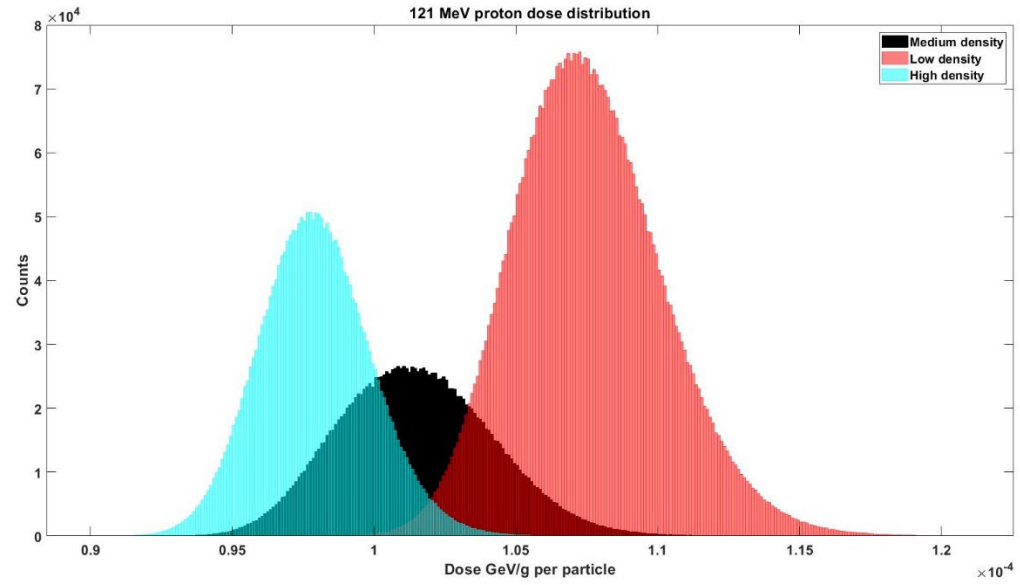

(f)

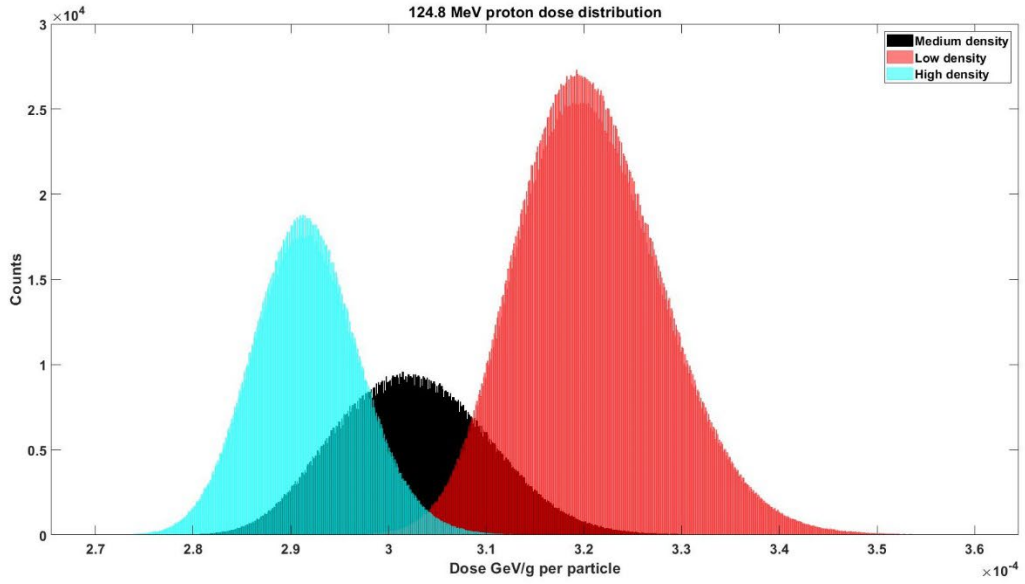

Figure 9.2: Histogram of the individual beam dose distribution in the different density levels (a-f). Red denotes the low density, black the medium density, and blue the high-density materials.

9.5.2 Beam summation

The first part of this chapter discussed the behaviour of individual proton beam energies in the heterogeneous region at the Micro CT level. In order to relate this to clinical work, an understanding of the beam's summation with a weighted factor was calculated to mimic the TPS in cochlea depth. Figure 9.3 presents a histogram of the summation of the beams, showing a separation of the three-density dose deposition. Most of the dose distribution was at a low density,

and the second highest distribution was evident in the high-density region. As discussed previously, proton interaction with matter differs from photon interaction, which is why density has a minimal effect on high proton energies levels.

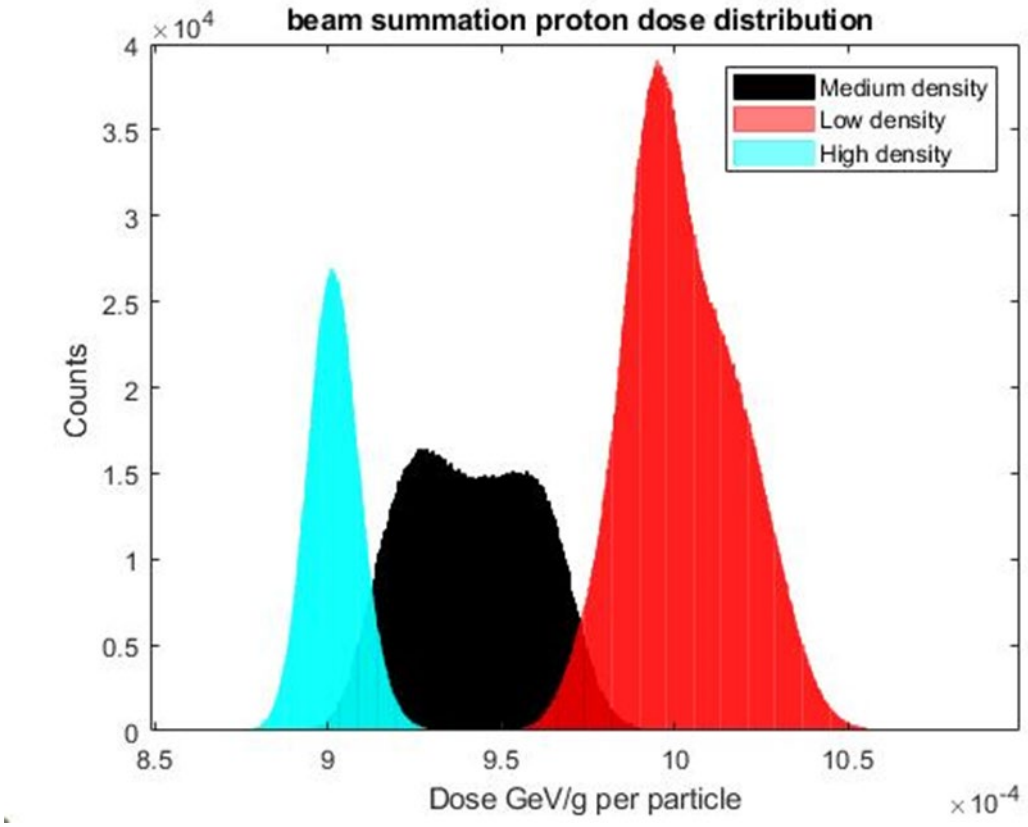

Figure 9.3: Histogram of the summation of all beam energies of the proton.

Table 9.5: The FHWM of the proton summation dose.

File	Mean value	Real mean	SD	FWHM	Real FWHM	FWHM fraction of dose
Final sum	9.63E-04		4.62E-05	1.09E-04		0.112
Low density	1.00E-03	1.04E+00	1.63E-05	3.82E-05	3.52E-01	0.038
Medium density	9.41E-04	9.77E-01	1.86E-05	4.37E-05	4.03E-01	0.046
High density	9.02E-04	9.36E-01	7.41E-06	1.74E-05	1.60E-01	0.019

An FWHM fraction of dose was calculated from the simulation data to demonstrate the widest peak of the three densities. This was found to be the medium density, which could not be

separated from other densities using the clinical CT resolution. The medium density in both the photon and the proton had the widest distribution, compared with the other densities. The highest mean dose was the low density, and the most deposited dose in the proton in terms of both protons and photons was also the low density.

This study addressed dose distribution and the effect of the heterogeneity in Micro CT levels. The proton dose distribution was found not to change significantly, compared with a photon, altering the distribution between the different energy levels. In heterogeneity, the proton could be predicted with more accuracy, in terms of dose distribution. However, the proton range could be affected dramatically in the present heterogenous area, particularly if the air was not tested. All of the simulations were conducted using MC, as it has the highest accuracy in simulation interaction in the heterogenous area. A limitation of this simulation was the fact that the proton range's effect was not included, and the samples had a lower air component than in normal DICOM. As mentioned previously, much of the air was extracted, in order to store the samples properly.

9.6 Conclusion

The availability of proton therapy has increased in recent years, due to its advantage of sparing OAR, particularly in the head and neck area. Understanding the behaviour of dose distribution in a heterogenous area in micro-CT data can add the need for correction factors in the TPS. In the previous chapter, photon behaviour was explored and found to display variations between different levels. micro-CT data added a more detailed density separation in the region of interest. For the proton, the difference in density did not affect the dose distribution between different energy levels significantly, as shown in the simulation. Furthermore, the low proton beam energy levels did not contribute significantly, affecting the final summation histogram. The simulation result concluded that the proton dose distribution was not affected significantly by the region's heterogeneity in micro-CT data. However, the simulation did not evaluate the effect on the proton range.

Chapter 10: Conclusion and future work

10.1 Summary and conclusion

This chapter summarizes the primary findings of this thesis and the subsequent effects on clinical routine. The chapter also discusses possible future work that might improve the uncertainty of dose distribution, using the findings of this thesis.

This thesis had two aims: 1) to investigate the dose distribution uncertainty in the presence of heterogeneity in micro-CT data for photon and proton beams in the temporal bone and cochlea, and 2) to assess how this uncertainty can affect the clinical routine. The second aim explored the effect of the high-density stent on dose distribution in pancreatic cancer patients. The effect of uncertainty was demonstrated using the multiscale approach and the FLUKA algorithm, in order to assess the effect in both photon and proton beams. In addition, an advanced model was created to connect the result with a clinical routine for radiotherapy and Gamma Knife treatment. The second aim was achieved by creating a new model that mimicked the stent material with improved contouring, and through the use of the PENELOPE algorithm. Finally, a comparison demonstrated the effect of the new model on dose distribution in single beam and VMAT treatment.

In Chapter 4, a Varian Truebeam was modelled using the PENELOPE code from the PRIMO interface. The fine-tuned parameters for 6 MV were a focal spot of 0.14 cm, an initial energy of 6.25 MV, beams divergent of 2.5, and energy of FWHM 0.15 MeV. After tuning the Varian Truebeam to the optimal configuration, validation tests were conducted using the PDD curve, dose profile, TPR, and output factor. The validation tests were compared with the data from the golden beam. The validation test for the MC model passed all of the criteria for the ranges from 5×5 to $40 \times 40\ cm$. Therefore, the MC model could be used to produce clinical MC plans for future studies.

In Chapter 5, a new model was created to increase the accuracy of the dose distribution in pancreatic cancer patients in the presence of a stent. Reducing the uncertainty in dose distribution is essential for dose escalation, especially in the presence of high-density materials. The new model mimicked the stent material and improved the contouring technique. Furthermore,

the gold standard MC algorithm, PENELOPE, provided the highest accuracy in treatment planning. The study conducted three different simulations, the first of which was the TPS plan with the Singleton hospital constraint. The second simulation used MC in the treatment plan, without changing any other factors. The last simulation was MC with a new model. The three simulation results showed a PA and GRP agreement between the MC and TPS, but the new MC model demonstrated a significant dose distribution difference. The significant difference occurred when the hardening effect and editing material of the stent in the new MC model was overcome. The VMAT reduced the dose enhancement, due to the stent, but was unable to adjust the dose in the distal area. The new model reduced the uncertainty of the dose distribution in pancreatic patients with a stent. Decreasing the uncertainty is essential when dose escalation is required, without passing the OAR threshold.

Chapter 6 employed micro-CT data to study the behaviour of dose distribution in temporal bone, with a focus on the cochlea. An MC was used to enhance the interaction's accuracy. The understanding obtained by this study helped to reduce the toxicity of the treatment plan. A three-level density was recorded in a micro-CT data, compared with two density levels in a medical CT. The cells in the soft bone are considered to be sensitive to radiation and can be damaged more easily than other cells. The photoelectric effect that dominated in the low-energy beams did not add a significant dose to the soft tissue, but deposited most of it in the high-density areas. The relative dose to FWHM showed that the highest rate between the three densities was the medium density, which contained soft bones. The study possessed certain limitations, such as the fact that the start point was not proportional to the density. Therefore, the findings of the study in this chapter were unable to provide a clear answer to whether the high resolution and MC could increase the treatment plan's accuracy significantly. However, the results could be used in a more advanced model for application in an actual clinical routine, in which the effect of using MC with high-resolution CT might be studied.

In Chapter 7, an advanced model was created to connect the results of the previous chapter to the clinical routine. A comparison was made between an advanced model that employed an MC and micro-CT data with a clinical TPS to a medical CT. A total of 280 glioma cases were filtered into 11 different scenarios. These scenarios were categorized into two groups. The first group had an energy fluence lower than that of the original data, and the second group had an energy fluence higher than that of the original data. In both groups, a difference in dose distribution was noticed

between the advanced model and the TPS, especially in the Dmin and Dmax. Most of the scenarios in both groups were not clinically significant, but some cases were clinically significant in terms of dose distribution and the NTCP model. The first group showed a non-significant difference in all cases, while some cases in the second group demonstrated a significant difference in dose distribution. The cases with clinically significant differences had a short distance of less than 1 cm between the target and the cochlea. A short distance allowed a more uniform dose distribution to the cochlea, increasing the difference between the advanced model and the TPS. A more in-depth investigation was conducted by selecting an extra case with a distance of less than 1 cm. The extra cases were divided into three groups. The two groups whose energy fluence was lower than that of the original data showed a non-significant outcome in dose distribution and the NTCP model. The third group with energy fluence that was higher than that of the original data demonstrated a clinically significant difference in dose distribution and the NTCP model. The results of the advanced model therefore demonstrated that some cases had higher uncertainty and require more attention when creating a treatment plan.

In Chapter 8, an advanced model was created to connect the data from Chapter 6 to the clinical routine of treatment using a Gamma Knife. The advanced model used an MC with a micro-CT data. The advanced model calculated the weighted factor for a scattered dose to the cochlea. A total of 34 schwannoma cases were used, all of which demonstrated a difference in dose distribution between the advanced model and the TPS. Furthermore, the TPS underestimated the dose in four cases significantly, compared with the advanced model. In some cases, the TPS and MC reported a cochlea dose that was higher than the recommended threshold, which could affect the plan. However, in the advanced model, the same cases reported lower doses than the threshold for the cochlea. The main difference was due to the fact that the TPS ignored the effect of secondary scattering and electrons in equilibrium, which increased the uncertainty in calculating the dose distribution, particularly in heterogeneous areas. The advanced model helps to decrease the uncertainty in dose distribution to the cochlea, allowing the dose to increase if needed.

Chapter 9 addressed the dose distribution of proton therapy in the heterogenous area using micro-CT data and MC. Proton therapy interacts differently than a photon in a heterogeneous area. The advantage of the Bragg peak in proton therapy is that it decreases the dose to OAR. It was found that the dose distribution in proton therapy did not affect different densities significantly, although a range of energy levels was tested. Moreover, the low beam energy did not alter the final

histogram. The chapter concluded that the dose distribution of the proton did not affect heterogenous areas significantly, with an MC model and micro-CT data. The simulation employed in the chapter did not test or evaluate the proton range, focusing only on dose distribution.

10.2 Clinical impact

The results shown in previous chapters reveal interesting findings that could prove more beneficial when incorporated into clinical practice. However, implementing these results into clinical routines requires several steps, such as conducting trials with a larger sample size. The most logical approach involves addressing each chapter individually and illustrating how it can be integrated into clinical procedures.

Chapter 5: The impact of pancreatic stents on dose distribution is evident from the results. A series of incremental steps is recommended to integrate these findings into clinical routines. Initially, the chapter should be published with a focus on practical clinical applications. This involves adapting the stereotactic ablative body radiotherapy (SABR) protocol used in UK trials for treating pancreatic cancer. The objective is to demonstrate that, despite utilizing advanced technology like the MR Linac, the stent effect remains a physics and simulation challenge rather than a patient positioning issue. The SABR protocol employs hypofractionation, delivering a higher dose over fewer fractions, which might introduce dose distribution uncertainties around the stent area. Subsequently, the stent should be re-tested using various designs—single bare stent, double bare stent, and large open cell stent. Ensuring accurate material concentrations for each stent may involve collaboration with the manufacturer or conducting material testing. A universal model can be introduced to be used. A straightforward approach involves incorporating the stent material into the treatment planning system, possibly using the TPS with a Monte Carlo algorithm like Raystation. However, since not all departments have access to Monte Carlo-based systems, an alternative is to validate and utilize a Monte Carlo algorithm for plan evaluation. Optimal outcomes may involve connecting to a supercomputer or building a high-performance computer. The final step involves automating the advanced contouring technique detailed in Chapter 5. Streamlining stent contouring—mainly extracting the inner portion—is essential, whether through an auto-segmentation model or an AI algorithm capable of distinguishing different density levels and extracting the inner segment. These sequential actions facilitate the integration of the stent

model into clinical routines, reducing dose distribution uncertainties. Furthermore, this process can serve as a model for implementing other stents in various body regions.

Chapters 6, 7, and 8: The multiscale model for the temporal bone and cochlea reveals notable dose distribution discrepancies in specific cases of glioma patients treated with VMAT and schwannoma cases treated with gamma knife. Cases where the target is less than one centimetre from the cochlea and involves high energy fluence distribution demand cautious evaluation due to pronounced differences between MC and TPS. While these findings can already be incorporated into clinical practice, further investigation is necessary. The current model is straightforward yet effective. Developing a more comprehensive and versatile model for testing with diverse head, neck, and brain tumour cases is essential. If these findings align with the chapter's outcomes, a general guideline could be established to identify cases with dose distribution differences. Such cases could be directed to a treatment planning system equipped with Monte Carlo capabilities, simplifying their handling. Alternatively, validating a Monte Carlo code and employing it primarily for these scenarios is another avenue, although a high-performance computer is necessary. It's important to note that connecting to supercomputers can present challenges, requiring coding expertise to resolve any simulation issues. Alternatively, cloud computing offers a more accessible option. The gamma knife treatment planning system can evolve from basic calculations, assuming water-like properties of the target and organs at risk, to more sophisticated algorithms similar to those in systems like Eclipse or Raystation, delivering greater accuracy in results.

10.3 Future work

The dose escalation approach is currently used more frequently than others, however dose distribution uncertainty is a challenge faced by all radiotherapy treatments, especially in treating areas of the body with high heterogeneity and sensitive OAR. This thesis contributed to the current understanding of this matter by evaluating dose distribution using a high-resolution micro CT with MC simulation in a specific heterogenous area, for proton and photon therapy. The methodology employed could be used in different parts of the human body, such as the skull base and femoral head. In both of these areas, heterogeneity and higher resolution are considered to provide more detailed information. As an advanced model was created for the data collection in this thesis, in order to connect it with clinical work, it was essential to include different clinical cases, in order

to evaluate the effect of dose distribution when testing different parts of the human body. The new model created for the pancreatic stent could be mimicked and applied to an oesophageal stent. Patients diagnosed with oesophageal cancer have a low survival rate, due to the nature of the cancer. A new approach treats oesophageal cancer with dose escalation photon or proton therapy. However, the dose distribution can differ in the presence of a stent, and using the new model proposed by this thesis can decrease the uncertainty of the dose distribution. In terms of the pancreatic stent, this thesis focused on photon therapy, and how the distribution differed in the new model. The next step required to improve the work would be to create a proton therapy plan, and to simulate the plan using MC to study the effect of the new model on dose distribution and proton range.

References

1. Wiley.com [Internet]. [cited 2022 Sep 20]. Foundations of Medical Imaging | Wiley. Available from: https://www.wiley.com/en-us/Foundations+of+Medical+Imaging-p-9780471545736

2. Falk S. Principles of cancer treatment by radiotherapy. Surg - Oxf Int Ed. 2006 Feb 1;24(2):62–5.

3. Lambert GD. Radiation therapy physics. (Medical radiology: Diagnostic imaging and radiation oncology), A.R. Smith (Ed.). Springer, Berlin (1995), ISBN: 3-540-55430-0. Clin Oncol. 1995;7.

4. Routledge & CRC Press [Internet]. [cited 2022 Sep 20]. Linear Accelerators for Radiation Therapy. Available from: https://www.routledge.com/Linear-Accelerators-for-Radiation-Therapy/Greene-Williams/p/book/9780750304764

5. Routledge & CRC Press [Internet]. [cited 2022 Sep 20]. The Physics of Three Dimensional Radiation Therapy: Conformal Radiotherapy, Radiosurgery and Treatment Planning. Available from: https://www.routledge.com/The-Physics-of-Three-Dimensional-Radiation-Therapy-Conformal-Radiotherapy/Webb/p/book/9780750302548

6. Joiner MC. Basic Clinical Radiobiology. :19.

7. Hinkelbein W, Bruggmoser G, Frommhold H, Wannenmacher M, editors. Acute and Long-Term Side-Effects of Radiotherapy: Biological Basis and Clinical Relevance [Internet]. Berlin, Heidelberg: Springer Berlin Heidelberg; 1993 [cited 2021 Nov 1]. (Herfarth Ch, Senn HJ, Baum M, Diehl V, Gutzwiller F, Rajewsky MF, et al., editors. Recent Results in Cancer Research; vol. 130). Available from: http://link.springer.com/10.1007/978-3-642-84892-6

8. Hopewell JW, Trott KR. Volume effects in radiobiology as applied to radiotherapy. Radiother Oncol. 2000 Sep;56(3):283–8.

9. Dawson LA, Normolle D, Balter JM, McGinn CJ, Lawrence TS, Ten Haken RK. Analysis of radiation-induced liver disease using the Lyman NTCP model. Int J Radiat Oncol. 2002 Jul;53(4):810–21.

10. Barnett GC, West CML, Dunning AM, Elliott RM, Coles CE, Pharoah PDP, et al. Normal tissue reactions to radiotherapy: towards tailoring treatment dose by genotype. Nat Rev Cancer. 2009 Feb;9(2):134–42.

11. Cancer Research UK - Cancer News [Internet]. 2018 [cited 2022 Nov 28]. NHS radiotherapy changes could see more patients having modern treatment. Available from:

https://news.cancerresearchuk.org/2018/01/31/nhs-radiotherapy-changes-could-see-more-patients-having-modern-treatment/

12. Endo M. Robert R. Wilson (1914–2000): the first scientist to propose particle therapy—use of particle beam for cancer treatment. Radiol Phys Technol. 2018 Mar 1;11(1):1–6.

13. Chen Z, Dominello MM, Joiner MC, Burmeister JW. Proton versus photon radiation therapy: A clinical review. Front Oncol. 2023 Mar 29;13:1133909.

14. PTCOG - Facilities in Operation [Internet]. [cited 2022 Sep 20]. Available from: https://www.ptcog.ch/index.php/facilities-in-operation

15. Burnet NG, Mackay RI, Smith E, Chadwick AL, Whitfield GA, Thomson DJ, et al. Proton beam therapy: perspectives on the National Health Service England clinical service and research programme. Br J Radiol. 2020 Mar;93(1107):20190873.

16. Crellin A. The Road Map for National Health Service Proton Beam Therapy. Clin Oncol R Coll Radiol G B. 2018 May;30(5):277–9.

17. Welsh Health Specialised Services Committee [Internet]. [cited 2022 Sep 20]. 2018/2019 Meeting Papers. Available from: https://whssc.nhs.wales/joint-committee/committee-meetings-and-papers/2018-2019-meeting-papers/

18. Clarke B. Normal Bone Anatomy and Physiology. Clin J Am Soc Nephrol. 2008 Nov;3(Supplement 3):S131–9.

19. Lillie EM, Urban JE, Lynch SK, Weaver AA, Stitzel JD. Evaluation of Skull Cortical Thickness Changes With Age and Sex From Computed Tomography Scans: SKULL CORTICAL THICKNESS CHANGES WITH AGE AND SEX FROM CT SCANS. J Bone Miner Res. 2016 Feb;31(2):299–307.

20. Skull | Definition, Anatomy, & Function | Britannica [Internet]. 2023 [cited 2023 Aug 6]. Available from: https://www.britannica.com/science/temporal-bone

21. Gray H. Anatomy of the human body. Bartleby.com edition.

22. Le Fèvre C, Brinkert D, Menoux I, Kuntz F, Antoni D, El Bitar Z, et al. Effects of a metallic implant on radiotherapy planning treatment-experience on a human cadaver. Chin Clin Oncol. 2020 Apr;9(2):14.

23. Son SH, Kang YN, Ryu MR. The effect of metallic implants on radiation therapy in spinal tumor patients with metallic spinal implants. Med Dosim Off J Am Assoc Med Dosim. 2012;37(1):98–107.

24. Almatani TU. A Rapid Dosimetric Assessment Method Using Cone Beam CT in Prostate Cancer Patients [Internet] [PhD]. [Swansea]: Swansea University; 2017 [cited 2022 Nov 25]. Available from: https://cronfa.swan.ac.uk/Record/cronfa50330

25. ESTRO - Abstract [Internet]. [cited 2022 Dec 31]. Available from: https://www.estro.org/Abstract?a=a8a73104-b154-ed11-bba2-000d3adea461

26. CORECT-R DATA CATALOGUE V1.0. 2020;112.

27. What is radiotherapy? | Cancer treatment | Cancer Research UK [Internet]. [cited 2021 Nov 3]. Available from: https://www.cancerresearchuk.org/about-cancer/cancer-in-general/treatment/radiotherapy/about

28. Zindler JD, Thomas CR, Hahn SM, Hoffmann AL, Troost EGC, Lambin P. Increasing the Therapeutic Ratio of Stereotactic Ablative Radiotherapy by Individualized Isotoxic Dose Prescription. J Natl Cancer Inst. 2016 Feb;108(2):djv305.

29. Cheung K. Intensity modulated radiotherapy: advantages, limitations and future development. Biomed Imaging Interv J [Internet]. 2006 Jan [cited 2021 Nov 3];2(1). Available from: http://www.biij.org/2006/1/e19

30. Carver JR, Shapiro CL, Ng A, Jacobs L, Schwartz C, Virgo KS, et al. American Society of Clinical Oncology Clinical Evidence Review on the Ongoing Care of Adult Cancer Survivors: Cardiac and Pulmonary Late Effects. J Clin Oncol. 2007 Sep 1;25(25):3991–4008.

31. Newhauser WD, Zhang R. The physics of proton therapy. Phys Med Biol. 2015 Apr 21;60(8):R155–209.

32. Bryant AK, Banegas MP, Martinez ME, Mell LK, Murphy JD. Trends in Radiation Therapy among Cancer Survivors in the United States, 2000–2030. Cancer Epidemiol Biomarkers Prev. 2017 Jun;26(6):963–70.

33. Staffurth J. A Review of the Clinical Evidence for Intensity-modulated Radiotherapy. Clin Oncol. 2010 Oct;22(8):643–57.

34. Miah AB, Bhide SA, Guerrero-Urbano MT, Clark C, Bidmead AM, St. Rose S, et al. Dose-Escalated Intensity-Modulated Radiotherapy Is Feasible and May Improve Locoregional Control and Laryngeal Preservation in Laryngo-Hypopharyngeal Cancers. Int J Radiat Oncol. 2012 Feb;82(2):539–47.

35. Nutting CM, Morden JP, Harrington KJ, Urbano TG, Bhide SA, Clark C, et al. Parotid-sparing intensity modulated versus conventional radiotherapy in head and neck cancer (PARSPORT): a phase 3 multicentre randomised controlled trial. Lancet Oncol. 2011 Feb;12(2):127–36.

36. Wong FCS, Ng AWY, Lee VHF, Lui CMM, Yuen KK, Sze WK, et al. Whole-Field Simultaneous Integrated-Boost Intensity-Modulated Radiotherapy for Patients With Nasopharyngeal Carcinoma. Int J Radiat Oncol. 2010 Jan;76(1):138–45.

37. Van Esch A, Clermont C, Devillers M, Iori M, Huyskens DP. On-line quality assurance of rotational radiotherapy treatment delivery by means of a 2D ion chamber array and the

Octavius phantom: On-line quality assurance of rotational radiotherapy. Med Phys. 2007 Sep 17;34(10):3825–37.

38. Das IJ, Sanfilippo NJ, Fogliata A, Cozzi L. Intensity Modulated Radiation: A clinical overview [Internet]. IOP Publishing; 2020 [cited 2021 Dec 15]. Available from: https://iopscience.iop.org/book/978-0-7503-1335-3

39. Hall EJ, Wuu CS. Radiation-induced second cancers: the impact of 3D-CRT and IMRT. Int J Radiat Oncol Biol Phys. 2003 May 1;56(1):83–8.

40. Stathakis S, Li J, Ma CCM. Monte Carlo determination of radiation-induced cancer risks for prostate patients undergoing intensity- modulated radiation therapy. J Appl Clin Med Phys. 2007 Sep 17;8(4):2685.

41. Schneider U, Lomax A, Pemler P, Besserer J, Ross D, Lombriser N, et al. The impact of IMRT and proton radiotherapy on secondary cancer incidence. Strahlenther Onkol Organ Dtsch Rontgengesellschaft Al. 2006 Nov;182(11):647–52.

42. Stathakis S, Roland T, Papanikolaou N, Li J, Ma C. A prediction study on radiation-induced second malignancies for IMRT treatment delivery. Technol Cancer Res Treat. 2009 Apr;8(2):141–8.

43. Gibbons JP, Reft CS. Monitor Unit Calculations for External Photon and Electron Beams. Med Phys. 2002 Jan;29(1):106–7.

44. Murray L, Henry A, Hoskin P, Siebert FA, Venselaar J. Second primary cancers after radiation for prostate cancer: a review of data from planning studies. Radiat Oncol. 2013 Jul 8;8(1):172.

45. Ruben JD, Lancaster CM, Jones P, Smith RL. A Comparison of Out-of-Field Dose and Its Constituent Components for Intensity-Modulated Radiation Therapy Versus Conformal Radiation Therapy: Implications for Carcinogenesis. Int J Radiat Oncol. 2011 Dec 1;81(5):1458–64.

46. Verhaegen F, Seuntjens J. Monte Carlo modelling of external radiotherapy photon beams. Phys Med Biol. 2003 Nov 7;48(21):R107–64.

47. Fix MK, Stampanoni M, Manser P, Born EJ, Mini R, Rüegsegger P. A multiple source model for 6 MV photon beam dose calculations using Monte Carlo. Phys Med Biol. 2001 May 1;46(5):1407–27.

48. Paelinck L, Smedt BD, Reynaert N, Coghe M, Gersem WD, Wagter CD, et al. Comparison of dose–volume histograms of IMRT treatment plans for ethmoid sinus cancer computed by advanced treatment planning systems including Monte Carlo. Radiother Oncol. 2006 Dec;81(3):250–6.

49. Kwa SLS, Theuws JCM, van Herk M, Muller SH, Leubesque JV. 124 - Application of chamfer matching in three-dimensional correlation of CT-SPECT and CT-CT of the lungs. Radiother Oncol. 1995 Oct 1;37:S33.

50. Tan J, Joon DL, Fitt G, Wada M, Joon ML, Mercuri A, et al. The utility of multimodality imaging with CT and MRI in defining rectal tumour volumes for radiotherapy treatment planning: a pilot study. J Med Imaging Radiat Oncol. 54(6):562–8.

51. Wambersie A, Landberg TG, Chavaudra J, Dobbs J, Hanks G, Johansson KA, et al. PRESCRIBING, RECORDING, AND REPORTING PHOTON BEAM THERAPY PRESENTATION OF THE ICRU REPORT # 50. J Med Phys. 1992 Dec;17(4):5.

52. Kiffer JD, Berlangieri SU, Scott AM, Quong G, Feigen M, Schumer W, et al. The contribution of 18F-fluoro-2-deoxy-glucose positron emission tomographic imaging to radiotherapy planning in lung cancer. Lung Cancer Amst Neth. 1998 Mar;19(3):167–77.

53. Zelefsky MJ, Fuks Z, Leibel SA. Intensity-modulated radiation therapy for prostate cancer. Semin Radiat Oncol. 2002 Jul;12(3):229–37.

54. Cheung K. Intensity modulated radiotherapy: advantages, limitations and future developments. Biomed Imaging Interv J [Internet]. 2006 Jan 1 [cited 2018 Jul 27];2(1). Available from: https://www.ncbi.nlm.nih.gov/pmc/articles/PMC3097603/

55. Verellen D, Ridder MD, Storme G. A (short) history of image-guided radiotherapy. Radiother Oncol. 2008 Jan;86(1):4–13.

56. Xing L, Chen Y, Luxton G, Li JG, Boyer AL. Monitor unit calculation for an intensity modulated photon field by a simple scatter-summation algorithm. Phys Med Biol. 2000;45(3):N1.

57. Lobo J, Popescu IA. Two new DOSXYZnrc sources for 4D Monte Carlo simulations of continuously variable beam configurations, with applications to RapidArc, VMAT, TomoTherapy and CyberKnife. Phys Med Biol. 2010 Aug 21;55(16):4431–43.

58. Pisaturo O, Moeckli R, Mirimanoff RO, Bochud FO. A Monte Carlo-based procedure for independent monitor unit calculation in IMRT treatment plans. Phys Med Biol. 2009 Jul 7;54(13):4299–310.

59. Belec J, Ploquin N, La Russa DJ, Clark BG. Position-probability-sampled Monte Carlo calculation of VMAT, 3DCRT, step-shoot IMRT, and helical tomotherapy dose distributions using BEAMnrc/DOSXYZnrc: Monte Carlo VMAT dose calculations. Med Phys. 2011 Jan 28;38(2):948–60.

60. Bush K, Zavgorodni S, Gagne I, Townson R, Ansbacher W, Beckham W. Monte Carlo evaluation of RapidArc™ oropharynx treatment planning strategies for sparing of midline structures. Phys Med Biol. 2010 Aug 21;55(16):4465–79.

61. Fleckenstein J, Jahnke L, Lohr F, Wenz F, Hesser J. Development of a Geant4 based Monte Carlo Algorithm to evaluate the MONACO VMAT treatment accuracy. Z Für Med Phys. 2013 Feb;23(1):33–45.

62. Teke T, Bergman AM, Kwa W, Gill B, Duzenli C, Popescu IA. Monte Carlo based, patient-specific RapidArc QA using Linac log files: Monte Carlo RapidArc QA using Linac log files. Med Phys. 2009 Dec 4;37(1):116–23.

63. Low DA, Harms WB, Mutic S, Purdy JA. A technique for the quantitative evaluation of dose distributions. Med Phys. 1998 May;25(5):656–61.

64. Iftimia I, Cirino ET, Xiong L, Mower HW. Quality assurance methodology for Varian RapidArc treatment plans. J Appl Clin Med Phys. 2010 Sep;11(4):130–43.

65. Studenski MT, Bar-Ad V, Siglin J, Cognetti D, Curry J, Tuluc M, et al. Clinical experience transitioning from IMRT to VMAT for head and neck cancer. Med Dosim. 2013 Jun;38(2):171–5.

66. GOV.UK [Internet]. [cited 2021 Nov 4]. Radiotherapy Services in England 2012. Available from: https://www.gov.uk/government/publications/radiotherapy-services-in-england-2012

67. Jefferies S, Taylor A, Reznek R. Results of a National Survey of Radiotherapy Planning and Delivery in the UK in 2007. Clin Oncol. 2009 Apr;21(3):204–17.

68. Baum KG, Helguera M. Execution of the SimSET Monte Carlo PET/SPECT Simulator in the Condor Distributed Computing Environment. J Digit Imaging. 2007 Nov;20(S1):72–82.

69. Bertelsen A, Hansen CR, Johansen J, Brink C. Single Arc Volumetric Modulated Arc Therapy of head and neck cancer. Radiother Oncol. 2010 May;95(2):142–8.

70. The influence of increment of gantry on VMAT plan quality for cervical cancer [Internet]. [cited 2021 Dec 15]. Available from: https://www.tandfonline.com/doi/epub/10.1080/16878507.2019.1707400?needAccess=true

71. Olding T, Schreiner LJ. Cone-beam optical computed tomography for gel dosimetry II: imaging protocols. Phys Med Biol. 2011 Mar 7;56(5):1259–79.

72. Mackie TR, Holmes T, Swerdloff S, Reckwerdt P, Deasy JO, Yang J, et al. Tomotherapy: A new concept for the delivery of dynamic conformal radiotherapy. Med Phys. 1993 Nov;20(6):1709–19.

73. Bortfeld T, Webb S. Single-Arc IMRT? Phys Med Biol. 2009 Jan 7;54(1):N9–20.

74. Gill GS, Jakubovic RY, Baker J, Button T, Chang J. Dosimetric Advantages of Volumetric Modulated Arc Therapy Based Coronal Arc Delivery Technique in Brain

Stereotactic Radiosurgery: A Feasibility Study. Int J Med Phys Clin Eng Radiat Oncol. 2019 Mar 26;8(2):80–94.

75. Smyth G, Evans PM, Bamber JC, Bedford JL. Recent developments in non-coplanar radiotherapy. Br J Radiol. 2019 May;92(1097):20180908.

76. Bortfeld T. The number of beams in IMRT—theoretical investigations and implications for single-arc IMRT. Phys Med Biol. 2010 Jan 7;55(1):83–97.

77. Yu CX. Intensity Modulated Arc Therapy: Technology and Clinical Implementation. :14.

78. Cao D, Afghan MKN, Ye J, Chen F, Shepard DM. A generalized inverse planning tool for volumetric-modulated arc therapy. Phys Med Biol. 2009 Nov 7;54(21):6725–38.

79. Khan FM. The physics of radiation therapy. 3rd ed. Philadelphia: Lippincott Williams & Wilkins; 2003. 1 p.

80. Khan FM, Gibbons JP. Khan's The Physics of Radiation Therapy [Internet]. Philadelphia, UNITED STATES: Wolters Kluwer Health; 2014. Available from: http://ebookcentral.proquest.com/lib/swansea-ebooks/detail.action?docID=2031615

81. Hossain S, Islam MR, Lee G, Higby C, Ahmad S, Algan O. Comparison of volumetric modulated arc therapy (VMAT) and intensity modulated radiation therapy (IMRT) plannings for the treatment of left sided breast and regional lymphatic tissue. In 2016 [cited 2018 Aug 1]. p. 060002. Available from: http://aip.scitation.org/doi/abs/10.1063/1.4954112

82. Beckham W, Popescu C, Wai E, Ansbacher W, Salter L, Olivotto I, et al. Volumetric Modulated Arc Therapy (vmat) Improves Dosimetry and Reduces Treatment Time Compared to 9-Field Conventional Intensity Modulated Radiotherapy (cimrt) for Locoregional Radiotherapy of Left-Sided Breast Cancer. Australas Phys Eng Sci Med Dordr. 2008 Dec;31(4):493.

83. Doyle-Lindrud S. Proton Beam Therapy for Pediatric Malignancies. Clin J Oncol Nurs. 2015 Oct 1;19(5):521–3.

84. Mihailidis D. The Physics & Technology of Radiation Therapy. 2nd Edition. PN McDermott & CG Orton, Authors. Madison, WI: Medical Physics Publishing, 2018. 870. pp. Price: $165.00. ISBN: 9781930524989. Med Phys. 2019;46(8):3751–2.

85. Proton Beam Radiation Therapy. 2019;22.

86. Goitein M, Jermann M. The Relative Costs of Proton and X-ray Radiation Therapy. Clin Oncol. 2003 Feb;15(1):S37–50.

87. Olsen DR, Bruland ØS, Frykholm G, Norderhaug IN. Proton therapy – A systematic review of clinical effectiveness. Radiother Oncol. 2007 May;83(2):123–32.

88. Paganetti H. Range uncertainties in proton therapy and the role of Monte Carlo simulations. Phys Med Biol. 2012 Jun 7;57(11):R99–117.

89. Schulz-Ertner D, Tsujii H. Particle Radiation Therapy Using Proton and Heavier Ion Beams. J Clin Oncol. 2007 Mar 10;25(8):953–64.

90. Paganetti H, Kooy H. Proton radiation in the management of localized cancer. Expert Rev Med Devices. 2010 Mar;7(2):275–85.

91. Ladra M, Yock T. Proton Radiotherapy for Pediatric Sarcoma. Cancers. 2014 Jan 14;6(1):112–27.

92. Semwal MK. Khan's The Physics of Radiation Therapy. J Med Phys. 2020;45(2):134–5.

93. Encyclopedia of Radiation Oncology [Internet]. [cited 2022 Jul 4]. Available from: https://link.springer.com/book/10.1007/978-3-540-85516-3

94. Lee SH, Cho S, You SH, Shin D, Park SY, Lee SB, et al. Evaluation of radioactivity induced by patient-specific devices in proton therapy. J Korean Phys Soc. 2012 Jan;60(1):125–8.

95. Zou W. Tutorials in Radiotherapy Physics: Advanced Topics with Problems and Solution. Med Phys. 2017 Dec;45.

96. Pugh TJ, Choi S, Nguyen QN, Gillin MT, Ron Zhu X, Palmer MB, et al. Proton beam therapy for the treatment of prostate cancer. Pract Radiat Oncol. 2013 Apr;3(2):e87–94.

97. Wang D. A critical appraisal of the clinical utility of proton therapy in oncology. Med Devices Evid Res. 2015 Oct;439.

98. Albertini F, Gaignat S, Bosshardt M, Lomax A. Planning and optimizing treatment plans for actively scanned proton therapy. 2009 Jan;

99. Stathakis S. Practical Radiation Oncology Physics. A Companion to Gunderson & Tepper's Clinical Radiation Oncology. SDieterich, EFord, DPavord, JZeng. Philadelphia, PA: Elsevier, 2016. Softcover: 384. pp. Price: $143.00. ISBN: 978-0-323-26209-5. Med Phys. 2019 Sep;46(9):4285–4285.

100. Amaldi U, Cuccagna C, Lo Moro A, Rizzoglio V, Bernier J, Bulling S. Sparse proportional re-scanning with hadron beams. Phys Med. 2019 Sep;65:200–8.

101. Leksell DG. Stereotactic radiosurgery: Present status and future trends. Neurol Res. 1987 Jun;9(2):60–8.

102. LEKSELL L. The stereotaxic method and radiosurgery of the brain. Acta Chir Scand. 1951 Dec 13;102(4):316–9.

103. Lindquist C, Kihlström L. Department of Neurosurgery, Karolinska Institute: 60 years. Neurosurgery. 1996 Nov;39(5):1016–21.

104. Wu A, Lindner G, Maitz AH, Kalend AM, Lunsford LD, Flickinger JC, et al. Physics of gamma knife approach on convergent beams in stereotactic radiosurgery. Int J Radiat Oncol Biol Phys. 1990 Apr;18(4):941–9.

105. Khan FM. The physics of radiation therapy. 3rd ed. Philadelphia: Lippincott Williams & Wilkins; 2003. 1 p.

106. Hall EJ, Giaccia AJ. Radiobiology for the radiologist. 7th ed. Philadelphia, Pa. Londo: Wolters Kluwer Lippincott Williams & Wilkins; 2012. 546 p.

107. Buatti JM, Friedman WA, Meeks SL, Bova FJ. The radiobiology of radiosurgery and stereotactic radiotherapy. Med Dosim. 1998 Sep;23(3):201–7.

108. Hall EJ, Brenner DJ. The radiobiology of radiosurgery: Rationale for different treatment regimes for AVMs and malignancies. Int J Radiat Oncol. 1993 Jan;25(2):381–5.

109. Schlesinger DJ, Yen CP, Lindquist C, Steiner L. Gamma Knife: Technical Aspects. In: Lozano AM, Gildenberg PL, Tasker RR, editors. Textbook of Stereotactic and Functional Neurosurgery [Internet]. Berlin, Heidelberg: Springer; 2009 [cited 2022 Sep 14]. p. 897–928. Available from: https://doi.org/10.1007/978-3-540-69960-6_58

110. Mugler JP, Brookeman JR. Three-dimensional magnetization-prepared rapid gradient-echo imaging (3D MP RAGE). Magn Reson Med. 1990 Jul;15(1):152–7.

111. Casselman JW, Kuhweide R, Deimling M, Ampe W, Dehaene I, Meeus L. Constructive interference in steady state-3DFT MR imaging of the inner ear and cerebellopontine angle. AJNR Am J Neuroradiol. 1993 Feb;14(1):47–57.

112. Held P, Fellner C, Fellner F, Seitz J, Strutz J. MRI of inner ear anatomy using 3D MP-RAGE and 3D CISS sequences. Br J Radiol. 1997 May;70(833):465–72.

113. ICRU Report 62, Prescribing, Recording and Reporting Photon Beam Therapy (Supplement to ICRU 50) – ICRU [Internet]. [cited 2022 Feb 15]. Available from: https://www.icru.org/report/prescribing-recording-and-reporting-photon-beam-therapy-report-62/

114. van Herk M. Errors and margins in radiotherapy. Semin Radiat Oncol. 2004 Jan;14(1):52–64.

115. Metropolis N, Ulam S. The Monte Carlo Method. J Am Stat Assoc. 1949 Sep;44(247):335–41.

116. Wilson RR. Monte Carlo Study of Shower Production. Phys Rev. 1952 May 1;86(3):261–9.

117. Seco J, Verhaegen F. Monte Carlo Techniques in Radiation Therapy [Internet]. Taylor & Francis; 2016. (Imaging in Medical Diagnosis and Therapy). Available from: https://books.google.co.uk/books?id=veonvgAACAAJ

118. Andreo P. Monte Carlo techniques in medical radiation physics. Phys Med Biol. 1991 Jul 1;36(7):861–920.

119. Rogers DWO, Bielajew AF. Monte Carlo Techniques of Electron and Photon Transport for Radiation Dosimetry. In: The Dosimetry of Ionizing Radiation [Internet]. Elsevier; 1990 [cited 2021 Dec 9]. p. 427–539. Available from: https://linkinghub.elsevier.com/retrieve/pii/B9780124004030500099

120. Jenkins TM, Nelson WR, Rindi A. Monte Carlo Transport of Electrons and Photons. In 1988.

121. Marsaglia G, Zaman A. A New Class of Random Number Generators. Ann Appl Probab [Internet]. 1991 Aug 1 [cited 2021 Dec 9];1(3). Available from: https://projecteuclid.org/journals/annals-of-applied-probability/volume-1/issue-3/A-New-Class-of-Random-Number-Generators/10.1214/aoap/1177005878.full

122. Lüscher M. A portable high-quality random number generator for lattice field theory simulations. Comput Phys Commun. 1994 Feb;79(1):100–10.

123. Eckhardt R. STAN ULAM, JOHN VON NEUMANN, and the MONTE CARLO METHOD. :13.

124. Kawrakow I, Mainegra-Hing E, Rogers DWO, Tessier F, Walters BRB. Monte Carlo Simulation of Electron and Photon Transport. :314.

125. Khan FM. The physics of radiation therapy. 3rd ed. Philadelphia: Lippincott Williams & Wilkins; 2003. 1 p.

126. Konik A, Madsen M, Sunderland J. Evaluation of attenuation correction requirement in small animal PET and SPECT imaging. J Nucl Med. 2009 May 1;50(supplement 2):1465–1465.

127. Johns HE. THE PHYSICS OF RADIOLOGY. :34.

128. Knoll GF. Radiation Detection and Measurement. John Wiley & Sons; 2010. 857 p.

129. Jackson JD. Classical Electrodynamics. :8.

130. Paganetti H, editor. Proton Therapy Physics, Second Edition. 2nd ed. Boca Raton: CRC Press; 2018. 772 p.

131. Ma CM, Li JS, Jiang SB, Pawlicki T, Xiong W, Qin LH, et al. Effect of statistical uncertainties on Monte Carlo treatment planning. Phys Med Biol. 2005 Mar 7;50(5):891–907.

132. Goodall SK, Ebert MA. Recommended dose voxel size and statistical uncertainty parameters for precision of Monte Carlo dose calculation in stereotactic radiotherapy. J Appl Clin Med Phys. 2020 Dec;21(12):120–30.

133. Reynaert N, van der Marck SC, Schaart DR, Van der Zee W, Van Vliet-Vroegindeweij C, Tomsej M, et al. Monte Carlo treatment planning for photon and electron beams. Radiat Phys Chem. 2007 Apr;76(4):643–86.

134. Bielajew AF, Rogers DWO. Variance-Reduction Techniques. In: Jenkins TM, Nelson WR, Rindi A, editors. Monte Carlo Transport of Electrons and Photons [Internet]. Boston, MA: Springer US; 1988 [cited 2021 Dec 10]. p. 407–19. (Ettore Majorana International Science Series). Available from: https://doi.org/10.1007/978-1-4613-1059-4_18

135. Kawrakow I, Fippel M. Investigation of variance reduction techniques for Monte Carlo photon dose calculation using XVMC. Phys Med Biol. 2000 Aug 1;45(8):2163–83.

136. Rodriguez M, Sempau J, Brualla L. A combined approach of variance-reduction techniques for the efficient Monte Carlo simulation of linacs. Phys Med Biol. 2012 May 21;57(10):3013–24.

137. Mohammed M, Chakir E, Boukhal H, Saeed M, El Bardouni T. Evaluation of variance reduction techniques in BEAMnrc Monte Carlo simulation to improve the computing efficiency. J Radiat Res Appl Sci. 2016 Oct;9(4):424–30.

138. Sheikh-Bagheri_etal. :21.

139. Battistoni G, Bauer J, Boehlen TT, Cerutti F, Chin MPW, Dos Santos Augusto R, et al. The FLUKA Code: An Accurate Simulation Tool for Particle Therapy. Front Oncol [Internet]. 2016 May 11 [cited 2021 Dec 10];6. Available from: http://journal.frontiersin.org/Article/10.3389/fonc.2016.00116/abstract

140. Ferrari A, Sala PR, Fasso A, Ranft J. FLUKA: A Multi-Particle Transport Code [Internet]. 2005 Dec [cited 2021 Dec 10] p. SLAC-R-773, 877507. Report No.: SLAC-R-773, 877507. Available from: http://www.osti.gov/servlets/purl/877507-sC9S9L/

141. Andersen V, Ballarini F, Battistoni G, Campanella M, Carboni M, Cerutti F, et al. The fluka code for space applications: recent developments. Adv Space Res. 2004 Jan;34(6):1302–10.

142. Battistoni G, Cerutti F, Gadioli E, Garzelli MV, Muraro S, Rancati T, et al. APPLICATIONS OF THE FLUKA MONTE CARLO CODE IN HIGH ENERGY AND ACCELERATOR PHYSICS. :4.

143. Ballarini F, Biaggi M, De Biaggi L, Ferrari A, Ottolenghi A, Panzarasa A, et al. Role of shielding in modulating the effects of solar particle events: Monte Carlo calculation of absorbed dose and DNA complex lesions in different organs. Adv Space Res. 2004 Jan;34(6):1338–46.

144. Vlachoudis V. FLAIR: a powerful but user friendly graphical interface for FLUKA. In: Proc Int Conf on Mathematics, Computational Methods & Reactor Physics (M&C 2009), Saratoga Springs, New York. 2009.

145. Bidgood WD, Horii SC, Prior FW, Van Syckle DE. Understanding and Using DICOM, the Data Interchange Standard for Biomedical Imaging. J Am Med Inform Assoc. 1997;4(3):199–212.

146. Kahn CE, Carrino JA, Flynn MJ, Peck DJ, Horii SC. DICOM and radiology: past, present, and future. J Am Coll Radiol JACR. 2007 Sep;4(9):652–7.

147. Law MYY, Liu B. DICOM-RT and Its Utilization in Radiation Therapy. RadioGraphics. 2009 May 1;29(3):655–67.

148. Law MYY, Liu B, Chan LW. DICOM-RT–based Electronic Patient Record Information System for Radiation Therapy. RadioGraphics. 2009 Jul 1;29(4):961–72.

149. Battistoni G, Boehlen T, Cerutti F, Chin PW, Esposito LS, Fassò A, et al. Overview of the FLUKA code. Ann Nucl Energy. 2015 Aug 1;82:10–8.

150. Vlachoudis V, Sinuela-Pastor D. Numerically robust geometry engine for compound solid geometries. In: SNA + MC 2013 - Joint International Conference on Supercomputing in Nuclear Applications + Monte Carlo [Internet]. EDP Sciences; 2014 [cited 2021 Dec 10]. p. 02502. Available from: https://sna-and-mc-2013-proceedings.edpsciences.org/articles/snamc/abs/2014/01/snamc2013_02502/snamc2013_02502.html

151. PENELOPE-2018: A Code System for Monte Carlo Simulation of Electron and Photon Transport, Workshop Proceedings, Barcelona, Spain, 28 January-1 February 2019. 2019;420.

152. OECD. PENELOPE 2014: A code system for Monte Carlo simulation of electron and photon transport: Workshop, Barcelona, Spain, 29 June - 3 July 2015 [Internet]. Paris: Organisation for Economic Co-operation and Development; 2015 [cited 2022 Dec 1]. Available from: https://www.oecd-ilibrary.org/nuclear-energy/penelope-2014-a-code-system-for-monte-carlo-simulation-of-electron-and-photon-transport_4e3f14db-en

153. Park H, Paganetti H, Schuemann J, Jia X, Min CH. Monte Carlo methods for device simulations in radiation therapy. Phys Med Biol. 2021 Sep 14;66(18):10.1088/1361-6560/ac1d1f.

154. Salvat F. The PENELOPE code system. Specific features and recent improvements. In: SNA + MC 2013 - Joint International Conference on Supercomputing in Nuclear Applications + Monte Carlo [Internet]. EDP Sciences; 2014 [cited 2022 Dec 1]. p. 06017. Available from: https://sna-and-mc-2013-proceedings.edpsciences.org/articles/snamc/abs/2014/01/snamc2013_06017/snamc2013_06017.html

155. Tissue inhomogeneity corrections for megavoltage photon beams. AAPM Report No. 85, Task Group No 65 of the Radiation Therapy Committee of the American Association of Physicists in Medicine – ScienceOpen [Internet]. [cited 2022 Sep 21]. Available from: https://www.scienceopen.com/document?vid=e2557d8e-ca28-4b84-99e0-9c871f556091

156. Dutreix A. When and how can we improve precision in radiotherapy? Radiother Oncol J Eur Soc Ther Radiol Oncol. 1984 Dec;2(4):275–92.

157. Boyer AL, Schultheiss T. Effects of dosimetric and clinical uncertainty on complication-free local tumor control. Radiother Oncol J Eur Soc Ther Radiol Oncol. 1988 Jan;11(1):65–71.

158. Chetty IJ, Curran B, Cygler JE, DeMarco JJ, Ezzell G, Faddegon BA, et al. Report of the AAPM Task Group No. 105: Issues associated with clinical implementation of Monte Carlo-based photon and electron external beam treatment planning. Med Phys. 2007 Dec;34(12):4818–53.

159. Kry SF, Feygelman V, Balter P, Knöös T, Charlie Ma CM, Snyder M, et al. AAPM Task Group 329: Reference dose specification for dose calculations: Dose-to-water or dose-to-muscle? Med Phys. 2020;47(3):e52–64.

160. Han T, Mikell JK, Salehpour M, Mourtada F. Dosimetric comparison of Acuros XB deterministic radiation transport method with Monte Carlo and model-based convolution methods in heterogeneous media: Dosimetric evaluation of AXB in heterogeneities. Med Phys. 2011 May 6;38(5):2651–64.

161. Fogliata A, De Rose F, Stravato A, Reggiori G, Tomatis S, Scorsetti M, et al. Evaluation of target dose inhomogeneity in breast cancer treatment due to tissue elemental differences. Radiat Oncol. 2018 Dec;13(1):92.

162. Bush K, Gagne IM, Zavgorodni S, Ansbacher W, Beckham W. Dosimetric validation of Acuros XB with Monte Carlo methods for photon dose calculations. Med Phys. 2011 Apr;38(4):2208–21.

163. Tsuruta Y, Nakata M, Nakamura M, Matsuo Y, Higashimura K, Monzen H, et al. Dosimetric comparison of Acuros XB, AAA, and XVMC in stereotactic body radiotherapy for lung cancer. Med Phys. 2014 Aug;41(8):081715.

164. Alhakeem EA, AlShaikh S, Rosenfeld AB, Zavgorodni SF. Comparative evaluation of modern dosimetry techniques near low- and high-density heterogeneities. J Appl Clin Med Phys. 2015 Sep 8;16(5):142–58.

165. Kan MWK, Leung LHT, Yu PKN. Verification and dosimetric impact of Acuros XB algorithm on intensity modulated stereotactic radiotherapy for locally persistent nasopharyngeal carcinoma. Med Phys. 2012 Aug;39(8):4705–14.

166. Stathakis S, Esquivel C, Quino LV, Myers P, Calvo O, Mavroidis P, et al. Accuracy of the Small Field Dosimetry Using the Acuros XB Dose Calculation Algorithm within and

beyond Heterogeneous Media for 6 MV Photon Beams. Int J Med Phys Clin Eng Radiat Oncol. 2012 Nov 23;1(3):78–87.

167. Sterpin E, Tomsej M, De Smedt B, Reynaert N, Vynckier S. Monte carlo evaluation of the AAA treatment planning algorithm in a heterogeneous multilayer phantom and IMRT clinical treatments for an Elekta SL25 linear accelerator. Med Phys. 2007 May;34(5):1665–77.

168. Ono K, Endo S, Tanaka K, Hoshi M, Hirokawa Y. Dosimetric verification of the anisotropic analytical algorithm in lung equivalent heterogeneities with and without bone equivalent heterogeneities. Med Phys. 2010 Aug;37(8):4456–63.

169. Kry SF, Lye J, Clark CH, Andratschke N, Dimitriadis A, Followill D, et al. Report dose-to-medium in clinical trials where available; a consensus from the Global Harmonisation Group to maximize consistency. Radiother Oncol. 2021 Jun;159:106–11.

170. Lloyd S a. M, Ansbacher W. Evaluation of an analytic linear Boltzmann transport equation solver for high-density inhomogeneities. Med Phys. 2013 Jan;40(1):011707.

171. Howell RM, Scarboro SB, Kry SF, Yaldo DZ. Accuracy of out-of-field dose calculations by a commercial treatment planning system. Phys Med Biol. 2010 Dec 7;55(23):6999–7008.

172. Huang JY, Followill DS, Wang XA, Kry SF. Accuracy and sources of error of out-of field dose calculations by a commercial treatment planning system for intensity-modulated radiation therapy treatments. J Appl Clin Med Phys. 2013;14(2):186–97.

173. Linthout N, Verellen D, Van Acker S, Voordeckers M, Bretz A, Storme G. Evaluation of dose calculation algorithms for dynamic arc treatments of head and neck tumors. Radiother Oncol J Eur Soc Ther Radiol Oncol. 2002 Jul;64(1):85–95.

174. Onizuka R, Araki F, Ohno T, Nakaguchi Y, Kai Y, Tomiyama Y, et al. Accuracy of dose calculation algorithms for virtual heterogeneous phantoms and intensity-modulated radiation therapy in the head and neck. Radiol Phys Technol. 2016 Jan;9(1):77–87.

175. Rana S, Rogers K, Pokharel S, Lee T, Reed D, Biggs C. Acuros XB Algorithm vs. Anisotropic Analytical Algorithm: A Dosimetric Study Using Heterogeneous Phantom and Computed Tomography (CT) Data Sets of Esophageal Cancer Patients. 2013 Feb 7 [cited 2022 Sep 21];2013. Available from: http://www.scirp.org/journal/PaperInformation.aspx?PaperID=27789

176. Hughes J, Lye JE, Kadeer F, Alves A, Shaw M, Supple J, et al. Calculation algorithms and penumbra: Underestimation of dose in organs at risk in dosimetry audits. Med Phys. 2021 Oct;48(10):6184–97.

177. Padmanaban S, Warren S, Walsh A, Partridge M, Hawkins MA. Comparison of Acuros (AXB) and Anisotropic Analytical Algorithm (AAA) for dose calculation in treatment of

oesophageal cancer: effects on modelling tumour control probability. Radiat Oncol. 2014 Dec 23;9(1):286.

178. Low DA, Harms WB, Mutic S, Purdy JA. A technique for the quantitative evaluation of dose distributions. Med Phys. 1998 May;25(5):656–61.

179. Hussein M, Clark CH, Nisbet A. Challenges in calculation of the gamma index in radiotherapy – Towards good practice. Phys Med. 2017 Apr;36:1–11.

180. Aamri H, Fielding A, Aamry A, Sulieman A, Tamam N, Alkhorayef M, et al. Comparison between PRIMO and EGSnrc Monte Carlo models of the Varian True Beam linear accelerator. Radiat Phys Chem. 2021 Jan 1;178:109013.

181. Wendling M, Zijp LJ, McDermott LN, Smit EJ, Sonke JJ, Mijnheer BJ, et al. A fast algorithm for gamma evaluation in 3D: Fast 3D gamma evaluation. Med Phys. 2007 Apr 19;34(5):1647–54.

182. Nazir S. Range uncertainty and dose uniformity in proton therapy in the presence of inhomogeneities in tissue and phantom materials [Internet] [PhD]. [Swansea]: Swansea University; 2022 [cited 2022 Nov 25]. Available from: https://cronfa.swan.ac.uk/Record/cronfa59235

183. Hussein M, Rowshanfarzad P, Ebert MA, Nisbet A, Clark CH. A comparison of the gamma index analysis in various commercial IMRT/VMAT QA systems. Radiother Oncol. 2013 Dec;109(3):370–6.

184. Verhaegen F, Seuntjens J. Monte Carlo modelling of external radiotherapy photon beams. Phys Med Biol. 2003 Nov 7;48(21):R107–64.

185. Bacala AM. Linac photon beam fine-tuning in PRIMO using the gamma-index analysis toolkit. Radiat Oncol. 2020 Dec;15(1):8.

186. Sarin B, Bindhu B, Saju B, Nair RK. Validation of PRIMO Monte Carlo Model of Clinac®iX 6MV Photon Beam. J Med Phys. 2020;45(1):24–35.

187. An empirical formula to obtain tissue-phantom ratios from percentage depth–dose curves for small fields - IOPscience [Internet]. [cited 2023 Aug 16]. Available from: https://iopscience.iop.org/article/10.1088/0031-9155/58/14/4781/meta

188. Cancer Research UK [Internet]. 2015 [cited 2021 Oct 31]. Pancreatic cancer statistics. Available from: https://www.cancerresearchuk.org/health-professional/cancer-statistics/statistics-by-cancer-type/pancreatic-cancer

189. Mukherjee S, Symonds RP. The Role of Radiotherapy in the Management of Upper Gastrointestinal and Hepato-biliary and Pancreatic Cancers: Current Status and Future Directions. Clin Oncol. 2014 Sep;26(9):519–21.

190. Huguet F, André T, Hammel P, Artru P, Balosso J, Selle F, et al. Impact of Chemoradiotherapy After Disease Control With Chemotherapy in Locally Advanced Pancreatic Adenocarcinoma in GERCOR Phase II and III Studies. J Clin Oncol. 2007 Jan 20;25(3):326–31.

191. Chauffert B, Mornex F, Bonnetain F, Rougier P, Mariette C, Bouché O, et al. Phase III trial comparing intensive induction chemoradiotherapy (60 Gy, infusional 5-FU and intermittent cisplatin) followed by maintenance gemcitabine with gemcitabine alone for locally advanced unresectable pancreatic cancer. Definitive results of the 2000–01 FFCD/SFRO study. Ann Oncol. 2008 Sep;19(9):1592–9.

192. Crane CH. Hypofractionated ablative radiotherapy for locally advanced pancreatic cancer. J Radiat Res (Tokyo). 2016 Aug;57(Suppl 1):i53–7.

193. Moraru IC, Tai A, Erickson B, Li XA. Radiation dose responses for chemoradiation therapy of pancreatic cancer: An analysis of compiled clinical data using biophysical models. Pract Radiat Oncol. 2014 Jan;4(1):13–9.

194. Chung SY, Chang JS, Lee BM, Kim KH, Lee KJ, Seong J. Dose escalation in locally advanced pancreatic cancer patients receiving chemoradiotherapy. Radiother Oncol. 2017 Jun;123(3):438–45.

195. Krishnan S, Chadha AS, Suh Y, Chen HC, Rao A, Das P, et al. Focal Radiation Therapy Dose Escalation Improves Overall Survival in Locally Advanced Pancreatic Cancer Patients Receiving Induction Chemotherapy and Consolidative Chemoradiation. Int J Radiat Oncol. 2016 Mar;94(4):755–65.

196. Abu Dayyeh B, VanDamme J, Miller R, Baron T. Esophageal self-expandable stent material and mesh grid density are the major determining factors of external beam radiation dose perturbation: results from a phantom model. Endoscopy. 2012 Dec 19;45(01):42–7.

197. Atwood TF, Hsu A, Ogara MM, Luba DG, Tamler BJ, DiSario JA, et al. Radiotherapy Dose Perturbation of Esophageal Stents Examined in an Experimental Model. Int J Radiat Oncol. 2012 Apr;82(5):1659–64.

198. Chen YK, Schefter TE, Newman F. Esophageal cancer patients undergoing external beam radiation after placement of self-expandable metal stents: is there a risk of radiation dose enhancement? Gastrointest Endosc. 2011 Jun;73(6):1109–14.

199. Francis SR, Anker CJ, Wang B, Williams GV, Cox K, Adler DG, et al. Self-expanding stent effects on radiation dosimetry in esophageal cancer. J Appl Clin Med Phys. 2013 Jul;14(4):121–35.

200. Li XA, Chibani O, Greenwald B, Suntharalingam M. Radiotherapy dose perturbation of metallic esophageal stents. Int J Radiat Oncol. 2002 Nov;54(4):1276–85.

201. Hasegawa S, Endo I, Kubota K. Plastic or self-expandable metal stent: Which is the most suitable for patients with pancreatic head cancer in the upcoming era of neoadjuvant chemotherapy? A review. Dig Endosc. 2022;34(2):297–306.

202. Ikezawa K, Takada R, Takahashi H, Kiyota R, Imai T, Abe Y, et al. Efficacy of Larger-Diameter Plastic Stent Placement for Preoperative Biliary Drainage in Patients Receiving Neoadjuvant Chemoradiation for Pancreatic Cancer. Pancreas. 2020 Mar;49(3):e20.

203. Lee H, Yoon J, Park K, Rim CH, Chung MJ, Seong J. Dose perturbation by metallic biliary stent in external beam radiotherapy of pancreato-biliary cancers. Australas Phys Eng Sci Med. 2019 Sep;42(3):745–56.

204. Elhammali A, Patel M, Weinberg B, Verma V, Liu J, Olsen JR, et al. Late gastrointestinal tissue effects after hypofractionated radiation therapy of the pancreas. Radiat Oncol. 2015 Dec;10(1):186.

205. Ben-Josef E, Schipper M, Francis IR, Hadley S, Ten-Haken R, Lawrence T, et al. A Phase I/II Trial of Intensity Modulated Radiation (IMRT) Dose Escalation With Concurrent Fixed-dose Rate Gemcitabine (FDR-G) in Patients With Unresectable Pancreatic Cancer. Int J Radiat Oncol. 2012 Dec 1;84(5):1166–71.

206. Zschaeck S, Blümke B, Wust P, Kaul D, Bahra M, Riess H, et al. Dose-escalated radiotherapy for unresectable or locally recurrent pancreatic cancer: Dose volume analysis, toxicity and outcome of 28 consecutive patients. PLOS ONE. 2017 Oct 12;12(10):e0186341.

207. Morganti AG, Valentini V, Macchia G, Mattiucci GC, Costamagna G, Deodato F, et al. 5-fluorouracil–based chemoradiation in unresectable pancreatic carcinoma: phase I-II dose-escalation study. Int J Radiat Oncol. 2004 Aug 1;59(5):1454–60.

208. Morganti AG, Picardi V, Ippolito E, Massaccesi M, Macchia G, Deodato F, et al. Capecitabine based postoperative accelerated chemoradiation of pancreatic carcinoma. A dose-escalation study. Acta Oncol. 2010 Jan 1;49(4):418–22.

209. Nakamura A, Shibuya K, Matsuo Y, Nakamura M, Shiinoki T, Mizowaki T, et al. Analysis of Dosimetric Parameters Associated With Acute Gastrointestinal Toxicity and Upper Gastrointestinal Bleeding in Locally Advanced Pancreatic Cancer Patients Treated With Gemcitabine-Based Concurrent Chemoradiotherapy. Int J Radiat Oncol. 2012 Oct;84(2):369–75.

210. Huang J, Robertson JM, Ye H, Margolis J, Nadeau L, Yan D. Dose–Volume Analysis of Predictors for Gastrointestinal Toxicity After Concurrent Full-Dose Gemcitabine and Radiotherapy for Locally Advanced Pancreatic Adenocarcinoma. Int J Radiat Oncol. 2012 Jul;83(4):1120–5.

211. Kelly P, Das P, Pinnix CC, Beddar S, Briere T, Pham M, et al. Duodenal Toxicity After Fractionated Chemoradiation for Unresectable Pancreatic Cancer. Int J Radiat Oncol. 2013 Mar;85(3):e143–9.

212. Lee H, Yoon J, Park K, Rim CH, Chung MJ, Seong J. Dose perturbation by metallic biliary stent in external beam radiotherapy of pancreato-biliary cancers. Australas Phys Eng Sci Med. 2019 Sep;42(3):745–56.

213. Mayo-Smith WW, Dawson SL, Mauceri T, Mueller PR. Attenuation effects of biliary endoprostheses on therapeutic radiation. Radiology. 1996 May;199(2):571–2.

214. Jalaj S, Lee S, McGaw C, John B, Li Z, Awad Z, et al. Proton radiotherapy dose perturbations caused by esophageal stents of varying material composition are negligible in an experimental model. Endosc Int Open. 2014 Oct 24;03(01):E46–50.

215. Lee B, Cho S, Park HC, Kang SW, Kim JS, Chung JB. Assessment of dose perturbations for metal stent in photon and proton radiotherapy plans for hepatocellular carcinoma. Radiat Oncol Lond Engl. 2022 Jul 16;17(1):125.

216. Barrett JF, Keat N. Artifacts in CT: Recognition and Avoidance. RadioGraphics. 2004 Nov;24(6):1679–91.

217. Veikutis V, Budrys T, Basevicius A, Lukosevicius S, Gleizniene R, Unikas R, et al. 1571. Artifacts in computer tomography imaging: how it can really affect diagnostic image quality and confuse clinical diagnosis? . ISSN. 2015;17(2):9.

218. Boas FE, Fleischmann D. CT artifacts: causes and reduction techniques. Imaging Med. 2012 Apr;4(2):229–40.

219. Chen L, Huang B, Huang X, Cao W, Sun W, Deng X. Clinical evaluation for the difference of absorbed doses calculated to medium and calculated to water by Monte Carlo method. Radiat Oncol. 2018 Dec;13(1):137.

220. Siebers JV, Keall PJ, Nahum AE, Mohan R. Converting absorbed dose to medium to absorbed dose to water for Monte Carlo based photon beam dose calculations. Phys Med Biol. 2000 Apr 1;45(4):983–95.

221. Dogan N, Siebers JV, Keall PJ. Clinical comparison of head and neck and prostate IMRT plans using absorbed dose to medium and absorbed dose to water. Phys Med Biol. 2006 Oct 7;51(19):4967–80.

222. Paganetti H. Range uncertainties in proton therapy and the role of Monte Carlo simulations. Phys Med Biol. 2012 Jun 7;57(11):R99–117.

223. Yepes P, Adair A, Grosshans D, Mirkovic D, Poenisch F, Titt U, et al. Comparison of Monte Carlo and analytical dose computations for intensity modulated proton therapy. Phys Med Biol. 2018 Feb 9;63(4):045003.

224. Radojčić ĐS, Kolacio MŠ, Radojčić M, Rajlić D, Casar B, Faj D, et al. Comparison of calculated dose distributions reported as dose-to-water and dose-to-medium for intensity-modulated radiotherapy of nasopharyngeal cancer patients. Med Dosim. 2018;43(4):363–9.

225. Muñoz-Montplet C, Marruecos J, Buxó M, Jurado-Bruggeman D, Romera-Martínez I, Bueno M, et al. Dosimetric impact of Acuros XB dose-to-water and dose-to-medium reporting modes on VMAT planning for head and neck cancer. Phys Med. 2018 Nov;55:107–15.

226. Walters BRB, Kramer R, Kawrakow I. Dose to medium versus dose to water as an estimator of dose to sensitive skeletal tissue. Phys Med Biol. 2010 Aug 21;55(16):4535–46.

227. Sieber D, Erfurt P, John S, Santos GRD, Schurzig D, Sørensen MS, et al. The OpenEar library of 3D models of the human temporal bone based on computed tomography and micro-slicing. Sci Data. 2019 Jan 8;6(1):180297.

228. Yin Z, Hugtenburg RP, Beddoe AH. Response of silicon diode dosemeters to scattered radiation from megavoltage photon beams. Radiat Prot Dosimetry. 2002;101(1–4):415–8.

229. Green DE, Rubin CT. Consequences of irradiation on bone and marrow phenotypes, and its relation to disruption of hematopoietic precursors. Bone. 2014 Jun;0:87–94.

230. Manohara SR, Hanagodimath SM, Gerward L. Energy absorption buildup factors of human organs and tissues at energies and penetration depths relevant for radiotherapy and diagnostics. J Appl Clin Med Phys. 2011 Nov 15;12(4):296–312.

231. Goldbrunner R, Ruge M, Kocher M, Weiss Lucas C, Galldiks* N, Grau* S. The Treatment of Gliomas in Adulthood. Dtsch Ärztebl Int. 2018 May;115(20–21):356–64.

232. Pulte D, Brenner H. Changes in Survival in Head and Neck Cancers in the Late 20th and Early 21st Century: A Period Analysis. The Oncologist. 2010 Sep;15(9):994–1001.

233. Jereczek-Fossa BA, Zarowski A, Milani F, Orecchia R. Radiotherapy-induced ear toxicity. Cancer Treat Rev. 2003 Oct;29(5):417–30.

234. Scoccianti S, Detti B, Gadda D, Greto D, Furfaro I, Meacci F, et al. Organs at risk in the brain and their dose-constraints in adults and in children: A radiation oncologist's guide for delineation in everyday practice. Radiother Oncol. 2015 Feb;114(2):230–8.

235. Ding X, Zhou J, Li X, Blas K, Liu G, Wang Y, et al. Improving dosimetric outcome for hippocampus and cochlea sparing whole brain radiotherapy using spot-scanning proton arc therapy. Acta Oncol. 2019 Apr 3;58(4):483–90.

236. Mosleh-Shirazi MA, Amraee A, Mohaghegh F. Dose-response relationship and normal-tissue complication probability of conductive hearing loss in patients undergoing head-and-neck or cranial radiotherapy: A prospective study including 70 ears. Phys Med. 2019 May;61:64–9.

237. Zhang C, Liu L xiang, Li W zhan, Liang W, Chen Z hui, Huang X hai, et al. Cochlea sparing with a stratified scheme of dose limitation employed in intensity-modulated

radiotherapy for nasopharyngeal carcinoma: A dosimetry study. Med Dosim. 2019;44(3):226–32.

238. Grau C, Overgaard J. Postirradiation sensorineural hearing loss: A common but ignored late radiation complication. Int J Radiat Oncol. 1996 Sep;36(2):515–7.

239. Oh YT, Kim CH, Choi JH, Kang SH, Chun M. Sensory neural hearing loss after concurrent cisplatin and radiation therapy for nasopharyngeal carcinoma. Radiother Oncol. 2004 Jul;72(1):79–82.

240. Schmitt NC, Page BR. Chemoradiation-induced hearing loss remains a major concern for head and neck cancer patients. Int J Audiol. 2018 Aug 24;57(sup4):S49–54.

241. Lee TF, Yeh SA, Chao PJ, Chang L, Chiu CL, Ting HM, et al. Normal tissue complication probability modeling for cochlea constraints to avoid causing tinnitus after head-and-neck intensity-modulated radiation therapy. Radiat Oncol. 2015 Dec;10(1):194.

242. Johannesen TB, Rasmussen K, Winther FØ, Halvorsen U, Lote K. Late radiation effects on hearing, vestibular function, and taste in brain tumor patients. Int J Radiat Oncol. 2002 May;53(1):86–90.

243. Bhandare N, Jackson A, Eisbruch A, Pan CC, Flickinger JC, Antonelli P, et al. Radiation Therapy and Hearing Loss. Int J Radiat Oncol. 2010 Mar;76(3):S50–7.

244. Chan SH, Ng WT, Kam KL, Lee MCH, Choi CW, Yau TK, et al. Sensorineural Hearing Loss After Treatment of Nasopharyngeal Carcinoma: A Longitudinal Analysis. Int J Radiat Oncol. 2009 Apr;73(5):1335–42.

245. Cheraghi S, Nikoofar P, Fadavi P, Bakhshandeh M, Khoie S, Gharehbagh EJ, et al. Short-term cohort study on sensorineural hearing changes in head and neck radiotherapy. Med Oncol. 2015 Jul;32(7):200.

246. Rybak LP. Mechanisms of cisplatin ototoxicity and progress in otoprotection: Curr Opin Otolaryngol Head Neck Surg. 2007 Oct;15(5):364–9.

247. Low WK, Toh ST, Wee J, Fook-Chong SMC, Wang DY. Sensorineural Hearing Loss After Radiotherapy and Chemoradiotherapy: A Single, Blinded, Randomized Study. J Clin Oncol. 2006 Apr 20;24(12):1904–9.

248. Hua C, Bass JK, Khan R, Kun LE, Merchant TE. Hearing Loss After Radiotherapy for Pediatric Brain Tumors: Effect of Cochlear Dose. Int J Radiat Oncol. 2008 Nov;72(3):892–9.

249. Vieira WA, Weltman E, Chen MJ, da Silva NS, Cappellano AM, Pereira LD, et al. Ototoxicity evaluation in medulloblastoma patients treated with involved field boost using intensity-modulated radiation therapy (IMRT): a retrospective review. Radiat Oncol. 2014 Dec;9(1):158.

250. Pan CC, Eisbruch A, Lee JS, Snorrason RM, Ten Haken RK, Kileny PR. Prospective study of inner ear radiation dose and hearing loss in head-and-neck cancer patients. Int J Radiat Oncol. 2005 Apr;61(5):1393–402.

251. van der Laan HP, van de Water TA, van Herpt HE, Christianen MEMC, Bijl HP, Korevaar ErikW, et al. The potential of intensity-modulated proton radiotherapy to reduce swallowing dysfunction in the treatment of head and neck cancer: A planning comparative study. Acta Oncol. 2013 Apr;52(3):561–9.

252. Yock TI, Yeap BY, Ebb DH, Weyman E, Eaton BR, Sherry NA, et al. Long-term toxic effects of proton radiotherapy for paediatric medulloblastoma: a phase 2 single-arm study. Lancet Oncol. 2016 Mar;17(3):287–98.

253. Hitchcock YJ, Tward JD, Szabo A, Bentz BG, Shrieve DC. Relative Contributions of Radiation and Cisplatin-Based Chemotherapy to Sensorineural Hearing Loss in Head-and-Neck Cancer Patients. Int J Radiat Oncol. 2009 Mar;73(3):779–88.

254. Polkinghorn WR, Dunkel IJ, Souweidane MM, Khakoo Y, Lyden DC, Gilheeney SW, et al. Disease control and ototoxicity using intensity-modulated radiation therapy tumor-bed boost for medulloblastoma. Int J Radiat Oncol Biol Phys. 2011 Nov 1;81(3):e15-20.

255. Paulino AC, Mahajan A, Ye R, Grosshans DR, Fatih Okcu M, Su J, et al. Ototoxicity and cochlear sparing in children with medulloblastoma: Proton vs. photon radiotherapy. Radiother Oncol. 2018 Jul;128(1):128–32.

256. Mujica-Mota M, Waissbluth S, Daniel SJ. Characteristics of radiation-induced sensorineural hearing loss in head and neck cancer: A systematic review: Radiation-Induced Sensorineural Hearing Loss in Head and Neck Cancer. Head Neck. 2013 Nov;35(11):1662–8.

257. Nutting CM, Morden JP, Beasley M, Bhide S, Cook A, De Winton E, et al. Results of a multicentre randomised controlled trial of cochlear-sparing intensity-modulated radiotherapy versus conventional radiotherapy in patients with parotid cancer (COSTAR; CRUK/08/004). Eur J Cancer. 2018 Nov;103:249–58.

258. Ali M, Babaiah M, Madhusudhan N, George G. Comparative dosimetric analysis of IMRT and VMAT (RapidArc) in brain, head and neck, breast and prostate malignancies. Int J Cancer Ther Oncol. 2014 Dec 23;3(1):03019.

259. Gao J, Qian TL, Tao CZ, Zhang YH, Zhou Y, Yang J, et al. SmartArc-based volumetric modulated arc therapy can improve the middle ear, vestibule and cochlea sparing for locoregionally advanced nasopharyngeal carcinoma: a dosimetric comparison with step-and-shoot intensity-modulated radiotherapy. Br J Radiol. 2015 Sep;88(1053):20150052.

260. Dennis ER, Bussière MR, Niemierko A, Lu MW, Fullerton BC, Loeffler JS, et al. A Comparison of Critical Structure Dose and Toxicity Risks in Patients with Low Grade Gliomas Treated with IMRT versus Proton Radiation Therapy. Technol Cancer Res Treat. 2013 Feb;12(1):1–9.

261. Wang L, Yorke E, Chui CS. Monte Carlo evaluation of 6 MV intensity modulated radiotherapy plans for head and neck and lung treatments. Med Phys. 2002 Nov;29(11):2705–17.

262. Lyman JT. Complication probability as assessed from dose-volume histograms. Radiat Res Suppl. 1985;8:S13-19.

263. Kutcher GJ, Burman C. Calculation of complication probability factors for non-uniform normal tissue irradiation: the effective volume method. Int J Radiat Oncol Biol Phys. 1989 Jun;16(6):1623–30.

264. Allen Li X, Alber M, Deasy JO, Jackson A, Ken Jee KW, Marks LB, et al. The use and QA of biologically related models for treatment planning: short report of the TG-166 of the therapy physics committee of the AAPM. Med Phys. 2012 Mar;39(3):1386–409.

265. Papanikolaou N. Handbook of Radiotherapy Physics: Theory and Practice. Med Phys. 2008;35(9):4281–4281.

266. D'Avino V, Palma G, Liuzzi R, Conson M, Doria F, Salvatore M, et al. Prediction of gastrointestinal toxicity after external beam radiotherapy for localized prostate cancer. Radiat Oncol. 2015 Apr 8;10(1):80.

267. Cheraghi S, Nikoofar A, Bakhshandeh M, Khoei S, Farahani S, Abdollahi H, et al. Normal tissue complication probability modeling of radiation-induced sensorineural hearing loss after head-and-neck radiation therapy. Int J Radiat Biol. 2017 Dec;93(12):1327–33.

268. Hasenbalg F, Neuenschwander H, Mini R, Born EJ. Collapsed cone convolution and analytical anisotropic algorithm dose calculations compared to VMC++ Monte Carlo simulations in clinical cases. Phys Med Biol. 2007 Jul 7;52(13):3679–91.

269. Zhang C, Liu L xiang, Li W zhan, Liang W, Chen Z hui, Huang X hai, et al. GTV Cochlea Distance to Predict the Feasibility of Dose Limiting in Cochlea Sparing during Intensity Modulated Radiation Therapy for Nasopharyngeal Carcinoma. Clin Oncol [Internet]. 2019 Oct 10 [cited 2022 Jul 5];4(4). Available from: http://www.clinicsinoncology.com/pdfs_folder/cio-v4-id1665.pdf

270. Franzini A, Marchetti M, Brait L, Milanesi I, Messina G, Forapani E, et al. Deep brain stimulation and frameless stereotactic radiosurgery in the treatment of bilateral parkinsonian tremor: target selection and case report of two patients. Acta Neurochir (Wien). 2011 May;153(5):1069–75.

271. Kondziolka D, Flickinger JC, Lunsford LD. The principles of skull base radiosurgery. Neurosurg Focus. 2008 May;24(5):E11.

272. Sheehan JP, Yen CP, Lee CC, Loeffler JS. Cranial Stereotactic Radiosurgery: Current Status of the Initial Paradigm Shifter. J Clin Oncol. 2014 Sep 10;32(26):2836–46.

273. Rueß D, Pöhlmann L, Grau S, Hamisch C, Hellerbach A, Treuer H, et al. Long-term follow-up after stereotactic radiosurgery of intracanalicular acoustic neurinoma. Radiat Oncol. 2017 Apr 21;12(1):68.

274. Sims E, Doughty D, Macaulay E, Royle N, Wraith C, Darlison R, et al. Stereotactically Delivered Cranial Radiation Therapy: A Ten-Year Experience of Linac-Based Radiosurgery in the UK. Clin Oncol. 1999 Oct;11(5):303–20.

275. Walton L, Bomford CK, Ramsden D. The Sheffield stereotactic radiosurgery unit: physical characteristics and principles of operation. Br J Radiol. 1987 Sep;60(717):897–906.

276. Al-Dweri FMO, Rojas EL, Lallena AM. Effects of bone- and air-tissue inhomogeneities on the dose distributions of the Leksell Gamma Knife® calculated with PENELOPE. Phys Med Biol. 2005 Dec 7;50(23):5665–78.

277. Dağli Ö, Tanir, Ph.D. AG, Kurt G. Analysis of Radiation Dose Distribution Inhomogenity Effects in Gamma Knife Radiosurgery using Geant4. J Polytech [Internet]. 2020 Sep 18 [cited 2022 Aug 23]; Available from: https://dergipark.org.tr/en/doi/10.2339/politeknik.674718

278. Mathieu D, editor. Gamma Knife Radiosurgery [Internet]. InTech; 2011 [cited 2022 Aug 23]. Available from: http://www.intechopen.com/books/gamma-knife-radiosurgery

279. Régis J, Tamura M, Delsanti C, Roche PH, Pellet W, Thomassin JM. Hearing Preservation in Patients with Unilateral Vestibular Schwannoma after Gamma Knife Surgery. In: Régis J, Roche PH, editors. Progress in Neurological Surgery [Internet]. Basel: KARGER; 2008 [cited 2022 Aug 23]. p. 142–51. Available from: https://www.karger.com/Article/FullText/156901

280. Tamura M, Carron R, Yomo S, Arkha Y, Muraciolle X, Porcheron D, et al. HEARING PRESERVATION AFTER GAMMA KNIFE RADIOSURGERY FOR VESTIBULAR SCHWANNOMAS PRESENTING WITH HIGH-LEVEL HEARING. Neurosurgery. 2009 Feb;64(2):289–96.

281. Yuan J, Lo SS, Zheng Y, Sohn JW, Sloan AE, Ellis R, et al. Development of a Monte Carlo model for treatment planning dose verification of the Leksell Gamma Knife Perfexion radiosurgery system. J Appl Clin Med Phys. 2016 Jul;17(4):190–201.

282. Solberg TD, DeMarco JJ, Holly FE, Smathers JB, DeSalles AAF. Monte Carlo treatment planning for stereotactic radiosurgery. Radiother Oncol. 1998 Oct 1;49(1):73–84.

283. Cheung YC, Yu KN, Ho RTK, Yu CP. Stereotactic dose planning system used in Leksell Gamma Knife model-B: EGS4 Monte Carlo versus GafChromic ®lms MD-55. Appl Radiat Isot. 2000;4.

284. Peters GW, Tien CJ, Chiang V, Yu J, Hansen JE, Aneja S. Impact of tissue heterogeneity correction on Gamma Knife stereotactic radiosurgery of acoustic neuromas. J Radiosurgery SBRT. 2021;7(3):207–12.

285. Boari N, Bailo M, Gagliardi F, Franzin A, Gemma M, del Vecchio A, et al. Gamma Knife radiosurgery for vestibular schwannoma: clinical results at long-term follow-up in a series of 379 patients. J Neurosurg. 2014 Dec;121 Suppl:123–42.

286. Xu AY, Bhatnagar J, Bednarz G, Niranjan A, Flickinger J, Lunsford LD, et al. Dose differences between the three dose calculation algorithms in Leksell GammaPlan. J Appl Clin Med Phys. 2014 Sep;15(5):89–99.

287. Osmancikova P, Novotny J, Solc J, Pipek J. Comparison of the Convolution algorithm with TMR10 for Leksell Gamma knife and dosimetric verification with radiochromic gel dosimeter. J Appl Clin Med Phys. 2017 Dec 10;19(1):138–44.

288. Porter E, Fuentes P, Sala I, Siddiqui Z, Levitin R, Myziuk N, et al. Gamma Knife MR/CT/RTSTRUCT Sets With Hippocampal Contours (GammaKnife-Hippocampal) [Internet]. The Cancer Imaging Archive; 2022 [cited 2022 Aug 23]. Available from: https://wiki.cancerimagingarchive.net/x/UIX7B

289. Urie M, Goitein M, Holley WR, Chen GT. Degradation of the Bragg peak due to inhomogeneities. Phys Med Biol. 1986 Jan;31(1):1–15.

290. Sawakuchi GO, Titt U, Mirkovic D, Mohan R. Density heterogeneities and the influence of multiple Coulomb and nuclear scatterings on the Bragg peak distal edge of proton therapy beams. Phys Med Biol. 2008 Sep 7;53(17):4605–19.

291. Yamashita T, Akagi T, Aso T, Kimura A, Sasaki T. Effect of inhomogeneity in a patient's body on the accuracy of the pencil beam algorithm in comparison to Monte Carlo. Phys Med Biol. 2012 Nov 21;57(22):7673–88.

292. Bednarz B, Daartz J, Paganetti H. Dosimetric accuracy of planning and delivering small proton therapy fields. Phys Med Biol. 2010 Dec 21;55(24):7425–38.

293. Jia Y, Beltran C, Indelicato DJ, Flampouri S, Li Z, Merchant TE. Proton therapy dose distribution comparison between Monte Carlo and a treatment planning system for pediatric patients with ependymomaa): MC vs TPS. Med Phys. 2012 Jul 19;39(8):4742–7.

294. Bueno M, Paganetti H, Duch MA, Schuemann J. An algorithm to assess the need for clinical Monte Carlo dose calculation for small proton therapy fields based on quantification of tissue heterogeneity: Assessing the need for Monte Carlo dose calculation for small proton beams. Med Phys. 2013 Jul 10;40(8):081704.

295. Liang X, Li Z, Zheng D, Bradley JA, Rutenberg M, Mendenhall N. A comprehensive dosimetric study of Monte Carlo and pencil-beam algorithms on intensity-modulated proton therapy for breast cancer. J Appl Clin Med Phys. 2019;20(1):128–36.

296. Huang S, Souris K, Li S, Kang M, Barragan Montero AM, Janssens G, et al. Validation and application of a fast Monte Carlo algorithm for assessing the clinical impact of approximations in analytical dose calculations for pencil beam scanning proton therapy. Med Phys. 2018;45(12):5631–42.

297. Winterhalter C, Fura E, Tian Y, Aitkenhead A, Bolsi A, Dieterle M, et al. Validating a Monte Carlo approach to absolute dose quality assurance for proton pencil beam scanning. Phys Med Biol. 2018 Aug;63(17):175001.

Appendix

MATLAB code

loading all the files

```
clear
files = dir('fv*.asc');
numfiles = length(files);

for i=1:numfiles
    load(files(i).name);

end
load fvdvh17.txt;
```

reshaping the dose

```
rfv395=reshape (fv395',1,[]);
rfv495=reshape (fv495',1,[]);
rfv895=reshape (fv895',1,[]);
rfv995=reshape (fv995',1,[]);
rfv1095=reshape (fv1095',1,[]);
rfv1195=reshape (fv1195',1,[]);
rfv1295=reshape (fv1295',1,[]);
rfv1395=reshape (fv1395',1,[]);
rfv1495=reshape (fv1495',1,[]);
rfv1595=reshape (fv1595',1,[]);
rfv1695=reshape (fv1695',1,[]);
rfv1795=reshape (fv1795',1,[]);
rfv1895=reshape (fv1895',1,[]);
rfv1995=reshape (fv1995',1,[]);
rfv2095=reshape (fv2095',1,[]);
rfv2195=reshape (fv2195',1,[]);
rfv2295=reshape (fv2295',1,[]);
rfv2395=reshape (fv2395',1,[]);
rfv2495=reshape (fv2495',1,[]);
rfv2595=reshape (fv2595',1,[]);
rfv2695=reshape (fv2695',1,[]);
rfv2795=reshape (fv2795',1,[]);
rfv2895=reshape (fv2895',1,[]);
rfv2995=reshape (fv2995',1,[]);
rfv3095=reshape (fv3095',1,[]);
```

```
rfv3195=reshape (fv3195',1,[]);
rfv3295=reshape (fv3295',1,[]);
rfv3395=reshape (fv3395',1,[]);
rfv3495=reshape (fv3495',1,[]);
rfv3595=reshape (fv3595',1,[]);
rfv3695=reshape (fv3695',1,[]);
rfv3795=reshape (fv3795',1,[]);
rfv3895=reshape (fv3895',1,[]);
rfv3995=reshape (fv3995',1,[]);
rfv4095=reshape (fv4095',1,[]);
rfv4195=reshape (fv4195',1,[]);
rfv4295=reshape (fv4295',1,[]);
rfv4395=reshape (fv4395',1,[]);
rfv4495=reshape (fv4495',1,[]);
rfv4595=reshape (fv4595',1,[]);
rfv4695=reshape (fv4695',1,[]);
rfv4795=reshape (fv4795',1,[]);
rfv4895=reshape (fv4895',1,[]);
rfv4995=reshape (fv4995',1,[]);
rfv5095=reshape (fv5095',1,[]);
rfv5195=reshape (fv5195',1,[]);
```

reshaping the energy

```
rfv398=reshape (fv398',1,[]);
rfv498=reshape (fv498',1,[]);
rfv898=reshape (fv898',1,[]);
rfv998=reshape (fv998',1,[]);
rfv1098=reshape (fv1098',1,[]);
rfv1198=reshape (fv1198',1,[]);
rfv1298=reshape (fv1298',1,[]);
rfv1398=reshape (fv1398',1,[]);
rfv1498=reshape (fv1498',1,[]);
rfv1598=reshape (fv1598',1,[]);
rfv1698=reshape (fv1698',1,[]);
rfv1798=reshape (fv1798',1,[]);
rfv1898=reshape (fv1898',1,[]);
rfv1998=reshape (fv1998',1,[]);
rfv2098=reshape (fv2098',1,[]);
rfv2198=reshape (fv2198',1,[]);
rfv2298=reshape (fv2298',1,[]);
rfv2398=reshape (fv2398',1,[]);
```

```
rfv2498=reshape (fv2498',1,[]);
rfv2598=reshape (fv2598',1,[]);
rfv2698=reshape (fv2698',1,[]);
rfv2798=reshape (fv2798',1,[]);
rfv2898=reshape (fv2898',1,[]);
rfv2998=reshape (fv2998',1,[]);
rfv3098=reshape (fv3098',1,[]);
rfv3198=reshape (fv3198',1,[]);
rfv3298=reshape (fv3298',1,[]);
rfv3398=reshape (fv3398',1,[]);
rfv3498=reshape (fv3498',1,[]);
rfv3598=reshape (fv3598',1,[]);
rfv3698=reshape (fv3698',1,[]);
rfv3798=reshape (fv3798',1,[]);
rfv3898=reshape (fv3898',1,[]);
rfv3998=reshape (fv3998',1,[]);
rfv4098=reshape (fv4098',1,[]);
rfv4198=reshape (fv4198',1,[]);
rfv4298=reshape (fv4298',1,[]);
rfv4398=reshape (fv4398',1,[]);
rfv4498=reshape (fv4498',1,[]);
rfv4598=reshape (fv4598',1,[]);
rfv4698=reshape (fv4698',1,[]);
rfv4798=reshape (fv4798',1,[]);
rfv4898=reshape (fv4898',1,[]);
rfv4998=reshape (fv4998',1,[]);
rfv5098=reshape (fv5098',1,[]);
rfv5198=reshape (fv5198',1,[]);
```

multi with weighted factor for beam with electrons for energy bins (MeV) (weighted for 20X20)

```
EEW00175 = rfv5098*1.53E-04;
EEW0025 = rfv898*0.0017;
EEW0035 = rfv1098*1.05E-02;
EEW0045 = rfv1298*1.92E-02;
EEW0055 = rfv1498*2.19E-02;
EEW007 = rfv1698*4.20E-02;
EEW009 = rfv1898*3.62E-02;
EEW0125 = rfv2098*7.05E-02;
EEW0175 = rfv2298*4.93E-02;
EEW025 = rfv498*7.22E-02;
EEW035 = rfv2498*4.44E-02;
```

```
EEW045 = rfv2698*3.51E-02;
EEW0525 = rfv2898*2.09E-02;
EEW0605 = rfv3098*3.87E-02;
EEW073 = rfv3298*4.41E-02;
EEW09 = rfv3498*5.64E-02;
EEW1125 = rfv3698*6.23E-02;
EEW1375 = rfv3898*5.48E-02;
EEW175 = rfv4098*9.29E-02;
EEW25 = rfv4298*1.01E-01;
EEW35 = rfv4498*6.46E-02;
EEW45 = rfv4698*4.32E-02;
EEW55 = rfv4898*1.76E-02;
```

multi with weighted factor for beam without electrons for energy bins (MeV)

```
EW00175 = rfv5198*1.53E-04;
EW0025 = rfv998*1.73E-03;
EW0035 = rfv1198*1.05E-02;
EW0045 = rfv1398*1.92E-02;
EW0055 = rfv1598*2.19E-02;
EW007 = rfv1798*4.20E-02;
EW009 = rfv1998*3.62E-02;
EW0125 = rfv2198*7.05E-02;
EW0175 = rfv2398*4.93E-02;
EW025 = rfv398*7.22E-02;
EW035 = rfv2598*4.44E-02;
EW045 = rfv2798*3.51E-02;
EW0525 = rfv2998*2.09E-02;
EW0605 = rfv3198*3.87E-02;
EW073 = rfv3398*4.41E-02;
EW09 = rfv3598*5.64E-02;
EW1125 = rfv3798*6.23E-02;
EW1375 = rfv3998*5.48E-02;
EW175 = rfv4198*9.29E-02;
EW25 = rfv4398*1.01E-01;
EW35 = rfv4598*6.46E-02;
EW45 = rfv4798*4.32E-02;
EW55 = rfv4998*1.76E-02;
```

multi with weighted factor for beam with electrons for dose bins (MeV)

```
EDW00175 = rfv5095*1.53E-04;
```

```
EDW0025 = rfv895*1.73E-03;
EDW0035 = rfv1095*1.05E-02;
EDW0045 = rfv1295*1.92E-02;
EDW0055 = rfv1495*2.19E-02;
EDW007 = rfv1695*4.20E-02;
EDW009 = rfv1895*3.62E-02;
EDW0125 = rfv2095*7.05E-02;
EDW0175 = rfv2295*4.93E-02;
EDW025 = rfv495*7.22E-02;
EDW035 = rfv2495*4.44E-02;
EDW045 = rfv2695*3.51E-02;
EDW0525 = rfv2895*2.09E-02;
EDW0605 = rfv3095*3.87E-02;
EDW073 = rfv3295*4.41E-02;
EDW09 = rfv3495*5.64E-02;
EDW1125 = rfv3695*6.23E-02;
EDW1375 = rfv3895*5.48E-02;
EDW175 = rfv4095*9.29E-02;
EDW25 = rfv4295*1.01E-01;
EDW35 = rfv4495*6.46E-02;
EDW45 = rfv4695*4.32E-02;
EDW55 = rfv4895*1.76E-02;
```

multi with weighted factor for beam without electrons for Dose bins (MeV)

```
DW00175 = rfv5195*1.53E-04;
DW0025 = rfv995*1.73E-03;
DW0035 = rfv1195*1.05E-02;
DW0045 = rfv1395*1.92E-02;
DW0055 = rfv1595*2.19E-02;
DW007 = rfv1795*4.20E-02;
DW009 = rfv1995*3.62E-02;
DW0125 = rfv2195*7.05E-02;
DW0175 = rfv2395*4.93E-02;
DW025 = rfv395*7.22E-02;
DW035 = rfv2595*4.44E-02;
DW045 = rfv2795*3.51E-02;
DW0525 = rfv2995*2.09E-02;
DW0605 = rfv3195*3.87E-02;
DW073 = rfv3395*4.41E-02;
DW09 = rfv3595*5.64E-02;
DW1125 = rfv3795*6.23E-02;
```

```
DW1375 = rfv3995*5.48E-02;
DW175 = rfv4195*9.29E-02;
DW25 = rfv4395*1.01E-01;
DW35 = rfv4595*6.46E-02;
DW45 = rfv4795*4.32E-02;
DW55 = rfv4995*1.76E-02;
```

Sum of the all RUNS

```
finalsumED = rfv5095 + rfv895 + rfv1095 + rfv1295 + rfv1495 + rfv1695 +
rfv1895 + rfv2095 + rfv2295 + rfv495 + rfv2495 + rfv2695+ rfv2895 + rfv3095 +
rfv3295 + rfv3495 + rfv3695 + rfv3895 + rfv4095 + rfv4295 + rfv4495 + rfv4695
+ rfv4895;
finalsumD = rfv5195 + rfv995 + rfv1195 + rfv1395 + rfv1595 + rfv1795 +
rfv1995 + rfv2195 + rfv2395 + rfv395 + rfv2595 + rfv2795+ rfv2995 + rfv3195 +
rfv3395 + rfv3595 + rfv3795 + rfv3995 + rfv4195 + rfv4395 + rfv4595 + rfv4795
+ rfv4995;
finalsumEEW = EEW00175 + EEW0025 + EEW0035 + EEW0045 + EEW0055 + EEW007 +
EEW009 + EEW0125 + EEW0175 + EEW025 + EEW035 + EEW045 + EEW0525 + EEW0605 +
EEW073 + EEW09 + EEW1125 + EEW1375 + EEW175 + EEW25 + EEW35 + EEW45 + EEW55;
finalsumEW = EW00175 + EW0025 + EW0035 + EW0045 + EW0055 + EW007 + EW009 +
EW0125 + EW0175 + EW025 + EW035 + EW045 + EW0525 + EW0605 + EW073 + EW09 +
EW1125 + EW1375 + EW175 + EW25 + EW35 + EW45 + EW55;
finalsumEDW = EDW00175 + EDW0025 + EDW0035 + EDW0045 + EDW0055 + EDW007 +
EDW009 + EDW0125 + EDW0175 + EDW025 + EDW035 + EDW045 + EDW0525 + EDW0605 +
EDW073 + EDW09 + EDW1125 + EDW1375 + EDW175 + EDW25 + EDW35 + EDW45 + EDW55;
finalsumDW = DW00175 + DW0025 + DW0035 + DW0045 + DW0055 + DW007 + DW009 +
DW0125 + DW0175 + DW025 + DW035 + DW045 + DW0525 + DW0605 + DW073 + DW09 +
DW1125 + DW1375 + DW175 + DW25 + DW35 + DW45 + DW55;
```

comparing different energy deposit energy in the three different density

```
density = fv2998./fv2995;
sde=reshape (density',1,[]);
tmpE = finalsumEDW;
xstart = 2e-9;
interval = 2e-10;
xend = 200e-9;

h11 = histogram(tmpE(sde<1.75 & sde>1.25));
hold on;
h13 = histogram(tmpE(sde<1.25));
```

```
hold on
h12 = histogram(tmpE(sde>1.75));
hold on
figure(1);set(h11,'FaceColor',[0 0 0],'EdgeColor',[0 0
0],'EdgeAlpha',1,'facealpha',1);
set(h12,'FaceColor',[0 1 1],'EdgeColor',[0 1
1],'EdgeAlpha',0.5,'facealpha',0.5);
set(h13,'FaceColor',[1 0 0],'EdgeColor',[1 0
0],'EdgeAlpha',0.5,'facealpha',0.5);
hold off;

tmpE_A = sum(tmpE(sde<1.75 & sde>1.25));
tmpE_B = sum(tmpE(sde<1.25));
tmpE_C = sum(tmpE(sde>1.75));

tmpE_a_All = tmpE_A/(tmpE_A + tmpE_B+tmpE_C)
tmpE_b_All = tmpE_B/(tmpE_A + tmpE_B+tmpE_C)
tmpE_C_All = tmpE_C/(tmpE_A + tmpE_B+tmpE_C)

mean_value = mean(tmpE(sde<1.25))
```

MATLAB code

loading all the files

```
clear
files = dir('fv*.asc');
numfiles = length(files);

for i=1:numfiles
    load(files(i).name);

end
load fvdvh17.txt;
```

reshaping the dose

```
rfv395=reshape (fv395',1,[]);
rfv495=reshape (fv495',1,[]);
rfv895=reshape (fv895',1,[]);
rfv995=reshape (fv995',1,[]);
rfv1095=reshape (fv1095',1,[]);
rfv1195=reshape (fv1195',1,[]);
rfv1295=reshape (fv1295',1,[]);
rfv1395=reshape (fv1395',1,[]);
rfv1495=reshape (fv1495',1,[]);
rfv1595=reshape (fv1595',1,[]);
rfv1695=reshape (fv1695',1,[]);
rfv1795=reshape (fv1795',1,[]);
rfv1895=reshape (fv1895',1,[]);
rfv1995=reshape (fv1995',1,[]);
rfv2095=reshape (fv2095',1,[]);
rfv2195=reshape (fv2195',1,[]);
rfv2295=reshape (fv2295',1,[]);
rfv2395=reshape (fv2395',1,[]);
rfv2495=reshape (fv2495',1,[]);
rfv2595=reshape (fv2595',1,[]);
rfv2695=reshape (fv2695',1,[]);
rfv2795=reshape (fv2795',1,[]);
rfv2895=reshape (fv2895',1,[]);
rfv2995=reshape (fv2995',1,[]);
rfv3095=reshape (fv3095',1,[]);
rfv3195=reshape (fv3195',1,[]);
```

```
rfv3295=reshape (fv3295',1,[]);
rfv3395=reshape (fv3395',1,[]);
rfv3495=reshape (fv3495',1,[]);
rfv3595=reshape (fv3595',1,[]);
rfv3695=reshape (fv3695',1,[]);
rfv3795=reshape (fv3795',1,[]);
rfv3895=reshape (fv3895',1,[]);
rfv3995=reshape (fv3995',1,[]);
rfv4095=reshape (fv4095',1,[]);
rfv4195=reshape (fv4195',1,[]);
rfv4295=reshape (fv4295',1,[]);
rfv4395=reshape (fv4395',1,[]);
rfv4495=reshape (fv4495',1,[]);
rfv4595=reshape (fv4595',1,[]);
rfv4695=reshape (fv4695',1,[]);
rfv4795=reshape (fv4795',1,[]);
rfv4895=reshape (fv4895',1,[]);
rfv4995=reshape (fv4995',1,[]);
rfv5095=reshape (fv5095',1,[]);
rfv5195=reshape (fv5195',1,[]);
```

reshaping the energy

```
rfv398=reshape (fv398',1,[]);
rfv498=reshape (fv498',1,[]);
rfv898=reshape (fv898',1,[]);
rfv998=reshape (fv998',1,[]);
rfv1098=reshape (fv1098',1,[]);
rfv1198=reshape (fv1198',1,[]);
rfv1298=reshape (fv1298',1,[]);
rfv1398=reshape (fv1398',1,[]);
rfv1498=reshape (fv1498',1,[]);
rfv1598=reshape (fv1598',1,[]);
rfv1698=reshape (fv1698',1,[]);
rfv1798=reshape (fv1798',1,[]);
rfv1898=reshape (fv1898',1,[]);
rfv1998=reshape (fv1998',1,[]);
rfv2098=reshape (fv2098',1,[]);
rfv2198=reshape (fv2198',1,[]);
rfv2298=reshape (fv2298',1,[]);
rfv2398=reshape (fv2398',1,[]);
rfv2498=reshape (fv2498',1,[]);
```

```
rfv2598=reshape (fv2598',1,[]);
rfv2698=reshape (fv2698',1,[]);
rfv2798=reshape (fv2798',1,[]);
rfv2898=reshape (fv2898',1,[]);
rfv2998=reshape (fv2998',1,[]);
rfv3098=reshape (fv3098',1,[]);
rfv3198=reshape (fv3198',1,[]);
rfv3298=reshape (fv3298',1,[]);
rfv3398=reshape (fv3398',1,[]);
rfv3498=reshape (fv3498',1,[]);
rfv3598=reshape (fv3598',1,[]);
rfv3698=reshape (fv3698',1,[]);
rfv3798=reshape (fv3798',1,[]);
rfv3898=reshape (fv3898',1,[]);
rfv3998=reshape (fv3998',1,[]);
rfv4098=reshape (fv4098',1,[]);
rfv4198=reshape (fv4198',1,[]);
rfv4298=reshape (fv4298',1,[]);
rfv4398=reshape (fv4398',1,[]);
rfv4498=reshape (fv4498',1,[]);
rfv4598=reshape (fv4598',1,[]);
rfv4698=reshape (fv4698',1,[]);
rfv4798=reshape (fv4798',1,[]);
rfv4898=reshape (fv4898',1,[]);
rfv4998=reshape (fv4998',1,[]);
rfv5098=reshape (fv5098',1,[]);
rfv5198=reshape (fv5198',1,[]);
```

multi with weighted factor for beam without electrons for Dose bins (MeV)

```
DW0025 = rfv995*5.7;
DW0035 = rfv1195*12.34;
DW0045 = rfv1395*13.15;
DW0055 = rfv1595*12.99;
DW007 = rfv1795*26.44;
DW009 = rfv1995*27.38;
DW0125 = rfv2195*96.36;
DW0175 = rfv2395*94.76;
DW025 = rfv395*433.3;
DW035 = rfv2595*198.99;
DW045 = rfv2795*157.4;
DW0525 = rfv2995*76.37;
```

```
 DW0605 = rfv3195*162.82;
 DW073 = rfv3395*223.69;
 DW09 = rfv3595*395.75;
 DW1125 = rfv3795*811.97;
 DW1375 = rfv3995*276.92;
 finalsumDW =  DW0025 + DW0035 + DW0045 + DW0055 + DW007 + DW009 + DW0125 +
DW0175 + DW025 + DW035 + DW045 + DW0525 + DW0605 + DW073 + DW09 + DW1125 +
DW1375;
```

gamma knife 1.33 MeV

```
GS0025 = rfv895*5.7;
GS0035 = rfv1095*12.34;
GS0045 = rfv1295*13.15;
GS0055 = rfv1495*12.99;
GS007 = rfv1695*26.44;
GS009 = rfv1895*27.38;
GS0125 = rfv2095*96.36;
GS0175 = rfv2295*94.76;
GS025 = rfv495*433.3;
GS035 = rfv2495*198.99;
GS045 = rfv2695*157.4;
GS0525 = rfv2895*76.37;
GS0605 = rfv3095*162.82;
GS073 = rfv3295*223.69;
GS09 = rfv3495*395.75;
GS1125 = rfv3695*811.97;
GS1375 = rfv3895*276.92;

finalsumGS =  GS0025 + GS0035 + GS0045 + GS0055 + GS007 + GS009 + GS0125 +
GS0175 + GS025 + GS035 + GS045 + GS0525 + GS0605 + GS073 + GS09 + GS1125 +
GS1375 ;

MGS0025 = mean(GS0025);
MGS0035 = mean(GS0035);
MGS0045 = mean(GS0045);
MGS0055 = mean(GS0055);
MGS007 = mean(GS007);
MGS009 = mean(GS009);
MGS0125 = mean(GS0125) ;
MGS0175 = mean(GS0175);
MGS025 = mean(GS025);
```

```
MGS035 = mean(GS035);
MGS045 = mean(GS045);
MGS0525 = mean(GS0525);
MGS0605 = mean(GS0605);
MGS073 = mean(GS073);
MGS09 = mean(GS09);
MGS1125 = mean(GS1125);
MGS1375 = mean(GS1375);
MfinalsumGS = mean(finalsumGS);

stdGS0025 = std(GS0025);
stdGS0035 = std(GS0035);
stdGS0045 = std(GS0045);
stdGS0055 = std(GS0055);
stdGS007 = std(GS007);
stdGS009 = std(GS009);
stdGS0125 = std(GS0125) ;
stdGS0175 = std(GS0175);
stdGS025 = std(GS025);
stdGS035 = std(GS035);
stdGS045 = std(GS045);
stdGS0525 = std(GS0525);
stdGS0605 = std(GS0605);
stdGS073 = std(GS073);
stdGS09 = std(GS09);
stdGS1125 = std(GS1125);
stdGS1375 = std(GS1375);
stdfinalsumGS = std(finalsumGS);

stepGS0025 = GS0025-MGS0025;
stepGS0035 = GS0035-MGS0035;
stepGS0045 = GS0045-MGS0045;
stepGS0055 = GS0055-MGS0055;
stepGS007 = GS007-MGS007;
stepGS009 = GS009-MGS009;
stepGS0125 = GS0125-MGS0125 ;
stepGS0175 = GS0175-MGS0175;
stepGS025 = GS025-MGS025;
stepGS035 = GS035-MGS035;
stepGS045 = GS045-MGS045;
stepGS0525 = GS0525-MGS0525;
```

```
stepGS0605 = GS0605-MGS0605;
stepGS073 = GS073-MGS073;
stepGS09 = GS09-MGS09;
stepGS1125 = GS1125-MGS1125;
stepGS1375 = GS1375-MGS1375;
stepfinalsumGS = finalsumGS-MfinalsumGS;

zscoreGS0025 = (stepGS0025/stdGS0025) ;
zscoreGS0035 = (stepGS0035/stdGS0035);
zscoreGS0045 = (stepGS0045/stdGS0045);
zscoreGS0055 = (stepGS0055/stdGS0055);
zscoreGS007 = (stepGS007/stdGS007);
zscoreGS009 = (stepGS009/stdGS009);
zscoreGS0125 = (stepGS0125/stdGS0125);
zscoreGS0175 = (stepGS0175/stdGS0175);
zscoreGS025 = (stepGS025/stdGS025);
zscoreGS035 = (stepGS035/stdGS035);
zscoreGS045 = (stepGS045/stdGS045);
zscoreGS0525 = (stepGS0525/stdGS0525);
zscoreGS0605 = (stepGS0605/stdGS0605);
zscoreGS073 = (stepGS073/stdGS073);
zscoreGS09 = (stepGS09/stdGS09);
zscoreGS1125 = (stepGS1125/stdGS1125);
zscoreGS1375 = (stepGS1375/stdGS1375);
zscorefinalsumGS = (stepfinalsumGS/stdfinalsumGS);

density = fv2998./fv2995;
sde=reshape (density',1,[]);
tmpE = finalsumGS;
xstart = 2e-9;
interval = 2e-10;
xend = 200e-9;

h11 = histogram(tmpE(sde<1.75 & sde>1.25));
hold on;
h13 = histogram(tmpE(sde<1.25));
hold on
h12 = histogram(tmpE(sde>1.75));
hold on
figure(1);set(h11,'FaceColor',[0 0 0],'EdgeColor',[0 0
0],'EdgeAlpha',1,'facealpha',1);
```

```
set(h12,'FaceColor',[0 1 1],'EdgeColor',[0 1
1],'EdgeAlpha',0.5,'facealpha',0.5);
set(h13,'FaceColor',[1 0 0],'EdgeColor',[1 0
0],'EdgeAlpha',0.5,'facealpha',0.5);
hold off;

tmpE_A = sum(tmpE(sde<1.75 & sde>1.25));
tmpE_B = sum(tmpE(sde<1.25));
tmpE_C = sum(tmpE(sde>1.75));

tmpE_a_All = tmpE_A/(tmpE_A + tmpE_B+tmpE_C)
tmpE_b_All = tmpE_B/(tmpE_A + tmpE_B+tmpE_C)
tmpE_C_All = tmpE_C/(tmpE_A + tmpE_B+tmpE_C)




xstart = -2e-9;
interval = 1e-13;
xend = 2e-9;
h3 = histogram(zscorefinalsumGS,xstart:interval:xend);
hold on
h4 = histogram(zscoreGS025,xstart:interval:xend);
hold on
h5 = histogram(zscoreGS0525,xstart:interval:xend);
hold on
h6 = histogram(zscoreGS1125,xstart:interval:xend);
hold on
h7 = histogram(zscoreGS073,xstart:interval:xend);
hold on
h8 = histogram(zscoreGS009,xstart:interval:xend);
hold on
h9 = histogram(zscoreGS0025,xstart:interval:xend);
hold on
set(h3,'FaceColor',[0 0
0],'EdgeColor','none','EdgeAlpha',0.3,'facealpha',0.5)
set(h4,'FaceColor',[1 0
1],'EdgeColor','none','EdgeAlpha',0.3,'facealpha',0.5)
set(h5,'FaceColor',[0 0
1],'EdgeColor','none','EdgeAlpha',0.3,'facealpha',0.5)
```

```
set(h6,'FaceColor',[1 1
0],'EdgeColor','none','EdgeAlpha',0.3,'facealpha',0.5)
set(h7,'FaceColor',[1 0
1],'EdgeColor','none','EdgeAlpha',0.3,'facealpha',0.5)
set(h8,'FaceColor',[0 1
1],'EdgeColor','none','EdgeAlpha',0.3,'facealpha',0.5)
set(h9,'FaceColor',[0 1
0],'EdgeColor','none','EdgeAlpha',0.3,'facealpha',0.5)
hold off
```

DVH

```
load VS45.txt
DVH = VS45;
plot (DVH(:,3),DVH(:,4)); % DVH of the treatment plan
gp17=gradient(DVH(:,4));
figure; plot (DVH(:,3),-gp17);

meann=  sum(DVH(:,3).*-gp17)/sum(-gp17);
[h r]=hist(finalsumGS./finalsumDW*meann,0:0.2:120);
plot (r,h/9131020)
hold on
plot (DVH(:,3),-gp17/100);
c = conv(-gp17/100,h/9131020);
figure; plot (-meann:0.2:((length(c)-1)*0.2-meann),c)
figure ; plot(r,sum(h)-cumsum(h))


plot (DVH(:,3),DVH(:,4)/100);
hold on
plot(-meann:0.2:((length(c)-1)*0.2-meann),sum(c)-cumsum(c))
```